

Washington University in St. Louis

Washington University Open Scholarship

All Theses and Dissertations (ETDs)

January 2009

Feature Topography and Sound Intensity Level Encoding in Primary Auditory Cortex

Paul Watkins

Washington University in St. Louis

Follow this and additional works at: <https://openscholarship.wustl.edu/etd>

Recommended Citation

Watkins, Paul, "Feature Topography and Sound Intensity Level Encoding in Primary Auditory Cortex" (2009). *All Theses and Dissertations (ETDs)*. 370.

<https://openscholarship.wustl.edu/etd/370>

This Dissertation is brought to you for free and open access by Washington University Open Scholarship. It has been accepted for inclusion in All Theses and Dissertations (ETDs) by an authorized administrator of Washington University Open Scholarship. For more information, please contact digital@wumail.wustl.edu.

WASHINGTON UNIVERSITY
School of Engineering and Applied Science
Department of Biomedical Engineering

Dissertation Examination Committee:
Dennis L. Barbour, Chair
Dora E. Angelaki
Timothy E. Holy
Daniel W. Moran
William D. Smart
Kurt A. Thoroughman

FEATURE TOPOGRAPHY AND SOUND INTENSITY LEVEL ENCODING IN
PRIMARY AUDITORY CORTEX

by

Paul V. Watkins

A dissertation presented to the
Graduate School of Arts and Sciences
of Washington University in
partial fulfillment of the
requirements for the degree
of Doctor of Philosophy

December 2009

Saint Louis, Missouri

copyright by
Paul V. Watkins

2009

ABSTRACT OF THE DISSERTATION

Feature Topography and Sound Intensity Level Encoding in Primary Auditory Cortex

by

Paul V. Watkins

Doctor of Philosophy in Biomedical Engineering

Washington University in St. Louis, 2009

Research Advisor: Professor Dennis L. Barbour

The primary auditory cortex (A1) in mammals is one of the first areas in the neocortex that receives auditory related spiking activity from the thalamus. Because the neocortex is implicated in regulating high-level brain phenomena, such as attention and perception, it is therefore important in regards to these high-level behaviors to understand how sounds are represented and transformed by neuronal circuits in this area. The topographic organization of neuronal responses to auditory features in A1 provides evidence for potential mechanisms and functional roles of this neural circuitry. This dissertation presents results from models of topographic organization supporting the notion that if the topographic organization of frequency responses, termed tonotopy or cochleotopy, is aligned along the longest anatomical line segment in A1, as supported by some physiological studies, then it is unlikely that any other topography is mapped monotonically along the orthogonal axis. Thresholds of neuronal responses to sound intensity level represent a particular feature that may have a local, highly periodic topography and that is vital to the sensitivity of the auditory system. The neuronal representation of sound level in A1, particularly as it relates to encoding

accuracy, contains a distribution of neurons with varying amounts of inhibition at high sound levels. Neurons with large amounts of this high-level inhibition are described as nonmonotonic or level-tuned. This dissertation presents evidence from single neuron recordings in A1 that neurons exhibiting greater high-level inhibition also exhibit lower neuronal thresholds and that lower thresholds in these nonmonotonic neurons are preserved even when much of the neuronal population is adapted for accurately encoding more intense sounds. Evidence presented in this dissertation also suggests that nonmonotonic neurons have transient responses to time-varying (dynamic) level stimuli that adapt more quickly in response to low-level sounds than those of monotonic neurons. Together these results imply that under static, steady-state-dynamic and transient-dynamic sound level conditions, nonmonotonic neurons are specialized encoders of less intense sounds that allow the auditory system to maintain sensitivity under a variety of environmental conditions.

Acknowledgments

There are many to whom I owe gratitude for the completion of this dissertation. First and foremost I would like to thank my research advisor, Dr. Dennis Barbour. Throughout my graduate school tenure he has given me very thorough guidance and provided me with a rigorous and detail-oriented background, a solid foundation that will undoubtedly serve me well as I progress in my future scientific endeavors. I have counted numerous times when originally I found a piece of advice to be superfluous and in the end I was glad to have followed it. Secondly, I would like to thank the members of my thesis committee, for the feedback and suggestions they have provided on this work and also for being quite tolerant of my non-standard track to graduation. In particular, I owe special thanks to Dr. Kurt Thoroughman and Dr. Dora Angelaki. Kurt has made for an excellent lab neighbor during my tenure in the Barbour Lab. In addition he was one of my mentors during my participation in the CCSN pathway and his computational neuroscience course was the incubator out of which the work for Chapter 3 of this dissertation was born. I had the good fortune of working for over a semester in Dora's lab, and that experience has definitely influenced my growth as a scientist. Computational modeling that I performed during this time with Dora as a co-mentor resulted in a second-author publication for me, the first published study in which I have participated. I also owe thanks to my other co-mentor for this project, Dr. Greg DeAngelis, whose scientific perspectives I have always found insightful and whose teachings were always quite logically presented. At least two other Professors that are not on my committee deserve special mention for their guidance in my research, Dr. Charles Anderson and Dr. David VanEssen. In the category of scientific

mentors, I would also like to thank Dr. Frank Yin, the chair of the Biomedical Engineering Department during my time as a graduate student. I am constantly in awe of his ability to garner publicity and funding for the department while at the same time supporting a collaborative environment and paying personal attention to each and every graduate student. Finally, I thank Dr. David Sept, who was helpful in guiding course selections as my academic advisor for a good portion of my grad school tenure and who also served as a good role model for a successful scientist.

I would like to thank all of the graduate students, postdocs and undergrads in the Barbour Lab and in other labs that have provided me with feedback on work presented in this dissertation, and also several projects not presented here. In particular I would like to thank Yong Gu, first author on the work published from the Angelaki Lab, Woosung Kim, my lab partner in crime, Thomas Chen, a co-author on work published from Chapter 3 of this dissertation, Nathan Killian, whose work revitalized my first project in Dennis' lab and Jordan Taylor, Paul Wanda, Shane Heiney and Vinod Rao who all provided me with much thought-provoking discussion and with useful feedback on multiple projects. Special thanks to Justin Brooks, not only for useful discussions, but in particular for volunteering to take on the responsibilities of CCSN Journal Club coordinator after me. Although not directly scientific in nature, I am deeply indebted to Kim Kocher and Angela Gúzman, the current and previous lab technicians for the Barbour lab respectively. Kim's diligence especially allowed me to focus much more of my time on research.

Of course, I would like to thank my friends for their support during my years as a graduate student. Of friends of old I unfortunately have lost touch with many, but this is not the case of my longest-standing good friend, Graeme Dickinson. Of friends I have met while in St. Louis there are many. I pay special recognition here to those with whom I spent the most time in two categories: those who had to deal with me as a roommate and the rest. In the former category, I thank Dan Kuster, Ken Borrelli, Ben Filas and Matt Riordan and in the latter I thank Stephanie Willerth, Nick Anderson, Mena Morales, Eric Yttri, Paul Wanda, Molly Witges and Ryan Smith. If you're reading this and you didn't make the list, I apologize, but you know who you are. I've met scores of fun and amazing people in St. Louis, too many to enumerate here.

Ultimately I owe the most to my family, especially my parents, my siblings and my grandparents, who have shaped the most core parts of my personality. My parents have always provided me with an amazing amount of love and support, but in combination with affording me a good deal of independence and understanding. Although I try to be appreciative, I know that I can never really repay them for what they have done for me.

Paul V. Watkins

Washington University in St. Louis

December 2009

Contents

Abstract	ii
Acknowledgments	iv
List of Tables	ix
List of Figures	x
1 General Introduction	1
2 Experimental Methods	5
2.1 A Computational Framework for Topographies of Cortical Areas.....	6
2.1.1 Self-Organizing Feature Map.....	6
2.1.2 Unit Grid Initialization	8
2.1.3 Metrics of Topographical Characteristics	9
2.1.4 Conditions Driving Dominance and Global Orthogonality	18
2.2 Neuronal Responses to Sound Intensity Level.....	21
2.2.1 Electrophysiology	21
2.2.2 Acoustic Stimuli	23
2.2.3 Data Analysis.....	24
2.3 Neuronal Adaptation to Sound Intensity Level.....	30
2.3.1 Acoustic Stimuli	30
2.3.2 Data Analysis.....	34
2.4 Time Course of Neuronal Adaptation to Sound Intensity Level.....	39
2.4.1 Acoustic Stimuli	39
2.4.2 Data Analysis.....	44
3 A Computational Framework for Topographies of Cortical Areas	64
3.1 Introduction	64
3.2 Results	56
3.2.1 Primary Visual Cortex Topographies	56
3.2.2 Topographic Properties of Square Maps with Two Features	59
3.2.3 Conditions Driving Dominance and Global Orthogonality in Square Unit Grids.....	63
3.2.4 Conditions Driving Dominance in Other Grid Shapes.....	71
3.2.5 Conditions Driving Dominance and Global Orthogonality in Sets of Elliptical Grids	73
3.3 Discussion	81
3.3.1 Model Geometries	82
3.3.2 Feature Dominance.....	83

3.3.3	Global Orthogonality.....	85
3.3.4	Relevance to Cortical Physiology.....	86
3.3.5	Experimental Limitations.....	90
3.3.6	Future Studies.....	92
4	Neuronal Responses to Sound Intensity Level.....	94
4.1	Introduction.....	94
4.2	Results.....	97
4.3	Discussion.....	132
5	Neuronal Adaptation to Sound Intensity Level.....	138
5.1	Introduction.....	138
5.2	Results.....	141
5.2.1	Static Rate-Level Responses.....	142
5.2.2	Single Neuron Adaptation to Dynamic Level Stimuli.....	145
5.2.3	Population Adaptation to Dynamic Level Stimuli.....	149
5.2.4	Adaptation in Onset versus Sustained Spiking.....	181
5.2.5	Adaptation Dynamics.....	186
5.3	Discussion.....	190
5.3.1	Dynamic Range and Level Encoding.....	196
5.3.2	Relation to Previous Studies.....	199
6	Time Course of Neuronal Adaptation to Sound Intensity Level.....	203
6.1	Introduction.....	203
6.2	Results.....	205
6.2.1	Dynamic-Transition Stimuli.....	208
6.2.2	Adaptation Time Course in Single Neurons.....	209
6.2.3	Population Rate-Level Adaptation to Dynamic-Transition Stimuli.....	216
6.2.4	Population Mean-Rate Adaptation to Dynamic-Transition Stimuli.....	231
6.3	Discussion.....	240
Appendix A	Neuronal Correlations between Simultaneously Recorded Neurons and the Effect on Measures of Encoding and Decoding of Sound Intensity Level.....	247
A.1	Methods.....	248
A.2	Results.....	253
A.3	Discussion.....	266
References	268
Vita	277

List of Tables

Table 2.1: Summary of All Metrics Used to Quantify Trends in the SOFMs	29
Table 6.1: Comparison with Time Constants Measured in Other Studies	244

List of Figures

Figure 2.1:	Two-Tailed Split Gaussian Model Schematic	26
Figure 2.2:	Dynamic-Stimulus Protocol Design	33
Figure 2.3:	Example Dynamic-Transition Stimulus	42
Figure 2.4:	Schematics of Adaptation Models	48
Figure 3.1:	Topographies of V1 Generated by SOFM Algorithm	58
Figure 3.2:	Cartesian Map with Two Features	60
Figure 3.3:	Dominance in Two-Feature Square SOFM	62
Figure 3.4:	Dominance in Three-Feature Square SOFM	65
Figure 3.5:	Global Orthogonality in Four-Feature Square SOFM	67
Figure 3.6:	Graphical Depiction of Metric Calculations	69
Figure 3.7:	Two-Feature SOFM Experiments with Non-Square Unit Grids	72
Figure 3.8:	Dominance / Global Orthogonality Interrelationship in Elliptical Unit Grids.....	74
Figure 3.9:	Trends in Shared Local Orthogonality and Coverage in Elliptical Unit Grids.....	78
Figure 4.1:	Spectrum of Nonmonotonicity in Rate-Level Functions.....	99
Figure 4.2:	Dynamic Ranges as a Function of Characteristic Frequency.....	102
Figure 4.3:	Comparison of Monotonic and Nonmonotonic Neuron Residual Thresholds.....	105
Figure 4.4:	Dynamic Ranges Sorted by Residual Threshold.....	110
Figure 4.5:	Dynamic Range Magnitudes	113
Figure 4.6:	Residual Threshold as a Function of Monotonicity Index	116
Figure 4.7:	Correlation between Spontaneous Rate and Residual Threshold	119
Figure 4.8:	Maximum Discharge Rate as a Function of Monotonicity Index.....	121
Figure 4.9:	Correlation between Best Level and Dynamic Range	124
Figure 4.10:	Goodness of Fit and Neuron Depth Distributions for Monotonic and Nonmonotonic Neurons	127
Figure 4.11:	Columnar Organization of Characteristic Frequency and Monotonicity Index	130
Figure 5.1:	Monotonic and Nonmonotonic Rate-Level Examples	143
Figure 5.2:	Dynamic Rate-Level and Fisher information Functions for Example Neurons	147
Figure 5.3:	Average Dynamic Rate-Level and Fisher Information Functions.....	152
Figure 5.4:	Average Adapted Dynamic Ranges as a Function of Dynamic Stimulus Probability Plateau Center	156
Figure 5.5:	Dynamic Range Midpoints as a Function of Monotonicity Index	160
Figure 5.6:	Dynamic Range Midpoints as a Function of Dynamic Stimulus Probability Plateau Center and Segregated by Monotonicity Index Class.....	166
Figure 5.7:	Upper Dynamic Range Midpoints as a Function of Dynamic	

	Stimulus Probability Plateau Center for Nonmonotonic Neurons.....	169
Figure 5.8:	Lower and Upper Dynamic Ranges for Nonmonotonic Neurons over High-Probability Sound Level Ranges	173
Figure 5.9:	Lower and Upper Dynamic Ranges for Nonmonotonic Neurons over Low-Probability Sound Level Ranges	177
Figure 5.10:	Fisher Information Averages Calculated using 1-dB Level Bins	179
Figure 5.11:	Fisher Information Averages Calculated using Onset Responses	182
Figure 5.12:	Fisher Information Averages Calculated using Offset Responses	184
Figure 5.13:	Fisher Information Averages Excluding Adaptation Transients	188
Figure 5.14:	Sound Level Adaptation Schematic Summary.....	194
Figure 6.1:	Influence of Preceding Stimulus Sound Levels on Spiking Rates.....	207
Figure 6.2:	Example Responses to Dynamic-Transition Stimuli with Behavior Predicted by Static Rate-Level Monotonicity.....	212
Figure 6.3:	Example Responses to Dynamic-Transition Stimuli with Behavior Not Predicted by Static Rate-Level Monotonicity	215
Figure 6.4:	Distribution of Static Rate-Level Monotonicity Indices for Different Transition and Response Types.....	218
Figure 6.5:	Comparison of Rate-Level and Mean-Rate Adaptation Time Constants	222
Figure 6.6:	Average Responses for Different Categories of the High-to-Low Transients	224
Figure 6.7:	Average Responses for Different Categories of the Low-to-High Transients	225
Figure 6.8:	Comparison of Rate-Level Adaptation Time Constants for Dynamically-Monotonic and Dynamically-Nonmonotonic Neurons.....	229
Figure 6.9:	Comparison of Mean-Rate Adaptation Time Constants Estimated Using 1-second and 400-ms Time Windows	234
Figure 6.10:	Comparison of Mean-Rate Adaptation Time Constants for Mean- Dynamically Monotonic and Mean-Dynamically Nonmonotonic Neurons	238
Figure A.1:	Mean Coding Accuracy from Static Rate-Level Responses.....	255
Figure A.2:	Effect of Noise Correlations on Mean Coding Accuracy in Simultaneously Recorded Neurons	258
Figure A.3:	Mean Coding Accuracies for 10 dB and 20 dB Level Discrimination and Mean Correlations at Different Sound Levels.....	260
Figure A.4:	Mean Coding Accuracy and Effect of Noise Correlations versus Mean Monotonicity of Simultaneously Recorded Neurons.....	264

Chapter 1

General Introduction

Systems neuroscience is a facet of brain science that involves the study of how complex circuits of interconnected neurons in different brain areas work together to create observable behaviors. This endeavor incorporates neural physiology and anatomy over a range of spatial and temporal scales: from single neurons to circuits of neurons to brain areas and over timescales from milliseconds to years. Much of this research has been focused on the neocortex of mammalian species. At a high level, brain function can be seen as a transformation of inputs coming from the epithelium of sensory organs into signals which control muscles, or motor outputs. One predominant hypothesis is that information is transmitted in the brain via action potentials fired by single neurons, and that much of this information is encoded in the rate of these action potentials over short time periods (on the order of tens of milliseconds). Sensory neuroscience, a subset of systems neuroscience, aims to understand how physical aspects of sensory inputs are encoded via action potentials in single neurons and in populations of neurons. Spiking activity that is measured from single neurons recorded separately or simultaneously and that can be initiated with sensory stimuli is often called a neuronal response.

Auditory neuroscience is concerned in particular with how aspects of sound are transduced into action potentials initially by the cochlea of the inner ear, then how these signals from the cochlea are transformed in order to process auditory signals and finally how these transformed inputs are able to produce complex behaviors based on cues in an auditory scene. One general approach to understanding how circuits represent and transform these physical characteristics of sound is to use a single metal electrode, placed into brain tissue, to record spiking activity in a single neuron and then correlate the spiking rate with physical characteristics of the sound presented while this activity is occurring. This approach provides insight into how sounds are represented and transformed by single neurons. In general (when referring to multiple sensory systems) these are referred to as sensory representation and transformation. Averaging over a population of recorded neurons in turn can provide evidence for how these tasks are performed by neuronal circuits. The way that neurons and groups of neurons represent a particular property is referred to as neural encoding. In contrast, how postsynaptic neurons can use these encodings to infer the values of the property being encoded is referred to as neural decoding.

There is evidence from anatomical studies of sensory cortices suggesting that the majority of cortical interconnectivity is intrinsic to the cortical area (Creutzfeldt, 1977; Lee & Winer, 2008b). Therefore, the way that single neurons in a particular circuit and within a given cortical area are organized spatially, not only anatomically, but physiologically (i.e. how neuronal responses are organized spatially) also provides

evidence for what transformations are computed by these circuits and for the mechanisms of these transformations. If neuronal responses are organized spatially in a non-random manner, then the resulting map is called a topographic organization. Because neocortex is organized in layers that contain neurons having similar response properties (Mountcastle, 1997), termed a columnar organization, only the two spatial dimensions of the cortical surface are usually considered as a part of these topographical maps. A given brain area may contain multiple maps corresponding to different features of the neuronal response (Blasdel & Salama, 1986; Tootell, Hamilton, Silverman, & Switkes, 1988; Tootell, Silverman, Hamilton, De Valois, & Switkes, 1988; Tootell, Silverman, Hamilton, Switkes, & De Valois, 1988; Tootell, Switkes, Silverman, & Hamilton, 1988). The existence of a unique topography has historically been used as one of the criteria for establishing the existence of a cortical area because it provides evidence that neuronal circuits in this area are using coherent sensory representations and are likely working together on a single set of transformations within a hierarchy of processing (Felleman & Van Essen, 1991; Van Essen, 1985).

The primary auditory cortex (A1) in mammals is one of the first areas in the neocortex that receives auditory related spiking activity from the thalamus (Lee & Winer, 2008a; Winer, Diamond, & Raczkowski, 1977). Because the neocortex is implicated in regulating high-level brain phenomena, such as attention and perception, it is therefore important in regards to these high-level behaviors to understand how sounds are represented and transformed in this particular area. This dissertation describes the

results of testing hypotheses of topographic organization and of representation of sound intensity level, both in A1. As described above, topographic organization and representation of sound properties are both involved in understanding what types of transformations are accomplished by A1 circuits and in understanding the potential mechanisms of these transformations. Two very different approaches were taken towards testing these two general objectives: (1) A computational model was employed in the effort of testing hypotheses regarding A1 topographic organization (2) Single neurons were recorded in A1 and these data were analyzed in order to test the hypotheses regarding the representation of sound intensity level. The results of the first objective are presented and discussed in Chapter 3, and of the latter in Chapters 4 through 6. A more detailed introduction of each topic is given separately before the results in each chapter. The methods for each chapter are presented in different subsections of Chapter 2.

Chapter 2

Experimental Methods

A combination of two very different approaches was utilized to study auditory coding phenomena in Primary Auditory Cortex (A1): (1) A computational model was created to investigate how the neuronal circuits that are responsible for the representation and transformation of sound intensity level and of other features are organized topographically and (2) Single neurons were recorded in A1 of awake marmoset monkeys (*Callithrix jacchus*) in order to discern how these neurons represent and encode sound intensity level, particularly of the tone to which the neuron being recorded is the most sensitive. Methods for the first approach are presented in Section 2.1 and for the second approach in Sections 2.2 to 2.4.

2.1 A Computational Framework for Topographies of Cortical Areas

2.1.1 Self-Organizing Feature Map

The self-organizing feature map (SOFM) is a computational tool designed to project an N -dimensional observable feature vector onto a two-dimensional grid of spatially arrayed N -dimensional feature vectors, each of which is referred to as a “unit” (Kohonen, 1990). For the purposes of this study, the N features of the observable vector and the unit feature vectors are each meant to represent aspects of neuronal response properties that are hypothesized to be mapped topographically in a sensory cortical area. These neuronal features could include any receptive field parameter pertaining to a given sensory cortical area. The units of the SOFM grid are intended conceptually to represent cortical neurons or spatially clustered groups of similar neurons whose receptive fields are characterized by the elements of a particular unit feature vector. The SOFM algorithm is a dimensionality-reduction algorithm used to map the N feature dimensions of neuronal response parameter space onto the two physical dimensions of the cortical surface. The SOFM has been shown to produce:

[unit feature] vectors that asymptotically settle to equilibrium values, generating a map which 1) represents most faithfully dimensions of feature space along which the standard deviation is largest; 2) tries to preserve continuity, such that (metrically) similar patterns are mapped onto neighboring points in the network layer; 3) reflects inhomogeneities in the probability density such that regions with high density are mapped onto larger domains of the network layer. (Ritter & Schulten, 1988)

SOFMs are created using a competitive learning algorithm applied over the entire unit grid, such that units compete with one another for representation of any particular feature vector in the N -dimensional feature space (Kohonen, 1990). At each time step t , the iterative algorithm presents to the unit grid an observable vector \mathbf{v} having length N , each element of which has a value drawn randomly from one of the individual feature distributions. The algorithm then determines which of the unit feature vectors $\mathbf{w}_{\mathbf{r}}$ is closest to the current observable vector in terms of Euclidean distance:

$$\mathbf{s} = \min_{\mathbf{r}} \{ \|\mathbf{v} - \mathbf{w}_{\mathbf{r}}\| \} . \quad (2.1)$$

In this case \mathbf{r} represents a two-dimensional vector of grid coordinates for arbitrary unit feature vectors corresponding to cortical surface locations, and \mathbf{s} represents a two-dimensional vector of grid coordinates for the unit feature vector closest to \mathbf{v} . This vector $\mathbf{w}_{\mathbf{s}}$ is then moved closer to the observable vector \mathbf{v} , along with neighboring units in the grid. This update is given by

$$\mathbf{w}_{\mathbf{r}}(t+1) = \mathbf{w}_{\mathbf{r}}(t) + \varepsilon(t)h(\mathbf{r}, \mathbf{s}, \sigma)[\mathbf{v} - \mathbf{w}_{\mathbf{r}}(t)] , \quad (2.2)$$

where the $\mathbf{w}_{\mathbf{r}}$ vector refers to all the unit feature vectors in the grid. The direction of the update term on the right-hand side is determined by \mathbf{v} and the magnitude is governed by a learning rate ε and a neighborhood function h . The learning rate limits the magnitude of map change that can occur in any given time step and can be decreased as time progresses to promote convergence onto a local solution. The neighborhood function

limits the units in the grid that change substantially in any given time step and is given by a two-dimensional Gaussian centered on the winning unit with a width parameter (standard deviation) of σ :

$$h(\mathbf{r}, \mathbf{s}, \sigma) = \exp\left[-\frac{\|\mathbf{r} - \mathbf{s}\|^2}{\sigma^2}\right]. \quad (2.3)$$

Because learning in the SOFM algorithm is driven by serial presentation of observable vectors to the grid and incorporates a local Hebbian learning rule via the neighborhood function, the algorithm can be thought of as an activity-dependent model of cortical reorganization. Activity is driven by the observable vectors, and thus the probability distribution of each feature ultimately determines the number of units devoted to a particular subset of the feature space.

2.1.2 Unit Grid Initialization

In each computational experiment, SOFM unit grid maps were initialized using one of two methods. The first method of “random initialization” initialized feature vector elements randomly across the unit grid using a Gaussian distribution with mean of zero and standard deviation set at one-sixth of the standard deviation for the corresponding feature in the observable vector. This ratio of standard deviations was based upon a previous study utilizing SOFMs to investigate V1 topographies (Swindale, 2004). The second method of “Cartesian initialization,” used only with square unit grids, initialized

unit feature vectors such that the first two feature maps were monotonically spaced along the two orthogonal axes of the unit grid while the remaining feature maps, if any, were initialized randomly as in the first method. Cartesian initialization was explored to emulate a genetically predetermined topography (e.g., development of tonotopically mapped projections from the thalamus to A1). Following training, Cartesian initialization yielded stable maps similar to those resulting from random initialization in all conditions tested.

2.1.3 Metrics of Topographical Characteristics

Metrics of topographic map characteristics were devised to quantify observations made in stable SOFM maps and also to view trends over sets of repeated SOFM experiments. All metrics except the contour orientation metric were averaged (arithmetic mean) when compiled over sets of SOFM experiments having identical map parameters but using different random seeds for initialization.

We defined globally orthogonal features as two features that were mapped smoothly and monotonically along orthogonal orientations in the unit grid such that their contour lines intersected predominantly at right angles. We quantified smoothness and monotonicity of a feature with the cyclic contour metric (CCM). This metric measures the amount of grid area accounted for by units lying within the boundary of at least one closed iso-feature contour. A large percentage of units surrounded by iso-feature

contours in a particular feature map reflects either spatial periodicity or discontinuity of this feature. Therefore, when the CCM for a given feature is close to zero, this feature is smoothly and monotonically mapped along one direction through the grid. In order to assess whether two features were each smoothly and monotonically mapped (implying global orthogonality), we calculated a collective CCM as the union of units surrounded by iso-feature contours for each feature. If, for example, features 1 and 2 out of N were being evaluated for global orthogonality, the $CCM_{1,2}$ would be calculated by assessing the union of the number of units completely enclosed by at least one iso-feature contour of either feature 1 or feature 2 and dividing that number by the total number of units in the grid:

$$CCM_{i,j} = \frac{\text{units enclosed in } i \cup \text{units enclosed in } j}{\text{total number of units}} . \quad (2.4)$$

Unit enclosure was tested using 100 iso-feature contours evenly spaced over the total range of the feature. We accounted for periodicity along the grid edges by including units that were mostly but not entirely surrounded by iso-feature contours (details below).

We defined a Cartesian map as a two-feature map on a square unit grid where each feature topography could be well fit with a plane. These planes are oriented so that the iso-feature contours of one plane lie parallel to the vertical grid edges, and the iso-feature contours of the other plane lie parallel to the horizontal grid edges. In this case, the iso-feature contour plots for both features are aligned with the edges of the unit

grid. Two features that form a Cartesian map are globally orthogonal, and $CCM_{1,2}$ for such a situation is zero because the iso-feature contours do not close upon themselves. As two feature maps depart from mutual global orthogonality, their maps become more periodic or discontinuous and thus the grid contains a larger percentage of units enclosed by iso-feature contours. The higher values of the CCM in this case imply that global orthogonality does not exist between these feature maps, although local orthogonality may still be preserved.

Local orthogonality between two feature maps is a condition less strict than global orthogonality whereby the iso-feature contours of one feature intersect the contours of another feature predominantly at right angles but are not necessarily smoothly and monotonically mapped onto the unit grid. We evaluated local orthogonality with the contour intersection deviation metric (CIDM). It is difficult to calculate the angle of iso-feature contours without interpolation, so the metric was actually calculated at each unit in the grid by measuring the angle between the gradient vectors of the two features being tested for local orthogonality. Because each feature's gradient is perfectly orthogonal to its iso-feature contours, the angle between the gradient vectors is equal to the angle between the iso-feature contours. The contour intersection deviation metric was taken as the root mean squared deviation from 90° of gradient intersection angles between two features:

$$CIDM_{i,j} = \sqrt{\frac{1}{M-1} \sum_{m=1}^M \left(\cos^{-1} \left(\frac{\|\mathbf{g}_{i,m} \mathbf{g}_{j,m}\|}{\|\mathbf{g}_{i,m}\| \|\mathbf{g}_{j,m}\|} \right) - 90^\circ \right)^2} , \quad (2.5)$$

where M is the total number of units in the grid and $\mathbf{g}_i, \mathbf{g}_j$ represent the gradient vector for features i and j , respectively. For two features that are locally or globally orthogonal, this metric will approach zero. For two features whose contours run mostly parallel to one another (i.e., angles of intersection near zero degrees), this metric will approach 90° . Intersection angles drawn from a uniform distribution in the range $[0^\circ 180^\circ]$ have a root mean squared deviation from 90° equal to 52° ; therefore, if a particular probability distribution of iso-feature contour intersections has a CIDM of less than 52° , then the probability density function of this distribution will be clustered closer to 90° than to 0° and 180° .

Another property observed in some stable maps was termed dominance. We defined a dominant feature as one that 1) exhibits a monotonic gradient topography, 2) aligns its gradient axis closely with the longest line segment enclosed by the unit grid. We measured this characteristic with the contour orientation metric (COM). This metric was calculated as the angle between the longest line segment enclosed by the unit grid and the axis of gradation of the feature map in question. The axis of gradation direction was calculated by fitting grid features to a plane in three dimensions and measuring the orientation of the fitted plane:

$$z_i = ax + by + c \quad , \quad \theta_i = \arctan\left[\frac{b}{a}\right] \quad , \quad (2.6)$$

where x and y are the grid coordinates; z_i is the value of feature i represented by the unit at coordinates (x, y) ; a , b , and c are the parameters to be fit; and θ_i is the orientation of the fitted plane. The COM_i was calculated by subtracting the angle of the longest line segment in the grid from θ_i . The COM assumes that the feature map under consideration fits a plane well, so a coefficient of determination (r^2) for the fitted plane was also calculated to assess this assumption. This measure represents the goodness of the fit for the plane, i.e., the proportion of the variance in the data that is accounted for by the planar fit:

$$r^2 = 1 - \frac{\sum_i (z_i - \hat{z}_i)^2}{\sum_i (z_i - \bar{z})^2}, \quad (2.7)$$

where i indexes all the points in the plane, z_i is the feature value being fit (as above), \hat{z}_i is the fitted estimate of z_i at each point in the plane, and \bar{z} is the arithmetic sample mean of all the z_i values.

We observed that when a feature achieved dominance, its map often exhibited shared local orthogonality between itself and multiple secondary features. In other words, while each of the secondary feature maps exhibited local orthogonality with the primary feature map, only one of the secondary map gradients was substantially different from zero at any given point in the unit grid. Visually, this condition corresponds to secondary feature map contours that cluster together with other contours of the same feature and away from the contours of other secondary features. We quantified this

condition with the high gradient overlap metric (HGOM). We first found the maximum gradient for each of the secondary feature maps. For each secondary feature we then enumerated all units in the grid where the magnitude of the gradient was greater than half of this maximum. We then calculated the HGOM between two or more secondary features as the percentage of all such units included by at least two of the features:

$$\text{HGOM}_{f_1, f_2, \dots} = \frac{\bigcup_{f_i, f_j \in f_1, f_2, \dots} (\text{units with } \|\mathbf{g}_i\| > \max \|\mathbf{g}_i\|) \cap (\text{units with } \|\mathbf{g}_j\| > \max \|\mathbf{g}_j\|)}{\text{total number of units}}, \quad (2.8)$$

where f_1, f_2, \dots are the secondary features over which the HGOM is calculated and \mathbf{g}_i is the gradient vector for feature i . The metric does not indicate that secondary features are locally orthogonal with the dominant feature (this is measured with the CIDM), but the degree of overlap between iso-feature contours of secondary features. If secondary features have a CIDM with respect to the dominant feature of less than 52° , indicating a degree of local orthogonality with the dominant feature, then values of the HGOM near zero percent indicate that this local orthogonality with the dominant feature map is shared between multiple secondary feature maps. Large values of the HGOM indicate that secondary feature maps have iso-feature contours that mostly overlap with each other, and therefore any local orthogonality with the dominant feature map is not shared among the secondary features.

The metrics described previously were computed for a given combination of SOFM parameters by conducting multiple experiments with the same parameters yet different

random initialization seeds, computing a metric for each experiment, and taking the arithmetic mean of the resulting collection of metrics. The exception to this methodology was the measurement of contour orientation (i.e., the assessment for feature dominance). To compile population summaries of dominance we devised the contour orientation deviation metric (CODM), which summarized the dispersal in the primary feature map orientations across all the relevant experiments. The CODM was calculated as the root mean square deviation of the COMs from 0° (i.e., alignment with the longest line segment in the grid):

$$\theta_{dev} = \sqrt{\frac{1}{M-1} \sum_{i=1}^M \theta_i^2} , \quad (2.9)$$

where M is the number of SOFM experiments in the set and θ_i are the COMs.

The coverage uniformity metric (c') was used to measure the coverage of feature spaces in terms of feature distribution uniformity (Swindale, 1991). Greater values of c' indicate a lesser evenness or uniformity of feature space coverage and a biased distribution for a particular feature map toward one or a few values. Uniformity of feature space coverage is tested using a sampling of feature space values based upon their observable vector distributions, so that unevenness in the original distribution is not reflected in c' . In other words, the coverage uniformity metric measures how well the collective unit vector distributions (and, consequently, map areas) reflect the observable vector distributions. Coverage uniformity assessment was applied both to entire feature spaces and to subspaces of select features. Values were compared with c'

measured on a Cartesian map, which contains two globally orthogonal features equally spaced throughout the feature space and that yields the lowest c' we observed. The arithmetic mean was used to compile c' for sets of experiments with the same parameters. All the metrics used in this study are summarized in the Table 2.1.

Table 2.1 Summary of all metrics used to quantify trends in the SOFMs.

Metric	Acronym	Units	Number of Features	Used to Quantify
cyclic contour metric	CCM	% grid area	2 or more	global orthogonality
contour intersection deviation metric	CIDM	degrees	2	local orthogonality
contour orientation metric	COM	degrees	1	dominance
high gradient overlap metric	HGOM	% grid area	2 or more	shared local orthogonality
contour orientation deviation metric	CODM	degrees	1	average dominance in multiple SOFM maps
coverage uniformity	c'	dimensionless	1 or more	feature space coverage

2.1.4 Conditions Driving Dominance and Global Orthogonality

Sufficient uniformity of feature space coverage is generally possible, though not guaranteed, with up to ~ 4 uniformly distributed features or ~ 10 Gaussian distributed features (Swindale, 2004). We tested for conditions driving dominance and global orthogonality in stable feature maps having three, four or five uniformly distributed features. The main condition tested was the relative weight of a single unconstrained feature, with greater weights enforcing a more uniform coverage of the unconstrained feature (i.e., lower c' values). All features in the unit grids were initialized randomly (see Section 2.1.2). Observable vector probability distributions were uniformly distributed with a mean of zero. For any given map, the standard deviation of the first feature, referred to as the primary feature, was fixed arbitrarily at 3. The standard deviations of the third and higher features, referred to as the secondary features, were fixed at 0.3. The standard deviation of the second feature, referred to as the unconstrained feature, was varied systematically. We refer to the ratios between the observable vector standard deviations of the primary and unconstrained features as the relative weightings. The relative weighting of a feature indicates to the SOFM the importance of maintaining coverage uniformity and continuity for that feature. If a feature has a high relative weighting then its coverage uniformity metric will be low. Thus, in the SOFM algorithm, a greater standard deviation in the observable vector corresponds to a greater importance for that feature to be more uniformly mapped. This scenario will confer a

low c' for that particular feature relative to the features with smaller observable standard deviations. Relative weighting values used in these experiments were set arbitrarily for ease of comparison across disparate features, but monotonic transforms would maintain the resulting maps with a simple relabeling. For example, if the primary feature D_1 covers the range $[-10, 10]$ and is assumed to correspond to sound frequency, then the transform

$$f = 20e^{\frac{(D_1+10)}{2.9}} \quad (2.10)$$

would yield exponentially distributed frequencies f in the range $[20, 20000]$ Hz. Such relabeling does not alter any of the map characteristics determined from these experiments.

Because square unit grids have typically been used in SOFM studies to represent subsets of sensory cortical areas, we began our initial set of SOFM experiments with square grids of 150×150 units. Because square grids contain the confound of two longest line segments (i.e., the diagonals), thereby also confounding feature dominance, we ultimately utilized elliptical grids for the majority of our experiments. We extensively tested elliptical grids with major \times minor axis dimensions of 240×120 units. For the elliptical experiments, each unconstrained feature weighting of 10, 20, 30, 40, 50, 70 and 90% relative to the primary feature weighting was run 20 times for a total of 140 maps generated for each number of features. We conducted experiments with 3, 4, and 5 features, giving a total of 420 stabilized SOFMs tested.

As discussed above for the CCM, we accounted for periodicity along the grid edges by including units that were mostly, but not entirely surrounded by iso-feature contours. Contours were considered to enclose a group of units if the endpoints of the enclosing shape were separated by less than 10% of the grid edge length for square unit grids (15 units of distance for the 150×150 square grids) or by less than 10% of the mean length of the major and minor axes for elliptical unit grids (18 units of distance for the 240×120 elliptical grids). Because we defined a dominant feature as one that aligns with the longest line segment enclosed by the unit grid, we encountered a confound for square grids, since they possess two longest line segments of equal length (i.e., the diagonals). Therefore, the COM for the square grids was measured relative to the closest diagonal, causing the metric to fall within $[-45^\circ, 45^\circ]$. Only one longest line segment exists for elliptical grids (i.e., the major axis), so the metric in this case falls within $[-90^\circ, 90^\circ]$. In both cases the metric is symmetric around zero degrees, so the CODM is always measured about zero but takes on a maximum value of 45° for square grids and 90° for elliptical grids.

SOFMs were considered stabilized after 200 million observable vector presentations. All SOFMs in this study incorporated fixed isotropic Gaussian neighborhood functions (see Section 2.1.1) with standard deviation of $\sigma = 5$. Experiments with square grids had a fixed learning rate of $\epsilon = 0.05$ and experiments with elliptical grids had a fixed learning rate of $\epsilon = 0.1$. Learning rates were chosen empirically so that 200 million iterations

were sufficient to create stabilized SOFM maps. Only sets of experiments conducted with elliptical grids were used to measure trends with different parameters. Experiments with elliptical grids whose planar fit r^2 for the COM was less than 0.5 were discarded. These experiments typically resulted in a saddle point topography for the primary feature (see Section 3.3.4).

2.2 Neuronal Responses to Sound Intensity Level

2.2.1 Electrophysiology

All animal procedures were approved by the Washington University in St. Louis Animal Studies Committee. A head cap consisting of stainless steel screws, titanium head posts and dental acrylic was affixed to the skull of each marmoset monkey (*Callithrix jacchus*) under isoflurane anesthesia and with aseptic procedures. Immediately following temporalis muscle removal during surgery, the vasculature running within the lateral sulcus became visible through the skull and its location was marked on the skull. This landmark allows later microcraniotomies (<1 mm diameter) to be drilled through the skull with a custom drill directly over auditory cortex (just inferior to lateral sulcus). Following surgery, the animals were allowed to recover sufficiently prior to beginning experiments. During experimentation, the animals were awake and sat upright in a custom, minimally restraining primate chair inside a double-walled sound-attenuation

booth (IAC 120a-3, Bronx, NY) with their heads fixed in place by the head posts. The location of primary auditory cortex (A1) was identified anatomically using lateral sulcus and bregma landmarks and then confirmed physiologically by high driven rates (typically 20 – 70 spikes/s), short latencies (10 – 15 ms), robust responses to tones in middle layers and a cochleotopic frequency map oriented from low frequencies to high frequencies in the rostral to caudal direction parallel to lateral sulcus.

High-impedance tungsten-epoxy electrodes ($\sim 5 \text{ M}\Omega$ @ 1kHz, FHC, Bowdoin, ME) were advanced perpendicularly to the cortical surface within the microcraniotomies. Microelectrode signals were amplified using an AC differential amplifier (AM Systems 1800, Sequim, WA) with the differential lead attached to a grounding screw. Single-unit action potentials were sorted online using manual template-based spike-sorting hardware and software (Alpha Omega, Nazareth, Israel). When a template match occurred, the spike-sorting hardware relayed a TTL pulse to a DSP system (TDT RX6, Alachua FL) that temporally aligned recorded spike times (2.5 μs accuracy) with stimulus delivery. Raw waveforms were also bandpass-filtered at 300 – 5000 Hz and digitally sampled at 25 kilosamples/s (TDT RX6 24-bit ADC) for offline analysis. Both spike times and digitized raw waveforms were saved to hard disk on a PC running Microsoft Windows XP.

Acoustic stimuli were synthesized digitally online at approximately 100 kilosamples/s with custom MatLab software (MathWorks, Natick, MA). The stimuli were then passed

through a digital-to-analog converter (TDT RX6 24-bit DAC), amplified (Crown 40W D75A, Elkhart, IN) and delivered to a loudspeaker (B&W 601S3, Worthing, UK) located 1 m directly in front of the animal's head. Speaker output was calibrated so that the maximum sound level played was approximately 105 dB SPL with a flat frequency response (± 5 dB) from 60 Hz to 32 kHz (B&K 4191 Microphone with 2669 Preamplifier, Nærum, Denmark).

2.2.2 Acoustic Stimuli

Single neuron action potentials were isolated and recorded in primary auditory cortex as animals were presented with auditory stimuli as described in Section 2.2.1. Each single unit was analyzed with tones delivered at its characteristic frequency (CF), the frequency eliciting the greatest response from the neuron within 10 dB of threshold. Rate-level functions were measured by pseudorandomly delivering 100 ms CF tones of different amplitudes, typically 12 amplitudes spaced by 10 dB from -15 to 95 dB SPL, separated by at least 650 ms of silence. Absolute response latency was estimated from each neuron using an automated algorithm whose parameters were chosen empirically by noting how well the automated latency estimations compared to hand-estimated latencies. An overlapping peristimulus time histogram (PSTH) was calculated for the response to each sound level using a 20 ms spike window incremented in 2 ms steps. Time-points in the PSTH were aligned with the center time of the sliding spike window. Each PSTH was smoothed with a Gaussian kernel having a standard deviation of 4 ms, and a rate

threshold was calculated as either 15% of the maximum over all PSTHs (one corresponding to each sound-level response), or 15% of the maximum of the current PSTH if the maximum of the current PSTH was greater than 15% of the maximum over all PSTHs. For each PSTH the first time point after stimulus onset that (1) had a positive slope and (2) was greater than or equal to this rate threshold was chosen as the latency. The absolute response latency for each neuron was then taken as the minimum of these latencies measured over all of that neuron's PSTHs. Rates were calculated for the rate-level function from a time window beginning at the absolute response latency and ending 100 ms later. Each stimulus amplitude was presented pseudorandomly 10 times, and the mean rate over these repetitions was used for construction of the rate-level curve. In the context of dynamic sound level stimuli (see Section 2.3) rate-level functions measured in this manner are referred to as static rate-level functions.

2.2.3 Data Analysis

All neurons isolated in A1 that were responsive to tones and had positive driven rates (i.e., raw discharge rate minus spontaneous rate) at CF during the stimulus interval were analyzed. Rate-level functions were fit with a six-parameter, two-tailed split Gaussian function to evaluate response characteristics (Figure 2.1). The model was given as

$$r(l) = a \exp\left[-\frac{(l - \mu)^2}{2\sigma_{low}^2}\right] + c_{low} \quad \text{for } l \leq \mu \quad (2.11)$$

$$r(l) = a \exp\left[-\frac{(l - \mu)^2}{2\sigma_{high}^2}\right] + c_{high} \quad \text{for } l > \mu,$$

where r is the discharge rate of the neuron as a function of sound level l and where a , μ , σ_{low} , c_{low} , σ_{high} , and c_{high} are the parameters of the fit; a is the amplitude, μ is the best-level, σ_{low}^2 is the low sound-level variance, c_{low} is the low sound level offset, σ_{high}^2 is the high sound-level variance and c_{high} is the high sound level offset. This model allowed the upper and lower dynamic ranges of nonmonotonic neurons to be fit separately but could still fit monotonic functions easily by ignoring the upper dynamic range parameters. The sum squared error between the data and model was minimized using nonlinear optimization (fmincon medium scale algorithm in MatLab). Because the model contained a discontinuity where the two Gaussians joined, model values falling between the fit data points could in some cases be considerably different from interpolated values. For this reason, the visually depicted model values were linearly interpolated from the fit data points. The result is an overfitted representation of the original data, but one that eliminated spurious rate values quite successfully. This completely automated denoising procedure was particularly effective at providing quantitative estimates of threshold and saturation values that matched visual estimates for both monotonic and nonmonotonic neurons better than any other single technique we employed.

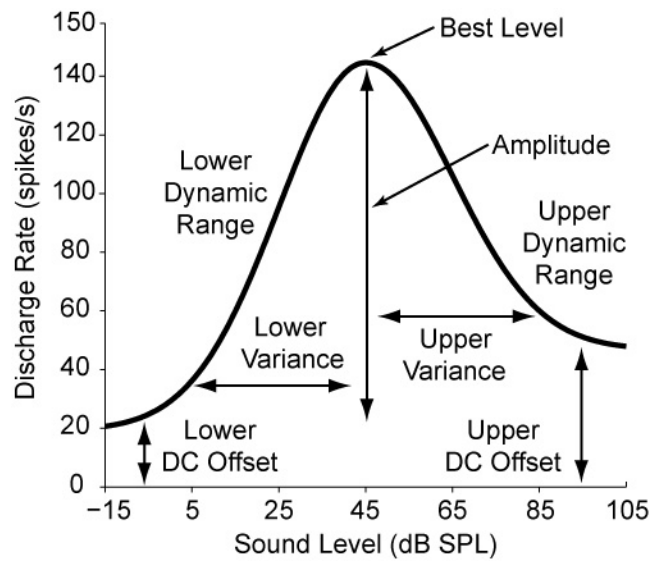


Figure 2.1 Six-parameter, two-tailed split Gaussian model used for fitting all rate-level functions. The model function has separate parameters (variance and offset) for the upper and lower dynamic ranges being fit. The remaining parameters (amplitude and mean) are the same for both dynamic ranges.

Threshold and saturation points were measured at 20% and 80%, respectively, of the maximum driven firing rate (i.e., discharge rate minus spontaneous rate) of the model functions linearly interpolated to the nearest dB. Spontaneous firing rate was averaged from time intervals when no audible stimulus was presented. Threshold and saturation were also measured for the upper dynamic range of nonmonotonic neurons, but the 20% and 80% points in these cases were calculated relative to the response to the most intense sound presented (typically 85 dB SPL). Best level was also taken from the model-fitted and linearly interpolated curves as the sound level eliciting the maximum firing rate.

Monotonicity index (MI) refers to the degree of reduced spiking at higher stimulus intensities and was calculated from the fitted rate-level responses as:

$$MI = \frac{(rate_{\max_level} - rate_{\text{spontaneous}})}{(\max(rate) - rate_{\text{spontaneous}})}, \quad (2.12)$$

where $rate$ is the fitted rate-level function, $rate_{\max_level}$ is the rate in response to the most intense sound presented and $rate_{\text{spontaneous}}$ is the spontaneous rate measured as indicated above. Neurons with MI less than or equal to 0.5 were classified as “nonmonotonic” and neurons with an MI greater than 0.5 were classified as “monotonic.” A similar metric of monotonicity has been used in previous studies (de la Rocha, Marchetti, Schiff, & Reyes, 2008; Recanzone, Guard, & Phan, 2000; Sadagopan & Wang, 2008; Sutter & Loftus, 2003; Sutter & Schreiner, 1995), but without subtracting the

spontaneous rate. By subtracting spontaneous rate, our MI reflects a ratio scale (as opposed to simply an interval scale) and is not influenced by systematic differences in maximum driven and spontaneous rates over the population. Additionally, negative MIs indicate neurons that are inhibited below their spontaneous rate at high sound levels, which is likely indicative of locally inhibitory processes.

Minimum population thresholds as a function of frequency were computed from the convex hull (Matlab `convhull` function) of the two-dimensional points represented by threshold and CF for each neuron. All neurons from all monkeys were used for this computation. The boundary lines from the convex hull were linearly interpolated (in log space for frequency) to find the minimum threshold as a function of frequency. This value was subtracted from threshold for each neuron to obtain residual threshold, which provided a fairer comparison of level encoding across frequencies than did raw thresholds.

The relationship between many variable properties of rate-level functions was assessed with either Pearson correlation or Spearman rank correlation. Pearson correlation measures a strictly linear relationship between two variables, whereas the Spearman rank correlation measures any monotonic relationship (not necessarily linear) between the variables. Because the Spearman rank correlation is more sensitive in this regard, it was used in instances where we claim no significant relationship exists. Pearson correlation was used in instances where we claim a specific linear relationship exists.

A permutation test was utilized to assess whether rate-level features such as characteristic frequency and monotonicity index were arranged non-randomly by electrode penetration, i.e., if these features were related between neurons recorded at different depths of the same electrode penetration. Because electrodes were advanced approximately perpendicularly to the cortical surface, significantly non-random arrangement of neurons at different depths provides evidence for a columnar organization of the particular rate-level feature. Neurons were first grouped according to penetration, and only penetrations with at least two recorded neurons recorded were included in this analysis. Although the permutation test can apply to any rate-level property, we discuss only MI here for illustration. For each penetration, the mean and standard deviation of neuronal MIs was calculated. Because we are interested in whether MI values recorded on the same penetration were similar to one another, we defined our test statistic for the permutation test as the mean of MI standard deviations from each penetration. For the permutation test, a random assortment of neurons was created with the same number of penetrations and the same number of neurons per penetration as in the original dataset. The same test statistic was calculated for the permuted set, and this was repeated 10 million times to create a distribution of test statistics (mean of the penetrations' standard deviations). Additionally, a sample permutation that was closest to the mean of the distribution was saved for later comparison. The original test statistic was then compared to the distribution. A p-value was calculated as the total number of distribution values that were less than or equal to

the original test statistic, divided by the number of iterations (10 million). Additionally, a z-score was calculated as the original test statistic, minus the mean of the test statistic distribution, divided by the standard deviation of this distribution.

2.3 Neuronal Adaptation to Sound Intensity Level

2.3.1 Acoustic Stimuli

Single neuron action potentials were isolated and recorded in primary auditory cortex as animals were presented with auditory stimuli as described in Section 2.2.1. Each single unit was analyzed with tones delivered at its characteristic frequency (CF), estimated as the frequency eliciting the greatest response from the neuron at a sound level no more than 10 dB above absolute threshold. A small number of neurons (4 / 47) were found to respond poorly to pure tones. These neurons were therefore probed for further experiments with bandpass noise centered at CF and with the narrowest bandwidths eliciting substantial spiking responses. “Static” rate-level functions were measured by delivering 100 ms CF tones (or CF narrowband noise) of different amplitudes, typically 12 amplitudes spaced 10 dB apart from -15 to 95 dB SPL, separated by at least 650 ms of silence. Static rate-level functions were measured and analyzed in the same manner as those described in Section 2.2.2, with the exception that occasionally very narrowband bandpass noise stimuli were used. Static rate-level functions essentially represent input-

output functions of the neurons when adapted to silence; hence we also refer to this condition as “silence adapted.”

Dynamic level stimuli were created using up to six different level distributions to probe adaptation effects in auditory cortical neurons (Figure 2.2). These distributions were probability mass functions with probabilities given discretely for each 1 dB. One stimulus consisted of all sound levels represented uniformly over the full 120 dB range tested. The remaining distributions each had nonoverlapping 20 dB level subranges (“probability plateaus”) that were more likely to occur than any of the other levels. Using such distributions allowed the sound levels from which stimulus amplitudes were drawn most commonly to be easily parameterized by the plateau midpoint or center (Dean, Harper, & McAlpine, 2005). An example of one such probability distribution can be seen in Figure 2.2A. Initial experiments used a “full set” of levels drawn from the full 120 dB range (−15 dB SPL to 105 dB SPL) with 20 dB-wide probability plateaus centered at 5, 25, 45, 65 and 85 dB SPL (Figure 2.2B). In the full set, plateau levels were ten times more likely to be drawn during any particular time interval than were levels outside the plateau. After a few experiments, however, it became clear that our awake animals poorly tolerated stimuli at the highest plateau, most likely because of the relatively high level of these stimuli. We then modified the stimulus paradigm into a “reduced set” of distributions that spanned a 100 dB range (−15 dB SPL to 85 dB SPL) and omitted the highest level plateau at 85 dB SPL (Figure 2.2C). In the reduced set, plateau levels were fifteen times more likely to be occur within any particular time

interval than were levels outside the plateau. This latter alteration allowed the adaptation effects to be more clearly observed. The full set was run for 12 out of a total of 47 neurons, so the 85 dB SPL plateau is only represented by 9 nonmonotonic and 3 monotonic neurons. Because of the smaller number of neurons recorded at the highest probability plateau, regression analyses exclude these data points, although they are included for visual comparison in the relevant figures.

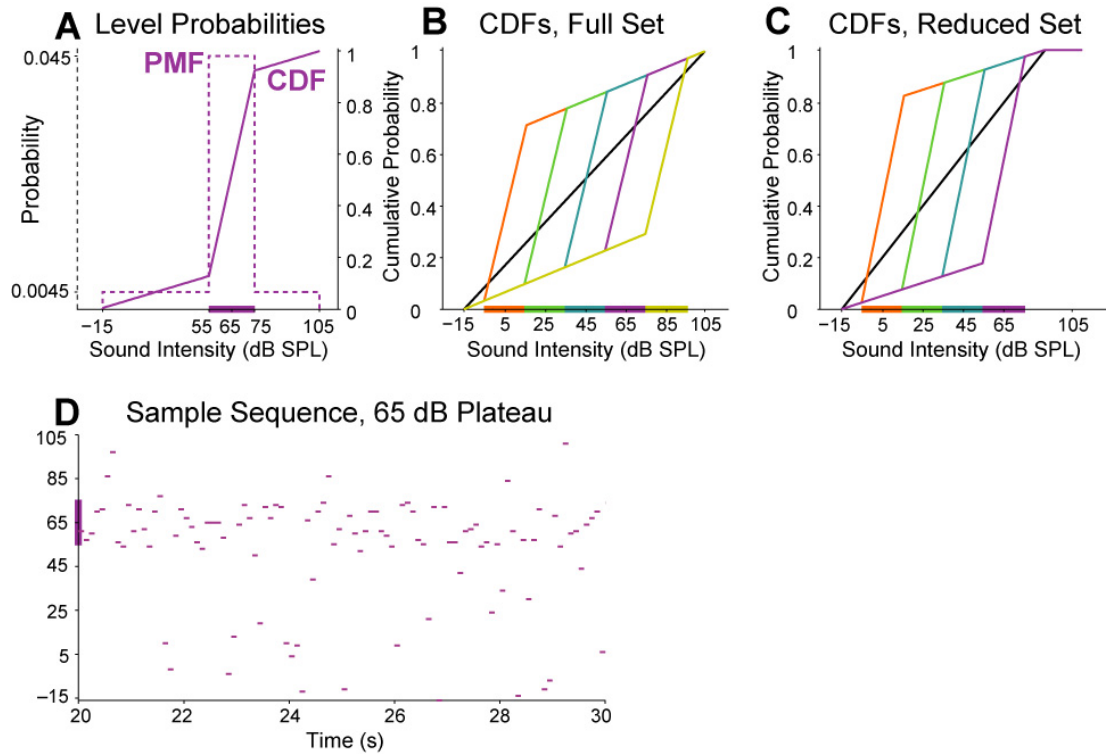


Figure 2.2 **A**, Probability mass function (PMF) and cumulative density function (CDF) of an example dynamic stimulus with probability plateau centered at 65 dB SPL. Probability plateaus on this and later plots are indicated by thick colored lines on the level axis. Dynamic stimulus PMFs are discretized at 1 dB intervals. Each CDF depicted in the “full set” (**B**) and “reduced set” (**C**) of dynamic stimulus distributions corresponds to a single dynamic stimulus. The uniform CDF where all levels occur with equal probability is indicated by a black line. **D**, Sample dynamic stimulus amplitudes as a function of time corresponding to the distribution in **A**.

At every 100 ms time interval of a dynamic stimulus, a new level was drawn pseudorandomly from the same distribution and used to set the amplitude of a pure tone whose frequency matched the CF of the neuron under study. An example of the time-varying amplitude during a portion of one two-minute-long dynamic stimulus can be seen in Figure 2.2C. Amplitudes in the dynamic stimuli were linearly transitioned from one time interval to the next with 10 ms ramps to reduce acoustic transients (i.e., clicks). No transients were detected in any of the stimuli by three human listeners. Additionally, we used relatively long intervals in the dynamic stimuli (100 ms) to ensure that both neurons' initial onset responses and any sustained firing responses were both captured in the analysis.

For the full set, dynamic stimuli were delivered for three repetitions of two minutes each. For the reduced set, dynamic stimuli were delivered for two repetitions of three minutes each. All neurons for which a complete dynamic protocol (either all of the full or reduced set) was collected were included in the current analysis.

2.3.2 Data Analysis

All neurons isolated in A1 were analyzed if they met the following criteria: (1) were responsive to tones, (2) had positive driven rates during the stimulus interval under static rate-level conditions and (3) remained isolated during a complete full or reduced set (see Section 2.3.1) of dynamic level stimuli. Dynamic rate-level functions were

determined by averaging the rate response to the stimulus in each 100 ms temporal interval of a particular dynamic stimulus and across all level bins (see below) and repetitions. The latency of each neuron in response to the static level stimuli was estimated by hand by evaluating the spike rasters from the static rate-level responses and finding the minimum time from the stimulus onset until a driven onset response to any sound level. This was often identified as a synchronized increase in firing over the multiple repetitions of a single sound level. Latencies were estimated to the nearest 5 ms, but care was taken to ensure that this value always fell before the start of any onset response. The automated latency algorithm (see Section 2.2.2) was not used for neurons on which the dynamic protocols were run. Rates were calculated for the static rate-level functions from a time window beginning at the latency after stimulus onset and ending 100 ms later.

The latency of each neuron was also used to attribute spikes to a particular temporal interval of the dynamic stimuli. For example, if the response latency for a neuron when stimulated by the static stimuli was 15 ms, then spikes occurring within the first 15 ms of each 100 ms temporal interval were assigned to the previous temporal interval of the dynamic stimuli. Because the levels for each time interval were selected randomly and independently, spikes potentially associated with any offset response from a preceding time interval would therefore be distributed across the entire dynamic rate-level function and would not contribute systematically to any individual data point. Additionally, dynamic rate-level functions using spikes confined strictly to the stimulus

interval (i.e., with a latency estimate of 0) were similar to dynamic rate-level functions that accounted for response latency. Rates were averaged over all repetitions of temporal intervals with levels falling within a particular 10-dB bin. These level bins were centered from -10 to 100 dB SPL (12 bins) for the full set and -10 to 80 dB SPL (10 bins) for the reduced set. This averaging was necessary to reduce noise for single neuron responses in order to estimate thresholds, best levels and dynamic ranges. Good estimates of these single unit data were required over the population to determine adaptation trends.

Both dynamic and static rate-level functions were fit with the six-parameter, two-tailed split Gaussian function discussed in Section 2.2.3. Threshold, saturation, best level and monotonicity index were measured from the Gaussian fit and neurons were classified as monotonic or nonmonotonic, also in the same manner as discussed in Section 2.2.3. For the purpose of calculating mean rate-level functions across the population, rate-level functions were first normalized between zero and one to create a percentage-of-maximum rate-level function. The minimum and maximum rate over all the rate-level functions collected with both the static and dynamic paradigms were used to perform the normalization, so that adaptation of the response gain (i.e., the scaling of the rate-level curve) could be compared between neurons directly.

To evaluate coding accuracy in response to each dynamic stimulus distribution, we used an information theoretic measure called the Fisher information (FI). FI provides an

estimate of the upper bound on encoding accuracy or discriminability that can be conveyed by a coding element (Dayan & Abbott, 2001), i.e., an upper bound on how well an optimal decoder could recreate the encoded value based on the neuron's input-output function. If neuronal response variance is constant as a function of response, then a steeper slope in the rate-level function would allow greater discrimination of stimulus level. Response variance may vary with response, however, in which case an improved upper bound on discriminability would be the slope of the mean rate-level function divided by the variance, which is an estimate of FI. We calculated FI precisely by estimating response probabilities directly:

$$f_i(s) = \sum_r P_i[r|s] \left(\frac{d \ln P_i[r|s]}{ds} \right)^2, \quad (2.13)$$

where $f_i(s)$ is the FI of the i^{th} neuron to stimulus s and $P_i[r|s]$ is the probability that stimulus s elicited r spikes from the i^{th} neuron. In our case, s indexes stimulus level in dB SPL, grouped into 10 dB bins as described above. The conditional probability was calculated by measuring a 2D histogram of the number of times r number of spikes occurred during each 10 dB bin (over all time bins and repetitions). This histogram was smoothed with a 2D Gaussian kernel having standard deviations of 8 dB and 0.5 spikes, then normalized into a probability distribution (i.e., the spike probabilities sum to one for each 10 dB bin). Differentiation was performed with a 5 point numerical method, disregarding two points on either end of the rate-level curves (FI for these points was set to zero). The 2D histogram was also calculated using all sound levels present in the

dynamic stimulus (1 dB bins), in order to verify that the 10 dB binning did not necessarily affect the population mean FI (see below). The 10 dB bins had the added advantage of being less noisy on the single neuron level and also aligned with the dynamic rate-level functions as described above.

Overall coding accuracy across each of the two neuronal subpopulations was assessed by calculating the sample mean of the individual neuronal FIs:

$$F(s) = \frac{1}{n} \sum_{i=1}^n f_i(s), \quad (2.14)$$

where n represents the number of neurons in each subpopulation. A mean FI function was then computed separately for each of the two neuronal subpopulations (monotonic and nonmonotonic) and each of the dynamic stimuli. Averaging FI over a population of neurons inherently assumes that the neuronal responses are not correlated with each other (Averbeck, Latham, & Pouget, 2006). This topic is discussed and analyzed for paired recordings in response to sound level separately in Appendix A.

Mean FI for nonmonotonic populations was for some analyses computed by evaluating the mean of partial FI curves on only one side of the best level (BL). For this manipulation, the portion of the FI curve on the same side of BL as the stimulus level distribution's plateau center was averaged. Because nonmonotonic neurons have two dynamic ranges, this analysis provided a clearer estimation how FI curves for these neurons differed between dynamic stimuli by only analyzing the portion of the FI that is

most involved in encoding the most probable levels. A similar technique was applied to rate-level functions. The points on the same side of BL as the stimulus level distribution's plateau center were first normalized over all the dynamic rate-level functions for each neuron and the mean of these normalized curves was taken over all nonmonotonic neurons. Any points in this analysis that were represented by two or fewer neurons were removed.

2.4 Time Course of Neuronal Adaptation to Sound Intensity Level

2.4.1 Acoustic Stimuli

Single neuron action potentials were isolated and recorded in primary auditory cortex as animals were presented with auditory stimuli as described in Section 2.2.1. The characteristic frequency (CF) was estimated within 10 dB of threshold, and static rate-level functions were collected in the same manner as described in Section 2.3.1. The dataset collected for analysis of adaptation time constants included 15 / 97 neurons that responded poorly to tones so were driven instead with bandpass noise centered at CF and with the narrowest bandwidth eliciting a response. Once static rate-level responses were collected, the dynamic rate-level response to the uniformly distributed dynamic stimulus (see Section 2.3.1) was recorded for 86 / 97 neurons.

From our recordings of neuronal responses to the dynamical sound level stimuli we found that we were unable to extract time constants of adaptation by comparing rate-level functions over consecutive time windows, as has been done in previous studies (Dean et al., 2005), due to lower driven rates and higher response variance of cortical neurons as compared to subcortical neurons. These issues also prevented us from being able to characterize the time course of adaptation for the rate-level functions measured over the same 100 or 120 dB range used by dynamic stimuli described in Section 2.3.1. In addition, our aim was to test the hypothesis that in general nonmonotonic neurons are faster at adapting to low sound levels and monotonic neurons are faster at adapting to high sound levels. This did not require a full characterization of time constants as a function of the sound levels involved or necessarily over the entirety of our 100 or 120 dB range, but simply between high sound levels and low sound levels as determined by the threshold and dynamic range of each neuron recorded individually. Therefore, we instead created dynamic stimuli containing only transitions between sound levels chosen by two separate probability distributions that were uniform over smaller ranges (Dean, Robinson, Harper, & McAlpine, 2008). These stimuli were referred to as dynamic-transition stimuli to differentiate them from the dynamic stimuli described in Section 2.3.1.

Each of the two sound level probability distributions used for creating the dynamic-transition stimuli were 20 dB in width and were discretized at 1 dB intervals, making them similar to the probability plateaus of the dynamic stimuli constructed to analyze

steady-state adaptation. Thus, in the context of a dynamic-transition stimulus, they were also referred to as probability plateaus. Because the plateaus were selected to be non-overlapping, they were further specified as the high-level plateau and the low-level plateau. The distributions were used to determine the sound level within a 100 ms time interval of a pure tone (or bandpass noise) carrier. The construction of the stimulus based on the probability distributions is the same as was described in Section 2.3.2. After a uniformly-distributed random interval between 30 and 40 seconds, the probability distribution currently determining the sound levels was switched to the other distribution (Figure 2.3). Switches from the high-level plateau to the low-level plateau were referred to as high-to-low transitions and from the low-level to the high-level plateau as low-to-high transitions. Each dynamic-transition stimulus contained 12 transitions (13 instances of different probability plateaus), 6 each of the high-to-low and the low-to-high transitions. Each of these dynamic-transition stimuli were on average 7.5 minutes in total duration and were repeated 1–5 times depending on how long the neuron remained isolated. For 3 / 97 neurons, stimuli contained only 10 transitions (5 of each type) and the minimum duration before a transition was 29.4 seconds, so neuronal examples and average responses are given over the time course of 29 seconds instead of 30 seconds, even though most neurons had the full 30 second duration before a transition.

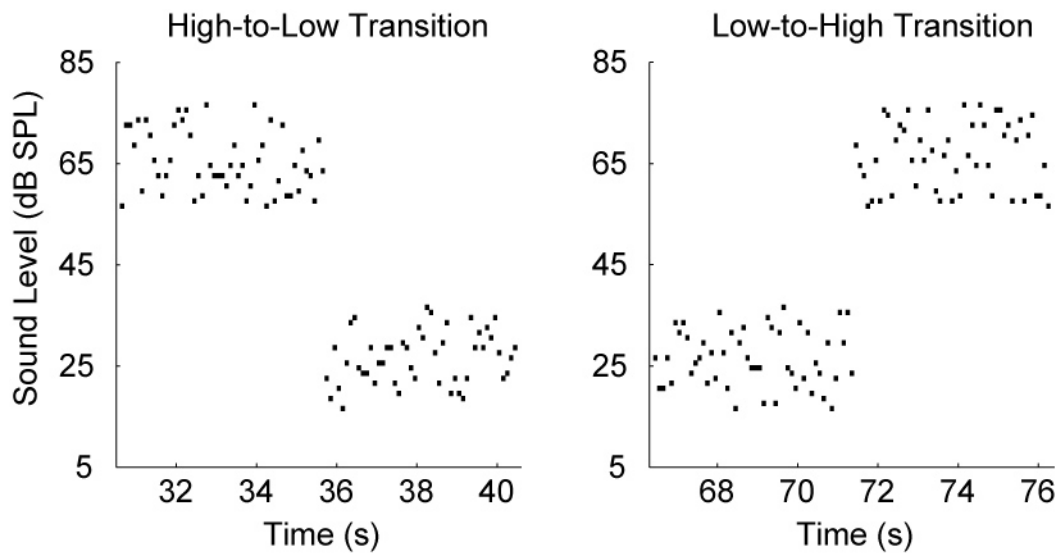


Figure 2.3 Example time courses of a dynamic-transition stimulus for the high-to-low transition (**A**) and the low-to-high transition (**B**). Each line represents the sound intensity level of the pure tone or bandpass noise carrier. The carrier is presented continuously with only the sound level changing in each 100 ms time interval.

The locations of the plateaus for a dynamic-transition stimulus were decided online based upon either the rate-level collected in response to uniformly distributed dynamic stimulus (see Section 2.3.1) or in cases where this stimulus was not played, based upon the static rate-level function. The uniformly distributed dynamic rate-level was a better indicator because it represents an adapted steady-state of the neuron. In the cases where this was available, the low-level plateau was chosen to be near to threshold along the lower dynamic range. For nonmonotonic neurons, the high-level plateau was chosen to be at slightly higher sound levels than the upper saturation (see Section 2.2.3) of the neuron, along the upper dynamic range. For monotonic neurons, the high-level plateau was typically chosen to be at the highest level, which for all responses recorded in this dataset was a plateau centered at 65 dB SPL. In cases where the uniformly distributed dynamic rate-level response was not recorded, plateau centers were chosen more conservatively, keeping in mind that responses to dynamic stimuli always shifted rate-level functions to higher thresholds (see Chapter 4). This meant choosing a center for the low-level plateau that was well above threshold along the lower dynamic range. For nonmonotonic neurons, the high-level plateau was centered closer to the upper threshold. For monotonic neurons the high-level plateau was again usually chosen at the highest sound levels (centered at 65 dB SPL for this dataset). A few nonmonotonic neurons were originally recorded by placing the high-level plateau at the highest levels in the same fashion as for monotonic neurons. The reason this placement was replaced by the strategy described above was because these first few neurons were quite often completely saturated or completely suppressed in response to the high-level plateau.

During analysis, responses were averaged over 1-second time windows (see Section 2.4.2), and this transition to complete saturation or suppression would occur faster than we could measure. The low level-plateau was placed so at least some of the levels were above threshold for the obvious reason that the neuron is not driven below threshold.

2.4.2 Data Analysis

All neurons isolated in A1 that were responsive to tones, had positive driven rates during the stimulus interval in their static-rate level responses and for which the neuron remained isolated for at least one complete repetition of a dynamic-transition stimulus (see Section 2.4.1) were analyzed. Static rate-level functions were fit with the six-parameter split Gaussian model and monotonicity index was determined from the fitted response (see Section 2.2.3). Spikes from the neuronal responses to the dynamic-transition stimuli were assigned to one of the 100-ms temporal intervals that corresponded to a specific sound level in the dynamic-transition stimulus in the same manner as for the dynamic stimuli of Section 2.3.1 (see Section 2.3.2). After this assignment, rates were averaged (mean) over all repetitions of temporal intervals with sound levels falling within a particular 2-dB bin. This was done separately in sequential non-overlapping 1-second time windows where time zero was defined as the point where a transition occurred. In other words, temporal sequences of rate-level functions were constructed separately for the high-level and low-level plateaus. The time sequence of rate-level functions was further averaged (mean) over all 10 or 12 transitions within a

single repetition of a dynamic-transition stimulus. We experimented with different sound-level bin sizes and also with different temporal window sizes and found that due to highly variable responses, the sequence of rate-level functions produced with bin sizes smaller than those described above were too noisy in order to estimate time constants of adaptation.

The time sequence of rate-level functions described above were also averaged over all the sound levels in each 20 dB wide plateau (either high-level or low-level) and in each time window to produce a time sequence of mean-rate responses. For these mean-rate responses we were able to use smaller time windows and still effectively estimate time constants of adaptation. Note that time constants of adaptation for the rate-level responses and for the mean-rate responses are not *a priori* necessarily the same, although it is like that they are related. Correlation between rate-level and mean-rate adaptation time constants and results using different time window sizes for the mean-rate responses are presented in Chapter 6.

The time sequence of rate-level functions was fit with a two-dimensional adapting sigmoid function with four free parameters. The sigmoid, given as a Gaussian cumulative probability distribution function, captured the rate-level functions in each time window, and the mean of the sigmoid was made to vary in time as a single exponential decay (Figure 2.4A). The model was given as

$$\begin{aligned}
r(l,t) &= F\left(l; \mu_0 \exp\left[-\frac{t}{\tau}\right] + \mu_c, \sigma^2\right) & \text{for } d > 0 & \quad (2.15) \\
r(l,t) &= 1 - F\left(l; \mu_0 \exp\left[-\frac{t}{\tau}\right] + \mu_c, \sigma^2\right) & \text{for } d \leq 0, &
\end{aligned}$$

where r is the discharge rate of the neuron as a function of sound level l and of time t and where μ_0 , τ , μ_c and σ are the parameters of the fit; μ_0 is the difference between the initial and the steady-state dynamic range midpoints, τ is the time constant of the adapting sound level, μ_c is the steady-state dynamic range midpoint and the σ is the standard deviation of the sigmoidal rate-level function. The sigmoid is a Gaussian cumulative probability distribution function, given as F in Equation 2.15. The sum squared error between the data and model was minimized using nonlinear optimization (`fmincon` medium scale algorithm in MatLab). The direction of the fitted sigmoid is determined by the static parameter d that is not a parameter of the fitting procedure. This static parameter was chosen to be greater than zero if the summed responses of the conditioned data (see below) from the high-level half a plateau were greater than those from the low-level half, averaged over all time. This indicated increasing rate-level functions. Otherwise d was chosen to be less than zero, indicating decreasing rate-level functions.

Before fitting the model to the time sequence of rate-level functions, the data were first conditioned to avoid over-fitting noise and to provide for a good estimate of the rate-level adaptation time constants (τ in Equation 2.15). We conditioned the data by

computing a “soft” range in order to avoid the effects of a few large or small outlying rates heavily influencing the fit. This process was done separately for the neuronal responses to each plateau. The lower bound of the range was taken as the median of the bottom 1% of rates and the upper bound as the median of the top 10% of rates over the entire time sequence of rate-level functions. These values were chosen empirically, as they qualitatively made for the best fits of the data. Most of the rate-level functions contained many points at or near zero discharge rate, but only a few points at very high rates, which is the reason for a larger percentage of high rates contributing to the upper bound. All rates in the rate-level time sequence were normalized to the range $[0, 1]$ using this soft range (again, this process was done separately for each plateau), and values outside of the range were rectified, i.e., points below zero were set to zero and points above one were set to one.

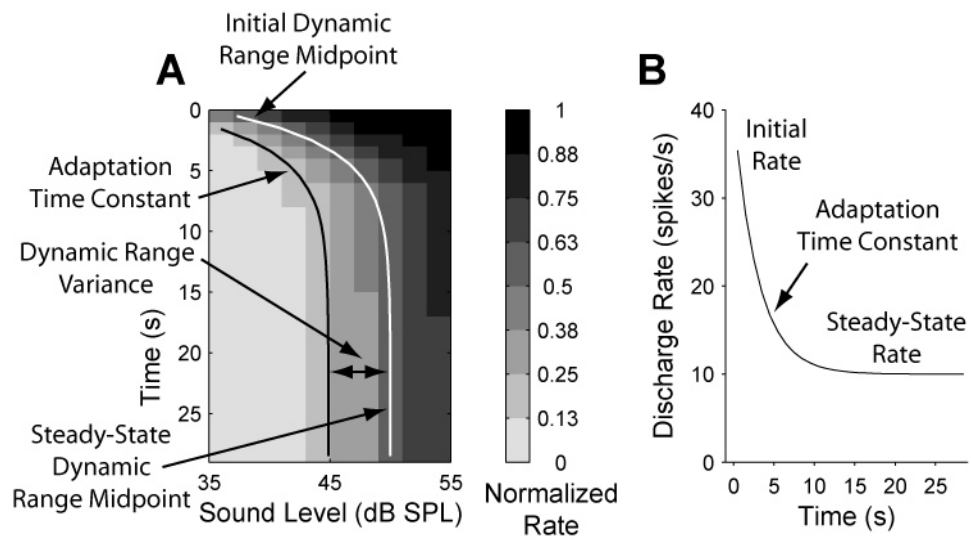


Figure 2.4 **A**, Schematic of the two-dimensional adapting sigmoid function with four free parameters used to fit transient responses to dynamic-transition stimuli. **B**, Schematic of the single exponential with three free parameters used to fit transient mean-rate responses.

In the course of selecting the particular model given by Equation 2.15 many other possibilities were evaluated, including models with a greater number of parameters that included an amplitude term or an adapting amplitude term, models that had adapting standard deviation instead of mean and very large models with separate parameters for each rate-level in the time sequence. These other models typically resulted in an overfitting of the noise or in less goodness of fit when compared with the model given by Equation 2.15. Conditioning the data by smoothing over one or both dimensions (time and sound level) typically either was not effective in reducing noise or smoothed out the adaptation effects as a byproduct of smoothing out the noise. We also tried comparing the rate-level functions at each time point with a steady-state rate-level, computed over a longer period of time just before a transition (Dean et al., 2005). In our dataset this estimated steady-state rate-level was often not a good estimate when compared to the trend apparent in the time-window sequence. Additionally, the technique of using a single or double exponential-decay function to fit mean-rates has been utilized in previous studies (Chimento & Schreiner, 1990, 1991; Dean et al., 2008; Nagel & Doupe, 2006) and the model used here is simply an extension of these one-dimensional exponential models to a two-dimensional dataset. The model described by Equation 2.15 was designed to only fit to rate-level functions that were monotonically increasing or decreasing over the 20 dB range of the dynamic-transition plateaus. The locations of the plateaus were chosen so that they did not overlap with the best-level region of nonmonotonic responses (see Section 2.4.1). This meant that the majority of neuronal responses to a single plateau were either monotonically non-decreasing or

monotonically non-increasing. A few neurons that did not fit well to the model for this reason were excluded for some analyses. Many neurons did not reach saturation within one or both of the plateau regions, but the mean of the adapting sigmoid was not constrained to be within a plateau, so these responses were best-fit using only the sloped portion of the sigmoid.

Because the model was fit to a time sequence of data that was normalized separately for each plateau, we were not able to differentiate between the effects of gain adaptation (i.e., a scaling of the rate response) and dynamic range shifting (i.e., a shifting of the rate-level function along the abscissa). The design of the dynamic-transition stimulus only revealed rate-level functions over a limited range of the full neuronal dynamic ranges, so this in itself would make teasing apart these two effects difficult, if not impossible. We therefore focused the model on the effect of dynamic range shifting only. To get a sense of gain adaptation without measuring rate constants, we calculated the amplitude index (AI) for some neurons, given by

$$AI = \frac{\max_{t,l} \{rate_{t,l}^{low-to-high}\}}{\max_{t,l} \{rate_{t,l}^{high-to-low}\}}, \quad (2.16)$$

where the subscript t indexes the time-window, subscript l indexes the sound-level bin, $rate_{t,l}^{low-to-high}$ is the discharge rate of the neuron in response to the high-level plateau and $rate_{t,l}^{high-to-low}$ is the discharge rate of the neuron in response to the low-level plateau. A value of one indicates that no gain adaptation is occurring between the low-level and

high-level plateaus. Values less than one are typically expected, particularly for monotonic neurons, since gain adaptation usually results in an overall decrease in discharge rates at greater sound intensities (see Chapter 5). Values greater than one indicate that the neuron is responding with a greater rate to the high-level plateau, which would be expected in the case of a monotonic neuron that does not adapt.

The time sequence of mean-rates (average obtained over sound level) was fit with a single exponential decay function with three free parameters (Figure 2.4B). This model was given as

$$r(t) = r_0 \exp\left[-\frac{t}{\tau}\right] + r_c, \quad (2.17)$$

where r is the discharge rate of the neuron as a function of time t and where r_0 , τ and r_c are the parameters of the fit; r_0 is the difference between the initial rate and the steady-state rate, τ is time constant of the rate decay and r_c is the steady-state rate. The sum squared error between the data and model was minimized using nonlinear optimization (`lsqnonlin` large scale algorithm in MatLab). Time sequences of mean-rate were normalized using the responses to both the high-level and the low-level plateau, so in contrast to the fitting of the time sequences of the rate-level functions, as described above, a comparison of initial and steady-state rate values could be made between plateau responses. The fitting worked equally as well without normalization and examples of single neurons are shown in Chapter 6 where the mean-rate function was not normalized prior to fitting.

Chapter 3

A Computational Framework for Topographies of Cortical Areas

3.1 Introduction

In many sensory cortical areas, physiological features of neurons are organized into functional columns perpendicular to the cortical surface, such that similar neuronal response features are evident in neurons throughout all cortical layers within a column (Mountcastle, 1997). Orderly, continuous changes in these features across the two-dimensional cortical surface create a topographic organization or a map. Neuronal response features along the surface of primary visual cortex (V1), for example, are organized into a topographic map of visual space reflecting the two spatial dimensions of the retina (Tootell, Switkes et al., 1988). In many species this retinotopic map is accompanied by maps of other neuronal features, such as ocular dominance, orientation selectivity, spatial frequency and color (Blasdel & Salama, 1986; Tootell, Hamilton et al., 1988; Tootell, Silverman, Hamilton, De Valois et al., 1988; Tootell, Silverman, Hamilton, Switkes et al., 1988; Yu, Farley, Jin, & Sur, 2005).

The visual and somatosensory systems each have a two-dimensional sensory epithelium (i.e., the retina and the skin, respectively). These two dimensions of sensory information naturally map onto the two-dimensional cortical surface. The auditory system, on the other hand, has only a one-dimensional sensory epithelium in the cochlea, which maps sound frequency along its length. Not surprisingly, sound frequency has been determined experimentally to be mapped along one dimension of primary auditory cortex (A1), resulting in a tonotopic frequency map of the neurons' characteristic frequencies or CFs (Merzenich, Knight, & Roth, 1973, 1975). The frequency map in A1 identifies collections of neurons that respond best to similar frequencies. These regions form band-like structures oriented orthogonally to the frequency axis (also known as the tonotopic axis). These isofrequency bands stretch from one border of A1 to the other and have evoked questions of what additional neuronal feature(s) might be mapped along their length. Several candidate features have emerged from neurophysiological studies conducted in multiple mammalian species having non-specialized auditory systems, including modulation frequency (Langner, Sams, Heil, & Schulze, 1997; Schulze & Langner, 1997a, 1997b), binaural dominance (Imig & Adrian, 1977; Kelly & Judge, 1994; Rutkowski, Wallace, Shackleton, & Palmer, 2000), sound source location (Clarey, Barone, & Imig, 1994; Middlebrooks, Xu, Eddins, & Green, 1998), frequency bandwidth (Cheung, Bedenbaugh, Nagarajan, & Schreiner, 2001; Philibert et al., 2005; Read, Winer, & Schreiner, 2001; Recanzone, Schreiner, Sutter, Beitel, & Merzenich, 1999; Schreiner & Mendelson, 1990), response threshold (Cheung et al., 2001; Esser & Eiermann, 1999; Philibert et al., 2005; Recanzone et al., 1999; Schreiner, Mendelson, &

Sutter, 1992), response latency (Cheung et al., 2001; Mendelson, Schreiner, & Sutter, 1997; Philibert et al., 2005), rate-level monotonicity (Clarey et al., 1994; Schreiner et al., 1992; Sutter & Schreiner, 1995) and frequency modulation (FM) sweep speed and direction (Godey, Atencio, Bonham, Schreiner, & Cheung, 2005; Mendelson, Schreiner, Sutter, & Grasse, 1993; Shamma, Fleshman, Wiser, & Versnel, 1993; L. I. Zhang, Tan, Schreiner, & Merzenich, 2003). These features appear to be non-randomly distributed in A1, but clear evidence for a single feature mapped orthogonally to frequency has been elusive.

Several computational models of V1 topography have been proposed, which to varying degrees recreate retinotopy, ocular dominance columns, and orientation preference as observed by neurophysiologists (for review see (Erwin, Obermayer, & Schulten, 1995)). In particular, the self-organizing feature map (SOFM) algorithm has been shown to be particularly successful at creating topographies similar to those observed experimentally in V1 (Farley, Yu, Jin, & Sur, 2007; Obermayer, Blasdel, & Schulten, 1992; Yu et al., 2005). Although multi-feature A1 topographies have been postulated schematically (Read et al., 2001; Read, Winer, & Schreiner, 2002; Schreiner, 1995), computational approaches have yet to be applied to auditory cortex. Such approaches may not have been attempted because unlike the case for V1, the patterns of physiologically-determined topographies beyond frequency are challenging to discern in A1. We have attempted to overcome this limitation by evaluating plausible sensory topographies

generated by SOFMs for abstracted neuronal features. Neuronal features could include any receptive field parameter relevant for a particular sensory cortical area.

We demonstrate characteristics of SOFM topographies that become apparent upon varying the relative weighting of these abstracted features. Relative weighting reflects the relative importance given to maintaining coverage uniformity for a particular feature (see Section 2.1.4). In particular, we focus on conditions that result in two features forming maps everywhere orthogonal to one another or that result in a feature mapping along the longest line segment in the modeled area. In V1 and primary somatosensory cortex (S1), conditions are more likely conducive to the creation of maps containing two orthogonal features corresponding to the two orthogonal dimensions of the sensory epithelium. Because acoustic frequency is only one-dimensional, however, an analogous orthogonal map may not necessarily exist in A1. Our abstracted SOFM experiments explore conditions in which everywhere-orthogonal feature maps do not typically form, and are therefore likely to have the most relevance for A1 or other tonotopically mapped auditory cortical areas.

The SOFM algorithm assumes that cortical topographies are constrained by the principles of coverage uniformity and continuity. These principles appear to reflect accurately the functional maps that have been observed physiologically in V1 (Farley et al., 2007; Swindale, Shoham, Grinvald, Bonhoeffer, & Hubener, 2000). By utilizing the SOFM algorithm to investigate potential topographies of arbitrary sensory cortical areas,

we therefore assume that the relevant cortical areas are organized by the same general principles as V1, including a continuous, smooth representation of the sensory epithelium. The results of these studies provide guidelines for anticipated topographic maps to be determined through physiological experiments.

3.2 Results

Self-organizing feature maps (SOFMs) were constructed under varying conditions to explore characteristics of the resulting stable feature topographies. SOFM features were not intended to correspond directly with specific neuronal response properties associated experimentally with sensory neurons; rather, the nature of the resulting topographies themselves was explored. Conditions leading to the creation of maps containing globally orthogonal or dominant features are of particular interest and potentially give insight into the fundamental difference between sensory cortical areas with a single dimension of the sensory epithelium (i.e. auditory) versus two dimensions of the sensory epithelium (i.e. visual or somatosensory).

3.2.1 Primary Visual Cortex Topographies

In order to test our implementation of the SOFM algorithm we first attempted to replicate results previously reported for functional maps of primary visual cortex (V1). These maps traditionally generate stable topographies resembling ocular dominance and

orientation-tuning maps observed in many species. We were able to obtain stable SOFMs closely resembling both these physiological feature maps as well as computational maps of V1 previously reported in the literature (Figure 3.1). Feature distributions and all SOFM variables were chosen to have the same values as (Obermayer et al., 1992).

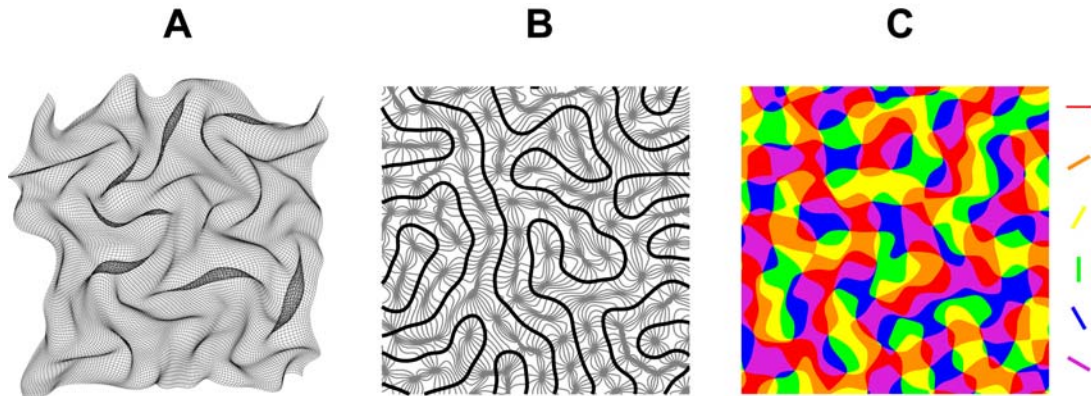


Figure 3.1 Topographies of V1 as generated by our SOFM implementation. **A**, Retinotopic coordinates (horizontal and vertical directions) of a 150×150 unit grid indicate a gross preservation of retinotopic space along with minor local inhomogeneities. In this representation units physically adjacent to one another are connected by lines. **B**, For the same grid section, ocular dominance (thick black lines) and orientation preference (thin gray lines) contours are overlaid, demonstrating that the maps of these features are closely related. In this representation and the next one, units physically adjacent to one another are plotted next to one another, so that the resulting maps could be superimposed directly onto the cortical surface. **C**, Preference to stimulus orientation (as indicated by oriented bars on right) reveals the distribution of this feature across the cortical surface in the classical pinwheel pattern.

3.2.2 Topographic Properties of Square Maps with Two Features

We began studying possible sensory topographies beyond V1 by implementing the SOFM algorithm with two uniformly distributed, equally weighted features on a square unit grid. These experiments generated topographies where the iso-feature contours ran parallel to either horizontal or vertical unit grid boundaries such that each feature increased monotonically from one side of the unit grid to the other. We termed this globally orthogonal topography a Cartesian map (Figure 3.2). In addition to global orthogonality, two equally weighted features also resulted in maps that did not contain any single feature aligned with the longest grid line segment (in this case, the grid diagonal). We have termed that type of map characteristic “dominance” in reference to the map’s attempt to colocalize units tuned to similar dominant feature values at the expense of other features. Thus, two equally weighted features mapped onto a square unit grid resulted in maps of two globally orthogonal features, neither of which was dominant.

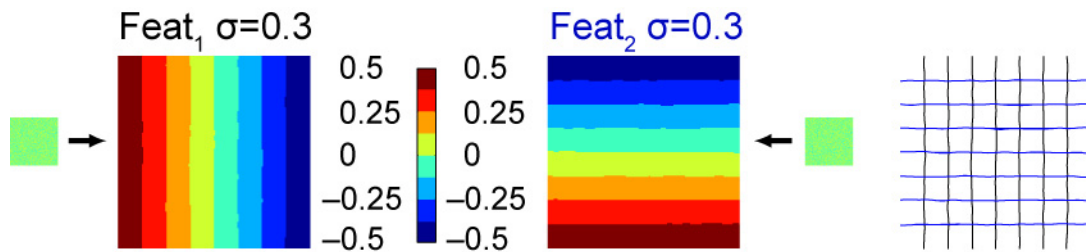


Figure 3.2 Cartesian maps generated by the SOFM algorithm with two equally and uniformly distributed features. Observable vector probability distributions for both features had a standard deviation of 0.3, corresponding to feature values in the approximate range $[-0.5, 0.5]$. Feature values within this range are color coded in the maps and colorbars in this and later figures. Maps were initialized randomly with feature values distributed near zero (indicated by small squares). Maps typically equilibrated with iso-feature contours running parallel with the grid borders. The overlay of iso-feature contours (right) shows global orthogonality between feature 1 (black, vertical) and feature 2 (blue, horizontal). The cyclic contour metric (CCM) between the two features is zero, indicating global orthogonality, and the absolute value of the contour orientation metric (COM) is 45° for each feature, indicating that neither is dominant (see Section 2.1.3).

We next considered maps of two features on square unit grids where the primary feature was weighted more heavily than the secondary feature. When the primary feature was weighted 10 times greater than the secondary feature (both uniformly distributed), we observed that the maps typically changed such that the primary feature became dominant. In other words, the axis of maximal primary feature gradation aligned with the unit grid diagonal (Figure 3.3). The same result held true for two-feature maps where the observable vector features were Gaussian distributed and for maps whose features were initialized to be Cartesian distributed instead of randomly distributed. For square unit grids, the secondary feature typically aligned its axis of gradation with the other diagonal. Because the square grids have two longest line segments, feature alignment could be with either diagonal, creating a potential confound for analysis. The iso-feature contours of both features still appeared to be smoothly and monotonically mapped and intersected predominantly at 90° angles. Therefore, SOFMs with only two features resulted in global orthogonality under all conditions tested.

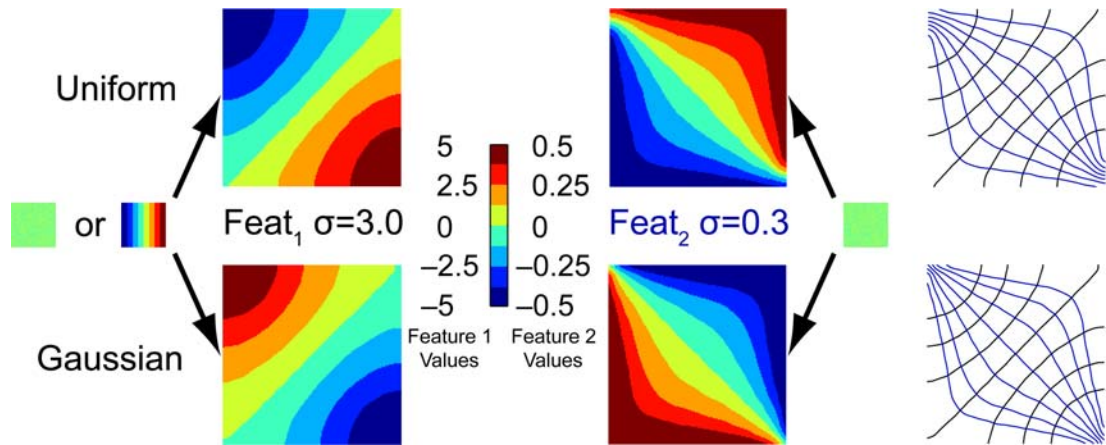


Figure 3.3 Dominance of the primary feature (Feat_1) occurs when its weighting relative to the secondary feature (Feat_2) is 10:1. Accordingly, the observable vector standard deviations are 3.0 for the primary feature and 0.3 the secondary feature, corresponding to feature values in the approximate range $[-5, 5]$ and $[-0.5, 0.5]$, respectively (shown by colorbar). Primary feature dominance occurs for both uniformly (top) and Gaussian (bottom) distributed feature values, as well as random or Cartesian initialization (small squares). Iso-feature contours for each feature are shown on the right. The CCM for both cases is very near zero, indicating global orthogonality, and the COM for both cases is about 2° (i.e., axis of maximal feature gradation is nearly aligned with the grid diagonal), indicating dominance of the primary feature.

3.2.3 Conditions Driving Dominance and Global Orthogonality in Square Unit Grids

Given that SOFMs with two features converged onto globally orthogonal maps, we next investigated the conditions under which three or more features might form globally orthogonal maps between any two features. At the same time, we investigated the conditions under which one feature might dominate the map topography. In these experiments, we fixed the relative weighting between a single primary feature and the secondary features at 10:1. The weighting between the primary feature and a single unconstrained feature was then systematically varied between 10:1 and 1:1. In cases where the relative weighting between the secondary and unconstrained features was 1:1, we also referred to the unconstrained feature as a secondary feature. We chose these relative weightings because empirically the relative weighting of 10:1 in SOFMs with two features always resulted in dominance of the more heavily weighted feature.

When the relative weighting of the unconstrained feature was set to be the same as that of the secondary features, SOFM maps did not equilibrate to a globally orthogonal structure. Instead, the secondary features tended to become locally orthogonal to the primary feature. In such cases, angles of contour line intersection were still clustered around 90° , but the secondary feature maps were periodic across the grid rather than monotonic. An example of this result with three features on a square unit grid can be seen in Figure 3.4. In this case, the primary feature aligned along the grid diagonal,

indicating dominance, and the secondary features mapped with spatial periodicity along the orthogonal diagonal, indicating that none was globally orthogonal to the dominant feature or to each other. An overlay of iso-feature contours showed that most secondary iso-feature contours did not overlap one another substantially. They tended to lie parallel to one another (intersection angles clustered around 0° or 180°) and orthogonal to the primary feature (intersection angles clustered around 90°). These clusterings can be readily summarized by the distribution of contour intersection angles between pairs of features, which demonstrates local orthogonality between the primary and secondary features.

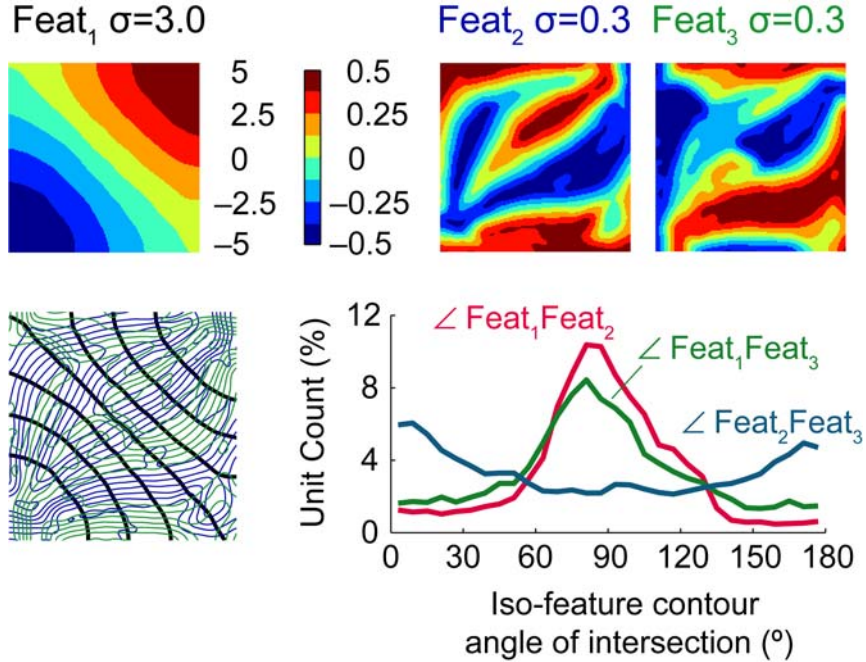


Figure 3.4 Example of a three-feature SOFM experiment with a square unit grid demonstrating dominance of the primary feature (Feat_1) and lack of global orthogonality between the primary feature and the secondary features (Feat_2 and Feat_3). The dominance of the primary feature is quantified by a COM_1 value of 0.4° . The contour overlay plot (lower left) demonstrates local orthogonality between the primary and both secondary features because the contour lines intersect predominately orthogonally. This map does not exhibit global orthogonality because $\text{CCM}_{1,2}$ and $\text{CCM}_{1,3}$ are 30.0% and 22.4%, respectively. The distribution of contour intersection angles (lower right) demonstrates a clustering around 90° between the primary feature and each of the secondary features, further indicating local orthogonality quantified with contour intersection deviation metric ($\text{CIDM}_{1,2}$ and $\text{CIDM}_{1,3}$) values of 31.3° and 39.1° , respectively. Intersection angles between the Feat_2 and Feat_3 are clustered around $0^\circ / 180^\circ$, indicating that their iso-feature contours largely run parallel to one another.

When the relative weighting between the primary feature and the unconstrained feature was about 10:5 or greater, the primary and unconstrained features tended to map globally orthogonally to one another. An example of this case with four features on a square unit grid can be seen in Figure 3.5. In this example, the axis of maximal gradation of the primary feature ran nearly horizontal while that of the unconstrained feature ran nearly vertical. The unconstrained feature showed little indication of periodicity in its map compared to experiments when its relative weighting was lower (data not shown). Neither the primary nor the unconstrained feature aligned along a diagonal, indicating that neither feature was dominant.

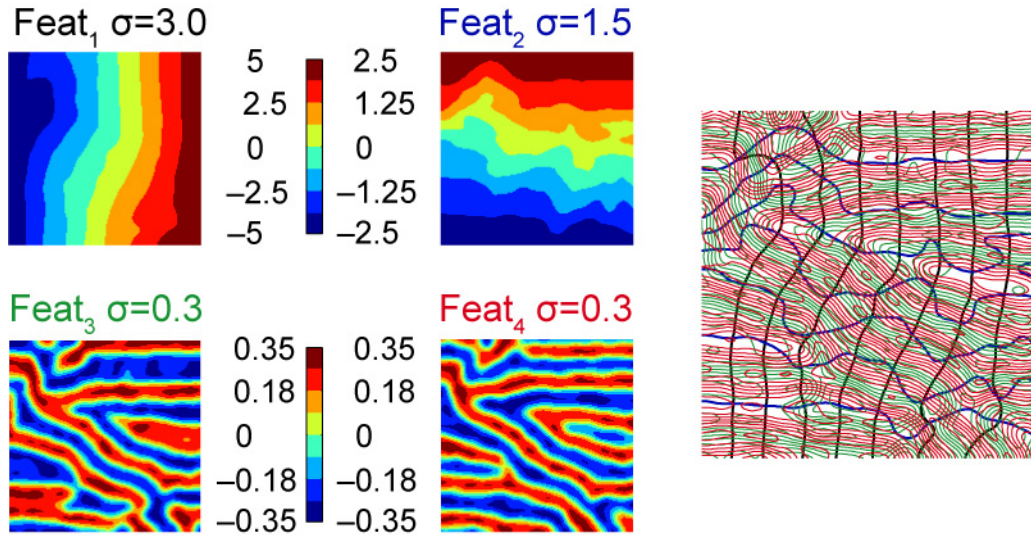


Figure 3.5 Example of a four-feature SOFM experiment with a square unit grid demonstrating global orthogonality between the primary and unconstrained features (Feat₁ and Feat₂, respectively). Secondary features (Feat₃ and Feat₄) demonstrate shared local orthogonality with both the primary and unconstrained features, and no single feature dominates the topography. $CCM_{1,2}$ is 9.7%, confirming global orthogonality between features 1 and 2. COM_1 and COM_2 are 35.8° and 38.0° , respectively, confirming that neither the primary nor the unconstrained feature is dominant. $CIDM_{1,3}$ and $CIDM_{1,4}$ are 30.8° and 27.1° , respectively, confirming that both secondary features are locally orthogonal with the primary feature. The high gradient overlap metric ($HGOM_{3,4}$) is 6.6%, confirming that this local orthogonality is shared between features 3 and 4.

Throughout the tested range of the unconstrained feature's relative weighting, the secondary features demonstrated spatial periodicity in all directions of the unit grid. In SOFM experiments where the primary feature became dominant, this periodicity was oriented predominantly along dominant iso-feature contours. In these cases the secondary features all shared local orthogonality with the primary feature. The periodicity of secondary features is clearly exhibited in both cases discussed above (Figures 3.4 and 3.5).

We quantified the qualitative trends discussed in the examples above with four metrics. Feature dominance was quantified with the contour orientation metric (COM), global orthogonality with the cyclic contour metric (CCM), local orthogonality with the contour intersection deviation metric (CIDM), and sharing of local orthogonality with the high gradient overlap metric (HGOM). Figure 3.6 demonstrates graphically how these metrics were calculated for square grids (for details, see Section 2.1.3) using the examples from Figures 3.4 and 3.5.

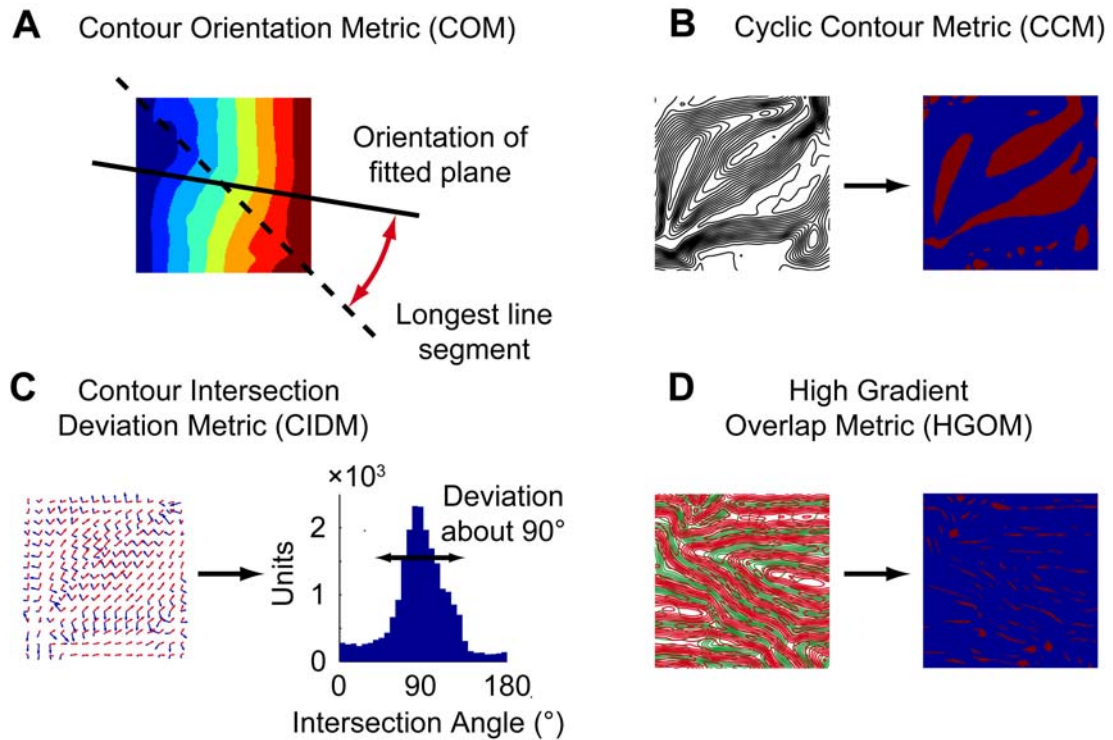


Figure 3.6 Graphical depiction of metric calculations. **A**, Feature dominance was quantified with the contour orientation metric (COM), demonstrated here with feature 1 from the example in Figure 3.5. **B**, Global orthogonality was quantified with the cyclic contour metric (CCM), demonstrated here with feature 2 from the example in Figure 3.4. **C**, Local orthogonality was quantified with the contour intersection deviation metric (CIDM), demonstrated here with features 1 and 2 from the example in Figure 3.4. **D**, Sharing of local orthogonality was quantified with the high gradient overlap metric (HGOM), demonstrated here with features 3 and 4 from the example in Figure 3.5.

For the example given in Figure 3.4, COM_1 was near zero (0.4°) and the coefficient of determination for the planer fit was high for the primary feature ($r^2 = 0.99$). $CCM_{1,2}$ and $CCM_{1,3}$ reflected a large percentage of the grid area (30.0% and 22.4%, respectively), indicating lack of global orthogonality. $CIDM_{1,2}$ and $CIDM_{1,3}$ were lower than the 52° expected for a uniform distribution (31.3° and 39.1° , respectively), indicating clustering of angles around 90° and therefore local orthogonality with the primary (dominant) feature. Additionally, $HGOM_{2,3}$ measured between the two secondary features was a low percentage of grid area (2.9%), implying that local orthogonality with the dominant feature was shared between the two secondary features.

For the example given in Figure 3.5, COM_1 and COM_2 were both far from 0° (35.8° and 38.0° , respectively), indicating that neither the primary nor the unconstrained feature was dominant. $CCM_{1,2}$ was a low percentage of grid area (9.7%), indicating that these two features were globally orthogonal. $CIDM_{1,3}$ and $CIDM_{1,4}$ for the secondary features (30.8° and 27.1° , respectively) indicated local orthogonality with the primary feature, even though in this case the primary feature was not dominant. $HGOM_{3,4}$ between the secondary features remained a low percentage of grid area (6.6%), again indicating a sharing of local orthogonality with the primary feature.

3.2.4 Conditions Driving Dominance in Other Grid Shapes

To evaluate the effects of unit grid shape on maps resulting from 2D features of equal or disparate weightings, we ran the SOFM algorithm with unit grids of different shapes. In these experiments we again refer to the more heavily weighted feature as the primary feature and the other as the secondary feature and used a relative weighting of 10:1. Example SOFM experiments with varying unit grid shapes are shown in Figure 3.7. The primary feature in rectangular unit grids under these conditions typically aligned with one of the diagonals (Figure 3.7A). In elliptical unit grids of varying eccentricities, the primary feature typically aligned along the major axis of the ellipse (Figure 3.7B). Elliptical grids contain only one longest line segment, the major diameter, thereby removing the potential confound of square and rectangular grids (i.e., equal-length diagonals). Experiments with elliptical grids thus demonstrated that the primary feature does in most cases align along the longest grid line segment, implying feature dominance. The SOFM algorithm was also run with asymmetric curve-shaped unit grids. These experiments demonstrated that the axis of gradation of the primary feature typically aligned itself along a curved contour running parallel with the boundaries of the unit grid (Figure 3.7C). In circular unit grids, which have an infinite number of longest line segments (diameters, in this case), the primary feature aligned along an arbitrary diameter. The remaining primary iso-feature contours resembled latitudes while the secondary iso-feature contours resembled longitudes as in the flat projection of a sphere (Figure 3.7D).

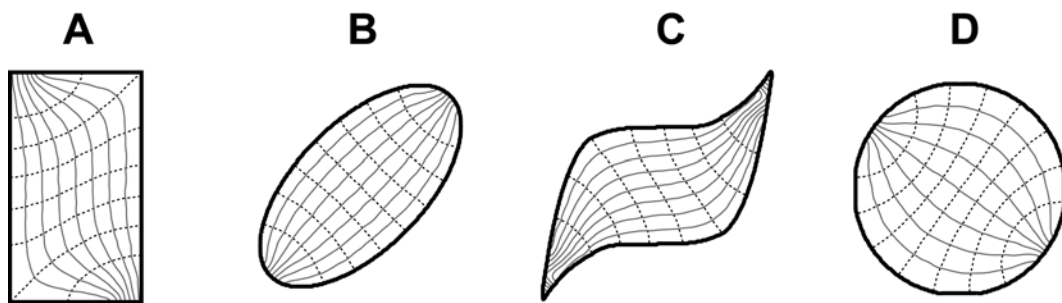


Figure 3.7 Example contours of two-feature SOFM experiments with non-square unit grids (grid borders in thick black lines). The primary feature (iso-feature contours in dotted lines) is weighted 10:1 over the secondary feature (iso-feature contours in gray lines). The primary feature aligns along one diagonal in rectangular grids (**A**), along the major axis in elliptical grids (**B**), along a curved path parallel to the grid border in asymmetric grids (**C**), and along an arbitrary diameter in circular grids (**D**).

3.2.5 Conditions Driving Dominance and Global Orthogonality in Sets of Elliptical Grids

The apparent generality of our results across grid shape and the potential confound of dominant features led us to extend the previous qualitative results to another grid type. We moved to elliptical unit grids, because unlike square or rectangular grids, elliptical grids contain only a single longest internal line segment, eliminating a potential confound when assessing feature dominance. Experiments with elliptical grids were parameterized the same as for square unit grids, by systematically changing the relative weighting of the unconstrained feature from that of the secondary features to that of the primary feature. The relative weightings between the primary and secondary features were fixed at 10:1. We again quantified resulting trends using four metrics; CODM for feature dominance, CCM for global orthogonality, CIDM for local orthogonality, and HGOM for sharing of local orthogonality (see Section 2.1.3 for details). Metrics were compiled over sets of stable SOFM elliptical maps resulting from experiments using the same parameters and then plotted over all parameters as a function of the relative weighting of the unconstrained feature (Figures 3.8 and 3.9).

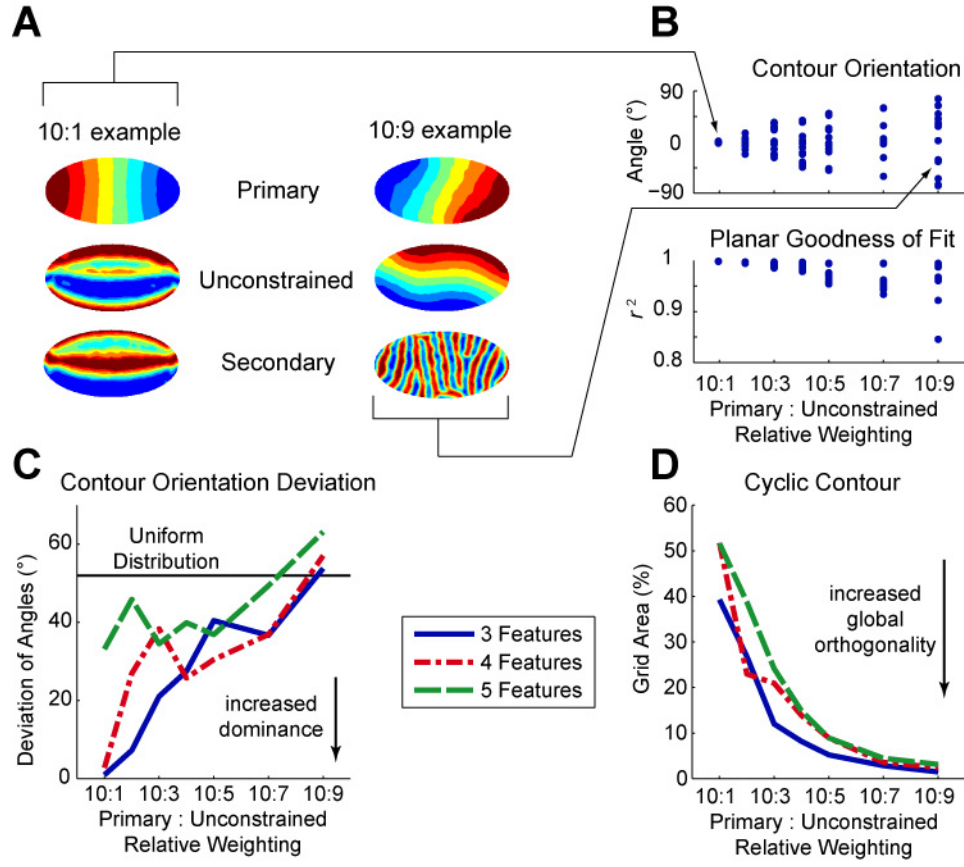


Figure 3.8 Dominance / global orthogonality interrelationship in elliptical unit grids.

A, Two example experiments with elliptical unit grids having three mapped features demonstrate dominance of the primary feature at lesser relative weightings of the unconstrained feature (left) and global orthogonality between the primary and unconstrained features at greater relative weightings (right). **B**, As the weighting of the unconstrained feature approaches the weighting of the primary feature, contour orientation becomes variable and the primary feature topography becomes less planar, depicted by the spread in COM and r^2 values. Examples shown in A are indicated by arrows. **C**, The deviation of the COM values about 0° is used to calculate the CODM. For all numbers of features, the primary feature tends toward dominance as the

weighting of the unconstrained feature decreases. Maps with higher numbers of features require the primary feature to be weighted more heavily in order for it to display dominance. **D**, The $CCM_{1,2}$ shows the converse, indicating that the primary and unconstrained features tend toward global orthogonality as the weighting of the unconstrained feature increases. Taken together, the trends from C and D indicate that dominance and global orthogonality are unlikely to occur in the same map.

The general trend demonstrated by the sets of stable elliptical maps was a transition from dominance of the primary feature and lack of global orthogonality at lower relative weightings of the unconstrained feature, to global orthogonality between the primary and unconstrained feature at higher weightings. Concomitantly with this observation, however, no feature dominated at higher relative weightings of the unconstrained feature. Examples with three features from each end of this spectrum are shown in Figure 3.8A. COM values for the primary feature for both examples are highlighted by arrows within the population scatter for three-feature elliptical experiments (Figure 3.8B). CODM values are calculated by taking the deviation of these values around 90° . As is clear from the population scatter of COM values, CODM values increased as the relative weighting of the unconstrained feature increased (Figure 3.8C), demonstrating increased dominance of the primary feature at lower relative weightings of the unconstrained feature. Curves for maps with more features were shifted to the left, meaning a greater weighting of the primary feature was required for it to dominate as the number of features increased. $CCM_{1,2}$ values decreased with increasing relative weighting of the unconstrained feature (Figure 3.8D). When the unconstrained feature was weighted approximately half that of the primary feature, each $CCM_{1,2}$ curve tended to reach an elbow point where it began to approach zero, indicating that for greater relative weightings, the unconstrained feature map was mostly globally orthogonal to the primary feature map. Taken together, these two plots (Figures 3.8C and 3.8D) indicate that at low relative weightings of the unconstrained feature, the primary feature became dominant and was not globally orthogonal to the unconstrained feature. At high

relative weightings, on the other hand, no feature was dominant, but the unconstrained and primary feature maps maintained global orthogonality.

The secondary features demonstrated shared local orthogonality with the primary feature across the majority of unconstrained feature relative weightings. The CIDM between the primary and secondary features was lower than expected for a uniform distribution in most conditions (Figure 3.9A), indicating a prevalence of local orthogonality between the primary and secondary features. Additionally, the HGOM among the secondary features remained a low percentage of grid area across all conditions (Figure 3.9B), indicating that this local orthogonality was shared among secondary features. HGOM values were calculated only between pairs of secondary features, so the metric was not included for maps with three features, which only contain a single secondary feature. Both metrics had a general trend for increasing as the relative weighting of the unconstrained feature increased. This trend may be attributable to an increased tendency for the secondary feature maps to be locally orthogonal with the unconstrained feature map as the relative weighting increases.

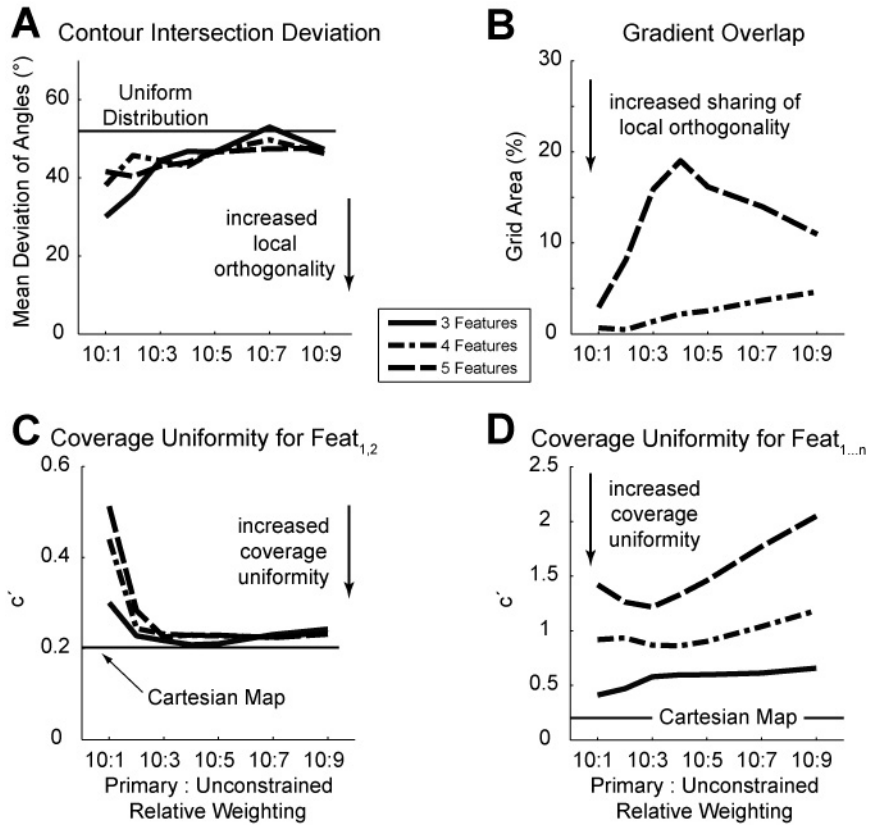


Figure 3.9 Trends in shared local orthogonality and coverage in elliptical unit grids as a function of the relative weighting of the unconstrained feature. **A**, The mean CIDM between the primary and secondary features is less than the standard deviation of the uniform distribution, indicating that the angles of contour intersection are clustered around 90° . This result implies that local orthogonality is maintained at all relative weightings and is consistent with three, four and five features. **B**, The HGOM between the secondary features remains a relatively low percentage of grid area for both four and five features, indicating that this local orthogonality is shared among the secondary features. The HGOM is only given for maps with four or more features because three-feature maps have only a single secondary feature. **C**, **D**, Coverage uniformity over the

primary and unconstrained features remains relatively constant except at low relative weightings (when the primary feature is dominant), while coverage uniformity between all feature pairs increases with increasing relative weighting of the unconstrained feature. These trends are consistent for three, four and five dimensions and collectively indicate that both feature dominance and global orthogonality are achieved at the expense of secondary feature coverage.

In addition to the metrics discussed previously, we calculated the coverage uniformity metric c' (Swindale, 1991) in order to assess whether the transition from dominance to global orthogonality had any effect of feature space coverage. Except at the lowest relative weightings of the unconstrained feature, the coverage over the primary and unconstrained features was approximately constant across all conditions (Figure 3.9C). Coverage uniformity asymptotically approached the expected value for a perfect Cartesian map of the 2D space at a relative weighting of about 10:3. This weighting was less than the weighting of about 10:5, beyond which we could safely say that the primary and unconstrained features were globally orthogonal. Therefore, adequate feature space coverage appears to be necessary but not sufficient for global orthogonality. In other words, global orthogonality implied adequate coverage, but stable maps were able to attain adequate coverage without global orthogonality. On the other hand, lower coverage at relative weightings of less than 10:3 corresponded with dominance of the primary feature. This finding indicates that feature dominance arose at the expense of coverage between the dominant and secondary features. We also measured coverage uniformity over all the features. In this case, c' declined with increasing relative weighting of the unconstrained feature (Figure 3.9D). Thus, increasing tendency toward global orthogonality between the primary and unconstrained feature map was achieved at the cost of secondary feature coverage.

3.3 Discussion

Visual, somatic and auditory sensory cortices are all known to contain topographies that recapitulate stimulus features transduced by the corresponding sensory epithelium. Retinotopy and somatotopy have a natural topographic mapping from the two dimensions of the sensory epithelium to the two dimensions of the cortical surface. The third dimension of cortex, depth, is not considered in these mappings because cortical neurons with similar response properties are generally arranged in a columnar fashion (Mountcastle, 1997). Primary auditory cortex (A1) is known to be organized by sound frequency along one physical dimension of cortical surface, such that neuronal tuning to frequency varies relatively smoothly from one end of A1 to the other (Merzenich et al., 1973, 1975). The feature or features mapped along the other (isofrequency) dimension of A1, however, have remained elusive in mammalian species with non-specialized auditory systems. Although many neuronal response features have been shown to be mapped non-randomly, it is unclear whether one of those features is mapped exclusively along isofrequency contours.

In this study we exploited a computational approach using self-organizing feature maps (SOFMs) to provide insight into the appearance of topographies along the continuum between global orthogonality, as one might expect in either primary visual (V1) or primary somatic (S1) sensory cortices, and feature dominance, as could be possible in A1. The principles governing V1 organization appear to be captured accurately by the

SOFM algorithm (Farley et al., 2007; Obermayer et al., 1992; Swindale et al., 2000; Yu et al., 2005). Such computational methods have not yet been applied to the examination of other cortical areas, but if the principles of V1 organization reflect general patterns of cortical organization, SOFM studies should be able to provide insight into the organization of other cortical areas such as A1. In this study we did not consider specialized auditory systems like that of the echolocating bat, or specific neuronal features of any particular sensory system; instead, the results can be interpreted to reflect topographic maps that might exist in any brain area exhibiting the organizational properties under study.

3.3.1 Model Geometries

We first found that the shape of the unit grid used to construct the SOFM could influence functional topographies that may be relevant for A1. Topographies with an underlying two-dimensional nature, such as retinotopy in V1 or somatotopy in S1, may not be as strongly influenced by the edge effects of the grid, possibly because the mapping does not involve a fundamental change in the number of dimensions. V1 and S1 both map the two dimensions of the sensory epithelium onto the two physical dimensions of the cortical surface. In such cases one might expect that the submaps from different regions of retinotopic space, for example, could then be tiled together to create an overall map of all visual space within V1. Edge effects appear to influence map topographies more substantially for conditions that might be found in A1,

however, possibly because the natural underlying physiological feature dimensionality inherited from the auditory periphery is one-dimensional (i.e., frequency). Because of this influence of grid shape upon map topographies, we evaluated the functional topographies resulting from several different grid shapes. All study findings generalized across all grid shapes tested, implying that as long as the entire grid geometry is taken into account, relationships between feature maps is predictable for any grid shape. Considering only a subset of the grid (or cortical area) when evaluating a feature map, however, could lead to erroneous conclusions of map structure, particularly regarding map periodicity and local versus global orthogonality.

3.3.2 Feature Dominance

Our activity-dependent, self-organizing networks predict that a heavily weighted feature will align its axis of maximal gradation (i.e., the map direction with the greatest changes in feature values per unit distance along the cortical surface) with the longest line segment in the unit grid (i.e., the longest line segment within an anatomically defined cortical area), an attribute we refer to as dominance. If relative weighting among features is interpreted as the relative importance for the system to map similar feature values compactly, then dominant features are the most compactly represented. Indeed, dominant features in our maps always demonstrated more compactness than nondominant features (data not shown), implying that units tuned to similar values of the dominant feature were physically closer to one another in the map. Note that with

two mapped features on a square unit grid, both features may align their axes of maximal gradation along a diagonal. Only one of these mappings is demonstrably more compact than the other, which still allows for a single dominant feature to be defined (c.f., Figures 3.3, 3.4). To eliminate this confound, however, later experiments made use of unit grids containing only a single longest internal line segment.

Given a sufficiently high relative weighting of the primary feature, dominance was observed for all unit grid topographies, feature distributions and numbers of features we tested. We demonstrated the range of relative feature weightings that resulted in dominance of a primary feature by systematically modifying the relative weighting of an unconstrained feature in elliptical unit grids with three, four and five features. These findings imply that if the tonotopic axis in A1 aligns along the longest anatomical line segment of that cortical area, then frequency is likely to be the dominant feature driving the topography in this region. Conversely, if frequency is expected to be a dominant feature in a particular cortical area, then one would expect the tonotopic axis to align itself with the longest anatomical line segment, or along a curve parallel with the longest border for complex anatomical shapes. To test this hypothesis, precise anatomical borders and physiological maps must be determined in the same cortical area in the same animal.

3.3.3 Global Orthogonality

If the relative weighting between a primary feature and another feature is near unity, the SOFM does not exhibit dominance. Instead, over much of the grid the two most highly weighted features tend to organize their gradients monotonically in orthogonal directions in a pattern we refer to as global orthogonality. Sets of SOFM experiments parameterized by the relative weighting of a single unconstrained feature demonstrated that the unconstrained feature became globally orthogonal to the primary feature when the relative weighting between the primary and unconstrained features decreased to a ratio of about 10:5. At that weighting the unconstrained feature no longer resembled the secondary features, i.e., it no longer demonstrated spatial periodicity along the primary iso-feature contours. As the relative weighting ratio decreased, the unconstrained feature transitioned from local orthogonality with the primary feature to global orthogonality, but no longer necessarily shared this orthogonality with the secondary features. At the same time, the primary feature lost its dominance of the grid and no other features came to dominate. This transition can be thought of as a continuum, where on one end the primary feature dominates the topography and no other feature is globally orthogonal to it, and where on the other end the primary and unconstrained features are globally orthogonal, but no single feature dominates the map. At the dominant end of this continuum, the unconstrained and secondary features share local orthogonality with the dominant feature and are periodic along primary iso-feature contours. At the globally orthogonal end of the continuum, the secondary features share local orthogonality with both the primary and unconstrained features. Our results show that the effect of feature

dominance was reduced when more features were added, i.e., the primary feature required a greater relative weighting to achieve dominance when more features were mapped. A previous study of the number of features likely to be mapped using SOFM algorithms (Swindale, 2004) gave an upper bound of about four uniformly distributed features in order to provide adequate coverage of feature space; therefore we confined our study to a maximum of five uniformly distributed features.

3.3.4 Relevance to Cortical Physiology

SOFMs have been successful at creating topographies similar to those observed experimentally in V1 (Farley et al., 2007; Obermayer et al., 1992; Swindale et al., 2000; Yu et al., 2005), implying that the algorithm reflects relevant properties of sensory cortex functional organization. Formation of topographic maps using the SOFM algorithm is based upon “activity” of virtual neurons (units) and the probability distributions of observable vectors that train these virtual neurons (see Section 2.2.1). Thus, the usefulness of the SOFM algorithm for predicting structures or trends in cortical topographies relies upon the assumption that topographies are formed in an activity-dependent manner. In the SOFM algorithm, this activity-dependence is driven by both local Hebbian learning, whereby local units develop similar tuning properties, and a global competitive learning rule, whereby non-local units compete for tuning properties. The activity-dependence assumption achieves credibility for A1 from physiological experiments demonstrating tonotopic plasticity based upon the probability

and behavioral relevance of sound frequencies in the local environment (Kilgard & Merzenich, 1998; Kilgard et al., 2001; L. I. Zhang, Bao, & Merzenich, 2001). Additionally, the SOFM algorithm creates maps that preserve feature continuity with compact unit arrangements. Such maps in cortical areas minimize wiring lengths between neurons, assuming that neurons with similar response properties have the greatest amount of interconnectivity. The SOFM would predict that for neurons having similar values of any particular feature, their interconnectivity would be proportional to the relative weighting of that feature in the model. Wire-length minimization models have been created that mimic orientation preference topography in V1 (Koulakov & Chklovskii, 2001). Cortical sensory neurons do appear to interconnect predominantly with other neurons having similar features (Read et al., 2001; Ts'o, Gilbert, & Wiesel, 1986), although it remains to be seen if relative feature weighting in computational maps predicts the degree of anatomical interconnectivity between different regions of a functional map.

The SOFM algorithm creates topographies that are driven by an activity-dependent process which tends to ensure continuity and uniformity of feature space coverage. If we assume that the formation and maintenance of topographies in cortical areas relies on analogous processes, then our results predict that in any given cortical area dominated by a single feature map, no other feature is likely to be mapped globally orthogonally to the dominant feature. As discussed previously, the changeover point in this continuum occurred for elliptical geometries when the relative weighting between

the primary and unconstrained features was about 10:5. At greater relative weightings the features became mostly globally orthogonal, and the orientation of the primary feature was far enough from the longest line segment that one would no longer consider it to be dominant. We may then conclude that if sound frequency is a dominant feature in A1 then we would be unlikely to find a single auditory feature mapped globally orthogonally to frequency. On the other hand, if frequency is not a dominant feature, one could expect to see another single feature that is globally orthogonal to frequency. Such a finding would have implications for the topographies of additional features that might be mapped. We would predict, for example, that the coverage uniformity of these additional features would be decreased and their topography would be periodic with a relatively high spatial frequency. In order to determine whether or not sound frequency represents a dominant feature of A1 or any other topographic auditory area, high-resolution physiological maps of multiple neuronal response properties that cover the full extent of the cortical area and that can be carefully aligned with anatomical maps of area boundaries should be analyzed.

Several anatomical studies of primary auditory cortex demonstrate cortico-cortical connections congruent with our SOFM topographic features. Neuroanatomical tracing studies have revealed horizontal connections in cat A1 that tended to be clustered in iso-frequency bands and were periodic in the iso-frequency direction (Ojima & Takayanagi, 2004; Ojima, Takayanagi, Potapov, & Homma, 2005). This result is analogous to our finding of periodicity in secondary features along the dominant iso-

feature (iso-frequency) contours. Other tracing studies in cat A1 have shown horizontal connections between patches with similar spectral tuning (Read et al., 2001). In this case, single unit microelectrode recordings and tracer injections revealed a periodicity of these intrinsic connections along iso-frequency contours, connecting iso-frequency regions of narrowband tuning. This finding is also analogous to the periodicity we found in our secondary features and implies that neuronal bandwidth (i.e., the bandwidth of the neurons' frequency tuning) may indeed be a secondary feature mapped in auditory cortex. Other studies in cat A1 (Matsubara & Phillips, 1988; Reale, Brugge, & Feng, 1983) revealed clustering of cortico-cortical connections along iso-frequency bands, consistent with our notion that units tuned to similar frequencies are preferentially connected.

Our SOFM experiments demonstrate shared local orthogonality between the secondary and more highly weighted features. Thus, even if a sensory cortical area does not contain two globally orthogonal features, we would still predict that in any small portion of the area only one secondary feature would have a high gradient parallel to the primary iso-feature contours. To date, the spatial resolution of physiological studies in auditory cortex has likely not been fine enough to determine the validity of this prediction. Depending upon the spatial frequency of the secondary feature periodicity, investigating the orthogonality of a particular secondary feature over even a relatively large subportion of A1 could reveal an orthogonal map. For example, in the SOFM experiment from Figure 3.4, we find that if one were to look at the central 2/3 of the

grid meant to represent A1, one might conclude that one of the secondary features is globally orthogonal to the dominant feature. Only when the whole map is revealed, however, can one observe that both secondary features share local orthogonality with the dominant feature at a low spatial frequency. Thus, any study that claims a single neuronal feature to be globally orthogonal to frequency but does not include the entire extent of A1 could actually have mistaken local orthogonality for global orthogonality. Therefore, clear topographies of A1 are only likely to be revealed with high-resolution functional mapping of the entire extent of the cortical area, confirmed by anatomical analysis.

3.3.5 Experimental Limitations

One possible concern with systematic unconstrained feature experiments was the choice to discard maps that did not converge to a non-periodic mapping of the primary feature. When the primary feature map did not have a good planar fit, the experiment was discarded ($r^2 < 0.5$). This occurred in about 15% out of the total set of elliptical SOFM experiments. These maps always included a saddle point such that the primary feature mapping was not monotonic along one orientation in the unit grid. These non-convergent maps may represent a local minimum in the space of equilibrated topographies. Given a noisier process driving the formation of the topographies (e.g., a simulated annealing process) the topographies would likely settle to a more stable structure. It is known that tonotopy in auditory cortex is not only driven by an activity

dependent process (Kilgard & Merzenich, 1998; Kilgard et al., 2001; L. I. Zhang et al., 2001), but is also partially genetically determined by biochemical markers during development (Y. Zhang, Dyck, Hamilton, Nathanson, & Yan, 2005). If sound frequency represents a dominant feature in A1 area, then axonal guidance of thalamic auditory inputs could likely provide an initial tonotopy that is mostly non-periodic and monotonic along one cortical orientation. Such a biological substrate could provide a consistent starting point from which to launch an activity-dependent process that would likely stabilize in a monotonic map for the primary feature. In other words, by randomly initializing our unit grids, we likely overestimated the amount of major topographic variability, such as the presence of saddle points, that might be expected biologically. We used random initialization specifically to diminish the possibility of constantly converging to a subset of local minima and obscuring the possible influence of relative feature weightings on resulting maps. Indeed, we found only a fourth as many saddle points for Cartesian initialization as for random initialization.

Another concern with the global orthogonality results is that uniformly distributed features may not be biologically realistic for all potential features. We did perform a small set of 2D experiments with Gaussian feature distributions and also found that primary features again dominate topographies at high relative weightings. Biologically accurate feature distributions were not pursued in these studies for several reasons. First, because the uniform distributions require the equilibrated maps to cover the entire range of each feature uniformly, these SOFM experiments are the most highly

constrained of all possible distributions in terms of coverage. Second, we deliberately chose not to label our generic features with specific auditory or other sensory features that are likely to be mapped. The precise topographic properties of physiologic features other than frequency are not entirely clear in A1, so we did not set out to make at this point strong claims about the topographies of these other features. Instead, our results provide boundary conditions that limit the range of possible functional topographies that might be expected for A1. Third, feature distributions are different for species with different acoustic environments, and the current study was not intended specifically to model A1 topography for any particular species.

3.3.6 Future Studies

To make quantitative assessments regarding the actual topographies in auditory cortex, additional anatomical and physiological details should be taken into account. First, estimating which features are actually mapped in the cortical area of interest establishes the requisite framework for construction of an appropriate SOFM. As mentioned previously, physiological mapping experiments in A1 of species with unspecialized auditory systems have indicated several nonrandomly distributed features that would represent logical candidates. Relevant mapped features have traditionally been more convincingly determined in specialized auditory systems, making echolocating bat auditory cortex an attractive physiological system for evaluating the model results. Second, estimating actual feature distributions would provide a more accurate

framework for the SOFM to operate upon. Coverage uniformity is tied to these distributions, and because coverage is a property the SOFM algorithm manipulates, different feature distributions could influence the final secondary feature maps, particularly if many features were mapped. For example, artificially over-representing the presence or behavioral relevance of a particular sound frequency in the acoustic environment of an experimental animal could potentially influence frequency, bandwidth and threshold maps of A1 as the cortical network reorganizes to devote more neurons to processing that frequency. Finally, the precise anatomical shape of the relevant cortical area is necessary to design a unit grid of the proper shape. Knowing this shape is important given our findings that feature maps with a single dominant feature take their shape from the anatomy. This information would also be necessary to verify whether or not sound frequency actually represents a dominant feature (as in Figure 3.4) or is mapped globally orthogonally with another feature (as in Figure 3.5). These anatomical data would ideally be collected in the same animal for which detailed physiological experiments are conducted. In order to verify the results of these computational studies, future physiological measurements of A1 neuronal function will need to be conducted at a high enough density to capture local map variations occurring at high spatial frequencies. Such experiments would also be able to confirm whether high feature gradients do not typically overlap in the same small region of cortex, as these computational studies predict.

Chapter 4

Neuronal Responses to Sound Intensity Level

4.1 Introduction

Acoustic information in sound pressure waves is transduced by the cochlea into action potentials that travel along cochlear nerve fibers (CNFs). Simply stated, sound at different frequencies causes different portions of the cochlea to vibrate so that different frequencies are represented by action potentials in separate CNFs. Sound intensity level, in units of dB SPL, is an absolute log scale by which the magnitude of sound pressure waves is measured. The minimum sound intensity level that causes a driven response in a particular CNF at any sound frequency is known as its threshold. This frequency to which the CNF is most sensitive—the frequency to which the CNF responds at its threshold—is referred to as the characteristic frequency (CF). Threshold and CF are also used to describe neuronal responses at higher auditory centers, postsynaptic to the auditory nerve (for an overview of above topics see (Geisler, 1998; Pickles, 1988)). Because pure tones are sounds that only contain a single frequency, at a given sound level they will activate the smallest section of the cochlea (von Békésy, 1960) and therefore are the simplest stimulus by which to probe neural responses. Pure tones are

also conveniently the eigenfunctions of linear systems, so it is possible that tone responses could completely characterize a neuron or neural system if it were linear.

In the auditory nerve, the sound intensity level of a pure tone centered at each nerve fiber's characteristic frequency is encoded monotonically such that each fiber shows a non-decreasing firing rate as sound level is increased (Galambos & Davis, 1943; Kiang, Watanabe, Thomas, & Clark, 1965; Palmer & Evans, 1980; Sachs & Abbas, 1974). Starting in the cochlear nucleus, and in higher auditory areas up to and including auditory cortex, some neurons show a nonmonotonic level response whereby neurons have a peak response at a particular level and the response decreases at higher levels. This response property is often referred to as intensity tuning or sound level tuning. Nonmonotonic level responses have been reported in the cochlear nucleus (Rose, Galambos, & Hughes, 1959; Young & Brownell, 1976), in the inferior colliculus (Aitkin, 1991; Ramachandran, Davis, & May, 1999; Rees & Palmer, 1988; Rose, Greenwood, Goldberg, & Hind, 1963; Ryan & Miller, 1978; Semple & Kitzes, 1985) and in the medial geniculate body (Galambos, 1952). Because this response is not present in the auditory nerve, it therefore must be created by neural circuits. Direct evidence of this phenomenon has also been reported (Faingold, Boersma Anderson, & Caspary, 1991; Sivaramakrishnan et al., 2004; Tan, Atencio, Polley, Merzenich, & Schreiner, 2007; Wu, Li, Tao, & Zhang, 2006). The active creation and maintenance of level tuning by the nervous system implies that this response feature is potentially important for encoding of stimulus intensity or a related stimulus property. Additionally, animals trained in level

discrimination tasks show an increased proportion of level-tuned neurons in A1 over control animals (Polley, Heiser, Blake, Schreiner, & Merzenich, 2004; Polley, Steinberg, & Merzenich, 2006), implying that nonmonotonic level encoding also plays an important behaviorally-relevant role.

At the level of primary auditory cortex (A1), various methods for characterizing nonmonotonic neurons, coupled with potential differences due to neuronal sampling, have resulted in a large range of percentages of nonmonotonic responses reported in different studies and have made direct comparisons difficult. Preparations that report at least 25% (conservative estimates) in anaesthetized A1 include cat (Clarey et al., 1994; Heil, Rajan, & Irvine, 1994; Phillips, 1990; Phillips & Irvine, 1981; Phillips, Semple, & Kitzes, 1995; Sutter & Loftus, 2003; Sutter & Schreiner, 1995), owl monkey (Recanzone et al., 1999) and bat (Suga, 1977; Suga & Manabe, 1982) and in awake A1 include macaque (Pfingst & O'Connor, 1981), squirrel monkey (Shamma & Symmes, 1985) and marmoset (Sadagopan & Wang, 2008). At least one study in awake macaque A1 reports percentages below 25% (Recanzone et al., 2000). Although estimates vary, the majority of these studies find a substantial portion of level-tuned neurons in A1, a result that is not true in other sensory systems, i.e., a very low percentage of nonmonotonic responders to contrast are reported in V1 (Peirce, 2007). Although reports again vary, a portion of level-tuned auditory neurons demonstrate inhibition below spontaneous rate at the highest levels (Pfingst & O'Connor, 1981), a property rarely described in other sensory systems.

In this chapter we present detailed results on responses of single A1 neurons to pure tones at different sound intensity levels. The tones are presented separately, surrounded by a period of silence, so that neuronal adaptation to sound level does not play a large role in their responses. In general we find a significant difference in neuronal thresholds and dynamic ranges between the monotonic and nonmonotonic populations across the frequency range of hearing for the species and when the effect of variable frequency sensitivity is removed. Statistics of several other neuronal response properties including best level, spontaneous rate and driven rate and are also presented. Lower non-adapted thresholds in nonmonotonic neurons than in monotonic neurons supports the hypothesis that nonmonotonic neurons may be specialized for encoding low sound levels. Although this is one potential role for nonmonotonic neurons, particularly in the context of dynamic level stimuli (see Chapter 5), it likely complements other functions that have been previously ascribed to level-tuned neurons (see Section 4.3).

4.2 Results

Altogether, 544 primary auditory cortex neurons from 12 hemispheres of 7 awake marmoset monkeys (*Callithrix jacchus*) were analyzed for sound intensity level coding properties in response to characteristic frequency (CF) tones. As expected, a wide variety of input-output functions with positive driven rates during the duration of the tone were recorded, including purely monotonically increasing functions, monotonically

nondecreasing functions with saturation at high levels and nonmonotonic functions with a best level eliciting the highest spiking rates (Figure 4.1). The degree of input-output monotonicity was quantified for each neuron by a monotonicity index (MI) calculated on interpolated, curve-fit rate-level functions (see Section 2.2.3). MIs of this population ranged from 1 (completely monotonic) to 0 (completely nonmonotonic, suppression to spontaneous rates at high levels) and beyond to about -0.4 (completely nonmonotonic, suppression below spontaneous rates at high levels). The smallest MI in our dataset was -0.72 and only 3 / 544 neurons had MIs less than -0.4 , while 78 neurons (14%) had MIs less than zero. Threshold and saturation levels were determined as 20% and 80% of maximum firing rate above spontaneous rates, respectively, and formed the bounds of a conservative estimate of dynamic range attributed to each neuron. Only one dynamic range was estimated for rate-level functions with $MI > 0.5$ (monotonic neurons); for rate-level functions with $MI \leq 0.5$ (nonmonotonic neurons), however, both a lower dynamic range and an upper dynamic range were defined by separate threshold and saturation values. Lower dynamic ranges (blue for monotonic neurons and red for nonmonotonic neurons in Figure 4.1) were measured as the range of sound levels from threshold to saturation. Upper saturation and upper threshold for nonmonotonic neurons were determined at 80% and 20% of maximum firing rate above the response at the maximum sound level presented. Upper dynamic ranges (green in Figure 4.1) were measured as the range of sound levels from upper saturation to upper threshold.

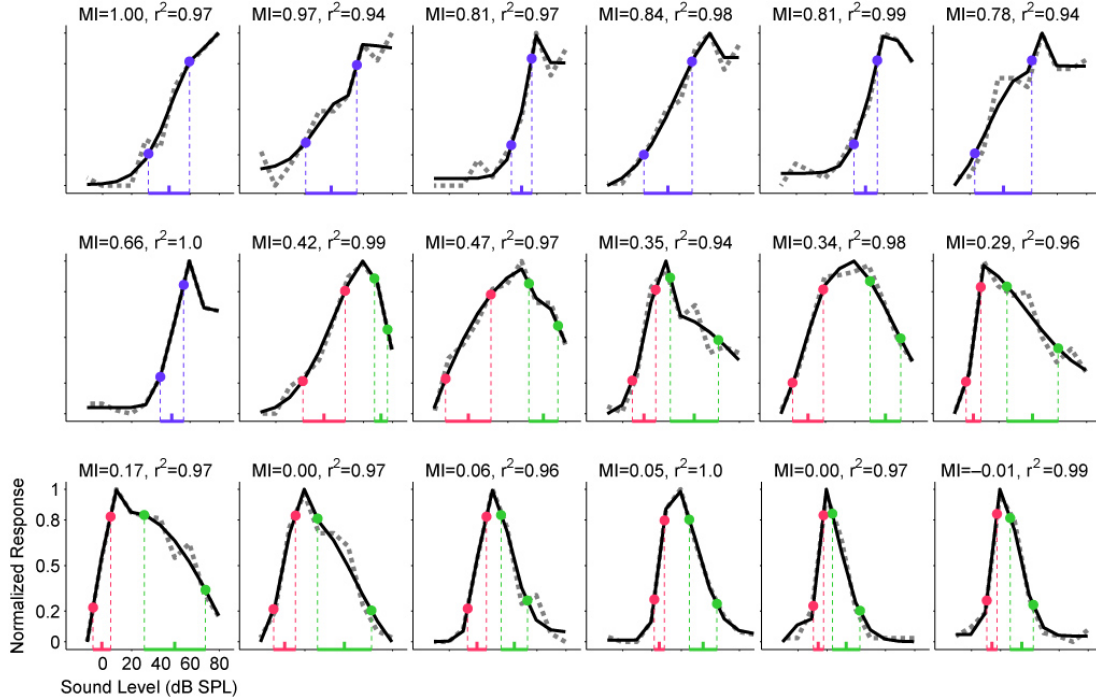


Figure 4.1 Normalized rate-level functions from a representative collection of primary auditory cortex neurons demonstrate the diversity of monotonicity observed in the current study. Neurons are arranged in order from most monotonic (monotonicity index or $MI = 1$, upper left) to most nonmonotonic ($MI = -0.01$, lower right). Rate-level functions were measured with 100 ms tones at characteristic frequency and are shown as dotted gray lines. Curve fits generated with a six-parameter split-Gaussian model (see Section 2.2.3) are shown as solid black lines and the goodness of fit (r^2) for each neuron is indicated. Threshold (20% of maximum) and saturation (80% of maximum) points are labeled on the curves themselves, and dynamic ranges are indicated by horizontal colored lines superimposed onto the sound level axis. Dynamic range midpoints are indicated by colored ticks. For neurons categorized as monotonic ($MI > 0.5$) only one dynamic range is labeled (blue); whereas for neurons categorized as

nonmonotonic ($MI \leq 0.5$) the lower dynamic range (red) and the upper dynamic range (green) are both labeled.

Collectively, the distribution of monotonic neuron dynamic ranges spanned the full range of sound levels tested, implying that this subpopulation of neurons has sufficient diversity to encode a wide intensity range of hearing (Figure 4.2A). About half of these neurons had dynamic ranges of 20 dB or less, but the apparent population spread in dynamic ranges and the spread in thresholds likely enables monotonic neurons to encode sound levels across the full range of levels and frequencies tested. The distribution of nonmonotonic neuron lower dynamic ranges, on the other hand, collectively did not span the full range of levels tested (Figure 4.2B). This difference is due partially to lower apparent thresholds in this subpopulation and narrower lower dynamic ranges (over 80% with dynamic ranges of 20 dB or less). If the upper dynamic ranges of these neurons are included, however, then the potential coding levels for this subpopulation of neurons matches that of the monotonic population. This finding is consistent with the apparent use of nonmonotonic upper dynamic ranges to encode sound level under dynamic stimulus conditions (see Chapter 5). Even with limited neuronal sampling across all the frequencies of hearing for this species, a dependence of the lowest neuronal thresholds on CF is apparent in Figure 4.2.

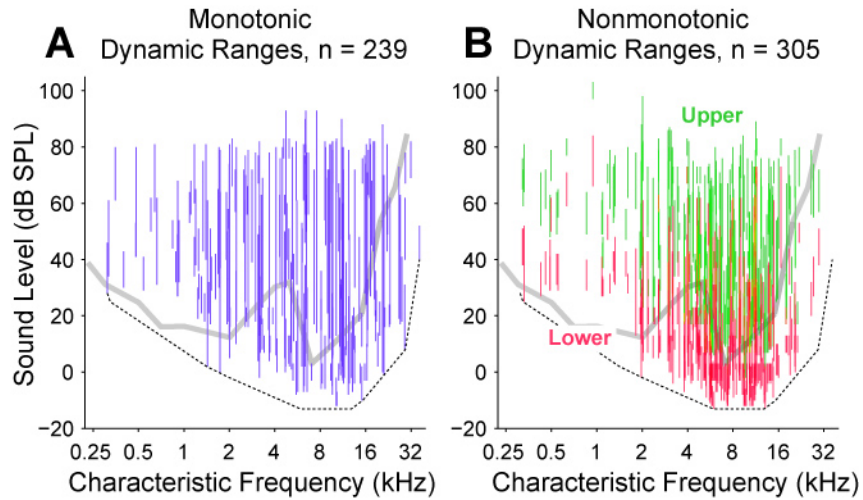


Figure 4.2 Dynamic ranges of all neurons in the study population plotted against CF. **A**, Thresholds for monotonic neurons are connected with a blue line to saturation values in order to depict the dynamic range for each neuron. **B**, Lower (red) and upper (green) dynamic ranges are shown for nonmonotonic neurons. Each neuronal population appears to be capable of coding most or all combinations of frequency and level. Dependence of threshold on CF is depicted as a dotted line in both panels. This line provides an estimate of the minimum sensitivity of a neuron at any particular frequency (see Section 2.2.3). The gray line in the background of both plots is the audiogram of the species measured with a behavioral paradigm (Seiden, 1957).

In order to make valid threshold comparisons between neurons independent of characteristic frequency (CF), the neuronal dependence of threshold on CF that is apparent in Figure 4.2 must be taken into account. The dataset contained a larger proportion of nonmonotonic neurons in the frequency range that also had the lowest thresholds in the population (Figure 4.3B); therefore, if the dependence of threshold on CF were not removed from the threshold estimates then this would bias larger numbers of nonmonotonic neurons towards lower thresholds relative to monotonic neurons simply due to this sampling difference. This dependence as measured over several animals is likely related to the overall behavioral frequency sensitivity (the audiogram) of the species, although other factors are certainly involved, e.g., how single neuron responses or more likely a population of neuronal responses are used for decision making (Britten, Newsome, Shadlen, Celebrini, & Movshon, 1996; Shadlen, Britten, Newsome, & Movshon, 1996). The minimum neuronal thresholds as a function of frequency are grossly consistent with the audiogram (thick gray line, Figure 4.2A,B) as measured with behavioral studies of tone thresholds in marmosets (Seiden, 1957). We estimated threshold dependence on CF and removed that value from our threshold estimates (see Section 2.2.3). This procedure created relative minimum thresholds of approximately 0 dB over all frequencies in our dataset (Figure 4.3A). The procedure did not fit the minimum thresholds perfectly, particularly in locations of higher threshold concavities or notches (for example from 250 Hz to 1 kHz in Figure 4.2A,B), but allowed for a relatively flat 0 dB minimum residual threshold measure for neurons at

most frequencies (Figure 4.3A) without over-fitting small variations in minimum neuronal threshold.

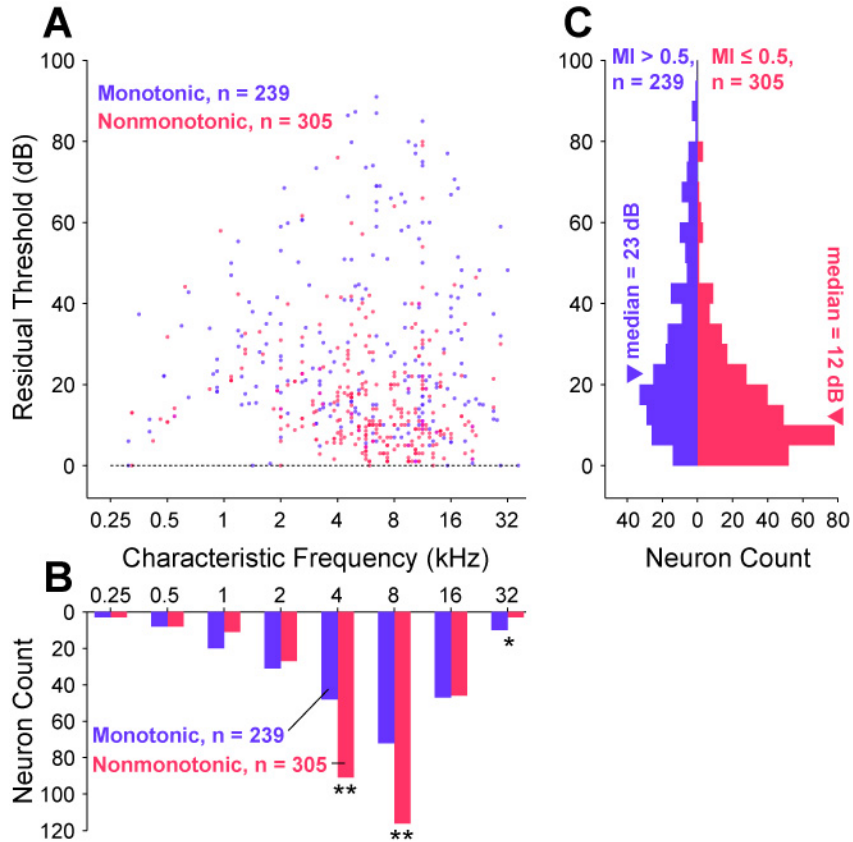


Figure 4.3 Comparison of monotonic and nonmonotonic neuron residual thresholds.

The residual threshold controls for the neuronal dependence of threshold on characteristic frequency (CF). **A**, Scatterplot of residual thresholds (i.e., neuronal thresholds with frequency-dependent neuronal threshold subtracted) as a function of frequency for monotonic (blue) and nonmonotonic (red) neurons. **B**, Monotonic and nonmonotonic neurons were separately collected into one-octave frequency bins based upon CF to evaluate their relative distribution across frequency. Frequency bins centered at 4 and 8 kHz contained significantly more nonmonotonic than monotonic neurons ($p = 1.7 \times 10^{-4}$ and $p = 8.2 \times 10^{-4}$, respectively; binomial test), and the frequency bin centered at 32 kHz contained significantly more monotonic than nonmonotonic

neurons ($p = 0.046$, binomial test). These bins are marked with asterisks. **C**, Collapsing residual thresholds across frequency reveals that the distribution of nonmonotonic neurons (median = 12 dB, interquartile range = 15 dB) has a lower central tendency and a smaller range than that of monotonic neurons (median = 23 dB, interquartile range = 28 dB). These two distributions are significantly different ($p = 7.2 \times 10^{-16}$, Wilcoxon rank sum test).

Both monotonic and nonmonotonic neurons were found with CFs distributed across the full frequency range of hearing for marmosets (Figure 4.3B). Out of the entire population, 305 / 544 (56%) neurons were classified as nonmonotonic ($MI \leq 0.5$) and 239 / 544 (44%) neurons were classified as monotonic ($MI > 0.5$). These values likely represent a lower bound on the relative proportion of nonmonotonic neurons because higher-level measurements of neurons with intermediate MIs would likely have revealed further decreased rate responses. Overall, more sampled neurons were tuned to the frequencies at which the marmoset is most sensitive, in the range [6, 13] kHz (Figure 4.3B). Marmoset vocalization energy is also greatest in this range (DiMattina & Wang, 2006). This over-representation of middle frequency CFs is consistent with previous studies sampling marmoset A1 (Philibert et al., 2005; Sadagopan & Wang, 2008) but cannot be used to conclude an overrepresentation of these frequencies actually exists without thoroughly evaluating the distribution of electrode penetrations, which was not done. This aside, significantly more nonmonotonic than monotonic neurons were observed in the 4 kHz ($p = 1.7 \times 10^{-4}$, binomial test) and 8 kHz ($p = 8.2 \times 10^{-4}$, binomial test) frequency ranges where marmoset vocalization energy is common, and significantly fewer nonmonotonic neurons were observed in the 32 kHz frequency range ($p = 0.046$, binomial test) where vocalization energy is less common.

Reasonable comparison of thresholds across CFs was made possible by subtracting out the regressed frequency dependence of absolute neuronal threshold (see Section 2.2.3). With this manipulation, the distribution of monotonic residual thresholds (median = 23

dB, interquartile range = 28 dB) was found to be significantly different ($p = 7.2 \times 10^{-16}$, Wilcoxon rank-sum test) from the distribution of nonmonotonic residual thresholds (median = 12 dB, interquartile range = 15 dB). As seen in Figure 4.3C, the distribution of residual thresholds is not uniform for either population. Overall, residual thresholds are skewed toward lower values for both populations, with 75% (409 / 544) of the combined population having residual thresholds of 30 dB or less. Some of this skew is undoubtedly caused by the limited effective range of sound levels tested at the highest and lowest frequencies due to this species' audiogram, but the skew is still apparent even if one considers only residual thresholds in the range [0, 40] dB, which can receive contributions from neurons having any CF. The skew is particularly evident for the nonmonotonic population and results in the lower median threshold for these neurons. Monotonic neuron thresholds appear to be more nearly uniform than those of nonmonotonic neurons, however, and as a consequence extend over a wider range of sound levels. Only a small number of nonmonotonic neurons were found to have high thresholds. For neurons with residual thresholds greater than 60 dB only 6 / 36 (17%) were nonmonotonic versus 30 / 36 (83%) that were monotonic.

A visual assessment of neuronal dynamic ranges independent of CF can be obtained by sorting neurons of each class by residual threshold and plotting their dynamic ranges (Figure 4.4). This depiction confirms that more nonmonotonic neurons have lower thresholds than monotonic neurons, reflecting the difference in residual threshold skew seen in Figure 4.3C. As also seen in Figure 4.2, the overall range of sound level spanned

by neuronal dynamic ranges is similar between the two populations, as long as both the upper and lower dynamic ranges of nonmonotonic neurons are taken into account. More apparent in Figure 4.4 is that the nonmonotonic lower dynamic ranges appear to be narrower than both the monotonic dynamic ranges and the nonmonotonic upper dynamic ranges.

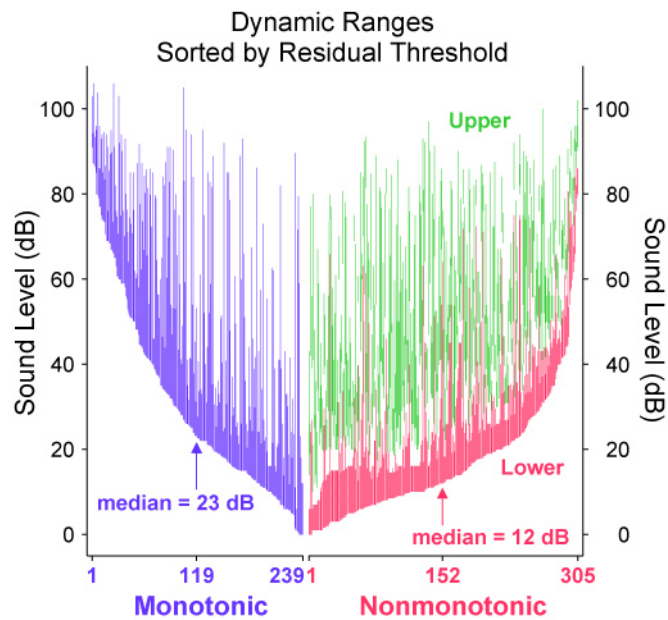


Figure 4.4 Monotonic (blue), nonmonotonic lower (red) and nonmonotonic upper (green) dynamic ranges, sorted by residual threshold separately for the monotonic and nonmonotonic populations. Visualizing in this manner shows the clustering of nonmonotonic thresholds closer to the minimum neuronal threshold (at 0 dB residual threshold). Also apparent is that neurons in either population can potentially encode intensities across the entire range of sound levels tested regardless of threshold.

All dynamic ranges are also skewed towards lower values. In fact, of the combined dynamic ranges for monotonic neurons and lower dynamic ranges for nonmonotonic neurons, 80% (433 / 545) span 30 dB or less. They also show the effect of the audiogram as seen for neuronal thresholds (Figure 4.2) since higher minimum absolute thresholds at the less sensitive frequencies forces neurons at these frequencies to have smaller dynamic ranges for a given fixed maximum sound level (Figure 4.5A). Indeed, distributions of dynamic ranges (Figure 4.5C–D) show that the lower dynamic ranges (median = 11 dB; interquartile range = 8 dB) of the nonmonotonic population are significantly smaller ($p = 8.0 \times 10^{-22}$, Wilcoxon rank sum test) than the monotonic dynamic ranges (median = 22 dB; interquartile range = 25 dB). The nonmonotonic upper dynamic ranges, however, account for most of the sound levels spanned by nonmonotonic neurons (median = 15 dB; interquartile range = 17 dB). These three distributions were significantly different from one another ($p = 0$, Kruskal-Wallis test with Tukey-Kramer correction for multiple comparisons). Dynamic ranges from both populations can stretch across large spans of sound level regardless of residual threshold, and the combined population of dynamic ranges for monotonic neurons and lower dynamic ranges for nonmonotonic neurons was bounded by but was not significantly linearly correlated with residual threshold ($p = 0.47$, regression F test; $p = 8.1 \times 10^{-5}$, Spearman rank correlation test). Some monotonic neurons near the threshold of hearing, for example, exhibit dynamic ranges that span almost the full range of hearing tested. The bounding of dynamic range depending on residual threshold occurs

because of the fixed maximum sound level of tones in our protocol (and ultimately by the dynamic range of the cochlea).

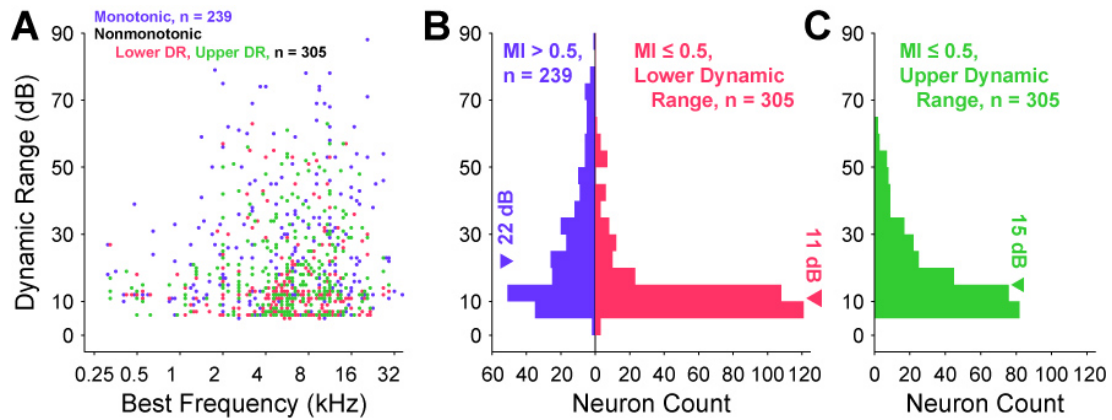


Figure 4.5 Dynamic range magnitudes for monotonic neurons (blue) and of lower (red) and upper (green) dynamic ranges for nonmonotonic neurons. **A**, Dynamic ranges as a function of characteristic frequency (CF) reveal that the maximum dynamic range at a particular frequency is limited by the audiogram of the species (as approximated by neuronal thresholds, see Figure 4.2). **B**, Distribution of dynamic ranges for monotonic neurons and of lower dynamic ranges for nonmonotonic neurons reveals a significantly lower median for nonmonotonic neurons ($p = 8.0 \times 10^{-22}$, Wilcoxon rank sum test). **C**, Median of nonmonotonic upper dynamic range distribution is in between those in **A** and significantly different from both ($p = 0$, Kruskal-Wallis test with Tukey-Kramer correction for multiple comparisons).

Up to this point, neurons in the study population have been classified into two groups according to the shape of their rate-level functions. While such a distinction is historical (Aitkin, 1991; Pfingst & O'Connor, 1981; Phillips & Irvine, 1981; Rees & Palmer, 1988; Ryan & Miller, 1978; Semple & Kitzes, 1985; Sutter & Schreiner, 1995), it does not capture the full variety of the rate-level functions depicted in Figure 4.1. In order to generalize the findings reported so far, we compared each neuron's rate-level response properties directly with the degree of monotonicity as measured by MI. Figure 4.6, for instance, depicts a scatterplot of MI and residual threshold. We found a significant correlation between residual threshold and MI using a linear regression fit over all MI values greater than -0.4 ($r^2 = 0.15$; $p = 0$, regression F test, black line in Figure 4.6). Only 3 / 305 neurons had MIs less than -0.4 (minimum MI was -0.73) and we did not want these few neurons to influence the regression. The correlation remained when the regression was calculated for monotonic neurons only ($MI > 0.5$; $r^2 = 0.13$; $p = 1.3 \times 10^{-8}$, regression F test), but not for nonmonotonic neurons only ($MI \leq 0.5$; $p = 0.91$, Spearman rank correlation test). In other words, the highest residual thresholds are disproportionately concentrated in the subpopulation of neurons that exclusively saturate their rate response at the highest intensities.

A large proportion of monotonic neurons (74 / 239, 31%) exhibited monotonically nondecreasing behavior indicated by an MI of 1. This subpopulation by itself had a median residual threshold of 42 dB with individual values that span nearly the full range of residual thresholds. This wide range of residual thresholds is particularly noteworthy

because 60% of all neurons measured with residual thresholds greater than 40 dB have an MI of exactly 1. The traditional definition of MI (de la Rocha et al., 2008; Recanzone et al., 2000; Sadagopan & Wang, 2008; Sutter & Loftus, 2003; Sutter & Schreiner, 1995) that does not subtract spontaneous rates (see Section 2.2.3) gave a qualitatively similar distribution as our definition of MI but with more neurons clustered at the extremes of 0 and 1. Amongst the nonmonotonic neurons, 78 / 305 (26%) had MIs less than 0, indicating suppression below spontaneous rate at the highest intensities and implying a local inhibitory process. This number represents an upper bound since many of these neurons had MIs near zero. For these neurons to provide evidence for locally inhibitory processes contributing to nonmonotonicity, a significance test would need to be applied in order to verify that spiking rates were indeed inhibited below spontaneous rates, which was not done here.

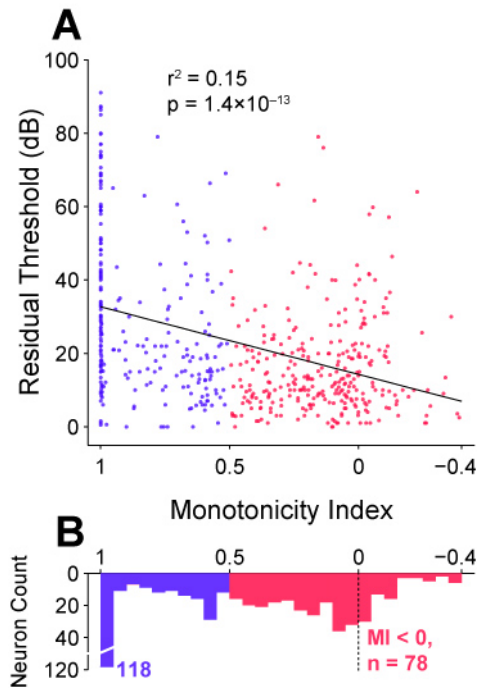


Figure 4.6 Residual threshold as a function of monotonicity index (MI). **A**, Scatterplot reveals that the highest residual thresholds are concentrated in the most monotonic subpopulation. Linear regression reveals that threshold and MI are significantly correlated across the entire population ($r^2 = 0.15$; $p = 0$, regression F test). Three neurons with $MI < 0.4$ were not included in the regression and not depicted in the scatter plot. **B**, Distribution of MI values with a large cluster of very monotonic neurons having MI equal to 1, and a large cluster of neurons having MIs less than or equal to 0.

Monotonicity Index (MI) and spontaneous rate of all neurons in the dataset were modestly monotonically related but not significantly linearly correlated ($r = 0.09$; $p = 0.035$, Spearman rank correlation test; $p = 0.26$, regression F test) and distributions of spontaneous rate were significantly different ($p = 0.014$, Wilcoxon rank sum test) between monotonic (median = 2.5 sp/s) and nonmonotonic (median = 1.6 sp/s) neurons. Neurons demonstrated an inverse correlation between residual threshold and spontaneous rate (Figure 4.7), similar to findings in auditory nerve fibers (Kiang, Liberman, & Levine, 1976; Kiang et al., 1965; Liberman, 1978; Rhode & Smith, 1985). While a linear regression of the cortical neurons revealed a significant relationship ($r^2 = 0.026$; $p = 1.5 \times 10^{-4}$, regression F test), the magnitude of the phenomenon appears to be smaller than that seen in auditory nerve. No significant correlation was apparent between dynamic range and spontaneous rate ($p = 0.90$, Spearman rank correlation test), contrary to findings in the auditory nerve (Schalk & Sachs, 1980). Spontaneous rates were approximately log normally distributed (Figure 4.7B), except for a cluster of neurons with spontaneous rates measured at zero (12 / 239 monotonic and 14 / 305 nonmonotonic). A log normal distribution of spontaneous rates in primary auditory cortex has been previously reported (Hromadka, Deweese, & Zador, 2008).

Dividing the neuron population into three similarly sized groups with low (rate ≤ 0.95 spike/s), medium ($0.95 < \text{rate} \leq 4$ spikes/s) and high (rate > 4 spikes/s) spontaneous rate (Figure 4.7C–E) revealed significantly different residual thresholds in pairwise comparisons amongst all groups ($p = 0$, Kruskal-Wallis test with Tukey-Kramer

correction for multiple comparisons). The median residual threshold for the low, medium and high spontaneous groups was 23 dB, 16 dB and 12 dB, respectively. Just as in the auditory nerve, low-spontaneous spiking cortical neurons appear to encode higher sound levels. Threshold and spontaneous rate were still negatively correlated just within the monotonic ($r^2 = 0.026$; $p = 0.012$, regression F test) and nonmonotonic ($r^2 = 0.069$; $p = 3.6 \times 10^{-6}$, regression F test) subpopulations. So, although based on the findings that (1) monotonicity index (MI) and threshold were positively correlated, (2) MI and spontaneous rate were positively correlated and (3) threshold and spontaneous rate were negatively correlated, one might expect only the nonmonotonic subpopulation to show the relationship between threshold and spontaneous rate; however, this was not the case, as the dataset still contained many monotonic neurons with low thresholds.

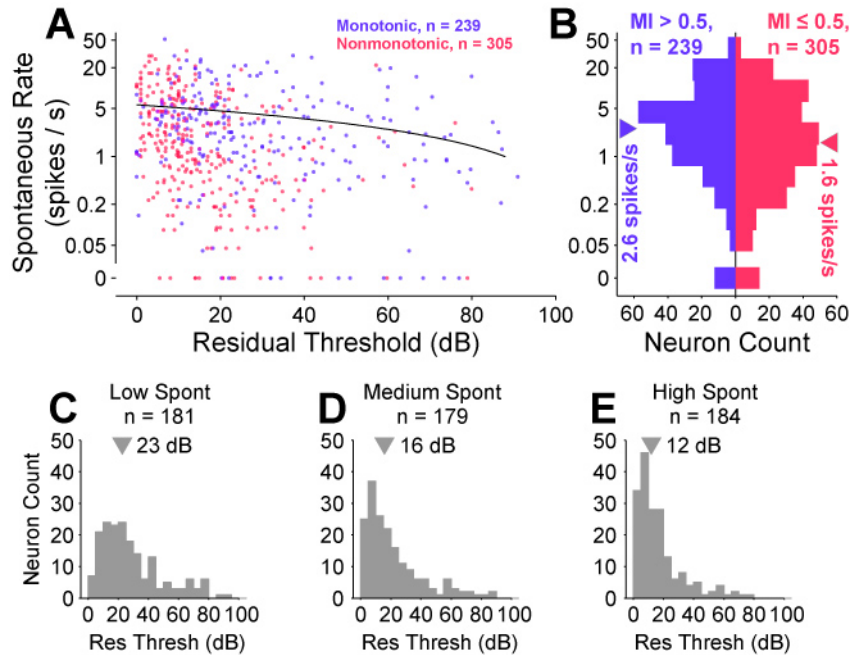


Figure 4.7 Spontaneous rate and residual threshold are weakly correlated. **A**, Scatterplot of spontaneous rate versus residual threshold for monotonic (blue) and nonmonotonic (red) neurons reveals that neurons in either population with higher residual thresholds tend to have lower spontaneous rates. A linear regression of this trend reveals a significant, though small effect ($r^2 = 0.026$; $p = 1.5 \times 10^{-4}$, regression F test). The regression was performed on a linear scale, leading to a curved line on this logarithmic plot. **B**, Collapsing across residual threshold reveals a significant difference between distributions of spontaneous rates for monotonic and nonmonotonic neurons ($p = 0.014$, Wilcoxon rank sum test). **C–E**, Residual threshold differs between groupings into approximate tertiles of spontaneous rate.

Contrary to spontaneous rate, neurons in our dataset did not show a significant linear relationship between monotonicity index and maximum discharge rate ($p = 0.13$, Spearman rank correlation test, Figure 4.8A). Likewise, there was not a significant difference in medians between the distributions of maximum discharge rate (Figure 4.8B) for monotonic (median = 35 spikes/s; interquartile range = 49 spikes/s) and nonmonotonic (median = 36 spikes/s; interquartile range = 49 spikes/s) neurons ($p = 0.48$, Wilcoxon rank-sum test). The driven rate of a neuron is the discharge rate minus the spontaneous rate, i.e., the amount that the neuron is excited above spontaneous firing. There was also not a significant difference in distributions of maximum driven rates ($p = 0.60$, Wilcoxon rank-sum test) for the two populations, both with a median of 32 spikes/s. Similar to spontaneous rates, distributions of maximum discharge rates and maximum driven rates were also approximately log normally distributed. There was a substantial and highly significant correlation between spontaneous rate and maximum driven rate ($r^2 = 0.46$; $p = 2.2 \times 10^{-74}$, regression F test). Thus, neurons with greater spontaneous rates often had higher driven rates above spontaneous.

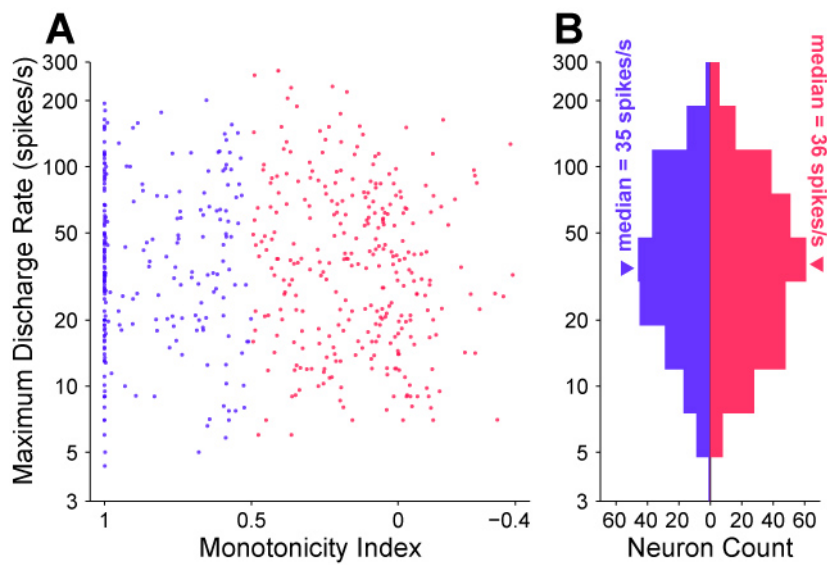


Figure 4.8 Monotonicity index (MI) and maximum discharge rate are not correlated. **A**, Scatter plot of MI versus maximum discharge rate reveals no significant linear trend ($p = 0.13$, Spearman rank correlation test). **B**, Collapsing maximum discharge rate across MI reveals that the monotonic and nonmonotonic populations are not significantly different ($p = 0.48$, Wilcoxon rank sum test).

Other significant correlation trends were consistent with those reported above. Residual best level (BL) and dynamic range were positively correlated (Figure 4.9A; $r^2 = 0.47$; $p = 2.4 \times 10^{-76}$, regression F test), which follows from the lack of correlation between threshold and dynamic range discussed above. That is, because threshold and dynamic range were not correlated, a neuron with a particular threshold could have a variety of dynamic ranges. Therefore, a larger or smaller dynamic range would result in a higher or lower BL, respectively, regardless of threshold. Residual best level was calculated by removing the approximate effect of frequency on the overall neuronal sensitivity, in the same fashion as for threshold (see Section 2.2.3) For completely monotonic neurons (MI equal to 1; 74 / 239 monotonic neurons), the BL was the same as the maximum sound level presented. The best level distribution (Figure 4.9B) for monotonic neurons (median = 66 dB; interquartile range = 50 dB) was much more nearly uniform than that for nonmonotonic neurons (median = 30 dB; interquartile range = 30 dB) and these two distributions were significantly different ($p = 3.8 \times 10^{-32}$, Wilcoxon rank-sum test). Consistent with the result for residual thresholds, there was a significant correlation between MI and BL for monotonic neurons ($r^2 = 0.33$; $p = 3.0 \times 10^{-22}$, regression F test) but not for nonmonotonic neurons ($p = 0.14$, Spearman rank correlation test). Finally, MIs were significantly positively correlated with dynamic ranges of monotonic ($r^2 = 0.13$; $p = 1.3 \times 10^{-8}$, regression F test) and nonmonotonic ($r^2 = 0.14$; $p = 0.015$, regression F test) neurons. This trend was not surprising based upon the fact that monotonic and nonmonotonic neurons had significantly different distributions of dynamic ranges (Figure 4.3B). A significant negative correlation was found between MI

and upper dynamic range for nonmonotonic neurons, but this correlation could easily be an artifact of the fixed maximum sound levels presented.

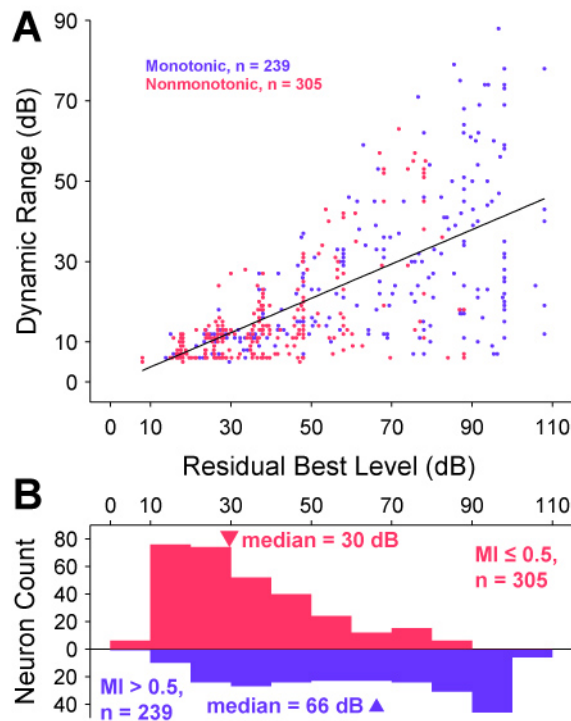


Figure 4.9 A, A significant correlation exists between a neuron’s best level (BL) and its dynamic range. Black line indicates a linear regression ($r^2 = 0.47$; $p = 2.4 \times 10^{-76}$, regression F test). **B**, The distribution of BLs for monotonic and nonmonotonic neurons are significantly different ($p = 3.8 \times 10^{-32}$, Wilcoxon rank-sum test). The distributions of BLs for monotonic neurons are relatively uniform except for a cluster of neurons with MI equal to 1 (74 / 239) whose best level is limited by the greatest sound intensity level presented to the neuron. The distribution of BLs for nonmonotonic neurons is skewed towards lower sound levels.

A comparison of the goodness of fit values (r^2) for the monotonic and nonmonotonic populations (Figure 4.10A) demonstrated that our results were not biased by fitting the rate-level functions with a split Gaussian (see Section 2.2.3). The distribution of r^2 (median = 0.94; interquartile range = 0.11) values over the entire population confirmed that overall our fitting procedure resulted in good fits for the rate-level functions. More importantly, there was not a significant difference between the r^2 distributions for the monotonic and nonmonotonic populations ($p = 0.12$, Wilcoxon rank-sum test). This means that the conclusions regarding lower median thresholds and lower median dynamic ranges for nonmonotonic neurons was not likely to be biased by this particular analysis.

Because of limitations of the recording setup, a potential topography of monotonicity that has been reported in other studies (Clarey et al., 1994; Schreiner et al., 1992; Sutter & Schreiner, 1995) was not explored. When looking at the recording depth alone (the depth of the recorded neuron relative to the dural surface), there was no significant correlation between MI and neuron depth for either monotonic ($p = 0.19$, Spearman rank correlation test) or nonmonotonic ($p = 0.20$, Spearman rank correlation test) neurons. Consistent with this finding, there was no significant difference ($p = 0.86$, Wilcoxon rank-sum test) between depth distributions (Figure 4.10B) for the two neuron groups. Based on the size and spontaneous rates of background activity during recording, we found that the cutoff between layer 4 and layer 2/3 responses was at approximately 1.25 mm below the dura. Using this approximate figure, about 50% of

both monotonic and nonmonotonic neurons were recorded in layer 2/3, and about 50% in deeper layers. Although it is more difficult to ascertain where layer 4 responses ended, neurons recorded at depths greater than 2 mm below the dura are almost certainly deeper layers. This gives about 30% of monotonic neurons and about 40% of nonmonotonic neurons recorded in layer 4. Thus, as can also be seen in Figure 4.10B, a slightly larger number of monotonic neurons were recorded in layers beyond layer 4 and slightly larger number of nonmonotonic neurons were recorded in layer 4. In these three depth subsets (depth ≤ 1.25 mm, depth > 1.25 mm and depth ≤ 2 mm, depth > 2 mm) there were 143 / 266, 120 / 186 and 35 / 82 nonmonotonic neurons, respectively. Depth information was not recorded correctly for 10 neurons. The main conclusion, that nonmonotonic neurons have significantly lower thresholds than monotonic neurons, was still valid and significant in each depth subset ($p = 1.8 \times 10^{-9}$, $p = 4.4 \times 10^{-8}$ and $p = 0.032$ respectively; Wilcoxon rank-sum tests).

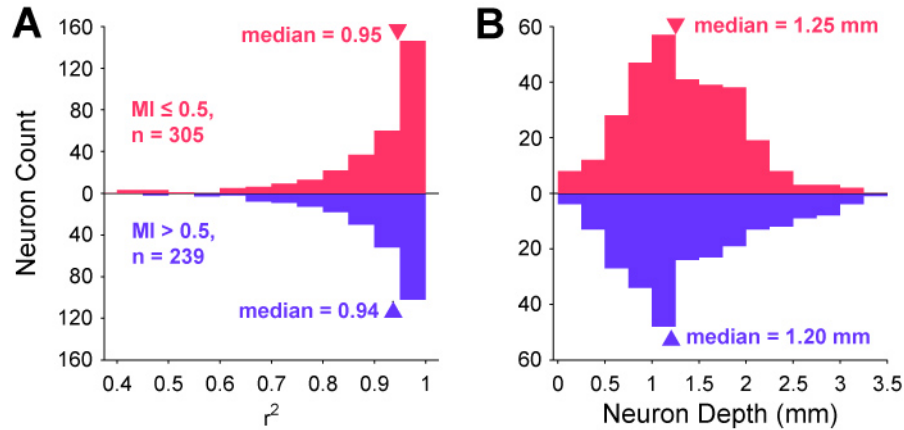


Figure 4.10 **A**, Distributions of rate-level goodness of fit (r^2) values with the six-parameter split Gaussian function for monotonic and nonmonotonic neuron populations are not significantly different. Therefore, this particular analysis did not likely result in a bias that would negatively affect the conclusions regarding differences between the populations. **B**, Neuron depth distributions for the two populations were also not significantly different. Very similar numbers of neurons from the two groups (about half of each group) were likely recorded in layers 2/3 (cutoff at approximately 1.25 mm neuron depth below the dura), whereas slightly more nonmonotonic neurons were likely recorded in layer 4 (cutoff at approximately 2 mm neuron depth below the dura) and slightly more monotonic neurons in deeper layers.

In order to investigate whether neurons were organized in a columnar fashion with regard to monotonicity index (MI), we separated neurons into groups that were recorded at different depths of a single electrode penetration. Electrodes were always advanced roughly perpendicular to the cortical surface; thus neurons recorded at different depths approximately represent neurons in different layers of the same cortical column. Between two and seven neurons were recorded at different depths in a total of 149 penetrations, encompassing 435 / 544 neurons in the dataset. Just over half (78 / 149) of the penetrations consisted of two neurons only. To validate our recording and analytic techniques, we first verified that CF was non-randomly organized by electrode penetration. Frequency is known to be organized within a columnar fashion within marmoset A1 (Abeles & Goldstein, 1970). A sorted plot of mean \pm standard deviation of neuronal CFs within each of the 149 penetrations is depicted in Figure 4.11A. In order to assess if the CF standard deviation within a penetration was significantly smaller than the standard deviation of neurons selected across penetrations, a permutation test comparing the actual penetrations with penetrations consisting of randomly permuted neurons was utilized. The permutation test resulted in a distribution of test statistics where the test statistic was the mean of the penetration standard deviations (see Section 2.2.3). As expected, CF was much more similar within penetrations than across penetrations ($p < 1.0 \times 10^{-7}$, permutation test). In this case, the permutation test did not result in a single instance where the test statistic was less than that of the actual penetrations, so the p-value from the permutation test in this instance is an upper bound based on the total number of permutation test iterations (10 million).

For this reason, and to get an assessment of the degree of columnar organization, we also ordered the actual penetrations by standard deviation (Figure 4.11B) and compared with an instance from one permutation test iteration that was near the mean of the test statistic distribution. The plot is marked with the mean standard deviation of the penetrations for the actual data and for the representative instance from the permutation test. The representative instance mean is also shown with an error bar giving \pm standard deviation of the test statistic distribution. The z-score of the actual penetrations' test statistic is -11 relative to this distribution.

Plotting mean \pm standard deviation of neuronal MIs within a penetration reveals a much less organized trend than that for frequency (Figure 4.11C). The within-penetration standard deviations are much greater than was observed for the case of CF, but they also exhibit significant organization ($p = 2.1 \times 10^{-6}$, permutation test). Sorted standard deviation of the MI penetrations was less than that of a near-mean representative instance from the permutation test (Figure 11D; z-score of mean standard deviation = -4.5), but again the difference was much less than that of CF. Thus, although columnar organization of neurons' MI has a much greater variance than that of neurons' CF, there is still a significant non-random correlation of MI between neurons in different layers of the same cortical column.

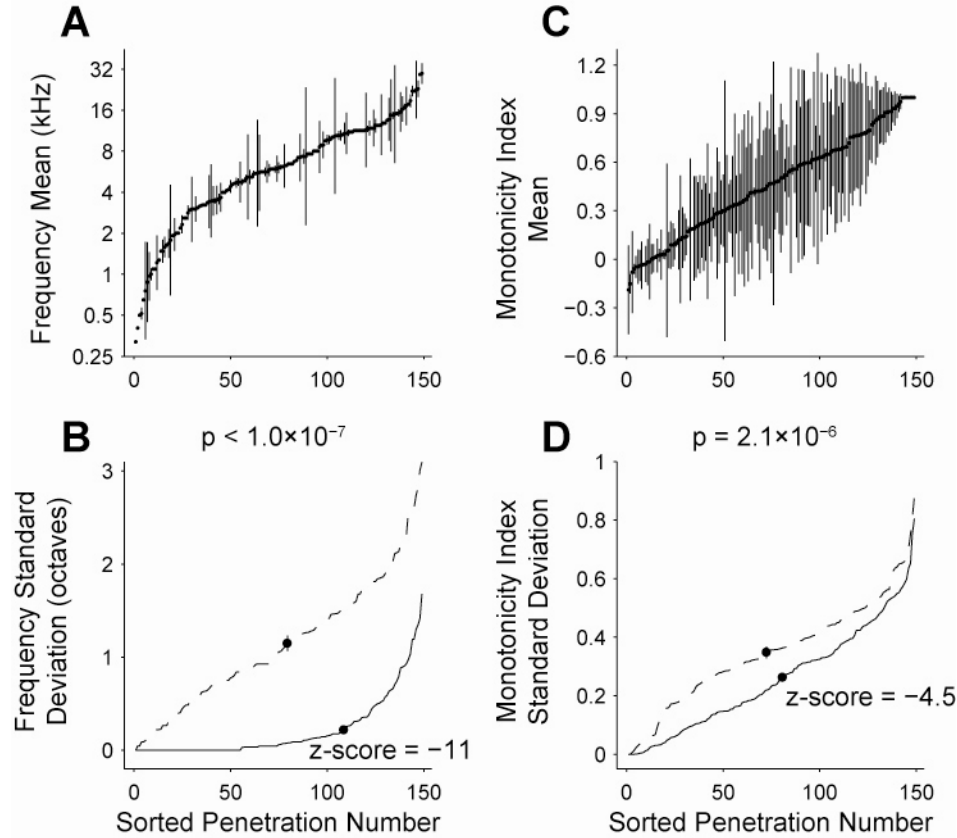


Figure 4.11 Neurons are highly organized in columns by characteristic frequency (CF) and loosely, but significantly organized in columns by monotonicity index (MI). **A**, Electrode penetrations with multiple neurons recorded at different depths sorted by the mean CF of the neurons and with error bars indicating the standard deviation of CFs indicate a high degree of columnar organization of CF ($p < 1.0 \times 10^{-7}$; permutation test). **B**, When penetrations are sorted by standard deviation of CF (solid line), penetrations have a much lower standard deviations than those of penetrations from a permuted set of neurons (dashed line) that is near to the mean of a permutation test statistic distribution (see Section 2.2.3). The mean standard deviation of the penetrations (marked with a dot on solid line) is very far from the mean of the permutation test

statistic distribution (marked with dot on dashed line; standard deviation marked with error bar; z-score = -11). **C**, Electrode penetrations sorted by mean MI of the constituent neurons have many more penetrations with large standard deviations as compared to CF (A). Despite this, neurons still have a non-random columnar organization of MI ($p = 2.1 \times 10^{-6}$; permutation test). **D**, Same plot as B, except penetrations sorted by standard deviation of MI (solid line) and compared with sorted MI standard deviation of penetrations containing permuted neurons (dashed line). The mean standard deviation of the penetrations (marked with dot on solid line) is quite far from the mean of the permutation test statistic distribution (marked with a dot on dashed line; standard deviation marked with error bar; z-score = -4.5).

4.3 Discussion

The relatively high percentage of level-tuned or nonmonotonic sound level responses in the auditory system, their absence in auditory nerve fibers and their relatively low numbers in other sensory systems collectively suggest the obvious question as to what functional role they play in sound level representation and transformation. In this study of tone-responsive neurons in the primary auditory cortex of awake marmosets using stimuli separated by periods of silence, we find that: (1) Nonmonotonic neurons have significantly lower residual thresholds (accounting for overall frequency sensitivity) than monotonic neurons. For monotonic neurons, the amount of on-CF inhibition, as measured by the monotonicity index (MI), is directly correlated with residual thresholds. There is no *a priori* reason to believe these neuronal characteristics would be related. (2) Both monotonic and nonmonotonic neurons have residual thresholds skewed towards lower sound levels. (3) Based on the neuronal sampling in this study, there are larger percentages of nonmonotonic neurons in the range from about 6–13 kHz. This region also corresponds with the most energy in marmoset vocalizations. (4) Nonmonotonic neurons have significantly smaller lower dynamic ranges than monotonic neurons and both are clustered below about 30 dB. Still, many monotonic neurons' dynamic ranges and the combination of nonmonotonic neurons' upper and lower dynamic ranges span the full range of sound levels tested. (5) Residual threshold and spontaneous rate are inversely correlated over the entire population of monotonic and nonmonotonic neurons. This same finding has been noted previously in auditory nerve fibers (Kiang et

al., 1976; Kiang et al., 1965; Liberman, 1978; Rhode & Smith, 1985), so it is possible that this property is inherited from subcortical inputs. (6) Spontaneous rates are significantly greater in the monotonic populations than in the nonmonotonic population and but discharge rates are not significantly different between these populations. Both are log-normally distributed. (7) There is not a significant difference between the number of monotonic and nonmonotonic neurons in superficial layers (above layer 4). (8) Neurons are organized in a columnar fashion by both CF and MI, although CF is much more highly organized in a cortical column.

The mechanism by which nonmonotonicity is created in higher levels of the auditory system remains the subject of investigation. Nonmonotonicity in primary auditory cortex can be inherited from input (J. Wang, McFadden, Caspary, & Salvi, 2002; Wehr & Zador, 2003) or it can be refined or even created locally by combinations of unbalanced excitation and inhibition (Faingold et al., 1991; Sivaramakrishnan et al., 2004; Tan et al., 2007; Wu et al., 2006). These findings are consistent with a general trend of increasing percentages of nonmonotonic responses at higher auditory centers. Given that this transformation in the neural code appears to occur gradually across multiple auditory stations, level-tuned neurons in auditory cortex seem unlikely to exhibit properties fundamentally different from analogous neurons in subcortical auditory areas.

Our finding of significantly lower thresholds of cortical nonmonotonic neurons when compared with monotonic neurons is consistent with results reported in cochlear nucleus (Spirou & Young, 1991; Young & Brownell, 1976), inferior colliculus (Aitkin, 1991; Ramachandran et al., 1999) and at least one report from anaesthetized auditory cortex (Sutter & Schreiner, 1995). Cortical monotonic neurons exhibit a more nearly uniform distribution of thresholds than nonmonotonic neurons, which tend to have thresholds clustered near hearing threshold. The properties of Type V/I and Type O neurons in inferior colliculus also exhibit these properties (Ramachandran et al., 1999). Lower thresholds for nonmonotonic neurons imply that they are not simply monotonic neurons with inhibition added at higher intensities (in which case thresholds would be expected to be similar for the two populations). Nonmonotonic neurons throughout the auditory system appear to inherit information preferentially arising from the most sensitive auditory nerve fibers. The careful preservation of this information all the way to auditory cortex in a consistent neuronal type implies that level-tuned neurons are involved in a fundamental auditory processing task.

The greatest percentages of nonmonotonic neurons in our study were found at frequencies from about 6–13 kHz. This range overlaps with frequencies exhibiting the greatest average power in marmoset vocalizations (DiMattina & Wang, 2006), implying that nonmonotonic neurons may play an important role in encoding behaviorally relevant sounds in the environment. Previous work in A1 of awake marmosets found greater numbers of nonmonotonic neurons around 2–4 kHz range, but not a statistically

significant difference (Sadagopan & Wang, 2008). However, the notion that nonmonotonic neurons play a behaviorally relevant role is supported by findings that rats trained to recognize a particular sound intensity level show significantly increased numbers of nonmonotonic cortical neurons with best levels near the trained level (Polley et al., 2004; Polley et al., 2006). Furthermore, the increased percentage of nonmonotonic neurons following training appear to have BLs concentrated in a range below the trained level (Polley et al., 2006), implying that these neurons may be using their upper dynamic range to encode the target level.

Distributions of best-level (BL) for monotonic neurons in the current dataset were fairly uniform, except with a cluster at the highest levels, whereas for nonmonotonic neurons BLs were clustered at lower sound levels. Previous studies in A1 have reported either a clustering of BLs at the highest intensities (Recanzone et al., 1999) or a more uniform distribution of BLs (Heil et al., 1994; Sadagopan & Wang, 2008). One likely difference may be due to a larger sampling of nonmonotonic neurons that have significantly lower spontaneous rates, as reported here and previously (Sadagopan & Wang, 2008). Differences in the latter study, since it is also from awake marmoset cortex with a large sampling of nonmonotonic neurons, may be due to experimental design. Our design involved a greater sampling of sounds levels (10 dB steps as opposed to 20 dB steps), a larger range of sound levels tested (100 dB as opposed to 80 dB) and a longer interval of silence between tone bursts (650 ms as opposed to 300 ms). The final difference likely

at least partially explains why we find lower BLs, because there is less effect of neuronal adaptation to sound level with a longer silence interval.

Several hypotheses have been proposed to explain the coding role of level-tuned neurons. The Best-Intensity Model (Shamma, 2003) proposes that nonmonotonic neurons represent a place code for intensity as sounds are transformed along spectral and intensity dimensions. In this model frequency and intensity are encoded over a population of neurons that are narrowly tuned to both stimulus parameters. Studies in the auditory cortex of bats have found evidence for this model, which has been termed an amplitude spectrum representation (Suga, 1977; Suga & Manabe, 1982). These studies also raised the possibility that level-tuned neurons create a “level-tolerant” representation of sounds generally. Later investigation in awake marmoset monkeys hypothesized that a major function of nonmonotonic neurons is to create a level-invariant representation for complex sounds (Sadagopan & Wang, 2008). Furthermore, nonmonotonic neurons have been hypothesized to play a role in the detection of tones in noise (Rees & Palmer, 1988), be responsible for detecting HRTF spectral notches used in sound source localization (Davis, Ramachandran, & May, 2003) and as previously discussed may contribute to stimulus level discrimination (Polley et al., 2004; Polley et al., 2006). Our results here, particularly that nonmonotonic neurons have significantly lower thresholds than monotonic neurons, imply that nonmonotonic neurons may be specialized for encoding low intensities. This hypothesis is investigated further under adapted conditions to dynamic level stimuli in Chapter 5. As discussed

above, our results indirectly imply that nonmonotonic neurons are useful for behaviorally relevant tasks, but do not directly address the issue of coding sound information across frequency. Thus, our hypothesis is likely complementary to other potential functions that may be performed by nonmonotonic neurons in cortex and subcortically.

Chapter 5

Neuronal Adaptation to Sound Intensity Level

5.1 Introduction

Audition in humans and other mammalian species encompasses a wide dynamic range of sound intensity level to which these species are behaviorally sensitive. In particular, the human auditory system is capable of maintaining a level discriminability of 2 dB or less across the entirety of the approximately 120 dB dynamic range of hearing (Rabinowitz, Lim, Braida, & Durlach, 1976). Neuronal dynamic ranges in the mammalian auditory system, on the other hand, typically contain a large number of neurons (often reported as a majority of neurons) with dynamic ranges of 40 dB or less (Aitkin, 1991; Phillips & Irvine, 1981; Rees & Palmer, 1988; Schalk & Sachs, 1980). Our recordings of neurons in the awake auditory cortex show that 80% of dynamic ranges span 30 dB or less and that 75% of neuronal thresholds are at 30 dB or less above the minimum sensitivity of their respective characteristic frequencies (see Chapter 4). This result implies that under these silence-adapted conditions, the neuronal population is limited to about a 60 dB dynamic range over which it can represent sound level at a reasonable accuracy. Therefore, in order for the auditory system to maintain equivalent

coding accuracy over a behavioral dynamic range of 120 dB, these neurons must be able to alter their response properties based upon the recent history of stimulus attributes—a characteristic typically referred to as adaptation.

A population of adapting neurons is certainly not the only possible coding strategy for encompassing a wide dynamic range. One potential alternative is to have sensory areas in the brain contain neurons with fixed responses that collectively represent the total behavioral dynamic range, a much simpler solution. One potential rationale for an adaptive coding strategy is that the accuracy with which a population of neurons can encode a range of values representing some aspect of a physical stimulus increases in proportion to the size of the neuronal population responsible for the encoding (Eliasmith & Anderson, 2004). Indeed, many hypotheses regarding the function of neuronal adaptation have focused on the idea that neurons adapt so that they can provide the most accurate encoding of a time-varying sensory input ((DeWeese & Zador, 1998). For a review of this topic see (Wark, Lundstrom, & Fairhall, 2007)). With regard to the representation of sound level, auditory neurons in songbirds (Nagel & Doupe, 2006) and in the inferior colliculus of mammals (Dean et al., 2005; Kvale & Schreiner, 2004) appear to adapt their response properties to be better suited for encoding the most probable sound levels in the environment.

Encoding accuracy is typically quantified with a measure of how well the neuronal discharge rate is able to discriminate between values of a sensory input (also referred to

as a neuronal input / output function). This is the same measure that is often used in behavioral studies, i.e., the minimum difference in sound level that the subject or neuron is reliably able to detect. The performance of the neuron can be evaluated by applying techniques from signal detection theory, that is, how well an ideal observer could estimate the value that a neuron is encoding based solely upon the neuronal response to any given single stimulus presentation. From the standpoint of a single neuron, an ideal observer would have the most information about the original value being encoded within portions of the neuronal input / output function with steep slope and also when the variance of the neuronal response is small. Flat portions of the neuronal input / output functions are not useful in terms of discriminability on the single neuron level, although there is some evidence that when sensory signals themselves are corrupted with a high level of noise, other aspects of the input / output functions, such as the value encoded by the maximum response, may be better utilized for encoding (Butts & Goldman, 2006).

The relevance of nonmonotonic encoding of sound intensity level in the auditory system has been introduced and discussed in Chapter 4. Many conclusions regarding the role of nonmonotonic neurons for representing and transforming acoustic information have been drawn using protocols that prevent the effects of neuronal adaptation (Davis et al., 2003; Rees & Palmer, 1988; Sadagopan & Wang, 2008; Shamma, 2003; Suga & Manabe, 1982). In this chapter we complement the results of Chapter 4 by studying steady-state neuronal responses to dynamic level stimuli. We focus our analysis on how

nonmonotonic neurons adapt their responses and evaluate this adaptation based on their change in encoding accuracy relative to monotonic neurons. Our analysis is therefore based upon the sloped portions of the neuronal response to sound level (the upper and lower dynamic ranges) which are likely the most relevant for discriminability.

We present further evidence based on adaptation to sound level statistics that nonmonotonic neurons may preferentially encode low sound levels. Specifically, in a dynamic context nonmonotonic level encoding appears to preserve sensitivity to low sound levels even when much of the neuronal population is adapted to high sound levels. We also present evidence that it is the lower dynamic range of nonmonotonic neurons that allows them to maintain low level sensitivity, while the upper dynamic range continues to adapt to high sound levels.

5.2 Results

We investigated the responses of 47 primary auditory cortex neurons from 7 hemispheres of 6 awake marmoset monkeys (*Callithrix jacchus*) for their adaptive coding properties in response to dynamic auditory stimuli (see Section 2.3.1).

5.2.1 Static Rate-Level Responses

Static rate-level functions for two example neurons reflect the extremes of rate-level shapes (Figure 5.1). Very monotonic neurons saturate at higher levels (Figure 5.1A,B), while very nonmonotonic neurons do not respond at higher levels (Figure 5.1C,D). For dynamic range and monotonicity analyses, rate-level functions were fitted with a six-parameter, two-tailed, split Gaussian model (see Section 2.2.3), which typically resulted in a very good fit ($r^2 > 0.95$), and are presented as solid black in Figure 5.1B,D. Threshold and saturation levels were determined from the model fits at 20% and 80% of maximum firing rate above spontaneous. The dynamic range for monotonic neurons was measured between saturation and threshold (Figure 5.1B, blue lines). For nonmonotonic neurons a lower dynamic range was measured in the same manner as for monotonic neurons (Figure 5.1D, red lines). An upper dynamic range for nonmonotonic neurons was measured from 80% to 20% of maximum firing rate above the response to the greatest level presented (Figure 5.1D, green lines). The same calculations were performed to determine threshold, saturation and monotonicity index for the dynamic rate-level functions. Neurons were classified as monotonic if the average monotonicity index for the static and dynamic rate-level curves was greater than 0.5 and as nonmonotonic if this value was less than or equal to 0.5. For a detailed discussion of static rate-level responses on a larger dataset, refer to Chapter 4.

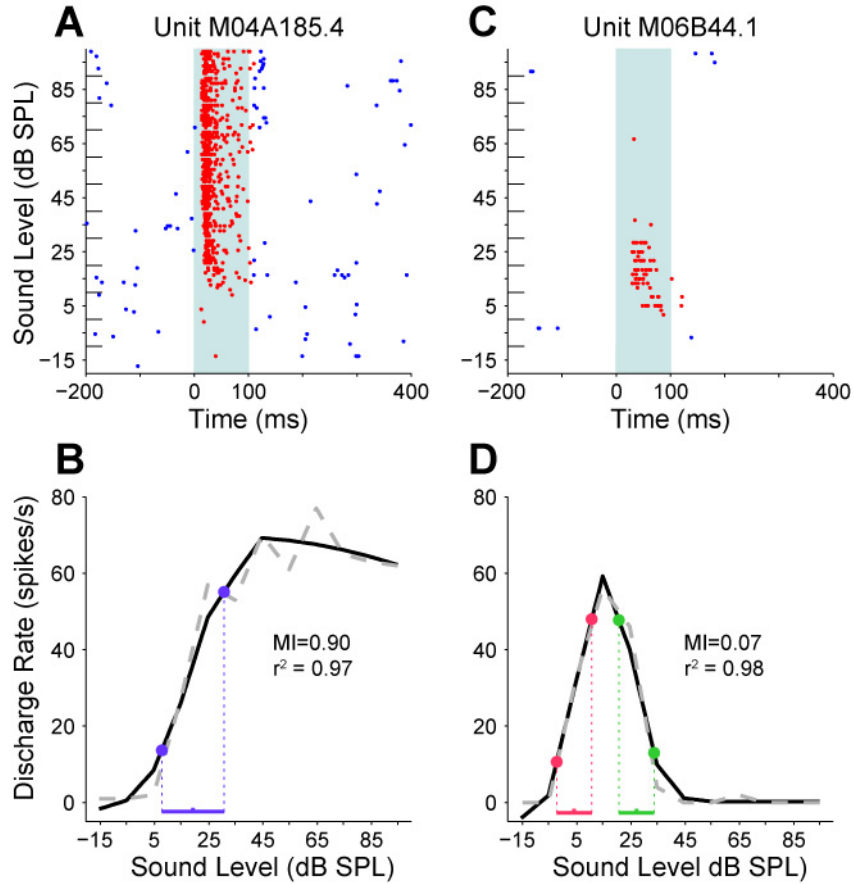


Figure 5.1 Example neurons demonstrating the extremes of input-output responses in primary auditory cortex. **A**, The peristimulus spike raster of a very monotonic neuron reveals little change in discharge rate at levels above about 35 dB SPL. Stimuli were 100 ms tones (duration indicated by shaded rectangle) delivered at the neuron's characteristic frequency (CF). **B**, The saturating nature of this neuron can be seen in its monotonic rate-level function. Rate is averaged over the length of the stimulus interval after the onset latency. The dynamic range from threshold to saturation is highlighted by a blue horizontal bar whose midpoint is indicated by an upward tick. **C**, The peristimulus spike raster of a very nonmonotonic neuron reveals response over only a limited range of levels around 15 dB SPL. **D**, The level-tuning nature of this neuron can

be seen in its nonmonotonic rate-level function. The lower dynamic range from threshold to saturation is highlighted with a red bar in the same fashion as the neuron in B. The upper dynamic range based upon similar measures is highlighted by a green bar.

5.2.2 Single Neuron Adaptation to Dynamic Level Stimuli

Although a few neurons showed little adaptation in response to dynamic level stimuli, most neurons adapted their rate-level functions with a combination of response gain adaptation (i.e., a scaling of the rate response) and dynamic range shifting (i.e., a shifting of the rate-level function along the abscissa). Individual neurons, however, exhibited a variety of adaptive changes in their rate-level responses. Example rate-level responses and Fisher information curves (see Section 2.3.2) calculated in response to dynamic stimuli (those depicted in Figure 2.2B or 2.2C) are shown for representative neurons in Figure 5.2. Fisher information gives an upper bound on how well an ideal observer could estimate the sound level based solely on the neuronal response, a quantification of encoding accuracy. Each curve is color coded to match the colored bars on the abscissa that indicate the location of the probability plateau for the dynamic stimulus that elicited the response curve (see Section 2.3.1). The solid black lines indicate the responses to the uniformly distributed dynamic stimulus, and the dashed black lines are the static rate-level responses.

All neurons demonstrated adaptation in their maximum firing rate (i.e., gain adaptation) for dynamic stimuli. These gain changes typically reduce the slope of the corresponding rate-level functions. Lower response rates usually brought about lower response variance, however, so measures of coding accuracy might not be expected to decrease in this situation. In actuality, Fisher information curves were mostly unaffected by pure

gain changes. The most variety in individual neuronal adaptation was exhibited in the amount of shifting of the rate-level responses in the direction of the dynamic stimuli probability plateaus. Monotonic neurons could demonstrate a large amount of shifting (Figure 5.2A,B) or a small amount of shifting (Figure 5.2C,D); similarly, nonmonotonic neurons could demonstrate a large (Figure 5.2E,F) or small amount of shifting (Figure 5.2G,H). Nonmonotonic neurons could also exhibit adaptation (causing both gain and shift changes) predominantly in their lower dynamic range (Figure 5.2C,D), in a combination of both dynamic ranges (Figure 5.2I,J), or predominantly in their upper dynamic range (Figure 5.2K,L). Because individual neurons demonstrated a variety of adaptation profiles, population analysis (Section 5.2.3) more clearly revealed global response trends in both monotonic and nonmonotonic neuron populations. Additionally, single neurons to varying degrees are better or worse at encoding sound level information, meaning that encoding accuracy on a single neuron level is not as relevant as how well the population together is able to encode sound level. Postsynaptic neurons will likely rely on a pool of neuronal inputs to decode sound level information, and not just on one neuron (Britten et al., 1996; Shadlen et al., 1996). Also, some neurons recorded here that respond to sound level may not actually be utilized at all by postsynaptic neurons to decode sound level, so the aggregate response of the population is more meaningful to how downstream brain areas are likely to utilize the encoded sound-level information.

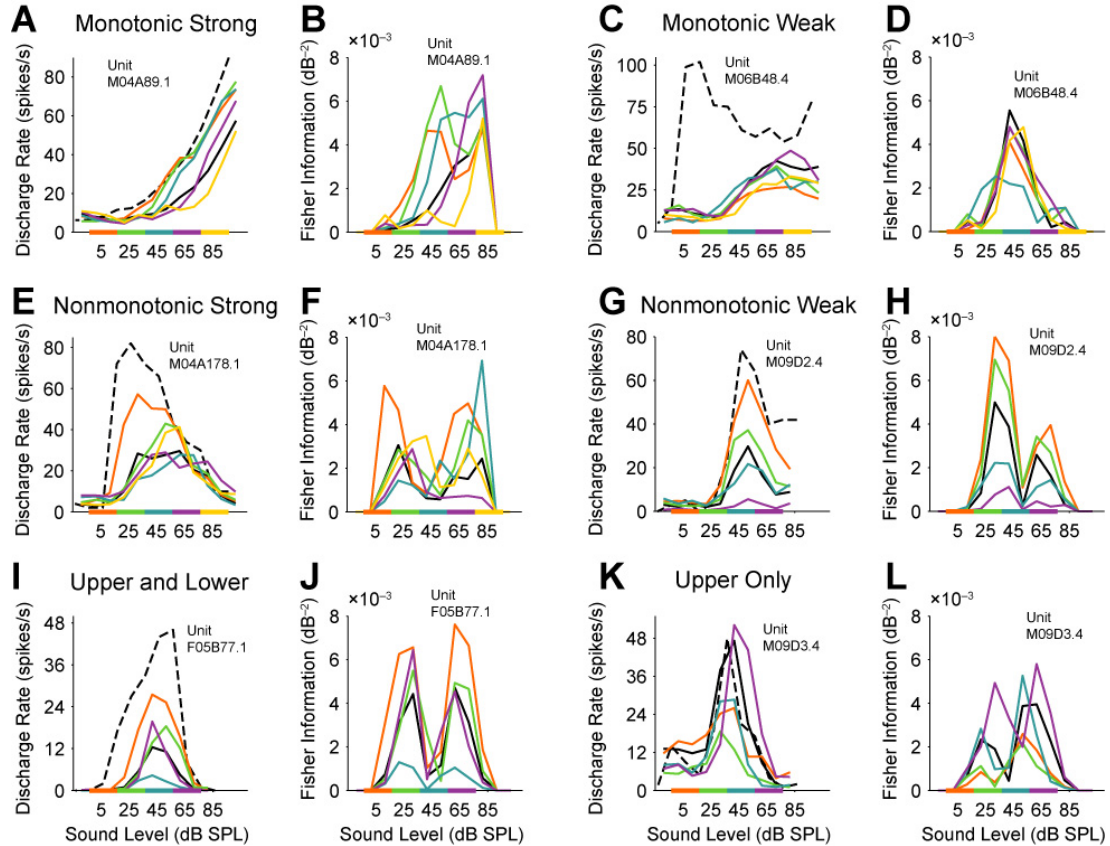


Figure 5.2 Dynamic rate-level and Fisher information (FI) functions for six example neurons. **A,B**, A strongly adaptive monotonic neuron reveals dynamic range shifts and corresponding FI peak shifts to align with probability stimulus level plateaus (see Figure 2.2). Plateaus are indicated by colored horizontal lines and corresponding curves have the same color. The neuron's response to the uniformly distributed stimulus is indicated by the solid black line, and the silence-adapted response is indicated by the dashed black line. **C,D**, A weakly adaptive monotonic neuron demonstrates nearly invariant coding properties with different stimulus statistics. **E,F**, The dynamic ranges of a strongly adaptive nonmonotonic neuron clearly shift in response to different stimulus statistics, but the result does not optimize coding accuracy. **G,H**, A weakly adaptive

nonmonotonic neuron demonstrates gain adaptation but no systematic shift in coding properties with different stimulus statistics. **I,J**, Some nonmonotonic neurons appear to adapt both their upper and lower dynamic ranges. **K,L**, Other nonmonotonic neurons appear only to adapt one dynamic range or the other, the upper dynamic range in this example.

5.2.3 Population Adaptation to Dynamic Level Stimuli

In the interests of understanding how well the population of adapting neurons was able to encode sound intensity level, mean Fisher information was calculated separately over the populations of monotonic and nonmonotonic neurons in response to each dynamic stimulus (see Section 2.3.2). Fisher information (FI) provides an upper bound on how well an optimal decoder would be able to discriminate sound level based on the neuronal responses to sound level. Intuitively, regions of high slope and low response variance in individual neuronal rate-level functions provide the best estimate of the sound level presented based on the response (see Section 2.3.2). In order for the average FI over the population to be meaningful, we are inherently assuming relatively low correlations between individual responses. For a discussion of how correlations affect neuronal encoding and analysis of correlations between simultaneously recorded pairs of neurons in response to sound level, see Appendix A.

Specialized Neuronal Adaptation for Preserving Input Sensitivity Inspection of the mean rate-level functions computed separately for the populations of monotonic and nonmonotonic neurons showed that monotonic neurons typically adjusted the sloped portion of their rate-level functions to match the most common sound intensity levels in the stimulus—the most accurate encoding strategy (Figure 5.3A). This encoding strategy was verified by the peak of the mean FI approximately aligning with the probability plateau for each dynamic stimulus (Figure 5.3B) Only 3 neurons are

represented in the mean rate-level and mean FI for the 85 dB plateau (see Section 2.3.2) so although there is an FI peak near the plateau, the trend is not as clear as the curves for the other plateaus. Nonmonotonic neurons adapted in a manner similar to monotonic neurons except at the highest levels, where the rising slope of their rate-level functions remained relatively constant (Figure 5.3C). In response to the 85 dB plateau dynamic stimulus (represented by 9 neurons, see Section 2.3.2) the mean rate-level function actually relaxed toward lower levels. Nonmonotonic neurons generally adapted to improve coding accuracy except when the highest levels were the most common, at which point the largest FI peak returned to lower sound levels (Figure 5.3D). The mean FI curve in response to the 65 dB plateau dynamic stimulus showed a larger peak at lower levels and the curve for the 85 dB plateau showed an almost equally large peak at lower levels.

We did not find dynamic rate-level thresholds that were lower than the static rate-level threshold for any neuron in the dataset (neither monotonic nor nonmonotonic). We refer to the static-rate level functions (mean rate-level shown as black dashed line in Figure 5.3A,C) as “silence-adapted” because in response to tone bursts presented during long periods of the silence, the neuron is adapted to respond to the lowest sound levels to which it is sensitive. Typically these silence-adapted rate-level functions also had a much larger maximum firing rate than the dynamic rate-level functions. Silence adaptation is therefore analogous to the maximum gain setting for the neuron. Thus,

silence-adapted responses were the most sensitive and had the largest gain in comparison with any dynamic-level-adapted response.

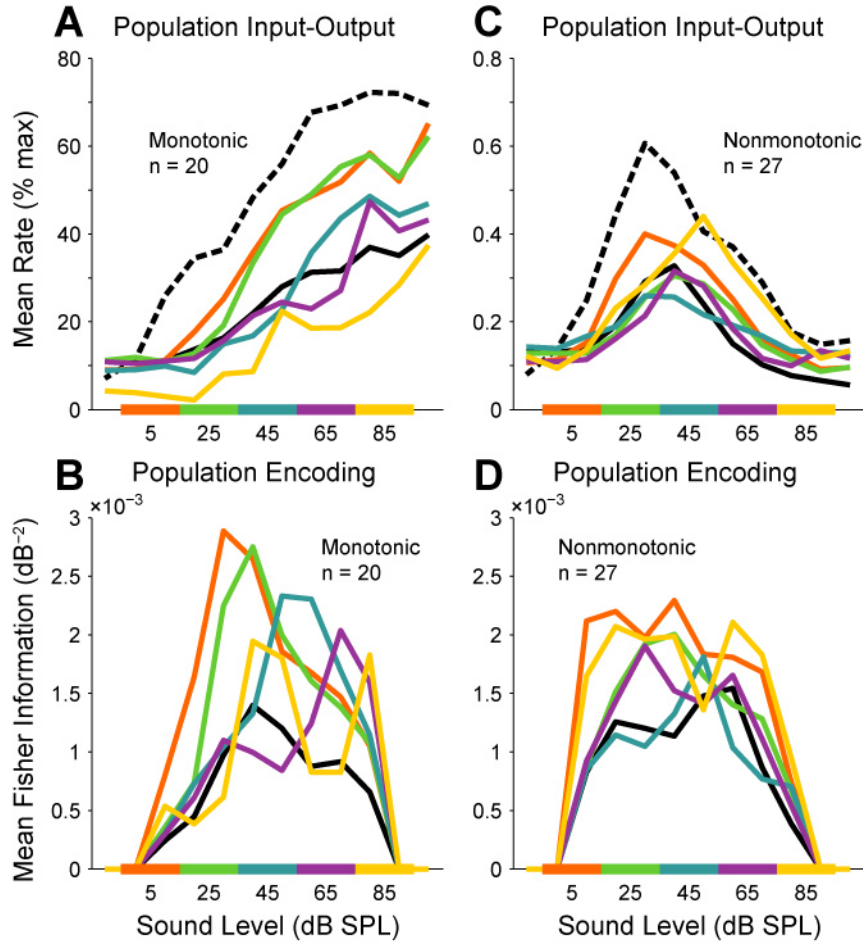


Figure 5.3 Average dynamic rate-level and Fisher information (FI) functions at different plateau centers. **A**, Mean rate-level functions indicate the adaptive behavior of the monotonic population. Neurons adapt their dynamic ranges in the direction of the most probable stimuli. Dotted black line in all plots represents silence-adapted population response. **B**, Mean FI across sound level for monotonic neurons. FI curve maxima tend to align with high-probability plateaus, with the exception of the lowest sound levels, which are lower than the thresholds of most monotonic neurons. Solid black line in all plots represents population response to the uniform dynamic stimulus. **C**, Mean rate-level functions indicate the adaptive behavior of the nonmonotonic

population, which demonstrates clear adaptation only at the highest and lowest plateaus.

D, Mean FI across sound level for nonmonotonic neurons. FI curve maxima are less prominent than those of monotonic neurons. Peaks in the FI curves corresponding to the low-level stimuli are near to high-probability plateaus. For the 65 and 85 dB stimuli, equally large or larger peaks remain at lower sound levels, showing that nonmonotonic neurons remain sensitive to low levels even while adapted to predominantly high level stimuli.

From this surprising result, that nonmonotonic neurons had higher levels of encoding accuracy to low sound level stimuli when dynamic stimuli contained predominantly high sound levels, we hypothesized that sound level tuning and dynamic low-level sensitivity could be directly related through the effects of adaptation. Intense acoustic events have the potential to rapidly desensitize an adaptive auditory neuron to less-intense events by shifting its threshold away from lower levels and toward higher levels. From the previous result, one might expect that nonmonotonic neurons would not shift their lower dynamic range much in response to the most intense sounds and would certainly shift less than monotonic neurons. Our next analysis was therefore to compare estimates of dynamic range adaptation between the populations of monotonic and nonmonotonic neurons.

Low Level Sensitivity Preserved in Nonmonotonic Lower Dynamic Range We calculated the mean dynamic ranges for neurons elicited by each dynamic stimulus (Figure 5.4). For monotonic neurons this measure consisted of a single contiguous dynamic range (depicted in blue in Figure 5.4A) from threshold to saturation. For nonmonotonic neurons this measure consisted of both lower (depicted in red in Figure 5.4A) and upper (depicted in green in Figure 5.4A) contiguous dynamic ranges corresponding to the two slopes of nonmonotonic rate-level responses on either side of BL. For both neuron types the average dynamic ranges (lower dynamic range of nonmonotonic neurons) adapted toward the probability plateaus (i.e., a shifting of the rate-level responses), although the amount of this change between any two dynamic

stimuli was less than the corresponding difference between the probability plateau centers (indicated by the diagonal line of unity slope). On average, monotonic neurons adapted their dynamic ranges more than nonmonotonic neurons (i.e., steeper slope of the blue curve in Figure 5.4A). Average dynamic ranges collected with static rate-level functions were consistently lower in both threshold and saturation than for any dynamic stimulus, as expected to be the case under silence-adapted conditions. For both monotonic and nonmonotonic neurons, the average dynamic ranges elicited by the uniformly distributed dynamic stimulus was closest to that elicited by the dynamic stimuli with probability plateau of 45 dB SPL. It is clear from Figure 5.4A that the lower dynamic range of nonmonotonic neurons is closer to the 5 dB and 25 dB dynamic stimuli probability plateaus and the upper dynamic range is closer to the 65 dB and 85 dB plateaus under all adapted conditions. This result, along with the nonmonotonic mean rate-level functions (Figure 5.3C), indicates that the lower dynamic range of nonmonotonic neurons on average remains aligned with lower sound levels even while adapted to high level dynamic stimuli.

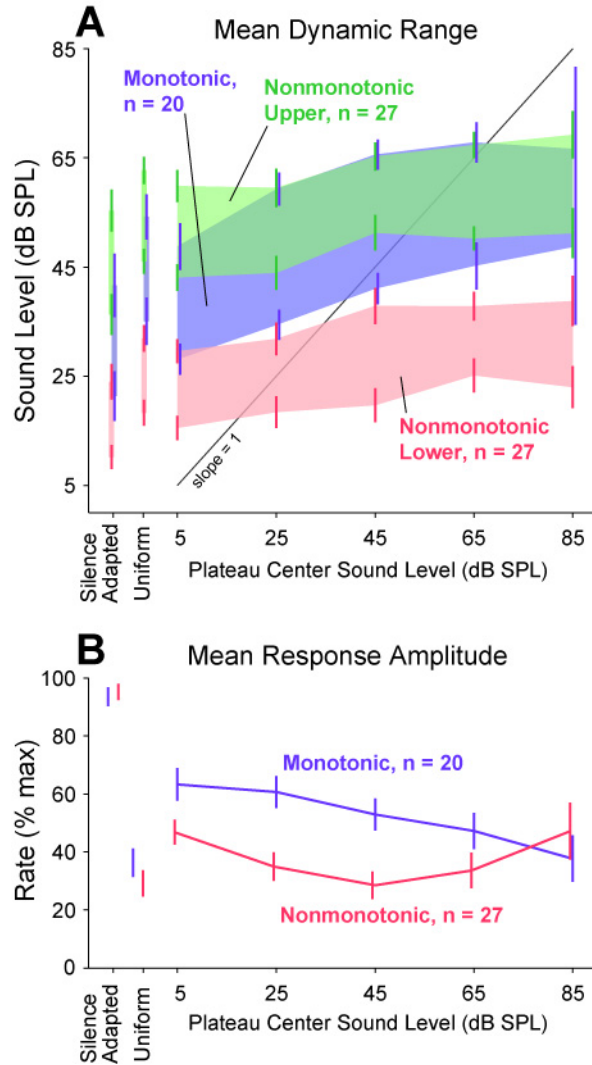


Figure 5.4 Average adapted dynamic ranges as a function of dynamic stimulus probability plateau center. **A**, Monotonic dynamic ranges are indicated in blue, nonmonotonic lower dynamic ranges in red and nonmonotonic upper dynamic ranges in green. Thresholds and saturations are indicated with vertical lines representing standard error of the mean. Dynamic ranges for the silence-adapted (static) rate-level functions and for the uniformly distributed dynamic stimulus are presented to the left for comparison. Changes in dynamic ranges with plateau center reflect adaptive

threshold shifts. Adaptation that always aligned the center of the dynamic ranges with the probability plateau would follow a line with a slope of 1. **B**, Changes in mean response amplitude with plateau center reflect gain adaptation.

We calculated the mean range of firing rates for each stimulus condition in order to quantify the other effect of adaptation: a change in the overall firing rate as a function of plateau center, termed response gain adaptation. Rate-level responses were normalized for each neuron over all dynamic and static stimuli and the mean was taken over these normalized values for each stimulus type (see Section 2.3.2). Although trends in the gain are visible in the average rate-level responses from Figure 5.3, gain adaptation is presented separately in Figure 5.4B to quantify these trends. Monotonic neurons on average showed monotonically decreasing response gain with increasing plateau center, whereas nonmonotonic neurons showed a nonmonotonic trend in response gain. In the latter case the response gain increased for the 65 dB and 85 dB plateau stimuli, coincident with the probability plateau being closer to the upper dynamic range of these neurons' rate-level functions than to the lower dynamic range.

In order to quantify the previously observed adaptation effects as a function of MI and under different stimulus conditions, we compiled dynamic range midpoints (midpoints of both lower and upper dynamic ranges for nonmonotonic neurons) as a simple summary of the coding region. Systematically lower midpoints for nonmonotonic neurons' lower dynamic ranges than for monotonic neurons' dynamic ranges (Figure 5.5A-E) reflect a lower average threshold and corresponding encoding of lower levels for nonmonotonic neurons, as discussed in Chapter 4. For all dynamic stimuli, a significant correlation between MI and the midpoint of the dynamic range existed. Four neurons out of 47 with a combination of low maximum firing rates and substantial

inhibition below spontaneous spiking rates in response to the highest levels yielded large negative MIs as the denominator of the MI calculation approached 0. The resulting ill-conditioned data points were omitted from this particular analysis because they exerted a disproportionate influence on the regression. A linear regression between MI and dynamic range midpoint for the remaining 43 neurons (all with an $MI \geq -0.4$) gave a slope of 21 dB SPL and intercept of 22 dB SPL ($r^2 = 0.35$; $p = 3.4 \times 10^{-5}$, regression F test) for the 5 dB plateau, a slope of 23 dB SPL and intercept of 28 dB SPL ($r^2 = 0.49$; $p = 2.1 \times 10^{-7}$, regression F test) for the 25 dB plateau, a slope of 29 dB SPL and intercept of 29 dB SPL ($r^2 = 0.56$; $p = 6.5 \times 10^{-9}$, regression F test) for the 45 dB plateau and a slope of 31 dB SPL and intercept of 32 dB SPL ($r^2 = 0.52$; $p = 5.9 \times 10^{-8}$, regression F test) for the 65 dB plateau. The regression intercepts become progressively larger with increasing plateau center, indicating that over the population, neurons adapted in the direction of the plateau center. The regression slopes also increased with increasing plateau center, indicating that monotonic neurons' dynamic ranges were shifting more in response to dynamic stimuli containing more high-level sounds than were nonmonotonic neurons' lower dynamic ranges. Note in this plot that monotonic neurons are plotted on the left and nonmonotonic neurons on the right, which results in MI values becoming more negative toward the right.

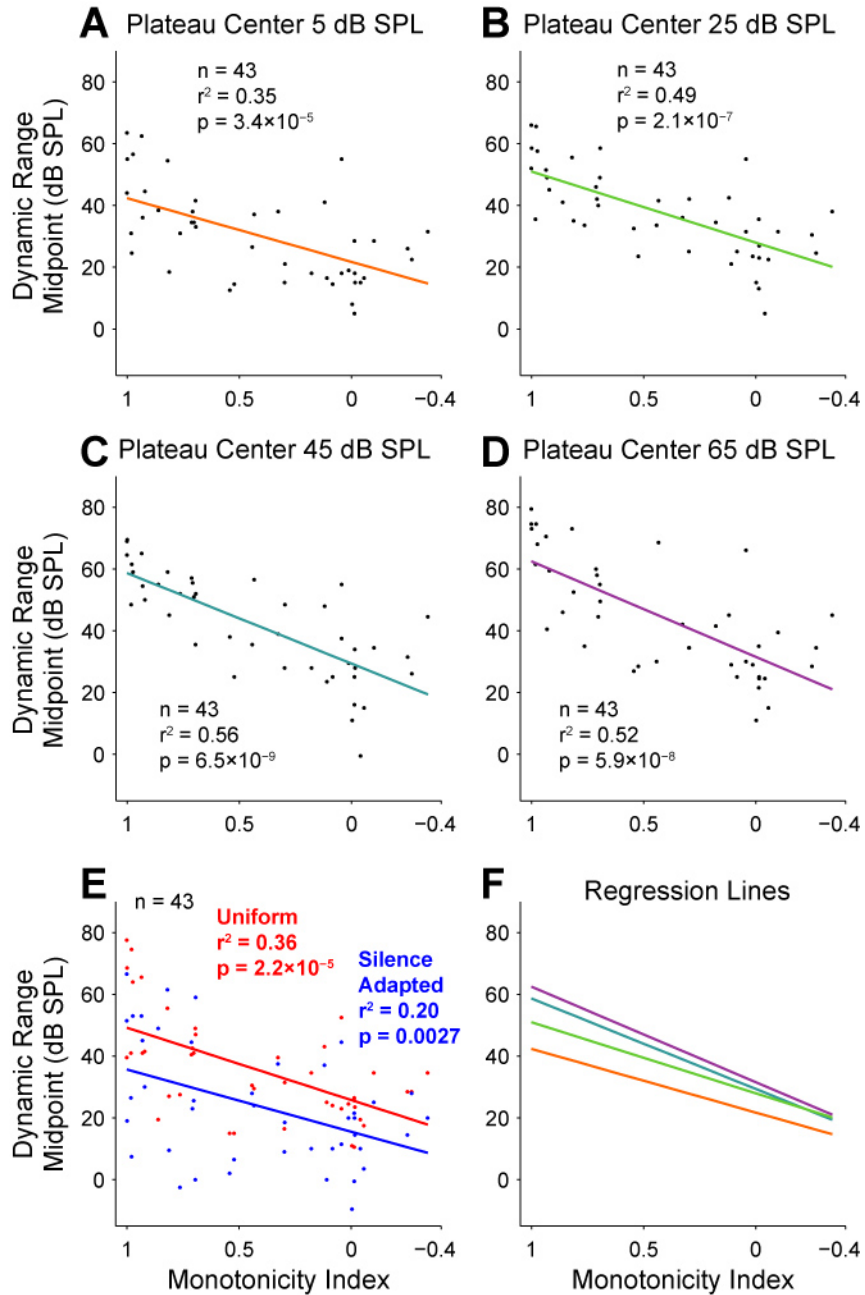


Figure 5.5 Dynamic range midpoints for each neuron as a function of MI. Midpoints of the lower dynamic range only are shown for nonmonotonic neurons. Four out of 47 neurons with $MI < -0.4$ were excluded from this analysis. **A–D**, Dynamic range midpoints are plotted against MI for the four plateaus used to stimulate all neurons.

Colored lines indicate linear regression. Regressions are significant for all plateaus ($p < 10^{-4}$). **E**, Dynamic range midpoints for silence-adapted stimuli (blue) and the uniform dynamic stimulus (red). Regressions are significant for both stimuli ($p < 0.01$), although the silence-adapted stimulus elicited the greatest variability of dynamic range. **F**, Overlaid regression lines from **A–D**, demonstrating by the greater separation at $MI = 1$ than $MI < 0$ that monotonic neurons adapt more than the lower dynamic range of nonmonotonic neurons.

Comparing the regression lines for each dynamic stimulus plateau directly (Figure 5.5F) reveals graphically that higher-level probability plateaus induce upward shifts and increasing regression slopes. This analysis confirms the results shown in Figure 5.4, but specifically as a function of monotonicity and not simply by dividing the neurons into two classes of monotonic and nonmonotonic. Figure 5.5 also shows that the 25, 45 and 65 dB regression lines are very close to each other for the most nonmonotonic neurons ($MI \leq 0$, 15 / 27 nonmonotonic neurons). The 5 dB regression line, however, is slightly below these three. This indicates that the lower dynamic range of these neurons adapts slightly between the dynamic stimuli with 5 dB and 25 dB plateau centers, but does not shift much in the direction of the probability plateau in response to the higher level dynamic stimuli. Because the lower dynamic ranges do not adapt much in response to the higher level dynamic stimuli, nonmonotonic neurons are able to remain sensitive to low level sounds even when adapted to predominantly high levels. Trends revealed in the above analysis thus support our hypothesis that level-tuning is involved in nonmonotonic neurons' ability to maintain low-level sensitivity, and that this low-level sensitivity is predominantly encoded by the lower dynamic range.

Potential Roles of On-CF Inhibition

Clearly if the lower dynamic range of level-tuned neurons preferentially encodes low sound levels under different adapted conditions, then this particular encoding task is not conducted by the on-CF inhibition that creates the upper dynamic range. There are at least two potential roles that the upper dynamic range might perform: (1) A potential strategy to preserve the sensitivity

of adaptive coders when the stimuli contain predominantly intense events could be to shield them from high-intensity events. In the shielding hypothesis, inhibition serves as a blockade of the normal adaptive processes apparent in the monotonic population. If inhibition serves in such a shielding role only, one would not expect any adaptive changes in the inhibitory regime of the dynamic rate-level functions. (2) A new type of adaptation that is able to capture the encoding of high sound levels is invoked by the inhibitory inputs themselves. In this capture hypothesis, the inhibitory regime of the dynamic rate-levels functions change so that encoding improves at high sound levels in response to predominantly high-level stimuli. In this case, the on-CF inhibitory inputs of nonmonotonic neurons play an adaptive role in response to dynamic stimuli, whereas in the shield hypothesis the on-CF inhibition statically shields the excitatory inputs so that they do not adapt to the high intensity stimuli. Thus, shielding might be thought of as a passive process while capturing might be thought of as an active process.

The previous analyses were extended to specifically look at the role of the upper dynamic range in encoding. Any adaptive processes that improved encoding accuracy in the upper dynamic range would provide support for the capture hypothesis discussed above. Although it is likely that on-CF inhibition is directly involved in the shielding hypothesis, we do not provide direct evidence of this phenomenon. If the regulation of overall firing rate is what is primarily responsible for the effects of adaptation, then this inhibition is certainly directly involved in shielding the lower dynamic range from adapting to higher sound levels by maintaining the mean-rate at reasonable levels when

intense sounds occur. We only briefly discuss potential adaptation mechanisms below (Section 5.2.4).

Support for the Capture Hypothesis By subdividing the neuronal population based upon MI and analyzing lower dynamic range midpoint trends as a function of plateau center, the monotonic neurons can be seen to shift their dynamic range toward each plateau center more than nonmonotonic neurons do (Figure 5.6). Note that data from the highest level plateau (9 nonmonotonic and 3 monotonic neurons) were not included in the regression analysis, although the regression line was extended (dotted line) toward the highest level plateau to demonstrate qualitatively that these data are consistent with the trends from the other four plateaus. Neurons were segregated based upon their mean monotonicity index (MI) into four groups: “very monotonic” ($1 \geq \text{MI} > 0.9$), “mostly monotonic” ($0.9 \geq \text{MI} > 0.5$), “mostly nonmonotonic” ($0.5 \geq \text{MI} > 0.1$) and “very nonmonotonic” ($\text{MI} \leq 0.1$). The analysis of Figure 5.5 captured slices along one dimension of the three dimensional dataset (dynamic range midpoint as a function of dynamic stimulus plateau center and neuron MI) and subdividing in this manner captured slices along the other dimension. The cutoffs were chosen because they divided monotonic and nonmonotonic categories approximately in half within the much larger static rate-level dataset (see Chapter 4). The very nonmonotonic category included the four neurons with $\text{MI} < -1$ that were excluded from the regression analysis of Figure 5.5. Very monotonic neurons showed the most correlation based upon a linear regression between plateau center and dynamic range midpoint (slope = 0.34, intercept

= 45; $r^2 = 0.35$; $p = 1.5 \times 10^{-4}$, regression F test), followed by mostly monotonic neurons (slope = 0.27, intercept = 33; $r^2 = 0.22$; $p = 0.0014$, regression F test), then mostly nonmonotonic neurons (slope = 0.23; intercept = 27; $r^2 = 0.20$; $p = 0.010$, regression F test) and finally very nonmonotonic neurons (slope = 0.12; intercept = 19; $r^2 = 0.036$; $p = 0.10$, regression F test), for which the regression was not significant.

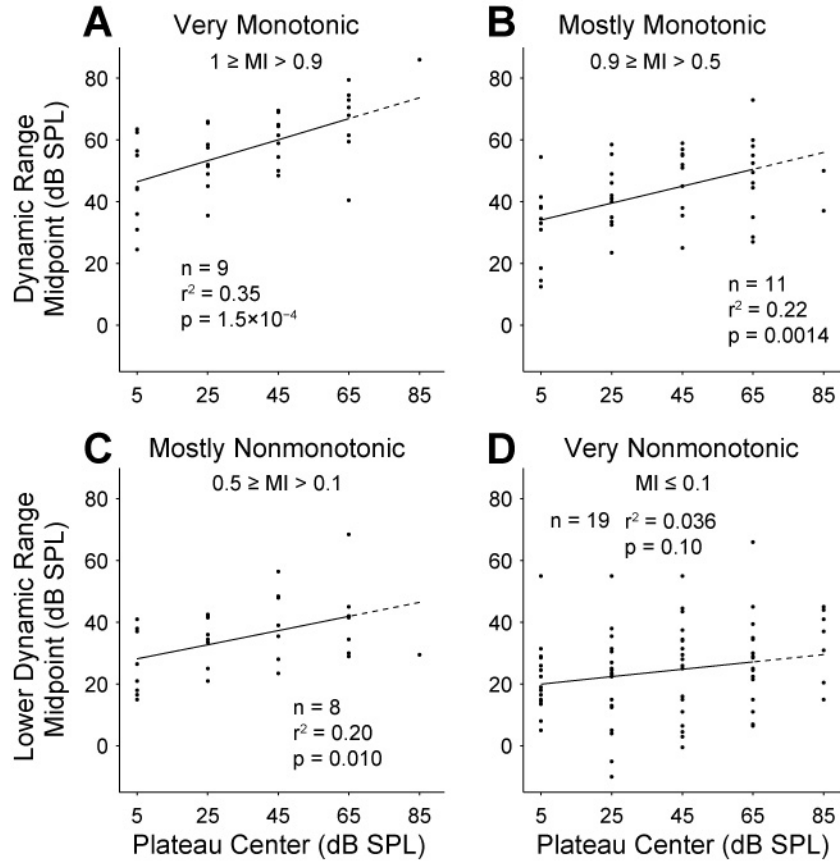


Figure 5.6 Dynamic range midpoints for each neuron as a function of dynamic stimulus probability plateau center segregated by MI class. For nonmonotonic neurons, data points represent the lower dynamic range midpoint only. **A–D**, Relationship between dynamic range midpoint and plateau center for very monotonic, mostly monotonic, mostly nonmonotonic and very nonmonotonic subpopulations. Regression lines were fit only for the 5, 25, 45 and 65 dB plateau centers because the 85 dB plateau center includes only 12 neurons. Dashed line indicates extrapolated regression out to the 85 dB plateau for visual comparison. Regressions indicate a significant ($p < 0.05$) dynamic range shift with plateau center for all monotonicity classes except for the very nonmonotonic neurons.

The very nonmonotonic neurons did not show significant adaptation of their lower dynamic range as a function of plateau center, but did for their upper dynamic range (Figure 5.7A,B). Very nonmonotonic neurons had a larger slope and significant correlation between upper dynamic range midpoints and dynamic stimuli plateau centers (slope = 0.17, intercept = 46; $r^2 = 0.065$; $p = 0.027$, regression F test) than did mostly nonmonotonic neurons, for which the fit was not significant (slope = 0.073, intercept = 60; $r^2 = 0.035$; $p = 0.30$, regression F test). Data from the highest level plateau were again not included in the regressions. This finding provides the first direct evidence for the capture hypothesis. The very nonmonotonic neurons showed a significant adaptation trend for upper dynamic ranges, but not for lower dynamic ranges, whereas the opposite was the case for the mostly nonmonotonic neurons. This means that the upper dynamic range of the most nonmonotonic neurons appears to shift in the direction of the most probable sound levels, thereby actively adapting to the high sound levels in a manner that captures the encoding of these levels.

We investigated other ways of segregating the nonmonotonic population as a way to evaluate whether adaptation in the upper dynamic range of very nonmonotonic neurons was truly due to their high degree of nonmonotonicity (corresponding to large on-CF inhibition at high sound levels) or whether other factors were better predictors. We found that segregating nonmonotonic responses by best level (BL) of the static rate-level curves (Figure 5.7C,D) revealed a slightly larger and more significant correlation between upper dynamic range midpoint and plateau center for neurons with $BL \leq 25$

dB (slope = 0.19; intercept = 44; $r^2 = 0.13$; $p = 0.0023$, regression F test). Neurons with $BL > 25$ dB did not show a significant correlation (slope = 0.061; intercept = 61; $r^2 = 0.0087$; $p = 0.57$, regression F test). As discussed in Chapter 4, there was not a significant correlation between MI and BL amongst the nonmonotonic population of static rate-level responses, so this difference may mean that low BL is a better predictor of adaptability of the upper dynamic range than is the degree of on-CF inhibition (as measured by MI), although the current data and analysis do not fully substantiate this claim. Regardless, two different methods of segregating nonmonotonic neurons both demonstrated shifting of the upper dynamic range for one of the subsets in a direction that would improve coding accuracy, providing substantial evidence for the capture hypothesis.

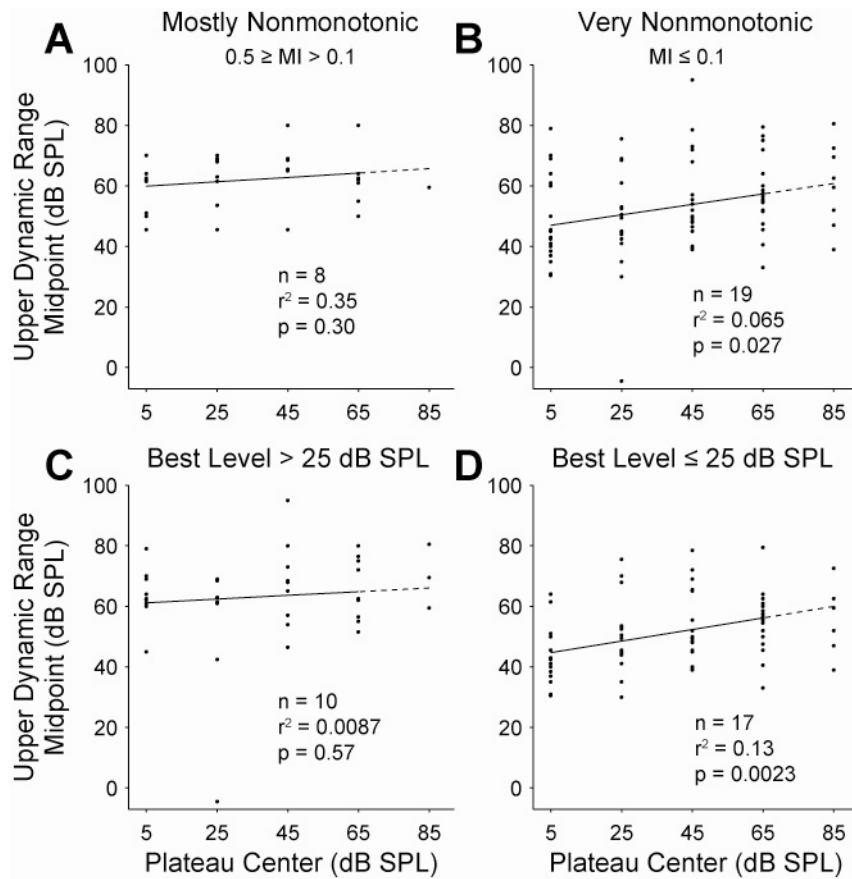


Figure 5.7 Upper dynamic range midpoints for each nonmonotonic neuron as a function of dynamic stimulus probability plateau center. **A–B**, Nonmonotonic neurons are segregated by monotonicity index (MI). The trend is significant for very nonmonotonic neurons but not for mostly nonmonotonic neurons. **C–D**, Nonmonotonic neurons are segregated by best level (BL) of the static rate-level function. The trend is significant for neurons with low BLs but not for those with high BLs. Both figures indicate that across the population of nonmonotonic neurons, the upper dynamic range is capturing the adaptation by shifting in the direction of the most probable sound levels. Whether the capture hypothesis is better represented by

nonmonotonic neurons with the most on-CF inhibition (lowest MIs) or those with the lowest BLs is currently inconclusive.

We performed the analogous segregation by best level (BL) for each nonmonotonic neuron's contribution to Fisher information (FI) curves (Figure 5.8). Fisher information was separated into upper and lower dynamic ranges for each neuron and Fisher information curves from the dynamic range on the same side of BL as the probability plateau center for each dynamic stimulus condition and for each neuron were averaged (see Section 2.3.2). This technique allowed us to measure the population effects of adaptation using strictly the portion of the FI that is most involved in encoding the most probable levels. These mean Fisher information curves showed peaks aligned near the 5, 25 and 45 dB plateaus for the lower dynamic ranges (Figure 5.8A) and near the 25, 45, 65 and 85 dB plateaus for the upper dynamic ranges (Figure 5.8B). Note that the averages are over all 27 nonmonotonic neurons in the dataset, but each point is not necessarily an average over all 27 neurons because of the manner in which the FI is split for each dynamic FI curve. Using this analysis, the adaptive nature of nonmonotonic neurons to dynamic level stimuli in a manner that improves coding accuracy can be readily discerned, and it in fact differs between the upper and lower dynamic ranges of these neurons. This result provides more support for the capture hypothesis—not only did upper dynamic ranges shift in the plateau direction, the encoding accuracy of the upper dynamic ranges, as measured by FI, also shifted so that the peaks aligned with the higher level plateaus. Mean rate-level functions computed using the same type of analysis (Figure 5.8C,D), show shifting of the respective dynamic range that is congruent with the shifting of the FI peaks. Note that in Figure 5.8B and all subsequent figures that present the plateau-side upper dynamic range, the curve for the 25 dB

stimulus is only represented by 3 neurons. This curve shows the most variability in later figures comparing FI results for different analyses (Figure 5.10 – 5.13).

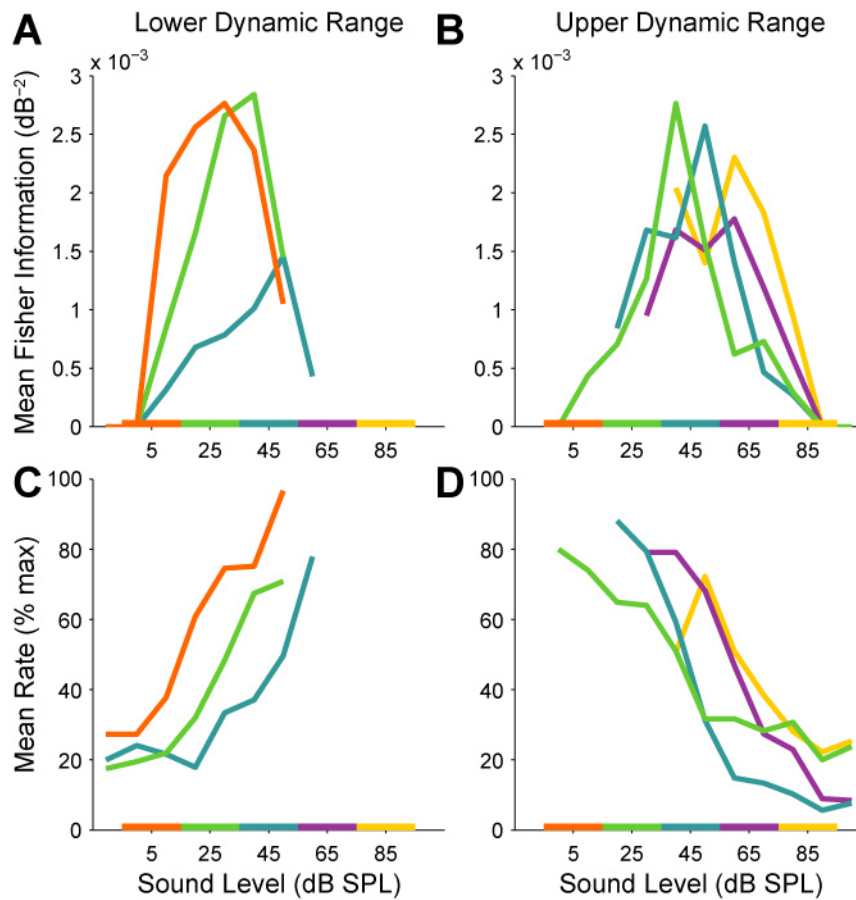


Figure 5.8 Nonmonotonic neurons were split into lower and upper dynamic ranges by separating responses on either side of best level (BL) for each dynamic stimulus. The lower dynamic ranges have increasing rate-level slopes and the upper dynamic ranges have decreasing rate-level slopes. **A–B**, Mean Fisher information (FI) for the upper and lower dynamic ranges respectively on the same side of BL as the high probability region of the corresponding dynamic stimulus. **C–D**, Mean of the corresponding rate-level functions. Separating upper and lower dynamic ranges in this manner for nonmonotonic neurons more clearly demonstrates adaptation to improve coding accuracy, in the lower dynamic range for the 5, 25 and 45 dB plateau stimuli (A) and in

the upper dynamic range for the 25, 45, 65 and 85 dB plateau stimuli (B). Note that averages are computed over all 27 nonmonotonic neurons in the dataset, but each point is not necessarily average over 27 neurons because only the portion of the FI and rate-level curves that is on the same side of BL as the plateau center is taken from each neuron.

Fisher information (FI) was also averaged separately for upper and lower dynamic ranges with the same analysis as that in Figure 5.8 but taking the dynamic range on the opposite side of best level (BL) from the plateau center. This method revealed how encoding accuracy changed for the dynamic range which was not actively involved in encoding the most probable sound levels in the dynamic stimulus. The peak FI for the lower dynamic range remained at relatively low sound levels in response to the high level dynamic stimuli (Figure 5.9A). This means that the lower dynamic range remained sensitive to low sound levels even when nonmonotonic neurons were adapted to high sounds levels, again confirming the previous result. Note that this is a completely different form of adaptation than the monotonic neurons exhibited.

The peak FI for the upper dynamic range did show some shifting in the direction of the low level plateaus (Figure 5.9B), even when these sound levels were most accurately encoded by the lower dynamic range (see Figure 5.8A). This result supports the notion that the neurons on average are shifting their BLs as well as their thresholds as they adapt to the lower level dynamic stimuli, thereby causing the shift in the upper dynamic range. This claim is not entirely conclusive, noting in particular that over the population of nonmonotonic neurons ($n = 27$), the correlation between dynamic rate-level BL and plateau center was not significant ($p = 0.080$, Spearman rank correlation test). When these neurons were subdivided by MI and BL (same analysis as Figure 5.7 but regressing BL instead of upper dynamic range midpoint), the trend was not significant for any category ($p > 0.10$, Spearman rank correlation test) except for nonmonotonic neurons

with $BL \leq 25$ dB SPL ($n = 17$; slope = 0.13; intercept = 30; $r^2 = 0.059$; $p = 0.046$, regression F test). Mean rate-level functions for the opposite side upper and lower dynamic ranges (Figure 5.9C,D) in general revealed very little shifting between dynamic stimuli.

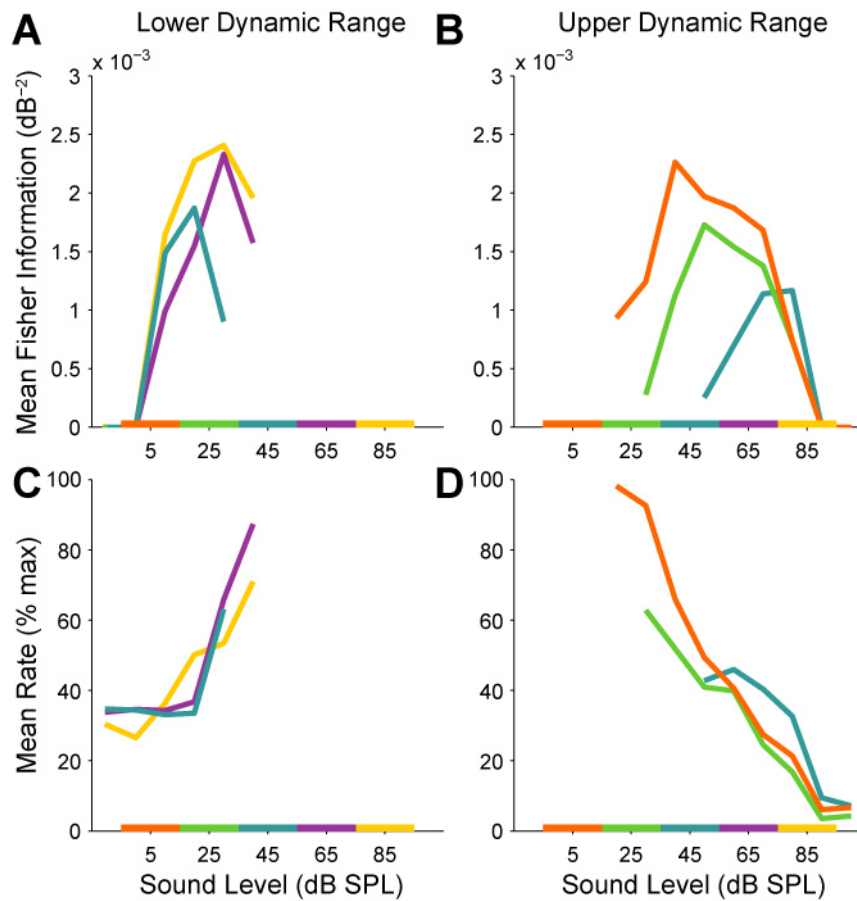


Figure 5.9 Same plots as in Figure 5.8 except using the dynamic range on the opposite side of BL from the dynamic stimulus plateau center. **A–B**, Mean Fisher information (FI) for the upper and lower dynamic ranges respectively on the opposite side of BL. **C–D**, Mean of the corresponding rate-level functions. Lower dynamic ranges remain sensitive to low levels even when adapted to high level dynamic stimuli (A,C). Although mean rate-level functions for the upper dynamic range (D) do not shift much in response to low level dynamic stimuli, the corresponding FI does show shifting in the direction of the plateau (B).

In order to ensure that calculating Fisher information using 10-dB bins from data collected in 1-dB increments (see Section 2.3.2) did not affect our population results, FI was also calculated using all sound levels present in the dynamic stimuli (1 dB bins). Qualitatively, the mean FI curves calculated in this manner (Figure 5.10) were similar with those previously presented (Figure 5.3), mostly differing in the magnitude of the FI peaks and not the location. We conclude that our choice for 10 dB bin size in order to reduce noise on the single neuron level, essential for accurately estimating dynamic rate-level thresholds and dynamic range midpoints, did not have a large effect on our conclusions regarding adaptation and encoding accuracy. Mean rate-level functions over the population using 1 dB bins (data not shown) were noisy, so the 10 dB bin size also allowed for better comparison between the mean FI and mean rate-level curves, particularly for the static rate-level curves for which only 10 dB increments were measured. Modifying the dynamic protocol so that dynamic level stimuli only contained 10 dB increments would likely have altered the effects of adaptation and would have been more difficult to compare with previous studies that also discretized sound level probability distributions into 1 dB or smaller bin sizes (Dean et al., 2005; Kvale & Schreiner, 2004).

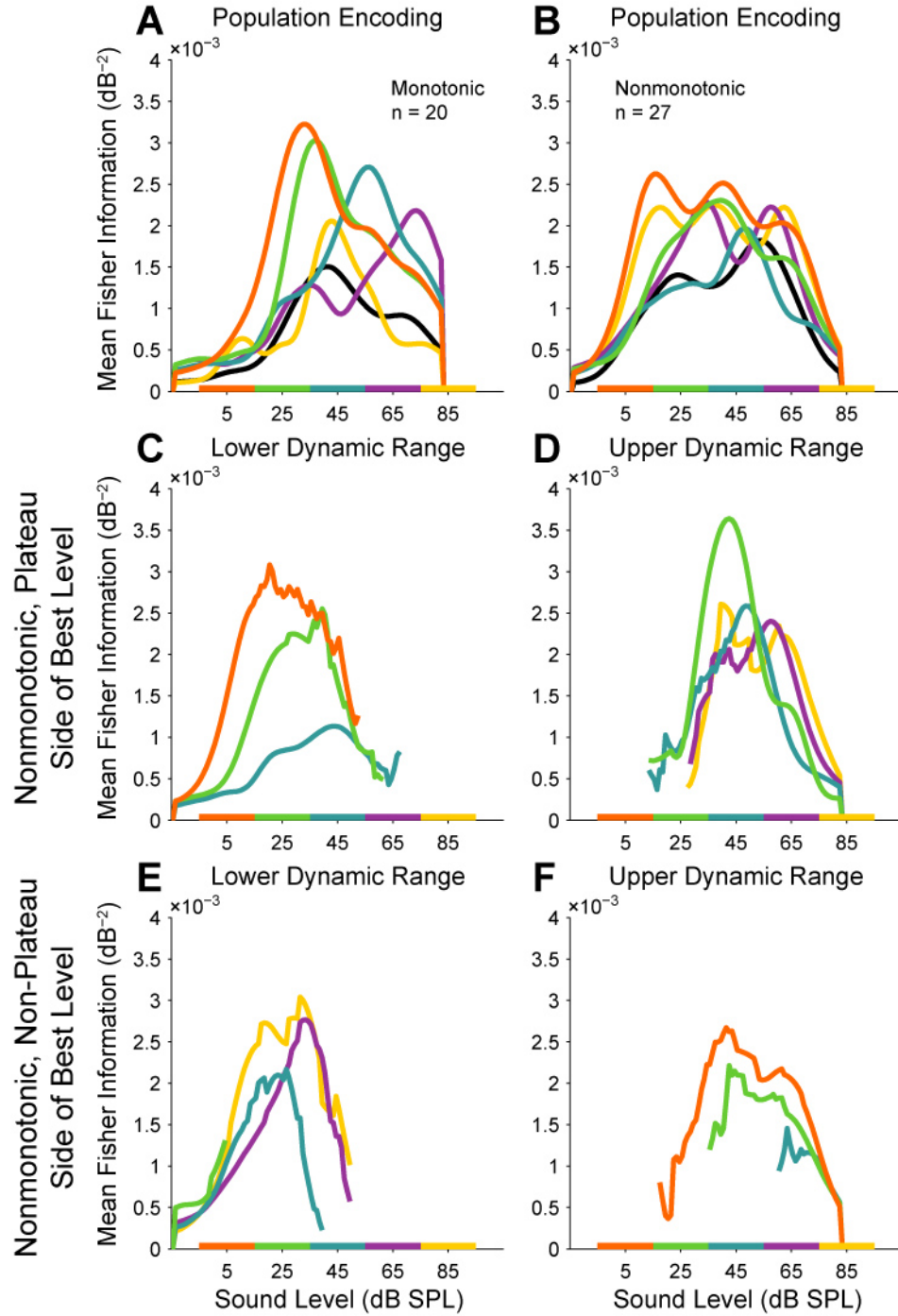


Figure 5.10 Fisher Information (FI) averages calculated using 1-dB sound level bins.

Mean FI for the monotonic (A) and nonmonotonic (B) populations (compare to 5.3A,B). C–D, Upper and lower dynamic range mean FI for the nonmonotonic

population taking only the FI on the same side of best level (BL) as the dynamic stimulus plateau center for each neuron (compare to 5.8A,B). **E-F**, Upper and lower dynamic range mean FI for the nonmonotonic population taking only the FI on the opposite side of best level (BL) as the dynamic stimulus plateau center for each neuron (compare to 5.9A,B).

5.2.4 Adaptation in Onset versus Sustained Spiking

As a first step towards exploring the mechanism of adaptation in monotonic and nonmonotonic neurons, the effects of adaptation to dynamic stimuli were studied using only the first 50 ms (Figure 5.11) of the spiking responses in each 100 ms time bin (still accounting for latency, see Section 2.3.2) and using only the last 50 ms (Figure 5.12). This type of analysis to differentiate onset from sustained responses has been utilized in previous studies (Sadagopan & Wang, 2008; X. Wang, Lu, Snider, & Liang, 2005). The first portion of spiking responses is typically referred to as onset spiking and the later portion typically referred to as sustained firing. The results indicate that in general the effect of adaptation in terms of shifting of the FI peaks is seen in both portions of the response, although the FI peaks are generally larger for the onset firing. The two exceptions to this are in the case of the nonmonotonic upper dynamic ranges capturing the adaptation for high-level stimuli (compare Figures 5.11D and 5.12D) and in the case of nonmonotonic lower dynamic ranges encoding low-level sounds when adapted to high-level stimuli (compare Figures 5.11E and 5.12E). In these cases the adaptive response is delayed, in that more information regarding this adaptation is available in the sustained portion of the response than in the onset portion. On-CF inhibition is known to be delayed relative to excitation (Tan et al., 2007; Wu et al., 2006), so this result provides additional evidence that on-CF inhibition is responsible for these adaptive features of nonmonotonic neurons, as previously hypothesized.

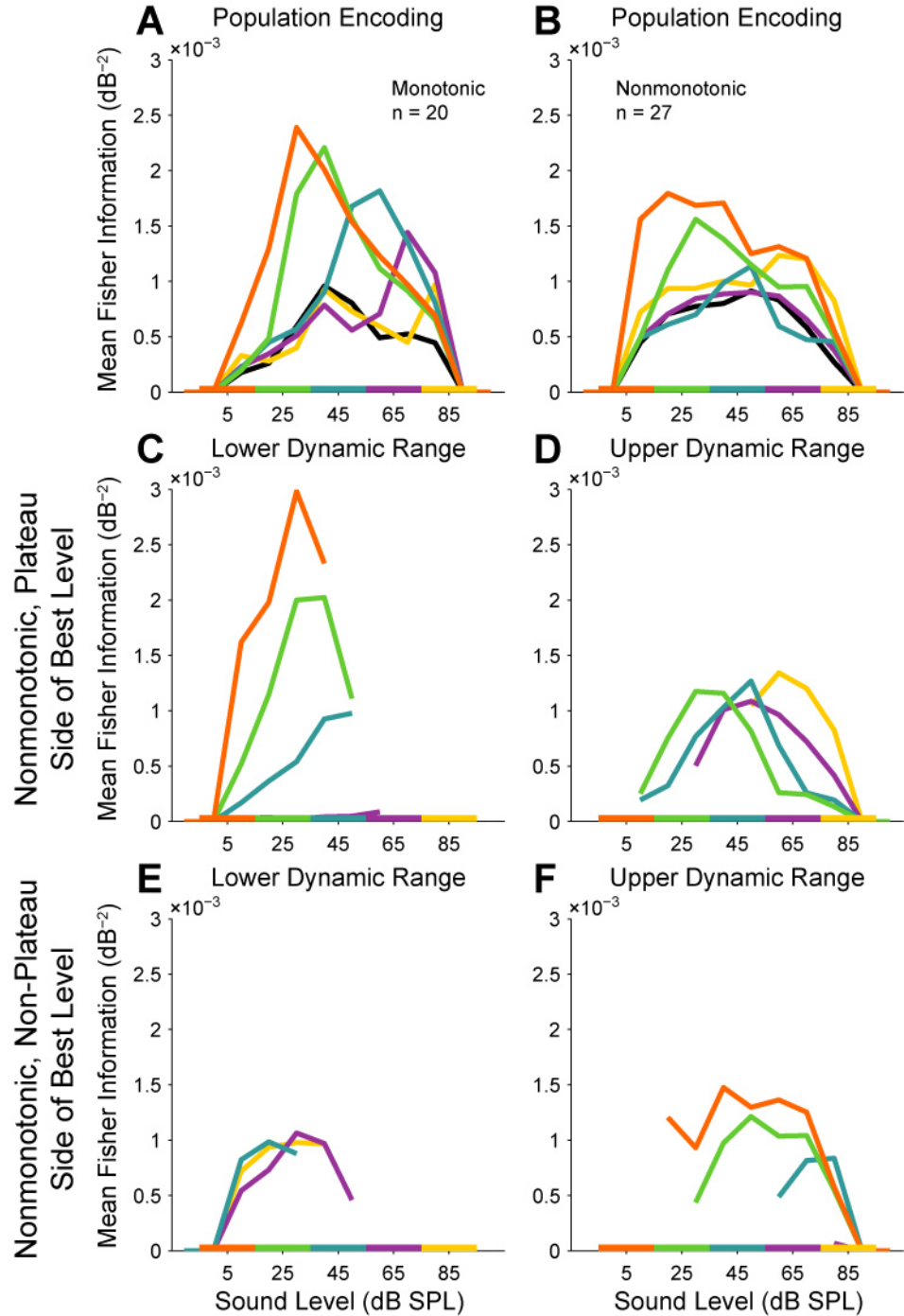


Figure 5.11 Fisher Information (FI) averages calculated using onset responses only (first 50 ms of response in each time bin, still accounting for individual neuron latencies). Mean FI for the monotonic (**A**) and nonmonotonic (**B**) populations (compare

to 5.3A,B). **C–D**, Upper and lower dynamic range mean FI for the nonmonotonic population taking only the FI on the same side of best level (BL) as the dynamic stimulus plateau center for each neuron (compare to 5.8A,B). **E–F**, Upper and lower dynamic range mean FI for the nonmonotonic population taking only the FI on the opposite side of best level (BL) as the dynamic stimulus plateau center for each neuron (compare to 5.9A,B).

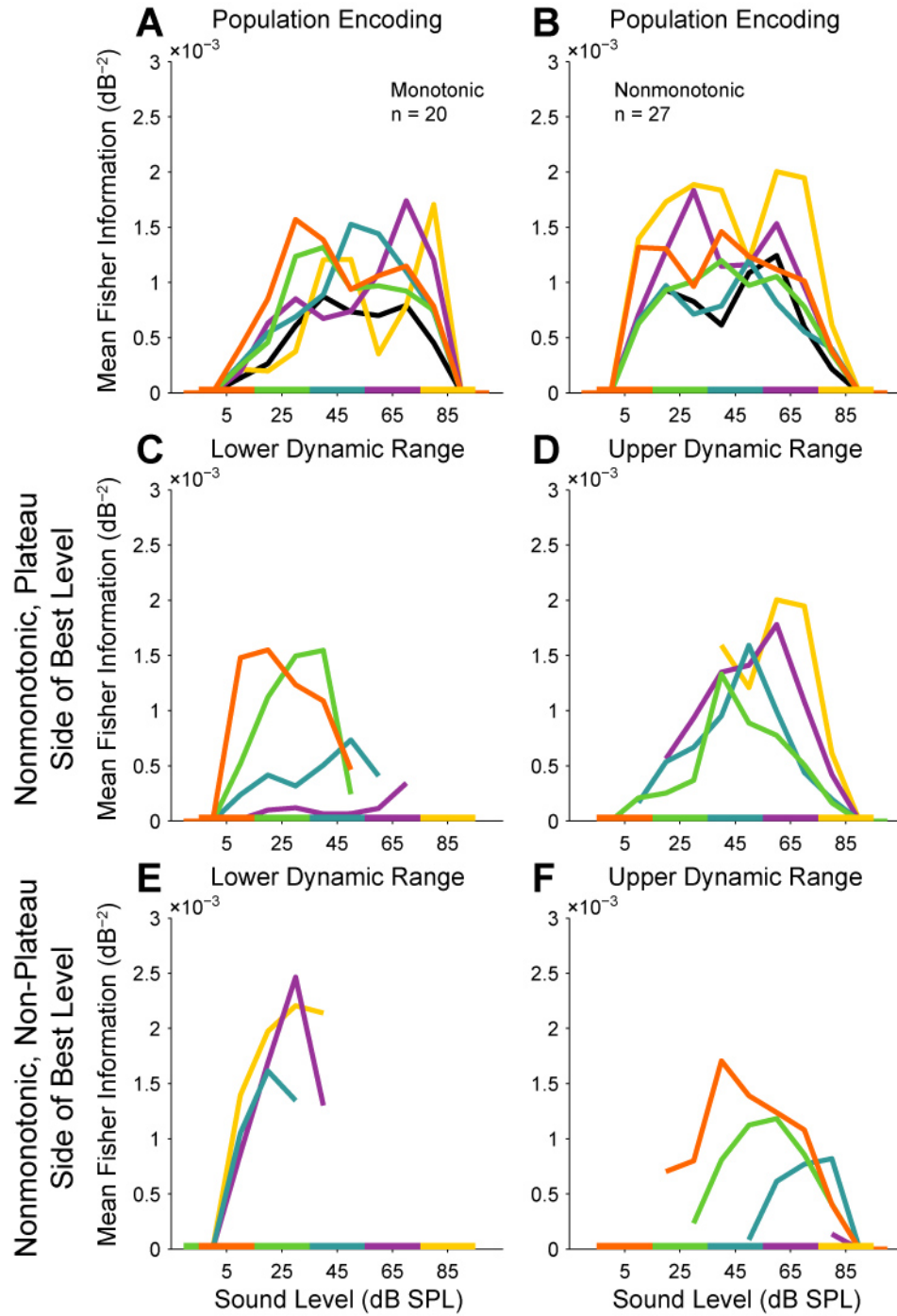


Figure 5.12 Fisher Information (FI) averages calculated using sustained responses only (second 50 ms of response in each time bin, still accounting for individual neuron latencies). Mean FI for the monotonic (**A**) and nonmonotonic (**B**) populations (compare

to 5.3A,B). **C–D**, Upper and lower dynamic range mean FI for the nonmonotonic population taking only the FI on the same side of best level (BL) as the dynamic stimulus plateau center for each neuron (compare to 5.8A,B). **E–F**, Upper and lower dynamic range mean FI for the nonmonotonic population taking only the FI on the opposite side of best level (BL) as the dynamic stimulus plateau center for each neuron (compare to 5.9A,B).

5.2.5 Adaptation Dynamics

The time course and rate of adaptation transients are discussed in-depth in Chapter 6. Lower driven rates and higher response variability in cortex did not allow adaptation time constants to be studied with the existing protocol alone (see Section 2.3.1) as has been done in previous studies subcortically (Dean et al., 2005; Dean et al., 2008). However, to verify that adaptation dynamics did not affect conclusions derived from the steady-state responses discussed in this chapter, mean FI responses were measured excluding the spiking responses collected during the first 60 seconds of each dynamic level stimulus (Figure 5.13). The shortest dynamic stimuli were two minutes in duration, so 60 seconds excludes the first halves of responses to the shortest stimuli. Both fast and slow components of adaptation have been reported subcortically with the median time constant of the fast component being well under one second (Dean et al., 2008; Kvale & Schreiner, 2004) and that of the slow component at approximately 12 seconds (Dean et al., 2008). This puts 60 seconds far outside the adaptation time course for all but a very small number of subcortical neurons. Although the possibility exists that cortical time constants may be longer, results using a forward-masking type design with complex stimuli in auditory cortex indicate that suppression and facilitation effects occur when stimuli are separated by times within the range of a few seconds (Bartlett & Wang, 2005). Qualitatively our results are again quite similar. The biggest differences are in the 25 dB curve for the plateau-side upper dynamic range (Figure 5.13D) and for the 85 dB curve for the mean monotonic FI (Figure 5.13A). Both of these curves, however,

are only represented by 3 neurons. The similarity of the results implies two things: (1) A large majority of cortical neurons are likely to have time constants of adaptation that are well below 60 seconds, both for fast and slow components. (2) Adaptation in a manner that improves coding efficiency is sustained over a period of several minutes or more.

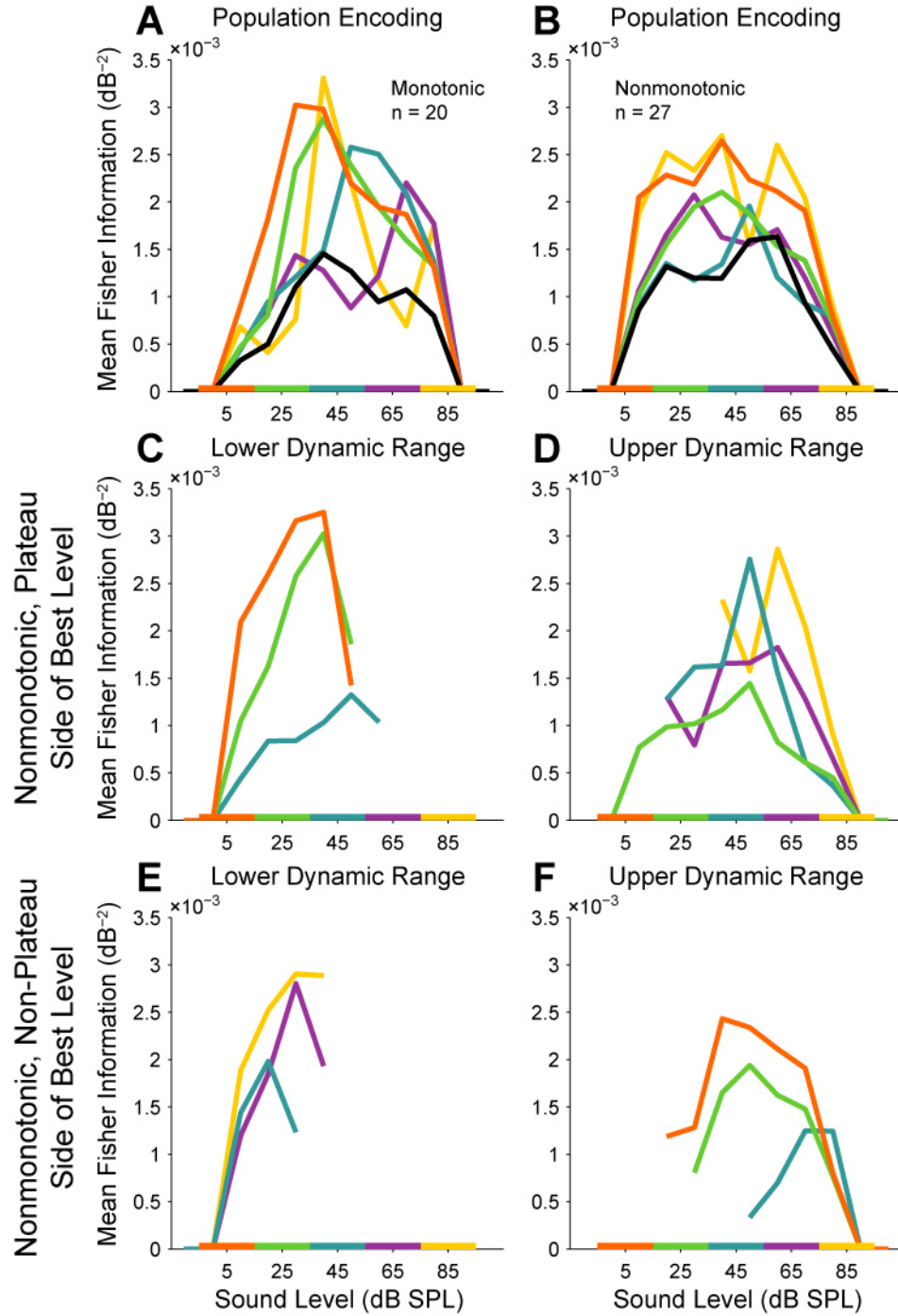


Figure 5.13 Fisher Information (FI) averages calculated by excluding spiking responses from the first 60 seconds of the dynamic stimuli. This method ideally captures only the steady state response in the means and not any component of the adaptation dynamics.

Mean FI for the monotonic (**A**) and nonmonotonic (**B**) populations (compare to 5.3A,B). **C–D**, Upper and lower dynamic range mean FI for the nonmonotonic population taking only the FI on the same side of best level (BL) as the dynamic stimulus plateau center for each neuron (compare to 5.8A,B). **E–F**, Upper and lower dynamic range mean FI for the nonmonotonic population taking only the FI on the opposite side of best level (BL) as the dynamic stimulus plateau center for each neuron (compare to 5.9A,B).

5.3 Discussion

Auditory neurons in different species and in multiple areas of the auditory system tend to adapt their responses in a manner that improves the encoding of sound level based on the level statistics of the stimulus (Dean et al., 2005; Kvale & Schreiner, 2004; Nagel & Doupe, 2006). Dynamic level stimuli have not previously been used to probe unique coding properties of auditory neurons with on-characteristic-frequency (on-CF) inhibition at higher sound levels called level-tuned or nonmonotonic neurons. Single neuron data recorded for this study from the primary auditory cortex of awake marmosets provide evidence that nonmonotonic neurons: (1) preferentially encode low sound levels by maintaining sensitivity to less intense sounds even when presented with high-level dynamic stimuli (2) preserve this sensitivity by encoding low-level sounds predominantly with their lower dynamic range even when intense sounds are common; and (3) capture encoding of high-levels using their upper dynamic range particularly when intense sounds are common. Using tones presented during periods of silence (static stimuli), we previously demonstrated that threshold and the amount of CF inhibition at high intensities (as measured by a low monotonicity index) were correlated (see Chapter 4). Those results imply that nonmonotonic neurons may preferentially encode low intensities. Here we reach a similar conclusion, but when the neurons are in an adapted steady-state induced by dynamic level stimuli. This behavior is potentially even more useful than the static property because under adapted conditions, monotonic neurons in A1 tend to shift their dynamic ranges toward the most probable sound levels

in a stimulus, consistent with findings in inferior colliculus (Dean et al., 2005). Consequently, monotonic neurons as a population do not retain much of their sensitivity to lower sound levels when high levels are common, meaning that the nonmonotonic neurons play a vital encoding role under these conditions. Both neuronal types appear to adapt similarly to softer sounds.

Level-tuned neurons are likely created in a hierarchical fashion starting in the cochlear nucleus and are present in larger percentages at higher auditory centers (see discussion in Section 4.3), implying an important role on on-CF inhibition in the auditory system. Given that this transformation in the neural code appears to occur gradually across multiple auditory stations, level-tuned neurons in auditory cortex seem unlikely to exhibit properties fundamentally different from analogous neurons in subcortical auditory areas. In fact, we would anticipate that subcortical level-tuned neurons would exhibit adaptive behavior similar to that reported here for cortex. In this Chapter, we posited two potential roles for on-CF inhibition in level-tuned neurons under dynamic level conditions, termed the shielding and capture hypotheses. In the shielding role, on-CF inhibition may prevent high intensity sound inputs from influencing the adaptation of nonmonotonic neurons' lower dynamic range. This is in contrast to monotonic neurons, which we know will adapt their dynamic range to higher levels when presented with mostly high-level sounds. Thus, the shielding hypothesis predicts that on-CF inhibition actively and directly prevents nonmonotonic neurons from adapting to intense sounds, thereby preserving their low-level sensitivity. We do not present direct

evidence for that hypothesis here, as the experiments to do so would involve direct manipulation of the on-CF inhibition of these neurons. The capture hypothesis posits that adaptation to dynamic stimuli, particularly those with predominantly high sound levels, is directly influenced by on-CF inhibition such that the inhibitory regime of the rate-level function (the upper dynamic range) adapts in a way that improves the encoding efficiency of high-level sounds. Results of the current study indicate that when loud sounds are common, nonmonotonic neurons tend to adapt their upper dynamic ranges toward the loud sounds, lending support to the adaptation capture hypothesis.

Collectively, monotonic neurons shift their dynamic ranges more than nonmonotonic neurons, and nonmonotonic neurons appear to exhibit two regimes of adaptation depending upon the ratio of high levels to low levels present in the stimulus at short time scales. A schematic summary of these findings based upon population averages can be seen in Figure 10. The monotonic population exhibits a decreasing response gain with increasing plateau center, whereas response gain for nonmonotonic neurons decreases with increasing plateau center up to about 45 dB, beyond which gain actually increases. This gain increase at high dynamic levels, in addition to decreases in response threshold, provides a mechanism for nonmonotonic neurons to encode low levels more accurately than monotonic neurons under dynamic conditions with frequent intense sounds. Note that the average nonmonotonic best level, where less information is available from the nonmonotonic population, always falls within the average dynamic range of the monotonic population. When information from both populations is

considered collectively, therefore, this complementary coding scheme enables high encoding accuracy over a larger dynamic range than either subpopulation is able to provide on its own and under a wide variety of stimulus dynamics. This effect is clearly evident when considering the mean Fisher information over the population in response to the uniformly distributed dynamic stimulus. Monotonic neurons demonstrate a peak near 35 dB SPL (Figure 5.3A, solid black line), while nonmonotonic neurons demonstrate two peaks, one near 20 dB SPL and one near 60 dB SPL (Figure 5.3C, solid black line). Again, the encoding accuracies of the two populations complement each other so that together they can cover a large portion of the wide dynamic range presented by the uniformly distributed dynamic stimulus.

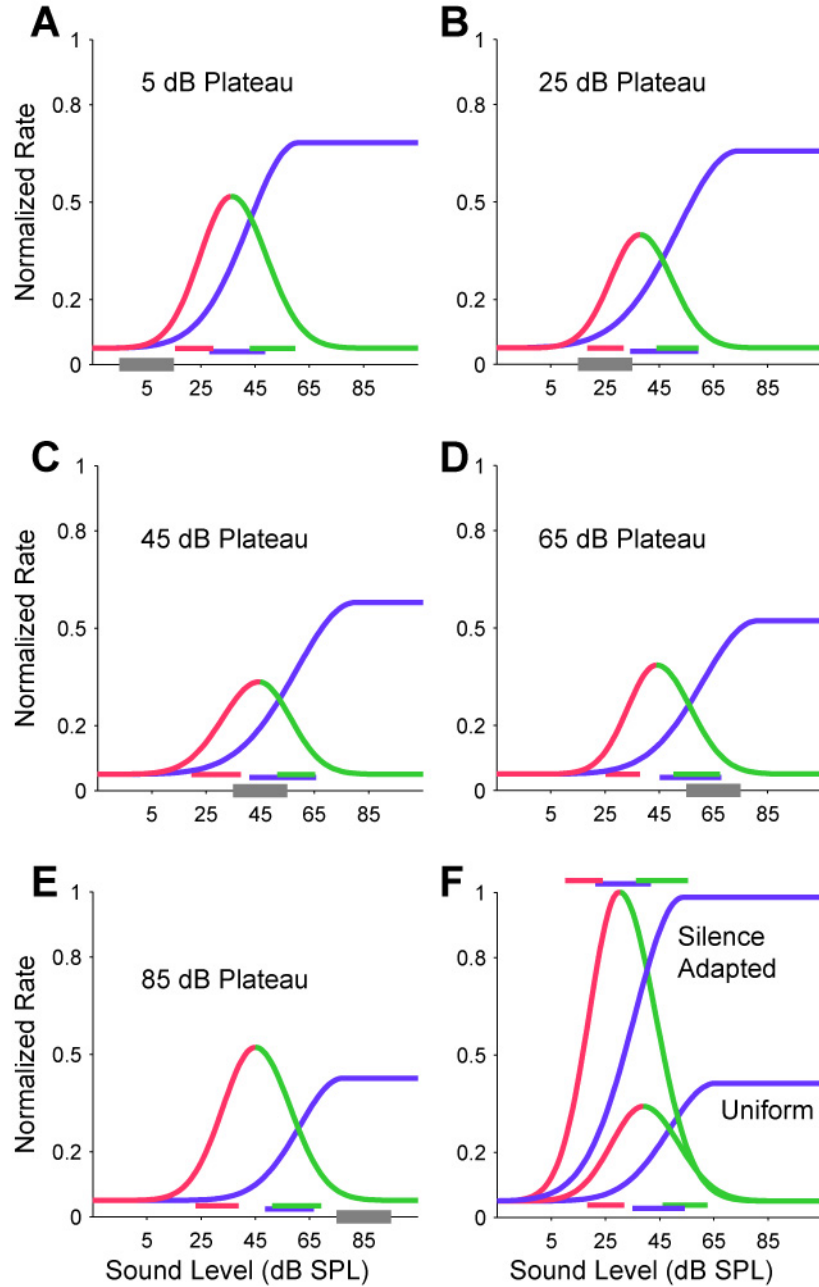


Figure 5.14 Average adaptive behavior of primary auditory cortex neuron in response to dynamic stimuli with different level statistics. **A–E**, Each panel displays schematic input-output functions for monotonic and nonmonotonic neurons in response to dynamic level stimuli with the high probability levels indicated by gray lines on the level

axis. Model functions are constructed as split-Gaussians (see Section 2.2.3) with mean dynamic range data (indicated by horizontal colored lines) from the population of neurons in this study. Both types of neurons exhibit threshold shifts and response gain adaptation. The result is a double encoding scheme at low levels and a complementary coding scheme at high levels. The separation between monotonic and nonmonotonic functions becomes greatest when high levels are most common, as depicted in **E**, **F**. A similar encoding scheme is apparent even under silence-adapted conditions and in response to a uniformly distributed dynamic stimulus.

5.3.1 Dynamic Range and Level Encoding

In the effort of distinguishing unique encoding properties of level-tuned neurons, we utilized the technique of subdividing each neuron's response into its upper and lower dynamic range—regions of negative and positive slope in the rate-level function respectively, separated by the neuron's best level (BL). We focused on the sloped portions of the rate level functions as the dynamic range of the neuron because in terms of sound level discriminability, the sloped portions convey the most information. Under noisy conditions other aspects of the rate-level response, particularly BL, may be more useful for encoding (Butts & Goldman, 2006). We do not consider this situation here for two reasons, first that our stimulus were not designed to measure differences in level encoding between clean and noise corrupted signals, and second that the focus of this study is on relative differences in encoding between the monotonic and nonmonotonic population and not necessarily on absolute discriminability properties. Discriminability was quantified with Fisher information (FI) which is typically used as a measure of the upper bound on the performance of an optimal decoder. In this study, however, we utilized FI only to infer encoding properties and do not present evidence here regarding specifically how postsynaptic neurons would decode this information. To do so would require proposing an actual decoder, which we do not do here.

As discussed above, we focused on encoding properties conveyed by sloped portions of each neuron's rate-level response. Because the slope at the maximum response (the best

level) is necessarily zero, this portion is not useful in terms of encoding, particularly with regards to level discrimination of pure tones without background noise. This qualifies BL as a logical point at which to separate the neuron into two dynamic ranges because it is a point of zero FI surrounded by two bumps of positive FI. Additionally, because we were interested in testing the hypothesis that on-CF inhibition of level tuned neurons is directly involved in the ability of level-tuned neurons to preferentially encode low sound levels, BL also represents a logical point to split the neuron into excitatory and inhibitory regimes of the rate-level function. Although it may seem that this analysis of splitting the neurons into an upper and lower dynamic range will by design result in our conclusion, that the lower dynamic range adapts to low-level stimuli and the upper dynamic range to high-level stimuli, this is not the case. For example, this analysis could have revealed that only the lower dynamic range adapted to accurately encode all of the plateaus. This case would have shown all the possible curves in Figure 5.8A aligning their peaks with the plateaus and no curves doing the same in Figure 5.8B.

For a portion of our analysis of dynamic rate-level functions we utilized the midpoint of either the lower or upper dynamic ranges as a single representative point (Figures 5.5, 5.6 and 5.7). This point was chosen because our interest was in understanding how the overall dynamic range shifted depending on the dynamic stimulus. Other choices are certainly possible, including threshold, saturation, best-level and point of maximum slope. The point of maximum slope would have the most meaning specifically in regards to level encoding for discriminability. The midpoint, however, is located at the

center between threshold and saturation, so not only is it quite likely to be near the point of maximum slope, it also encompasses changes in both threshold and saturation. We performed similar analyses with best-level, and although some results were significant, they were not as convincing as with the dynamic range midpoint, lending credence to the idea that most of the adaptation is taking place along the dynamic range and less is occurring at the best level itself.

The current results are consistent with studies of adaptation in cortical and subcortical levels of the auditory system indicating that preceding spiking rate alone is an incomplete predictor of the amount of observed adaptation (Bartlett & Wang, 2005; Dean et al., 2005; Malone & Semple, 2001; Nelson, Smith, & Young, 2009). Therefore it seems likely that additional processes, possibly inhibitory in nature, participate in creating the observed responses. Adaptation similar to that of the monotonic neurons in the present study have also been observed in inferior colliculus (Dean et al., 2005), implying that this type of adaptation emerges subcortically, as well. Level-tuned neurons remain to be tested subcortically, however, so a cortical origin or refinement of complementary level-tuned adaptation cannot presently be ruled out. The overall amount of adaptation observed by mean population rate alone in cortical neuron populations is insufficient to fully adjust neural coding for the stimuli used (best visualized in Figure 5.4A). Given that Fisher information measures do reveal adaptation matched well to stimulus statistics for both monotonic (Figure 5.3B) and nonmonotonic neurons (Figure 5.8A,B), the neural code is likely to include spiking properties beyond

simply mean rate. The overall variety in dynamic range location for dynamic stimuli evident in Figure 5.5 reflects a distributed code under dynamic conditions so that even though the population adapts to maintain coding accuracy for high-probability events, enough variability in individual responses remains to encode lower probability events.

5.3.2 Relation to Previous Studies

Other putative functions of nonmonotonic neurons for representing and transforming auditory information that have been put forth in other studies are based on recordings using predominantly non-time-varying level stimuli (see Section 4.3). It is likely that the role of nonmonotonic neurons as preferential encoders of low-intensity dynamic stimuli discussed here is complementary to these other potential functions. In addition, nonmonotonic specialization for low-levels does not directly address the issue of coding sound information across frequency but does imply that monotonic and nonmonotonic neurons encode level for different purposes. Nonmonotonic neurons, for example, would be particularly useful for encoding softer sounds interspersed amongst louder sounds, allowing the monotonic neurons to remain adapted and maintain coding accuracy to the more common loud sounds but without loss of soft sound level information.

Adaptive processes have been of considerable interest as a potential mechanism to help explain well-studied psychophysical phenomena such as forward masking. In classic

forward masking, the detection of a brief tone is degraded by the occurrence of a preceding tone at the same frequency, and all other factors being equal, the amount of masking is proportional to the level of the masker (Jesteadt, Bacon, & Lehman, 1982; Lüscher & Zwislocki, 1949). Auditory nerve studies reveal that while adaptation in the periphery is evident under these stimulus conditions, it alone cannot fully account for this masking phenomenon (Harris & Dallos, 1979; Relkin & Turner, 1988; Turner, Relkin, & Doucet, 1994). Subcortical excitatory and inhibitory circuits, on the other hand, appear to contribute substantially to forward masking (Nelson et al., 2009). While similar to masking protocols, the sound sequences used in the current experiments were sufficiently different to prohibit direct comparisons with forward masking studies. In particular, we were largely examining the suprathreshold behavior of cortical neurons, which does not necessarily mirror the behavior at threshold even for classic forward masking (Zeng, Turner, & Relkin, 1991). Nevertheless, the adaptation of level-tuned neurons to maintain coding accuracy for soft sounds when loud sounds are common appears to run counter to the type of adaptation underlying psychophysical forward masking. In masking paradigms, gain adaptation of nonmonotonic neurons has been shown in some cases to be a nonmonotonic function of masker level, although not systematically so (Bartlett & Wang, 2005; Brosch & Schreiner, 1997; Calford & Semple, 1995). A non-systematic gain trend has also been shown as songbird auditory neurons adapt to a mean level increase (Nagel & Doupe, 2006). The nonmonotonic gain adaptation for nonmonotonic neurons apparent in Figure 5.4B could be a reflection of a similar process.

The stimuli in this study were designed to look predominantly at rate-level changes depending on the mean of sound-level distributions. Because of the location of the high-probability plateaus relative to the rest of the distribution, a change in the mean also resulted in a change in the variance of the stimulus. However, this effect was small because of the relatively low probability of choosing any level outside of a plateau. We did not systematically investigate the effect of changing the width of the probability plateaus (fixed at 20 dB) that would have been required to thoroughly investigate adaptation to variance (Kvale & Schreiner, 2004; Nagel & Doupe, 2006), except solely for our use of the uniformly distributed dynamic stimulus. Our uniformly distributed stimulus, which has much higher level variance than the high-probability plateau stimuli, consistently resulted in a decrease in gain (see Figure 5.3, solid black lines), consistent with results in songbirds (Nagel & Doupe, 2006). Additionally, although the design of the dynamic stimuli used here is inherently time-varying, it is difficult to compare with studies of amplitude modulation or those that consider linear temporal receptive fields because each time interval of the dynamic stimulus is composed of a stationary signal (typically a pure tone at CF). Comparisons are difficult because the 100-ms time intervals are relatively short when compared to typical best modulation frequencies of cortical neurons in response to AM stimuli (Bartlett & Wang, 2005; Liang, Lu, & Wang, 2002) and relatively long when compared to the width of a typical cortical linear temporal receptive field (Depireux, Simon, Klein, & Shamma, 2001). There is however a nice parallel to another neural adaptation effect, stimulus-specific adaptation, created

from what is also a very different stimulus design—the oddball paradigm (Ulanovsky, Las, Farkas, & Nelken, 2004; Ulanovsky, Las, & Nelken, 2003). In this design a deviant, or low-probability amplitude event evokes a significantly larger response than that evoked by the more common amplitudes. Based on our conclusions, nonmonotonic neurons could very well serve this purpose when the common amplitudes are high-level and the deviant is low-level.

In conclusion, we have found that the level-dependent inhibition of level-tuned cortical neurons appears to drive neuronal adaptation when high intensities occur commonly in dynamic stimuli. Unlike classically studied neurons whose input-output functions increase or saturate at high levels, adaptation of level-tuned neurons does not appear simply to optimize overall coding accuracy. The nature of their adaptation implies that they purposefully remain sensitive to rare, faint sounds even when louder sounds are much more common. If sensory neurons with tuned input-output functions are truly specialized for encoding low input values and maintain this sensitivity even when the most common input values are high, we speculate that the high prevalence of such neurons in the auditory system relative to other sensory systems implies that behaviorally relevant sound processing uniquely requires the ability to preserve sensitivity over a wide dynamic range and on the relatively fast time scales contained in dynamic environmental sounds.

Chapter 6

Time Course of Neuronal Adaptation to Sound Intensity Level

6.1 Introduction

Neurons in sensory systems likely adapt their responses so that encoding accuracy is reflected in the statistical distribution of sensory inputs (for review see (Wark et al., 2007)). This type of adaptation prevents a large number of neurons from encoding sensory input feature values that are not particularly relevant given the current environment of the animal, allowing much of the population to instead focus its encoding on the most probable values. Given that the error of the optimal decoder for a neuronal population encoding a particular sensory feature scales inversely with the size of the population (Eliasmith & Anderson, 2004), a larger number of neurons representing a particular high-probability subset of possible feature values is advantageous for maximizing encoding accuracy. However, under many environmental conditions, the statistics of the sensory input are not stationary. Thus, the dynamics of neuronal adaptation to time-varying sensory stimuli have been proposed to reflect those of an optimal estimator, particularly of the mean and variance of the time-varying signal (DeWeese & Zador, 1998).

Auditory neurons adapt to changes in mean sound level (Dean et al., 2005; Nagel & Doupe, 2006) and to changes in higher order moments of the sound level distribution (Kvale & Schreiner, 2004; Nagel & Doupe, 2006) in a manner that improves their encoding of the sensory stimuli. Adaptation time constants of responses to changes in variance and higher order moments are asymmetric, showing faster adaptation from low-to-high variance (Kvale & Schreiner, 2004), as supported by models of optimal variance estimation (DeWeese & Zador, 1998). Although one might not expect a non-biased mean estimator to show such asymmetry, results using time-varying level stimuli in the inferior colliculus (Dean et al., 2008) and from forward masking experiments in auditory nerve fibers (Chimento & Schreiner, 1990, 1991) also show faster adaptation from low-to-high mean sound levels. This asymmetry in mean sound level adaptation has not been reported in all studies, however (Nagel & Doupe, 2006). The aforementioned forward masking experiments in auditory nerve fibers fit transient responses with a double model of exponential decay, with fast decay time constants near 10 ms and slow decay time constants near 100 ms. Fast and slow components are also evident in the inferior colliculus on longer time scales, with the fast components on the order of hundreds of milliseconds and the slow components on the order of seconds (Dean et al., 2008). A distribution of time constants allowing for suppression or facilitation of complex masker-probe type stimuli in auditory cortex range from hundreds of milliseconds to several seconds (Bartlett & Wang, 2005).

Previously (Chapters 4 and 5) we have presented evidence that nonmonotonic neurons may preferentially encode low sound levels under silence-adapted and level-adapted conditions. Based on these findings, we hypothesized that nonmonotonic neurons may adapt more quickly to a high-to-low mean level transition relative to a low-to-high mean level transition. Monotonic neurons, on the other hand, are likely to be consistent with previous studies showing faster adaptation to the low-to-high mean level transition. Here we present evidence demonstrating differences in the time course of adaptation between monotonic and nonmonotonic neurons.

6.2 Results

As an initial measure of the time course of neuronal adaptation in response to dynamic stimuli, the mean rate-level functions of monotonic and nonmonotonic neurons were plotted as a function of both the current and preceding time interval using the same population of neuronal responses presented in Chapter 5. Only adaptation responses to the uniformly distributed dynamic stimulus (see Section 2.3.2) were utilized for these initial studies, so that the effects of adaptation to high probability sound levels were not encountered. For monotonic neurons (Figure 6.1A,B), greater sound levels in the preceding time interval generally elicited higher response thresholds in the succeeding time interval. In other words, monotonic rate-level curves shifted to the right by an amount proportional to level of the preceding time interval. A qualitative comparison of single rate-level functions collected at three different preceding levels (Figure 6.1B) with

the overall average adaptation for monotonic neurons (see Chapter 5, Figure 5.3A), reveals that much of the adaptation apparent in the population average over the entire dynamic stimulus duration is already apparent after a single 100 ms time interval.

In contrast, second-order rate-level profiles for nonmonotonic neurons (Figure 6.1C,D) demonstrated a relatively consistent threshold regardless which level preceded the current time interval. Thresholds shifted slightly, but by an amount much less than monotonic neurons, up to a preceding sound level of about 50 dB SPL, at which point thresholds remained relatively constant. When the preceding tone was quite intense, the threshold average threshold remained near 20 dB SPL, possibly shifting back to lower thresholds in response to the highest preceding level. This trend allows nonmonotonic neurons to maintain most of their silence-adapted sensitivity, consistent with our findings in Chapter 5. Again by qualitatively comparing the amount of adaptation after a single 100 ms preceding level (Figure 6.1D) with that occurring over the duration of the dynamic stimulus (Figure 5.3C), much of the adaptation is already apparent. The trend of upper dynamic ranges capturing the adaptation at higher sound levels (see Chapter 5) is not entirely clear with this plot, possibly indicating that this effect is occurring on a slower time scale.

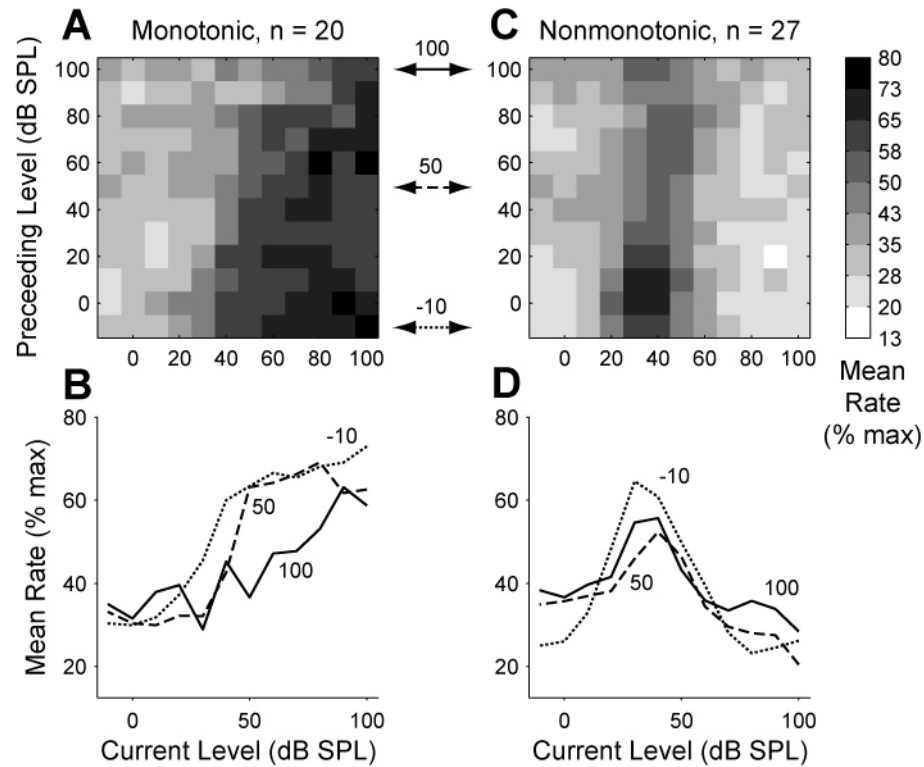


Figure 6.1 Influence of preceding stimulus sound levels on spiking rates. **A–B**, As level of an immediately-preceding tone increases, the mean monotonic rate-level function shifts toward higher thresholds. **C–D**, The mean threshold of nonmonotonic rate-level functions shifts to higher thresholds until a preceding level of about 50 dB SPL and then the lower dynamic range remains at lower thresholds. All plots demonstrate that a large amount of the overall adaptation response (see Figure 5.3) is already evident after only a single 100 ms preceding sound level.

Evidence presented previously (see Chapters 4 and 5) indicates that nonmonotonic neurons are able to remain sensitive to low-intensity sounds and therefore likely to be specialized encoders of low sound levels. Under the assumption that nonmonotonic neurons do preferentially encode low level sounds, we hypothesized that nonmonotonic neurons would also be more likely to adapt more slowly on average from low to high-intensity sounds but more quickly on average from high to low-intensity sounds when compared to monotonic neurons. This adaptive behavior would complement nonmonotonic neurons' steady-state low-level sensitivity at shorter time scales when the dynamics of the adaptation become important. Because of the generally low spiking rates and high response variability in cortex, we were unable to extract time constants of adaptation from the original adaptation paradigm as discussed in Chapter 5. Instead, we created a modified protocol that had a design similar to the previous one, but only contained transitions from a low level probability plateau to a higher level plateau, both 20 dB in width and with zero probability of a level outside the plateau (see Section 2.4.1).

6.2.1 Dynamic-Transition Stimuli

We recorded the responses of 97 primary auditory cortex neurons from 3 hemispheres of 3 awake marmoset monkeys (*Callithrix jacchus*) for their adaptive coding properties in response to a modified design of the dynamic level stimuli. Each modified stimulus, termed a dynamic-transition stimulus, focused solely on transitions between relatively

low and relatively high sound intensity levels (see Section 2.4.1). Sound levels during these periods were determined by non-overlapping 20-dB wide uniform probability distributions referred to as the high-level and low-level plateaus. The location of the plateaus was individualized for each neuron online by first measuring a rate-level function in response to the uniformly distributed dynamic stimulus (see Section 2.3.2). The low-level plateau was placed above threshold along the lower dynamic range for a neuron of any monotonicity. The high-level plateau was placed at the highest sound levels (centered at 65 dB SPL) for neurons that showed mostly monotonic rate-level functions and just below the saturation of the upper dynamic range for neurons that showed mostly nonmonotonic rate-level functions (see Section 2.4.1). For 11 / 97 neurons for which a rate-level response to the uniformly-distributed dynamic stimulus was not measured, the static rate-level response was used to estimate these points instead.

6.2.2 Adaptation Time Course in Single Neurons

For each neuron we calculated its mean rate-level response in 2 dB bins and in 1-second time windows subsequent to each transition type of the dynamic-transition stimuli (see Section 2.4.2). Transitions were either from high sound levels to low sound levels, eliciting the high-to-low transition response (or, equivalently, the response to the low-level plateau), or from low sound levels to high sound levels, eliciting the low-to-high transition response (or, equivalently, the response to the high-level plateau). Mean-rate

responses (averaged over all sound levels) were also calculated using the same time windows. The time sequence of rate-level functions was normalized separately for each plateau and fit with a two-dimensional adapting sigmoid function having four free parameters and whose mean was given by a single exponential decay function (see Section 2.4.2). We chose this method because a large degree of response variability made comparisons between rate-level functions from each time window difficult. The adaptation of mean rate was normalized using the range of discharge rates over both plateaus and fit with a single exponential decay function having three free parameters (see Figure 6.2B, for example).

Example neurons are shown in Figures 6.2 and 6.3. Each example has two gray-scale images that capture the time sequence of neuronal rate-level functions in response to the high-to-low transition (e.g., Figure 6.2A) and the low-to-high transition (e.g., Figure 6.2B). Model fits are displayed as contour overlays on the images where the black line represents 20% of maximum and the white line 50% of maximum. Mean-rate responses are also shown, along with their respective model fits for both transition types (e.g., Figure 6.2C,D). For each neuron, the static rate-level function—collected with single 100 ms tone bursts surrounded by silence (see Section 2.2.2)—and the dynamic rate-level function corresponding to the uniformly distributed dynamic stimulus (see Section 2.3.1) are displayed for a sense of where the transition plateaus were located relative to the full rate-level functions and also in order to compare monotonicity in these two different adapted conditions. Static rate-level functions were fitted with a six-parameter

split Gaussian model in the same manner as in Chapters 4 and 5 (see Section 2.2.3) in order to obtain a monotonicity index (MI).

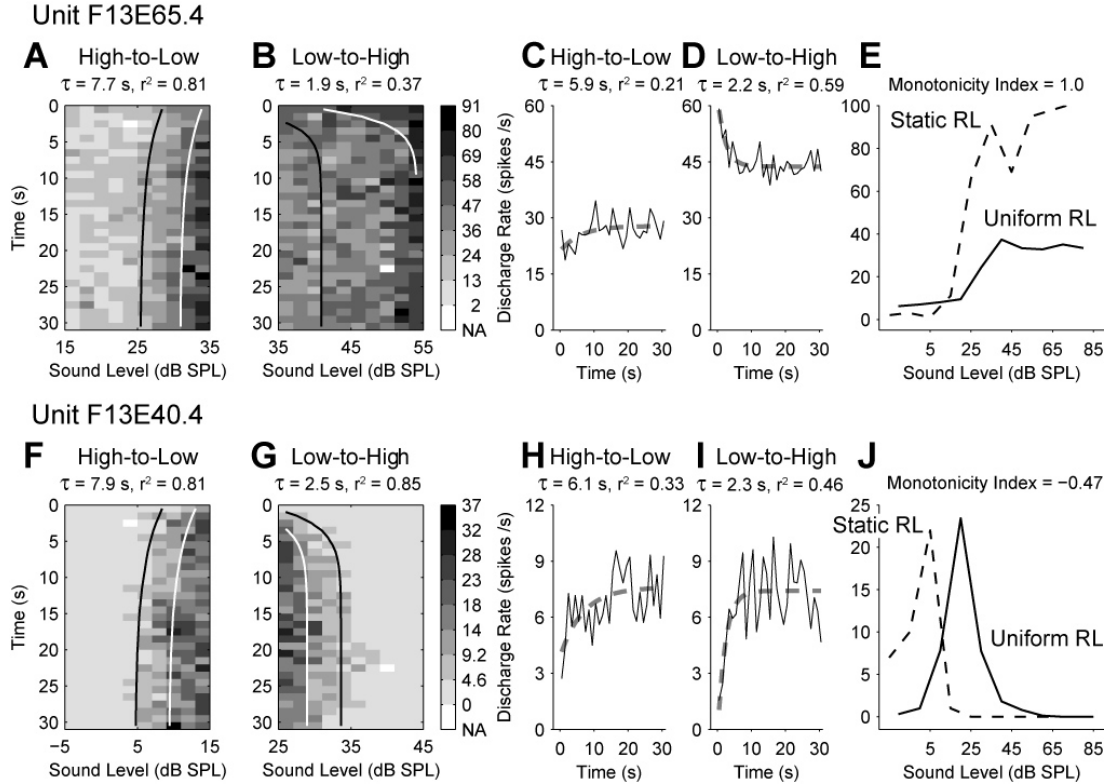


Figure 6.2 Example neurons with responses to the dynamic-transition stimuli that would be expected given their static rate-level functions. A neuron with a highly monotonic static rate-level function shows increasing rate-level functions after the high-to-low transition (**A**) and also after the low-to-high transition (**B**). These grayscale image plots show rate-level functions during 1-second time windows subsequent to each transition and are overlaid with the 20% (black line) and 50% (white line) contours of the two-dimensional adapting sigmoid function fitted to the rate-level data. Goodness-of-fit values (r^2) and fitted time constants (τ) are labeled for each transition. For this neuron, the time course of the mean-rate adaptation increases for the high-to-low transition (**C**) and decreases for the low-to-high transition (**D**). Mean-rate adaptation was fitted with a single exponential decay function for which goodness-of-fit (r^2) and

fitted time constants (τ) are given for each transition. The increasing rate-level profiles in response to the low-to-high transition in A are what would be expected from a neuron with a static rate-level (**E**) monotonicity index (MI) of 1.0. **F–J**, The same plots are shown for a neuron that is inhibited below spontaneous rate at the highest sound levels in its static rate-level profile and consequently shows decreasing rate-level functions for the high-to-low transition.

A variety of response types to the dynamic-transition stimuli were recorded, regardless of the monotonicity of the respective neuron's static rate-level function (as measured with the monotonicity index (MI), see Section 2.2.3). For example, some neurons that had very monotonic static rate-levels showed increasing rate level functions in response to both low and high-level plateaus (Figure 6.2A–E). Some neurons with very nonmonotonic static rate-levels showed increasing rate-level responses to the low plateau and decreasing rate-level responses to the high plateau (Figure 6.2F–J). These responses are what would be expected based on the monotonicity of the static rate-level function and on the placement of the plateau centers. On the other hand, a few monotonic neurons showed decreasing (Figure 6.3A,B) and a few nonmonotonic neurons showed increasing (Figure 6.3F,G) responses after the low-to-high transition. These responses are the opposite of what would be expected based on their respective MIs. These examples outline two major response categories—neurons with increasing rate-level functions or neurons with a decreasing rate-level functions—that can be applied to either transition type (either high-to-low or low-to-high transition).

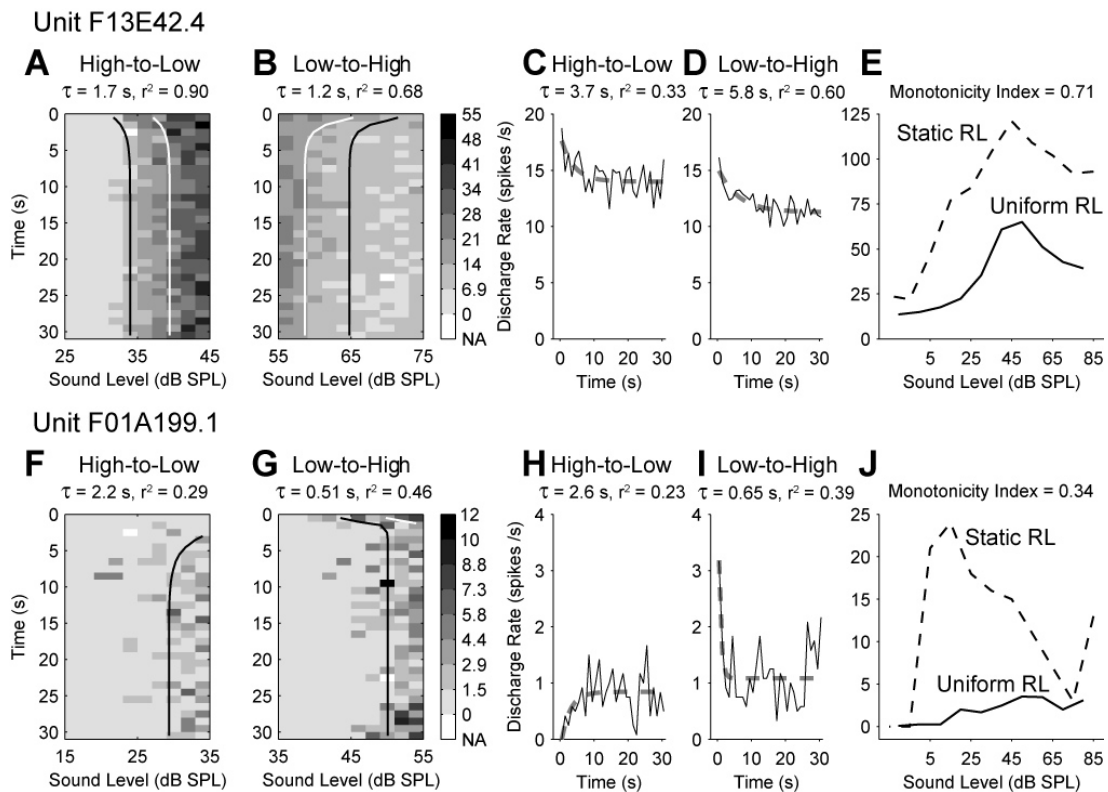


Figure 6.3 Example neurons with responses to the dynamic-transition stimuli that would not be expected given their static rate-level functions. Plots are the same as described in the legend for Figure 6.2. **A–E**, Profile of a neuron that has a static rate-level monotonicity index (MI) of 0.71, indicating that it is partially suppressed at the highest sound levels but does not meet the defined classification of 0.5 for a fully nonmonotonic neurons (see Chapter 4). This neuron adapts to dynamic-transition stimuli with decreasing rate-level functions for the high plateau. **F–J**, The same plots are shown for a neuron that is suppressed to a rate that is approximately 50% below the max rate at the highest sound level in its static rate-level profile but still shows increasing rate-level functions for the high-to-low transition.

6.2.3 Population Rate-Level Adaptation to Dynamic-Transition Stimuli

The neuronal responses to dynamic-transition stimuli in this dataset were highly variable in time and many transition responses were either completely suppressed or completely saturated. For this reason, the time course of rate-level adaptation after a transition for many neurons did not fit well to our two dimensional adapting sigmoid model. Typically this occurred for one of three reasons: (1) The neuron showed almost zero driven rate in response to one of the plateaus (usually the high-level plateau). (2) The neuron showed a nonmonotonic response profile within the plateau. This type of adaptation was not systematic across the population, so we were unable to characterize a model that would ascribe time constants to these transitions. (3) The neuron showed a very flat driven rate within the plateau, indicating that, despite being driven by levels within the plateau, it was doing a very poor job of encoding these levels. A total of 64 / 97 high-to-low transitions and 51 / 97 low-to-high transitions were well-fit by the model. This outcome was determined by a criterion of 25% variance accounted for by the model, which was established empirically by qualitatively assessing the model fits.

Although the possible directions of rate-level functions, either increasing or decreasing, in response to the two transition types—high-to-low and low-to-high—were distributed across the range of monotonicity indices (MIs) as measured in the static rate-level functions, most of the neurons with static MIs below 0.5 had decreasing rate-levels in

response to the high-level plateau (Figure 6.4). Also, of the neurons with static MIs greater than 0.9, the majority revealed increasing rate-levels in response to the high plateau. Finally, only 3 / 64 neurons demonstrated decreasing rate-level functions in response to the low-level plateau.

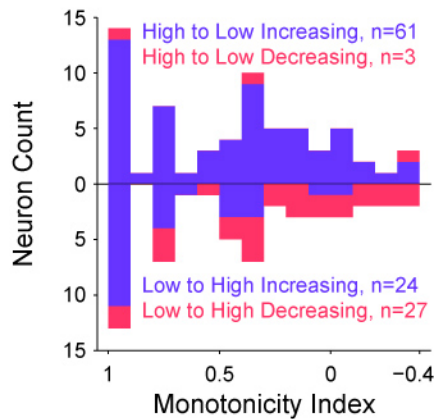


Figure 6.4 Distribution of static rate-level monotonicity indices (MIs) for transitions from each neuron in the dataset that were well fit by a two-dimensional adapting sigmoid model. Neurons were not required to have both transitions well fit in order to be included in this analysis. For the total of 97 neurons, 64 had well fit high-to-low transitions (top distribution) and 51 had well fit low-to-high transitions (bottom distribution). For each transition type, the direction of the model fit, either increasing (blue) or decreasing (red) is indicated. The majority of neurons with nonmonotonic static rate-levels ($MI \leq 0.5$) had decreasing responses to the high-level plateau. The majority of neurons with $MI \geq 0.9$ had increasing responses to the high-level plateau. Only a small number of neurons demonstrated decreasing responses to the low level plateau.

Of the populations of transitions with rate-level functions well fit by the two-dimensional adapting sigmoid, neurons that had fitted time constants outside of the range that could be reasonably measured with the current analysis (less than 0.5 seconds or greater than 30 seconds) were excluded. Neurons with time constants outside of an acceptable range most likely were in one of four categories: (1) The neuron adapted its rate-level function faster than could be measured using 1-second time windows. (2) The neuron's time course of adaptation was slower than can be measured with the approximately 30 second plateau duration. (3) The neuron did not adapt. (4) Any adaptation trends were not discernable because of a very large amount of overall response variability. After these exclusions, the remaining transitions (considered separately for each neuron) were considered to have a monotonic and robustly-adapting rate-level profile. A total of 46 / 64 high-to-low transition responses and 37 / 51 low-to-high transition responses met this combination of criteria. The remaining transitions were further characterized depending on the direction of adaptation of the rate-level functions. For some transitions, the adaptation caused the thresholds of the rate-level functions to decay towards higher sound levels and for some to decay towards lower sound levels. These categories are referred to as "up" or "down" respectively. These additional possibilities created a total of eight response categories, which are the combinations of the stimulus transition type (high-to-low or low-to-high), the orientation of the rate-level functions (monotonically increasing or monotonically decreasing) and the direction of the adaptation (decaying toward higher sound levels or

decaying toward lower sound levels). The time constants and counts of neurons in each category are presented in Figure 6.5.

The population of responses to level transitions demonstrated a highly significant correlation between the estimated time constants of rate-level adaptation and mean-rate adaptation ($r^2 = 0.67$; $p = 0$, regression F test, Figure 6.5A). The distributions of rate-level adaptation time constants (Figure 6.5B) for the high-to-low (median = 3.2 ms, interquartile range = 4.3 ms) and for the low-to-high (median = 4.4 ms, interquartile range = 6.3 ms) transitions were not significantly different ($p = 0.53$, Wilcoxon rank sum test). The distributions of mean-rate adaptation time constants (Figure 6.5C) for the high-to-low (median = 3.9 ms, interquartile range = 4.7 ms) and for the low-to-high (median = 4.1 ms, interquartile range = 6.1 ms) transitions were also not significantly different ($p = 0.96$, Wilcoxon rank sum test). Our conclusions from this first analysis do not reveal the same time constant asymmetry for mean level adaptation. The lack of asymmetry from this analysis is the same as results reported in songbirds (Nagel & Doupe, 2006), but contrary to subcortical (Dean et al., 2008) and auditory nerve fiber (Chimento & Schreiner, 1990, 1991) results in mammals. The high correlation between level and rate adaptation time constants, is however consistent with the subcortical study, and provides evidence that rate regulation may be involved in the mechanism of adaptation to sound level for dynamic stimuli. The data reported here do not reveal an easy dividing point that would indicate for two unique time scales of adaptation, but

instead reveal a continuum of time constants in the range from a few hundred milliseconds up to tens of seconds.

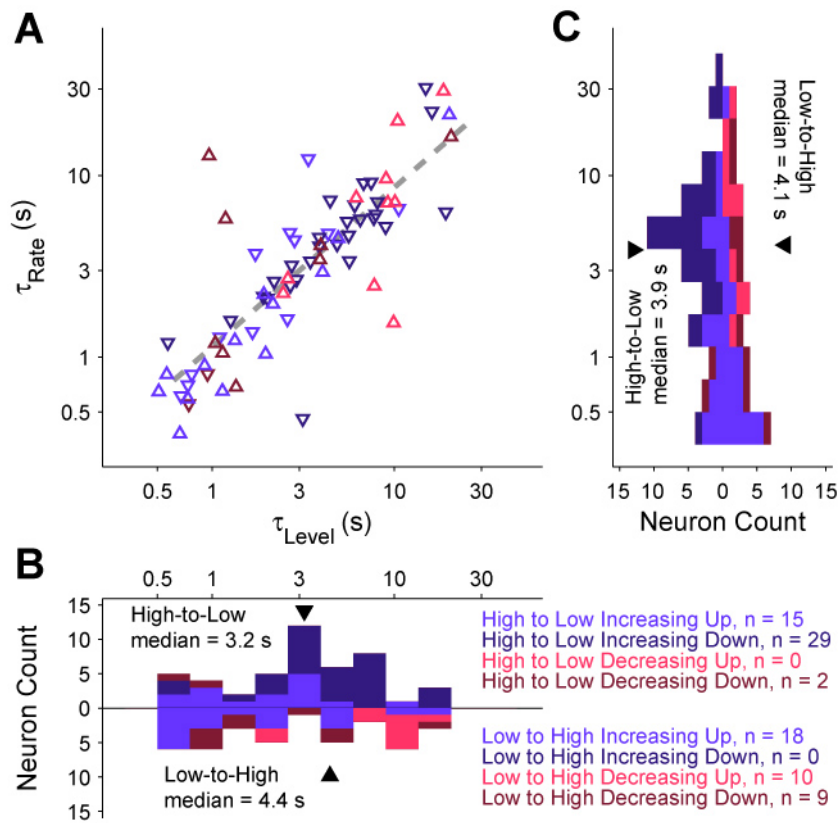


Figure 6.5 Comparison of rate-level and mean-rate adaptation time constants, divided into four categories describing the shape of the neuronal rate-level functions in response to either the high-to-low or low-to-high dynamic level transitions. **A**, Time constants estimated from the time course of adaptation for the rate-level functions and those from that of the mean-rate are strongly correlated ($r^2 = 0.67$; $p = 0$, regression F test). **B**, Distributions of rate-level adaptation time constants are not significantly different between the high-to-low and low-to-high transitions ($p = 0.53$, Wilcoxon rank sum test). **C**, The same is true for the distributions of time constants for the mean-rate adaptation ($p = 0.96$, Wilcoxon rank sum test).

For each of the six out of eight categories that were represented by at least one transition response in our dataset, we calculated mean rate-level and mean-rate responses for both the raw data and for the fitted models (Figures 6.6 and 6.7). Averages calculated in this manner displayed the effects of adaptation for rate-level responses for which we could measure an adaptive response. The categorization of neurons into subpopulations based upon both the direction of the rate-level function and the direction of the adaptive decay prevented adaptation effects in opposing directions from averaging each other out. In general, for the high-to-low transition, neurons that adapted down (Figure 6.6A) were slower than those that adapted up (Figure 6.6B). For the low-to-high transitions, neurons with increasing rate-level functions were generally fastest at adapting to high-level plateaus (Figure 6.7A). In general, of the neurons with decreasing rate-level functions, those that adapted down (Figure 6.7B) were faster than those that adapted up (Figure 6.7C). Also note that the average of the model fits converges quite well with the average of the neuronal responses, meaning that our particular choice of analysis likely did not lead to a bias in the estimation of time constants.

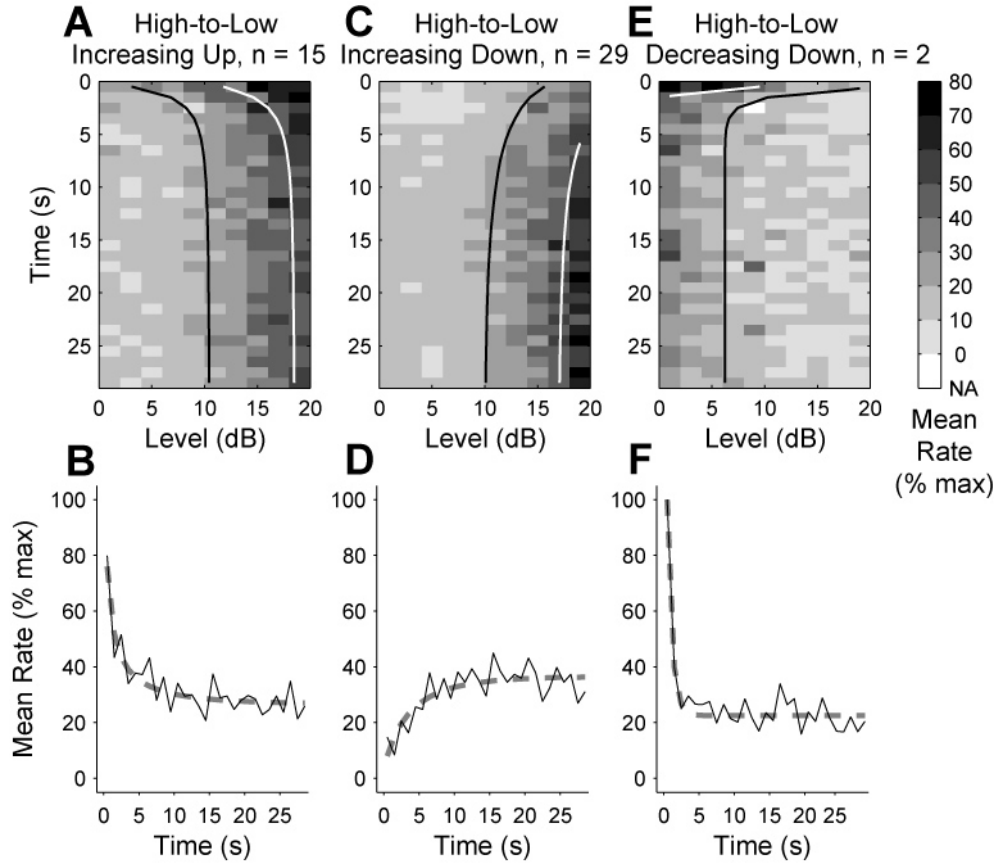


Figure 6.6 Mean rate-level and mean-rate responses for the different categories of the high-to-low transients given in Figure 6.5. Only neurons that have robustly adapting responses for the low-level plateau are included. Mean rate-level (**A**) and mean mean-rate (**B**) for 15 neurons with increasing responses that decay to higher sound levels (up). Mean rate-level (**C**) and mean mean-rate (**D**) for 29 neurons with increasing responses that decay to lower sound levels (down). Mean rate-level (**E**) and mean mean-rate (**F**) for 2 neurons with decreasing responses that decay to lower sound levels (down). We did not record any neurons with decreasing responses to the low-level plateau that decayed to higher sound levels.

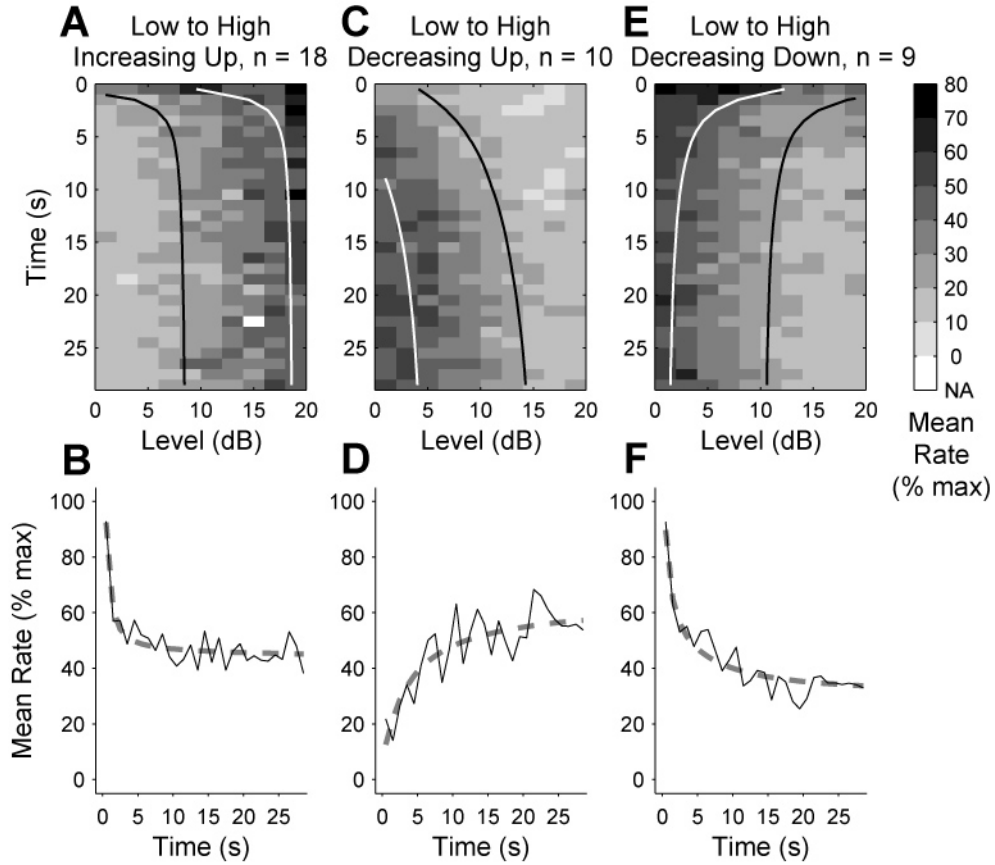


Figure 6.7 Mean rate-level and mean-rate responses for neurons represented in Figure 6.5 that have robustly adapting responses for the high-level plateau. Mean rate-level (**A**) and mean mean-rate (**B**) for 18 neurons with increasing responses that decay to higher sound levels (up). Mean rate-level (**C**) and mean mean-rate (**D**) for 10 neurons with increasing responses that decay to higher sound levels (up). Mean rate-level (**E**) and mean mean-rate (**F**) for 9 neurons with decreasing responses that decay to lower sound levels (down). We did not record any neurons with increasing responses to the high-level plateau that decayed to lower sound levels.

In the interest of comparing how adaptation between levels occurred within the same neuron, we pruned the dataset further so that only neurons that met the criteria previously discussed for both transition types were included. These conditions were met for 20 / 97 neurons in the dataset. Our rationale for only looking at this subset of neurons is that we are interested in potential asymmetries in adaptation dynamics for single neurons. Without comparisons within the same neuron, it is otherwise difficult to compare the high-to-low and low-to-high transitions by simply evaluating distributions across neurons collectively encompassing a large range of time constants (about two orders of magnitude). Of the remaining neurons, 10 showed increasing rate-level functions in response to the low-to-high transition, all of which also showed increasing rate-level functions that decayed down in response to the high-to-low transition. The other 10 neurons showed decreasing rate-level functions in response to the low-to-high transition; 5 of these decayed down and 5 decayed up. For these neurons, the response to the high-to-low transition was mixed amongst all possibilities (except for decreasing up, which was not present in the dataset at all, see Figure 6.5).

Because there were seven total possibilities of combinations between transition categories in our dataset (see above) and because of the small number of remaining neurons with robustly adapting responses to both transitions, the remaining neurons were categorized only based upon whether the response to the low-to-high transition was increasing or decreasing (10 each in these categories). In the context of the dynamic-transition stimuli, we considered the increasing responses to be the analogs of

monotonic neurons and the decreasing responses to be the analogs of nonmonotonic neurons, even though the monotonicity index from static rate-level responses was not entirely indicative of these dynamic-transition categories (Figure 6.4). These dynamically nonmonotonic neurons (red, Figure 6.8A) were in general separable from dynamically monotonic neurons (blue, Figure 6.8A) based on adaptation time constants for the two transitions. The approximate line separating the two populations was found empirically and was given by:

$$\tau_{High-to-Low} = 2\tau_{Low-to-High}^2, \quad (6.1)$$

which is a line with slope of 2 on the log-log plot (dotted line, Figure 6.8A). In other words, dynamically monotonic neurons are typically faster at adapting to the low-to-high transition. Dynamically nonmonotonic neurons, on the other hand, are not necessarily faster at adapting to the high-to-low transition, but on average do not show the same disparity in the time constant transition speed as do dynamically monotonic neurons.

Based on theoretical principles of optimal gain control, one would expect that if a neuron were acting as an optimal estimator of variance transitions, it would adapt twice as fast to the low-to-high transition compared to the high-to-low transition (DeWeese & Zador, 1998). On the other hand, if a neuron were acting as an optimal estimator of mean transitions, one would not expect asymmetric time constants for the two transition types. However, such asymmetries are actually observed experimentally

(Chimento & Schreiner, 1990, 1991; Dean et al., 2008). The dotted line in Figure 6.8A (Equation 6.1) empirically divides the categories well, although the significance is uncertain. Our finding represents evidence supporting the hypothesis that dynamically nonmonotonic neurons are specialized for high-to-low transients in dynamic-level stimuli. This function would likely work in conjunction with their sensitivity to lower levels based on their non-adapted responses (Chapter 3) and their steady-state-adapted responses (Chapter 4).

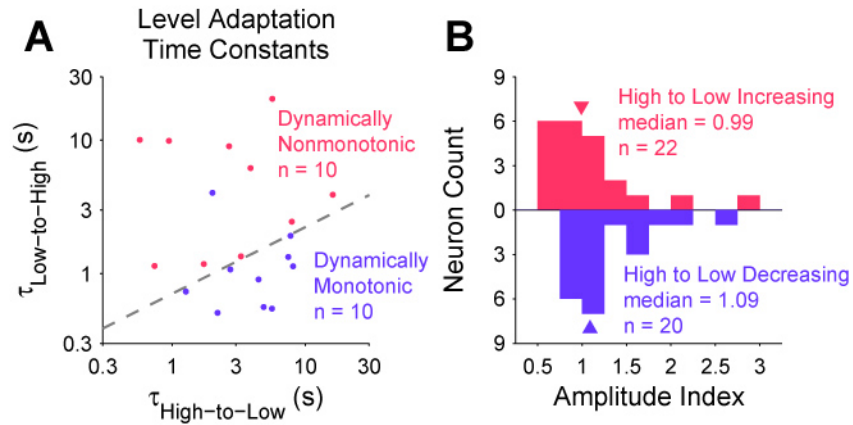


Figure 6.8 **A**, Comparison of estimated rate-level adaptation time constants for neurons that have monotonic and robustly adapting rate-level functions for both transitions. Most dynamically monotonic neurons (blue), those with increasing rate-level functions in response to the high-level plateau, are clustered apart from most dynamically nonmonotonic neurons (red), those with decreasing rate-level functions in response to the high-level plateau. The dotted line (well below the diagonal representing equal time constants) is able to separate most of the two populations. **B**, Amplitude index distributions for the same categories demonstrate that the role of changes in gain—part of the adaptive response to higher level sounds—is slightly greater for dynamically nonmonotonic neurons than for dynamically monotonic neurons, but is not significant ($p = 0.068$, Wilcoxon rank sum test). Both distributions have medians near 1, indicating that in general gain adaptation to dynamic-transition stimuli was small.

The method of estimating time constants by using a two-dimensional adaptive sigmoid model fit was unable to differentiate between the effects of gain changes (scaling of the maximum response rate) and dynamic range shifting (shifting of rate-level curves along the abscissa). Additionally, the dynamic-transition stimuli themselves may not be able to differentiate these effects because the entire dynamic range of each neuron was not collected in order to counter the high variance of the neuronal responses encountered by presenting more repetitions of fewer stimuli. To obtain an estimate of the gain adaptation effect, we calculated an amplitude index (AI)—the maximum response to the high-level plateau divided by the maximum response to the low-level plateau (see Section 2.4.2). This metric was calculated for all neurons whose responses were well fit to the two-dimensional adaptive sigmoid model, regardless of the fitted time constants. Only well-fit neurons were included so that dynamically monotonic and dynamically nonmonotonic neurons could be compared. The median AI was slightly greater for dynamically monotonic neurons (median = 1.1) than for dynamically nonmonotonic neurons (median = 0.99), but this difference was not significant ($p = 0.068$, Wilcoxon rank sum test). Gain adaptation in steady-state dynamic responses typically resulted in a reduction in overall rates for higher sound level plateaus, except for nonmonotonic neurons for which the overall rates typically increased at the highest sound levels (see Figure 5.4B). Given this, a majority of AI values below one would be expected, which was true for some neurons, particularly for dynamically nonmonotonic neurons. However, since both AI medians were near one and not significantly different, in

general the effect of gain adaptation for dynamic-transition stimuli appeared to be rather small.

6.2.4 Population Mean-Rate Adaptation to Dynamic-Transition Stimuli

Although the high response variance of our dataset did not allow analysis of rate-level adaptation time constants smaller than about 500 ms (half of the original analysis time window width), we were able to use smaller time windows to estimate mean-rate adaptation time constants. Time constants measured with a 1-second window size and with a 400-ms window size were compared directly. Both techniques have an upper bound for time constants that can be reasonably estimated of 30 seconds, the approximate duration between transitions. We chose a reasonable lower bound on the estimate to be half the window size since this value represents a neuron whose discharge rate has decayed to approximately 13% of its original value within one time window, and values smaller than this are typically within the steady-state response variance. Four clusters of points in the scatter plot between time constants measured with the two different window sizes (Figure 6.9A, cluster numbers in the same order as presented here) were identified: (1) Points along the unity line from about 0.5 seconds to about 30 seconds that have quite similar time constants when measured with either window size. (2) Points that have reasonable time constants when using the 400-ms windows but with values below 0.2 seconds when using the 1-second windows. These cases represent

transitions with one or two outlying mean-rates in time that heavily influence the mean-rate and cause a poor fit using the 1-second windows. (3) Points that have reasonable values when using 1-second windows, but values below 200 ms when using the 400-ms windows. In these cases the noise is over-fitted when using the smaller window size. (4) A small number of points that have reasonable time constant values when measured with either method, but are on the order of a few seconds when using the 1-second windows and on the order of several hundred milliseconds when using the 400-ms windows. These neurons often clearly exhibited two time scales of adaptation when the fits were observed directly. We chose not to utilize time window sizes below 400-ms because the effect of over-fitting short term noise or neuronal variability (cluster 3, described above) became obviously and dramatically worse. Such analysis would have caused many neurons with valid adapting mean-rate time courses to be excluded.

Distributions of time constants and steady-state normalized mean-rates were compiled for mean-rates that were fit using the 1-second window size (Figure 6.9B,C) and using the 400-ms window size (Figure 6.9D,E). Only transition responses with reasonable time constants were included (half the window size up to 30 s). Counts of transitions included for each category are given in Figure 6.9. Because by using the 400-ms window size we were able to better estimate time constants for neurons that adapted quickly, a stronger asymmetry between the responses to the two transition types was revealed. When using the 1-second windows, there was not a significant difference between the high-to-low and low-to-high time constant medians ($p = 0.26$, Wilcoxon rank sum test,

Figure 6.9B) nor for the steady-state mean-rate medians ($p = 0.18$, Wilcoxon rank sum test, Figure 6.9C). This is the same result that was revealed by the time constant analysis in Figure 6.5C. When using the 400-ms windows, however, there was a significant difference between the distributions of time constants for the high-to-low and low-to-high transition responses ($p = 0.020$, Wilcoxon rank sum test, Figure 6.9D). The distributions of steady-state mean-rates demonstrated a greater asymmetry than with the 1-second time windows, but the difference did not reach significance ($p = 0.083$, Wilcoxon rank sum test, Figure 6.9E). Thus, with smaller time windows that can more accurately measure the shorter time constants, our dataset reveals a similar time constant asymmetry as has been reported subcortically (Dean et al., 2008).

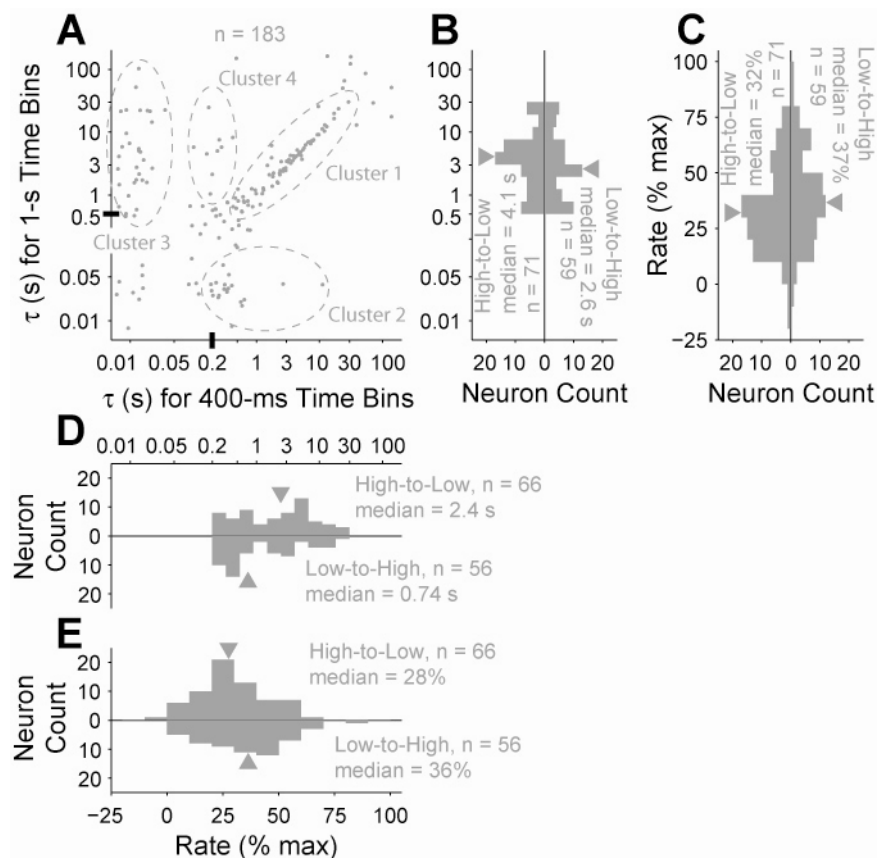


Figure 6.9 **A**, Comparison of mean-rate adaptation time constants estimated using 1-second and 400-ms time windows. Points along the diagonal (Cluster 1) represent similar estimates with either window which occur mostly in the range from about 0.5 – 30 seconds, the range we chose for estimating time constants of rate-level adaptation using the 1-second window size. Points near the bottom (Cluster 2) represent transitions with outlying low responses that cause poor fits with the larger window size. Points along the left (Cluster 3) represent transitions that are over-fitted by the smaller window size. A few transitions (Cluster 4) qualitatively appear to genuinely contain two time scales of adaptation. Distribution of time constants using the 400-ms window size (**B**) show a greater number of small rate constants particularly for the low-to-high

transitions than the same distribution using the 1-second window size (**D**). Most of the general distribution shape remains the same using both sizes. Distributions of steady-state rate from the exponential fits for the 400-ms window size (**C**) show a better disparity between the transition types than those for the 1-second window size (**E**).

The results presented in Figure 6.8A regarding the separability of rate-level adaptation time constants for the two transition types were complemented with the same analysis using with mean-rate adaptation time constants. We compiled another set that included all neurons for which we could reasonably measure mean-rate adaptation time constants using 400-ms time windows for both transition types which included 36 / 97 neurons. Here we again redefined the classes of monotonic and nonmonotonic based on the direction of rate decay in response to the low-to-high transition. In response to this transition, the neurons that decayed to lower mean-rates were classified as mean-dynamically monotonic neurons while those that decayed to higher mean-rates were classified as mean-dynamically nonmonotonic neurons. Again, these categories are not the same as the analogous ones defined with static rate-level functions (see Figure 6.4).

By and large, mean-dynamically nonmonotonic neurons were faster at adapting to the high-to-low transition than to the low-to-high transition (Figure 6.10A). The opposite was true of mean-dynamically monotonic neurons. This trend is consistent with that of the rate-level adaptation (Figure 6.8A) evaluated using a slightly larger dataset, but in this case the categories were approximately separable along a line of equal time constants for the two transition types (dotted line, Figure 6.10A). For the low-to-high transition (Figure 6.10B) the mean-dynamically nonmonotonic median time constant was significantly greater than the mean-dynamically monotonic median ($p = 0.0013$, Wilcoxon rank sum test), and for the high-to-low transition (Figure 6.10D) it was less, but not significantly so ($p = 0.15$, Wilcoxon rank sum test). The opposite trend was true

of the steady-state rates. For the low-to-high transition the mean-dynamically monotonic distribution of steady-state rates was less than the mean-dynamically nonmonotonic distribution (Figure 6.10C) but the difference was not significant ($p = 0.19$, Wilcoxon rank sum test), while the same comparison was significant for the high-to-low transition ($p = 0.018$, Wilcoxon rank sum test, Figure 6.10E).

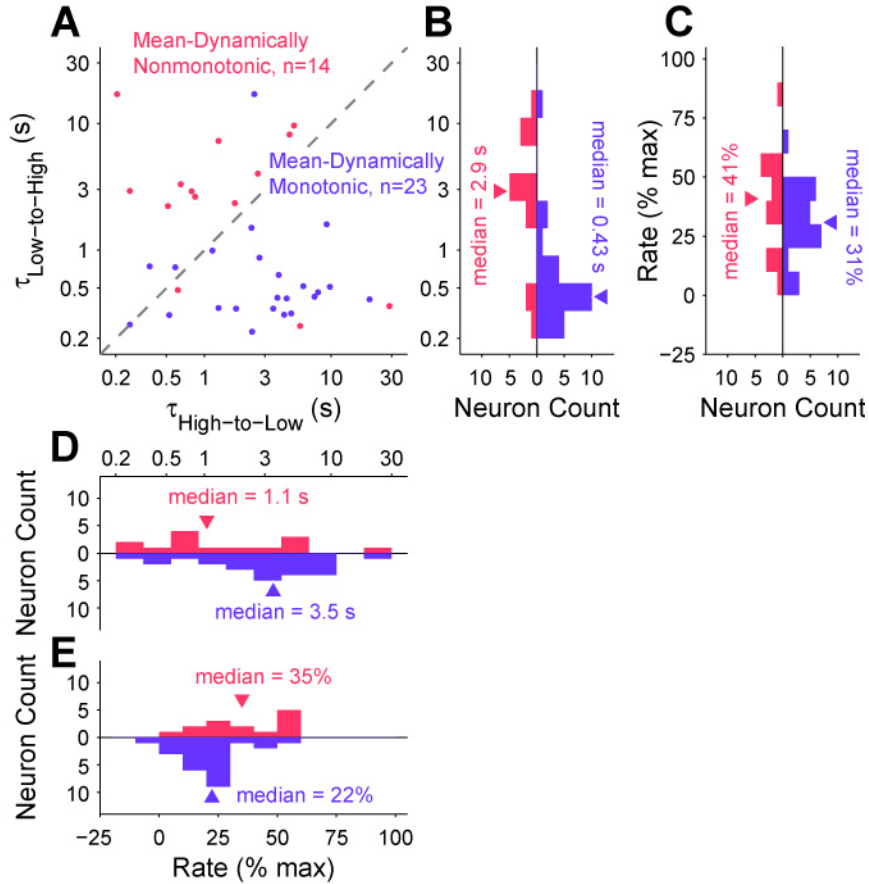


Figure 6.10 A, Comparison of estimated mean-rate adaptation time constants for mean-dynamically monotonic (blue) and mean-dynamically nonmonotonic (red) neurons. In general, mean-dynamically monotonic neurons are faster in response to the low-to-high transition while mean-dynamically nonmonotonic neurons are faster in response to the high-to-low transition, since the populations are approximately separable along a line of equal time constants (dotted line). The distribution of time constants for the low-to-high transition is significantly less for mean-dynamic monotonic neurons than for mean-dynamic nonmonotonic neurons (**B**, $p = 0.0013$, Wilcoxon rank sum test). The median time constant of mean-dynamic nonmonotonic neurons for the high-to-low transition is less than that of mean-dynamic monotonic

neurons, but the difference is not significant (**D**, $p = 0.15$, Wilcoxon rank sum test). Distributions of steady-state rates have relatively similar medians between the two populations for both transitions (**C**, **E**); however, there is a significant difference for the high-to-low transition ($p = 0.018$, Wilcoxon rank sum test).

6.3 Discussion

Time constants of adaptation to sound level in the auditory systems have been explored using forward-masking and dynamic-level paradigms (see Section 6.1). Some studies have reported asymmetric adaptation to mean sound level with neurons on average adapting faster from a high mean to a low mean than vice versa (Chimento & Schreiner, 1990, 1991; Dean et al., 2005). For neurons recorded in this study we find evidence that:

- (1) Nonmonotonic neurons adapt mean-rate more quickly in response to the high-to-low transitions as compared with responses to the low-to-high transitions. Monotonic neurons, on the other hand, show the opposite trend—an asymmetry which is consistent with previous studies. This difference between monotonic and nonmonotonic neurons is apparent for rate-level time constants as well, but a good portion of nonmonotonic neurons also adapt more quickly in response to the low-to-high transition than in response to the high-to-low transition. However, this disparity between the two rates of adaptation is less than that seen in monotonic neurons.
- (2) The estimated time constants of rate-level and mean-rate adaptation are highly correlated.
- (3) A large variety of different transient responses to high-to-low and low-to-high dynamic transitions exist that are related to but not entirely predicted by the monotonicity of the static-rate level function (that measured with tones presented in periods of silence).
- (4) Neurons that have increasing rate-level functions in response to high dynamic levels (dynamic monotonic neurons) also always had increasing rate-level

functions that decayed to lower sound levels in response to the high-to-low mean level transition.

Of the analyses performed on neurons' responses to the dynamic-transition stimuli, several of them excluded a large number of neurons. We encountered a large number of neurons that despite having robust tonal responses, either did not respond well or were completely saturated in response to one or both plateaus of the respective dynamic-transition stimulus. In the effort of estimating adaptation time constants, we did not want to include neurons that did not show clear rate-level or steady-state mean-rate responses. Because most of the neurons in our dataset revealed monotonic rate-level functions over the 20-dB range of the plateaus, an adapting-sigmoid model was used for fitting to the data. Our final model choice was based on qualitative assessment of fits and overall goodness of fit values. For the minority of neurons that did not show monotonic rate-level responses in response to one or both plateaus, we were not able to even visually discern any time course of adaptation. Finally, many neurons that did show monotonic rate-level functions over one or both plateaus still did not show a visually discernable adaptation response based on the 1-second time windows. These neurons were eventually also excluded for the final level of analysis because we did not want to report time constants that were not reflective of real trends in the data. The choice of 1-second time windows for the rate-level functions and minimum 400-ms time windows for the mean-rate was so that time constants were not misestimated due to model overfitting of the data. Neuronal variance on short time scales can easily obscure adaptation

trends that are more readily discernable using longer time averages. The chosen time windows were a tradeoff between these considerations and the ability to measure short time constants.

One of our primary conclusions was that of a strong correlation between time constants of adaptation for rate-level and for mean-rate responses, consistent with previous studies in inferior colliculus (Dean et al., 2008). The implication of this finding is that rate-level adaptation, (the adaptation of input / output functions for these neurons) that is created locally is likely to rely on a mechanism of mean-rate regulation. Clearly, because our findings in cortex are consistent with those found subcortically, much of the adaptation reported here may be inherited, and we expect that the difference in time constant asymmetry between dynamic monotonic and dynamic nonmonotonic neurons is also likely to be found subcortically as well. Time constants measured in this study span a range from 200 ms up to 30 seconds that could be accurately estimated with our particular protocol and analysis. The distributions of time constants for both transition types were fairly uniform on a log scale. It was therefore difficult to separate out what would be considered two different time scales of adaptation. We only found clear evidence of multiple time-scales that would be fit with a double exponential decay in a very few neurons in our dataset, so we did not explore this effect systematically.

In general the effect of adaptation is likely smaller in auditory cortex than subcortically and in the auditory nerve, reflected by our low number of neurons that showed robust

adaptation in response to the dynamic-transition stimuli. Multiple time scales of adaptation are present in auditory nerve fibers (Chimento & Schreiner, 1991), but the slower time scale reported there is much faster than slow time scales reported in the inferior colliculus and auditory cortex (Bartlett & Wang, 2005; Dean et al., 2008). Because we were not able to fully discern a cutoff between long term and short term adaptation in this study, a comparison of time constants from this and other related studies is presented in Table 6.1. The table uses mean values from other studies, but medians for our study, since we found a relatively uniform distribution of log transformed time constants over a range from a few hundreds of milliseconds up to tens of seconds. Values in Table 6.1 from this dissertation are taken from the analysis for Figure 6.9 using the 400-ms time windows.

Table 6.1 Comparison of time constants measured in this and other studies of adaptation involving sound level. All values reported are distribution means, except for this dissertation where we report medians (see text). Means from other studies marked with an asterisk (*) indicate that the study reported a significant difference between the high-to-low and low-to-high means. Means marked with a plus sign (+) indicate that they were not directly reported but reconstructed from a published figure. Values either not collected or not reported are marked with NA (not available).

First Author (Year)	Auditory Area Sampled	Species	Paradigm	High-to-Low Transition (Fast/Slow) (ms / sec)	Low-to-High Transition (Fast/Slow) (ms / sec)
Watkins (2009)	auditory cortex	marmoset monkey	dynamic level	2400 / NA	740 / NA
Dean (2008)	inferior colliculus	guinea pig	dynamic level	331.8* / 12.3	159.7* / NA
Nagel (2006)	field-L	zebra finch	dynamic level	670 ⁺ / NA	690 ⁺ / NA
Kvale (2004)	inferior colliculus	cat	dynamic variance	140 / NA	300 / NA
Bartlett (2005)	auditory cortex	marmoset monkey	forward masking variant	(suppression / facilitation) 600 ms / 500 ms	
Chimento (1991)	auditory nerve fibers	cat	forward masking	8.3 / 682	5.5 / 93.7

Monotonicity index (MI) measured in silence-adapted rate-level functions did not completely predict neuronal responses to dynamic-transition-stimuli plateaus. Certainly, a few example neurons under steady-state adapted conditions demonstrated changes in their MI depending on the mean sound level of the dynamic stimulus (for example, see Figure 5.2G). In the steady-state analyses this issue was addressed by using the mean MI over all static and dynamic responses. For the dynamic-transition stimuli we recorded responses to uniformly distributed dynamic stimuli (see Section 2.3.1), which often gave a better estimate of responses to plateaus of dynamic-transition stimuli. However, in general some monotonic neurons demonstrated decreasing rate-level functions in response to the high-level plateau, and some nonmonotonic neurons demonstrated increasing rate-level functions in response to the high-level plateau (Figure 6.3), contrary to what would be expected given the static MI. For steady-state responses to dynamic stimuli, MIs were all considered separately and in general still conformed to decreasing amount of adaptation with decreasing MI (Figure 5.5), but this analysis considered this effect across the population and not in the same neuron. Therefore, we based our monotonic / nonmonotonic categorization for responses to the dynamic-transition stimuli on whether the responses themselves were increasing or decreasing for the low-to-high transition and not considering the MI from the silence-adapted rate-level. In general, these considerations mean that the amount of on-CF inhibition present in the neuronal responses is also a function of sound-level, with a rate-level profile that is distinct from that of the excitatory inputs, consistent with intracellular studies (Tan et al., 2007).

The result that the subset of dynamic monotonic neurons considered in the analysis for Figure 6.8 always had increasing responses that decayed to higher sound levels in response to the high-level plateau and always had increasing responses that decayed to lower sound levels in response to the low-level plateau is compelling. Neurons of this type are likely to be responsible for the general finding in other studies that neurons adapt more quickly for the low-to-high level transition (compare Figures 6.6B and 6.7A). Dynamic nonmonotonic neurons, on the other hand, seem to come in at least two varieties, separated by whether their decreasing responses to the high-level plateau decay to lower sound levels or to higher sound levels (compare Figures 6.7B and 6.7C). Dynamic nonmonotonic neurons that decayed to higher sound levels (Figure 6.7B) showed a much greater average time constant than those that decayed to lower sound levels (Figure 6.7C). Additionally, for neurons in our dataset, these subsets of dynamic nonmonotonic neurons were not predictive of how the same neuron would adapt to the low-level plateau. These results imply that nonmonotonic neurons may very well be composed of several other categories either that have response characteristics preserved from particular auditory nerve fibers inputs or whose dynamic properties are created from central neural circuits. These two populations could then be serving even more specific tasks in regards to transient dynamic level responses.

Appendix A

Neuronal Correlations between Simultaneously Recorded Neurons and the Effect on Measures of Encoding and Decoding of Sound Intensity Level

As alluded to briefly in the Methods (Section 2.3.2) and Results (Section 5.2.3) for Chapter 5, drawing conclusions based on the mean Fisher Information (FI) calculated over a population of neurons inherently assumes that the neural responses are not correlated. Such correlations, referred to as noise correlations are correlations between neurons in response to a fixed stimulus, and thus are not correlations strictly due to the effect of the stimulus (referred to signal correlations). Noise correlations in the neural responses change the amount of information regarding the signal that is conveyed by the population. Such correlations can either increase or decrease the amount of information encoded by the population, but only have the effect of decreasing the amount of information that can be decoded from the population response (for review see (Averbeck et al., 2006)). This appendix presents the results of analyzing the discrete analog of FI, discriminability (d' , a measure of the decoding accuracy possible from an ideal observer) for a population of simultaneously recorded neurons in response to different sound levels of a pure tone stimulus, at or very close to the

characteristic frequency (CF) of the recorded neurons. We calculate the effect of noise correlations on each measure of discriminability from these rate-level responses. Other aspects of these responses, termed static rate-level responses or silence-adapted responses in the context of dynamic stimuli, were described in detail in Chapter 4. The same type of noise correlation analysis could be performed on the Fisher Information directly; unfortunately, our dataset only contained two pairs of neurons that were recorded simultaneously in response to the dynamic level stimuli.

A.1 Methods

Methods for recording single action potentials from neurons in the primary auditory cortex and constructing rate-level responses are described in Sections 2.2.1 and 2.2.2 respectively. Out of the dataset of rate-level responses evoked with pure tone stimuli at the characteristic frequency (CF) of the neuron we analyzed neurons that were recorded simultaneously on one electrode for the noise correlation analysis. Because we utilized online template-based spike sorting, up to 4 distinct action potentials could be isolated from a single electrode simultaneously (see Section 2.2.1). We chose a time bin width of 100 ms for the purposes of computing noise correlations. This was chosen because this is the same as the time interval utilized in the dynamic-level stimuli (see Section 2.3.1) for which Fisher Information was calculated and averaged (see Section 5.2.3) and is also the duration of our static rate-level stimuli. In order to make a more informed choice on an appropriately sized time bin for the noise correlation analysis, our experiments would

require some measure of decoding performance (possibly based on a behavioral task) with which to evaluate different time bin sizes (Averbeck & Lee, 2003), which we did not have. Noise correlations were analyzed over the 100 ms interval starting at the shortest neuronal latency of the simultaneously recorded neurons (for a description of how latency was estimated for each neuron, see Section 2.2.3).

Discriminability was calculated using d-prime, a measure of the separation between two Gaussian distributions, defined as:

$$d^2 = \frac{(\mu_2 - \mu_1)^2}{\sigma^2} = \frac{\Delta \mu^2}{\sigma^2}, \quad (\text{A.1})$$

where d^2 is d-prime squared, μ_i are the mean spike counts in response to two different stimuli (two different sound levels in this case), and σ^2 is the variance of the spike count distribution. This latter value was taken as the average variance of the two respective spike count distributions. Discriminability was calculated for all possible pairs of sound levels that were collected for most of the rate-level dataset from -15 dB SPL to 85 dB SPL in increments of 10 dB. This amounts to a total of 55 possible pairs of sound levels for which d^2 was calculated for each neuron. Discriminability was extended for multiple neurons recorded simultaneously using a multivariate generalization involving the covariance matrix of the neurons and then re-calculated in order to understand the changes in both the information encoded and that can be decoded when neuronal correlations are ignored. The calculations were reproduced in exactly the same manner

as given by (Averbeck & Lee, 2006). For completeness, the next paragraph briefly describes these calculations.

The multivariate extension of d^2 is given by:

$$d^2 = \Delta \boldsymbol{\mu}^T \boldsymbol{Q}^{-1} \Delta \boldsymbol{\mu} , \quad (\text{A.2})$$

where $\Delta \boldsymbol{\mu}$ is the difference in mean spike counts in response to two different sound levels and \boldsymbol{Q} is the mean covariance matrix for these spike count distributions. The dimensionality of the $\Delta \boldsymbol{\mu}$ vector and the \boldsymbol{Q} matrix is given by the product of the number of time bins and the number of neurons. For the purposes of this analysis, only 100 ms time bins for 100 ms duration stimuli were used, resulting in only a single time bin. Thus, the dimensionality was given as the number of simultaneously recorded neurons. The effect of ignoring correlations on the amount of information encoded by the simultaneously recorded neurons was measured by removing the correlations between neurons:

$$d_{shuffled}^2 = \Delta \boldsymbol{\mu}^T \boldsymbol{Q}_d^{-1} \Delta \boldsymbol{\mu} , \quad (\text{A.3})$$

where \boldsymbol{Q}_d is the mean covariance matrix with off diagonal elements set to zero. The effect of how much information can be decoded from the simultaneously recorded neurons without knowledge of the correlations was measured by deriving the optimal decoder using the diagonalized covariance matrix:

$$d_{diag}^2 = \frac{(\Delta \mu^T Q_d^{-1} \Delta \mu)^2}{\Delta \mu^T Q_d^{-1} Q Q_d^{-1} \Delta \mu} . \quad (\text{A.4})$$

Each d-prime value was converted into a coding accuracy metric, which essentially gives an upper bound on the percentage of times that an optimal decoder would correctly classify the sound level, based on any of the d-prime measurements (see (Averbeck & Lee, 2006) for derivation):

$$A = \int_{-\infty}^{d/2} \exp\left(\frac{-z^2}{2}\right) dz . \quad (\text{A.5})$$

where A is the coding accuracy and d is the square root of one of the discriminability metrics measured above (either d^2 , $d_{shuffled}^2$ or d_{diag}^2). The expression is equivalent to the value of the standard normal cumulative density function at $d / 2$, and was evaluated as such. The changes in encoding accuracy,

$$\Delta A_{shuffled} = A - A_{shuffled} , \quad (\text{A.6})$$

and decoding accuracy,

$$\Delta A_{diag} = A - A_{diag} , \quad (\text{A.7})$$

quantified the amount of information that was gained or lost by ignoring noise correlations between neurons. Here $A_{shuffled}$ and A_{diag} are computed from Equation A.5 using $d_{shuffled}$ and d_{diag} respectively. $A_{shuffled}$ can be positive, meaning encoding information is lost without accounting for correlations, or negative, meaning encoding information is

gained without accounting for correlations. A decoder without knowledge of the correlations can only lose information, so A_{diag} is always positive.

For the purposes of this appendix, the primary interest is to show the effect, if any, that noise correlations in auditory cortex neurons may have on our conclusions drawn from averaging FI in Chapter 5 (for example, Figure 5.4B,D). In Chapter 5, the primary purpose of the mean FI analysis was to determine differences in encoding between monotonic and nonmonotonic neurons. Thus, any significant differences in noise correlation or coding accuracy between monotonic and nonmonotonic neurons could potentially introduce a caveat for conclusions drawn based on mean FI. To investigate this issue, simultaneously recorded neurons were characterized by both the mean and standard deviation of neurons' monotonicity indices (MIs, see Section 2.2.3). Simultaneously recorded neurons were classified as monotonic if all the neurons had $MI > 0.5$ and as nonmonotonic if all the neurons had $MI \leq 0.5$. Although some simultaneously recorded groups had neurons with MIs on both sides of 0.5, any correlation relationships amongst these groups was not relevant for the current analysis, and we did not find any significant effects. Because of the large number of possible comparisons for which coding accuracy measures were derived, an overall accuracy for each simultaneously recorded group was calculated as the mean across all possible sound level discriminability comparisons. In addition, we calculated mean coding accuracies and correlations for each possible stimulus comparison, averaged separately for the monotonic and nonmonotonic classes of simultaneously recorded neurons.

Some calculations for coding accuracy, as described above, resulted in a singular matrix or a divide by zero situation. These values were considered as empty data points and were removed for the averages across stimulus pairs or across simultaneously recorded groups.

A.2 Results

As described in Section 4.2, 544 primary auditory cortex neurons from 12 hemispheres of 7 awake marmoset monkeys (*Callithrix jacchus*) were analyzed for sound intensity level coding properties in response to characteristic frequency (CF) tones. From these responses, (static) rate-level functions were computed as described in Section 2.2.3. Of these 544 rate-level functions, 541 contained the standard set of sound levels from -15 dB SPL to 85 dB SPL in increments of 10 dB for which 55 pairs (all combinations of 11 sound levels taken 2 at a time) of coding accuracy measurements were collected. These measurements reflect the coding accuracy of single “silence-adapted” neurons (not necessarily simultaneously recorded). Neurons were classified as monotonic if their monotonicity index (MI, see Section 2.2.3) was greater than 0.5 and nonmonotonic if their MI was less than or equal to 0.5 . Of the 541 neurons containing the standard sound levels, 238 were classified as monotonic and 303 as nonmonotonic. Coding accuracies averages for all 55 possible pairs of the standard sounds levels showed that nonmonotonic neurons are better at discriminating amongst the lower sound levels than monotonic neurons (Figure A.1A,B). This is also consistent with the hypothesis that

nonmonotonic neurons are specialized encoders of low sounds levels, for which a good deal of evidence was presented in Chapters 4 through 6. Nonmonotonic neurons also generally have better average coding accuracy for discriminating the closest sounds levels (Figure A.1C) at 10 dB (solid lines) and 20 dB (dashed lines) increments. These increments are represented as the first and second diagonals below the main diagonal (red line) in Figure A.1A,B.

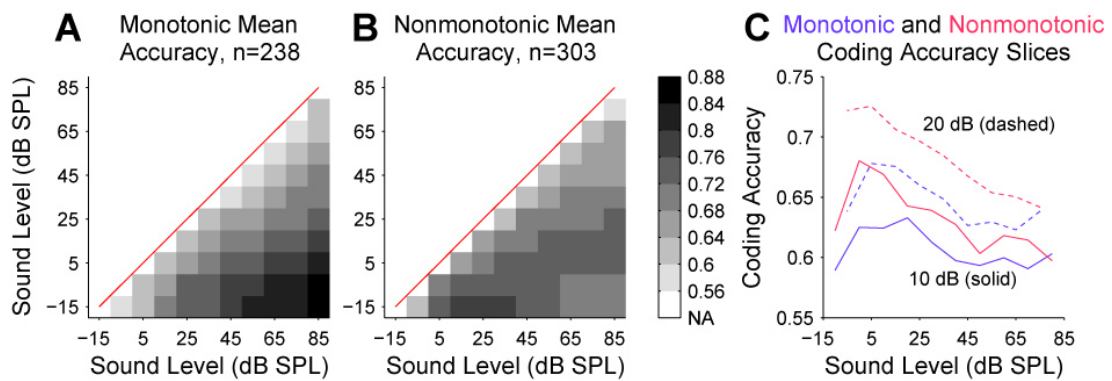


Figure A.1 Average coding accuracy of the population of single monotonic neurons (**A**) versus that of single nonmonotonic neurons (**B**) shows better coding of low sound intensities by nonmonotonic neurons. **C**, Coding accuracy from the first and second diagonals below the main diagonal in A and B represents discriminability between sound levels separated by 10 dB (solid lines) and 20 dB (dashed lines) respectively. Mean accuracy is better at larger separations of sound level and overall better in the nonmonotonic population.

Of the 541 neurons whose responses were recorded with the standard set of sound levels, 206 of these neurons were involved in simultaneous recordings. This total consisted of 86 groups of two simultaneously recorded neurons, 10 groups of three and one group of four for a total of 97 groups of simultaneously recorded neurons. Of these groups, 27 had all neurons classified as monotonic ($MI > 0.5$), 40 had all neurons classified as nonmonotonic ($MI \leq 0.5$) and the remaining 30 had a combination of monotonic and nonmonotonic neurons recorded simultaneously. In general, average coding accuracy was greater for the simultaneously recorded groups than that of the individual neurons composing the groups for both monotonic (Figure A.2A versus Figure A.2C) and nonmonotonic (Figure A.2B versus Figure A.2D) neurons. Mean accuracy of the all monotonic or all nonmonotonic simultaneously recorded groups showed similar trends to that over the whole population, with nonmonotonic groups having better accuracy at the lowest intensities. No trends revealing a systematic relationship of change in encoding accuracy (Figure A.2E,F) or change in decoding accuracy (Figure A.2G,H) when correlations were ignored were immediately apparent across the different stimulus pairs.

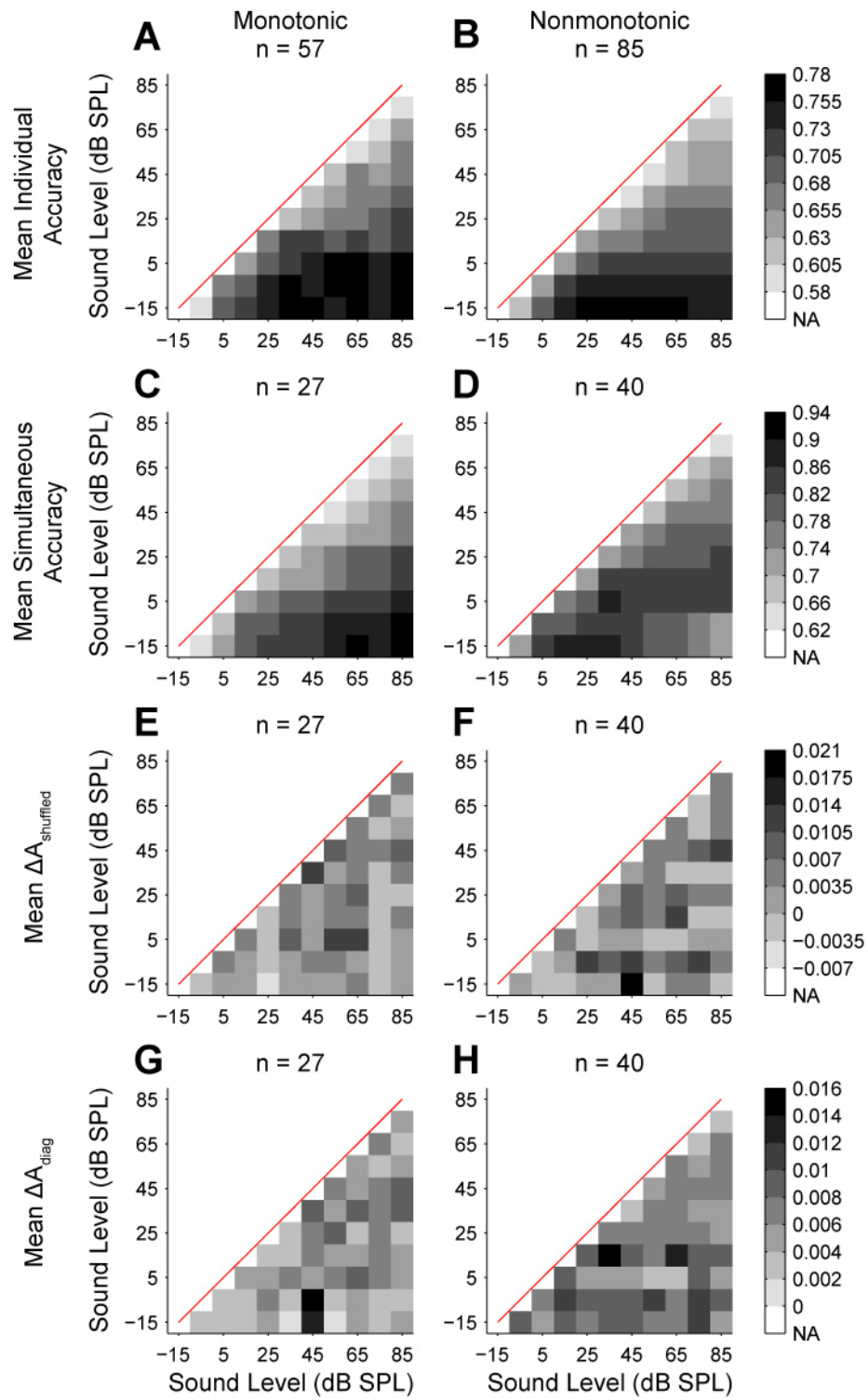


Figure A.2 Mean single neuron coding accuracy from the populations of simultaneously recorded monotonic (**A**) and nonmonotonic neurons (**B**). Mean coding accuracy of the simultaneously recorded groups that contain either all monotonic (**C**) or all nonmonotonic (**D**) neurons. Mean coding accuracy for the simultaneously recorded groups (C,D) is in general greater than that of the individual neurons composing the groups (A,B). The change in encoding accuracy when correlations are ignored can be negative, meaning encoding accuracy improves, or positive, meaning encoding accuracy degrades, when correlations are ignored for the same monotonic (**E**) and nonmonotonic (**F**) groups of simultaneously recorded neurons in C,D. **G–H** On the other hand, the change in decoding accuracy is always positive when the decoder has no knowledge of noise correlations.

The change in encoding and decoding accuracy for the simultaneously recorded groups of neurons was relatively small in comparison with the overall coding accuracy (Figure A.3A–D). For discrimination between levels that were 10 dB and 20 dB apart (first and second diagonals below the main diagonals in A.2) it is apparent that nonmonotonic groups have a slightly larger deficit in decoding accuracy than monotonic groups when correlations are ignored at the lowest sounds levels. This can be seen by a larger distance between blue line and green line in Figure A.3B versus Figure A.3A for 10 dB discriminability, and the same in Figure A.3C versus A.3D for 20 dB discriminability. Indeed, there are larger correlations between nonmonotonic groups than between monotonic groups at sound levels less than or equal to 35 dB SPL (Figure A.3E).

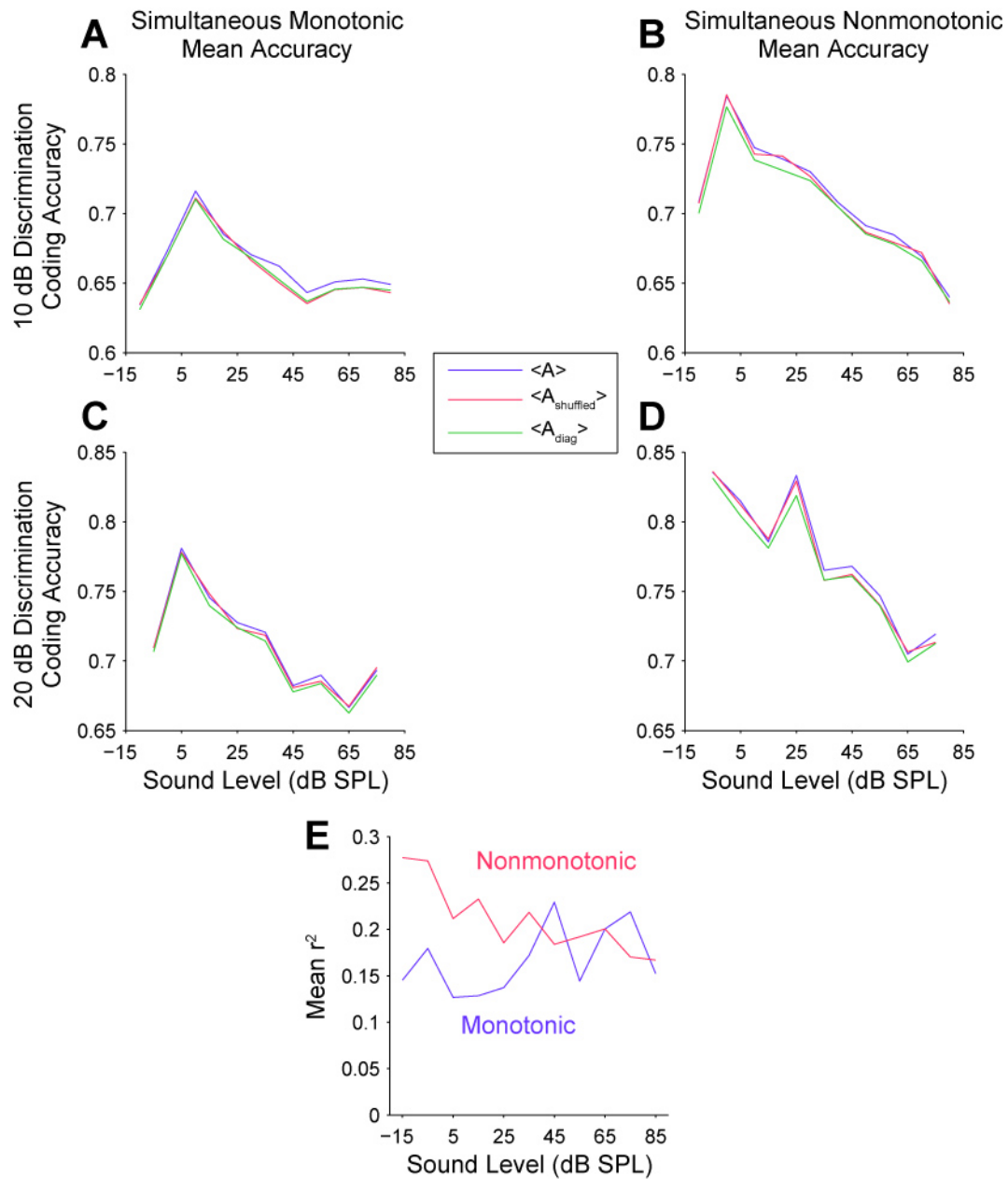


Figure A.3 A–D, First and second diagonal slices below main diagonal from Figure A.2 show the relatively small difference between coding accuracy (blue lines) and coding accuracy that does not account for correlations in encoding (red lines) or decoding (green lines). A larger difference is apparent for the decoding in the nonmonotonic

groups at lower sound levels. This difference is because of large correlations amongst the nonmonotonic groups at sound levels below 35 dB SPL relative to the monotonic groups (**E**). Both populations are near a mean correlation coefficient (r^2) of about 0.2 across all sound levels.

For mean coding accuracy averaged across all stimulus pairs, there was not a significant difference ($p = 0.45$, Wilcoxon rank sum test) between monotonic and nonmonotonic groups of simultaneously recorded neurons (Figure A.4A). All plots in Figure A.4, show mean coding accuracies, coding accuracy differences or correlations across all stimulus pairs expressed as a function of the mean MI of the simultaneously recorded neurons. Again, only groups with all monotonic or all nonmonotonic neurons were included for this analysis. Significance was tested by comparing central tendencies of the monotonic and nonmonotonic distributions (split at MI of 0.5) of these coding measures. A p-value is shown above each plot where a significant difference ($p < 0.05$) was found. There was also not a significant difference in the change in encoding accuracy when noise correlations were ignored ($p = 0.27$, Wilcoxon rank sum test) between monotonic and nonmonotonic groups (Figure A.4B). The change in decoding accuracy (Figure A.4C), however, was significantly greater for nonmonotonic groups ($p = 0.0071$, Wilcoxon rank sum test), likely due to a significantly greater mean correlations in nonmonotonic groups (Figure A.4D, $p = 0.0080$, Wilcoxon rank sum test). Thus, these results show that slightly larger average noise correlations amongst groups of simultaneously recorded nonmonotonic neurons resulted in more information lost by a decoder with no knowledge of the correlations, although not resulting in significantly more encoding information lost. Additionally, this result is not due to an overall difference in overall coding accuracy.

When these same coding accuracy and correlation measurements plotted in Figure A.4A–D were calculated by averaging over stimuli with sound levels greater than 15 dB SPL, the significant trends were no longer revealed (Figure A.4E–H). The same measurements averaged over sound levels less than or equal to 15 dB SPL first revealed significantly better coding accuracy in nonmonotonic groups (Figure A.4I, $p = 0.0014$, Wilcoxon rank sum test). There was again no significant difference in encoding information changed by ignoring correlations (Figure A.4J, $p = 0.75$, Wilcoxon rank sum test), but nonmonotonic groups showed significantly more information lost in decoding (Figure A.4K, $p = 0.0081$, Wilcoxon rank sum test) and significantly greater correlations (Figure A.4L, $p = 0.0018$, Wilcoxon rank sum test). This final result is consistent with Figure A.4E, showing more correlations in nonmonotonic neurons at lower sound levels. So, nonmonotonic neurons show significantly better coding accuracy, but more decoding information lost due to noise correlations and only at lower sound levels.

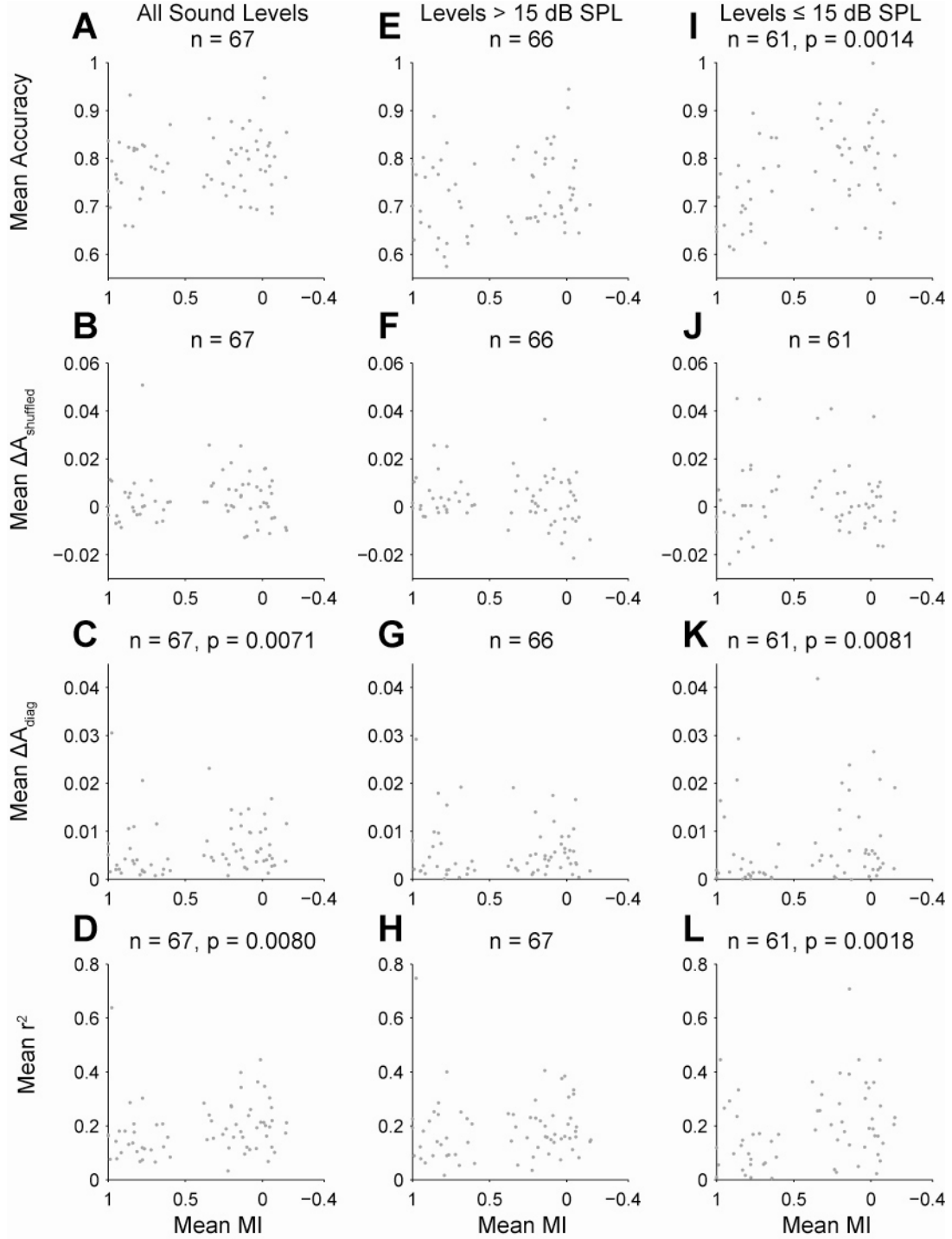


Figure A.4 Mean coding accuracy and correlation measurements similar to Figures A.2 and A.3 but with the average taken across all stimulus pairs and expressed as a function

of mean MI of the simultaneously recorded neurons, where only simultaneous groups where all the neurons were monotonic or all the neurons were nonmonotonic are shown. Plots where there is a significant difference ($p < 0.05$) in medians between the monotonic and nonmonotonic groups are labeled with the p-value. Mean coding accuracy (**A**) is not significantly different between monotonic and nonmonotonic groups ($p = 0.45$, Wilcoxon rank sum test), nor is the change in encoding accuracy when correlations are ignored (**B**, $p = 0.27$, Wilcoxon rank sum test). Nonmonotonic simultaneously recorded groups showed significantly more decoding information lost than did monotonic groups when correlations were ignored (**C**, $p = 0.0071$, Wilcoxon rank sum test) and showed significantly greater correlations (**D**, $p = 0.0080$, Wilcoxon rank sum test). **E–H**, The same measures as in A–D, but only averaged across sound levels greater than 15 dB SPL do not show any significant differences between the monotonic and nonmonotonic groups. **I–L**, The same measures as in A–D, but only averaged across sound levels less than or equal to 15 dB SPL show nonmonotonic groups having significantly greater mean accuracy ($p = 0.0014$, Wilcoxon rank sum test), significantly more information lost in decoding by ignoring noise correlations ($p = 0.0081$, Wilcoxon rank sum test), and significantly more noise correlations ($p = 0.0018$, Wilcoxon rank sum test).

A.3 Discussion

Our purpose for using Fisher Information (FI) in Chapter 5 was to compare relative differences in encoding properties between monotonic and nonmonotonic neurons. In particular we did not propose necessarily how these responses would be decoded by postsynaptic neurons. Thus, a large degree of correlations in auditory cortex neurons would not have necessarily been a problem, but only if there was a difference in these correlations between the nonmonotonic and monotonic population. We did indeed find this effect to be significant in neurons that were either all monotonic or all nonmonotonic and recorded simultaneously on the same electrode. Although this potentially presents a caveat for our conclusions in Chapter 5, this effect was quite small overall (see Figure A.3A–D). Additionally, we would expect the effect to be much smaller when correlations were measured between neurons separated by greater distance in the cortex (Smith & Kohn, 2008), as opposed to the close proximity of simultaneously recorded neurons from one electrode that were analyzed here. Therefore, we still do not anticipate that accounting for noise correlations would have such a large effect as to change our conclusions from Chapter 5 drawn based upon mean FI analyses. In addition the analysis presented in Appendix A potentially provides preliminary data for two additional hypotheses: (1) that nonmonotonic neurons are more likely to be involved in the same circuitry and (2) that at the lowest sound levels, the auditory system may be sacrificing discriminability for detectability, as is done in the

visual system where receptive fields become larger at lower contrasts (Sceniak, Ringach, Hawken, & Shapley, 1999).

References

- Abeles, M., & Goldstein, M. H., Jr. (1970). Functional architecture in cat primary auditory cortex: columnar organization and organization according to depth. *J Neurophysiol*, 33(1), 172-187.
- Aitkin, L. (1991). Rate-level functions of neurons in the inferior colliculus of cats measured with the use of free-field sound stimuli. *J Neurophysiol*, 65(2), 383-392.
- Averbeck, B. B., Latham, P. E., & Pouget, A. (2006). Neural correlations, population coding and computation. *Nat Rev Neurosci*, 7(5), 358-366.
- Averbeck, B. B., & Lee, D. (2003). Neural noise and movement-related codes in the macaque supplementary motor area. *J Neurosci*, 23(20), 7630-7641.
- Averbeck, B. B., & Lee, D. (2006). Effects of noise correlations on information encoding and decoding. *J Neurophysiol*, 95(6), 3633-3644.
- Bartlett, E. L., & Wang, X. (2005). Long-lasting modulation by stimulus context in primate auditory cortex. *J Neurophysiol*, 94(1), 83-104.
- Blasdel, G. G., & Salama, G. (1986). Voltage-sensitive dyes reveal a modular organization in monkey striate cortex. *Nature*, 321(6070), 579-585.
- Britten, K. H., Newsome, W. T., Shadlen, M. N., Celebrini, S., & Movshon, J. A. (1996). A relationship between behavioral choice and the visual responses of neurons in macaque MT. *Vis Neurosci*, 13(1), 87-100.
- Brosch, M., & Schreiner, C. E. (1997). Time course of forward masking tuning curves in cat primary auditory cortex. *J Neurophysiol*, 77(2), 923-943.
- Butts, D. A., & Goldman, M. S. (2006). Tuning curves, neuronal variability, and sensory coding. *PLoS Biol*, 4(4), e92.
- Calford, M. B., & Semple, M. N. (1995). Monaural inhibition in cat auditory cortex. *J Neurophysiol*, 73(5), 1876-1891.
- Cheung, S., Bedenbaugh, P., Nagarajan, S., & Schreiner, C. (2001). Functional Organization of Squirrel Monkey Primary Auditory Cortex: Responses to Pure Tones. *Journal of Neurophysiology*, 85(4), 1732-1749.
- Chimento, T. C., & Schreiner, C. E. (1990). Time course of adaptation and recovery from adaptation in the cat auditory-nerve neurophonic. *J Acoust Soc Am*, 88(2), 857-864.
- Chimento, T. C., & Schreiner, C. E. (1991). Adaptation and recovery from adaptation in single fiber responses of the cat auditory nerve. *J Acoust Soc Am*, 90(1), 263-273.
- Clarey, J. C., Barone, P., & Imig, T. J. (1994). Functional organization of sound direction and sound pressure level in primary auditory cortex of the cat. *J Neurophysiol*, 72(5), 2383-2405.
- Creutzfeldt, O. D. (1977). Generality of the functional structure of the neocortex. *Naturwissenschaften*, 64(10), 507-517.

- Davis, K. A., Ramachandran, R., & May, B. J. (2003). Auditory processing of spectral cues for sound localization in the inferior colliculus. *J Assoc Res Otolaryngol*, 4(2), 148-163.
- Dayan, P., & Abbott, L. F. (2001). *Theoretical Neuroscience: Computational and Mathematical Modeling of Neural Systems*. Cambridge, MA: The MIT Press.
- de la Rocha, J., Marchetti, C., Schiff, M., & Reyes, A. D. (2008). Linking the response properties of cells in auditory cortex with network architecture: cotuning versus lateral inhibition. *J Neurosci*, 28(37), 9151-9163.
- Dean, I., Harper, N. S., & McAlpine, D. (2005). Neural population coding of sound level adapts to stimulus statistics. *Nat Neurosci*, 8(12), 1684-1689.
- Dean, I., Robinson, B. L., Harper, N. S., & McAlpine, D. (2008). Rapid neural adaptation to sound level statistics. *J Neurosci*, 28(25), 6430-6438.
- Depireux, D. A., Simon, J. Z., Klein, D. J., & Shamma, S. A. (2001). Spectro-temporal response field characterization with dynamic ripples in ferret primary auditory cortex. *J Neurophysiol*, 85(3), 1220-1234.
- DeWeese, M. R., & Zador, A. M. (1998). Asymmetric dynamics in optimal variance adaptation. *Neural Comput*, 10, 1179-1202.
- DiMattina, C., & Wang, X. (2006). Virtual vocalization stimuli for investigating neural representations of species-specific vocalizations. *J Neurophysiol*, 95(2), 1244-1262.
- Eliasmith, C., & Anderson, C. (2004). *Neural Engineering: Computation, Representation, and Dynamics in Neurobiological Systems*. Cambridge, MA: The MIT Press.
- Erwin, E., Obermayer, K., & Schulten, K. (1995). Models of orientation and ocular dominance columns in the visual cortex: a critical comparison. *Neural Comput*, 7(3), 425-468.
- Esser, K. H., & Eiermann, A. (1999). Tonotopic organization and parcellation of auditory cortex in the FM-bat *Carollia perspicillata*. *Eur J Neurosci*, 11(10), 3669-3682.
- Faingold, C. L., Boersma Anderson, C. A., & Caspary, D. M. (1991). Involvement of GABA in acoustically-evoked inhibition in inferior colliculus neurons. *Hear Res*, 52(1), 201-216.
- Farley, B. J., Yu, H., Jin, D. Z., & Sur, M. (2007). Alteration of visual input results in a coordinated reorganization of multiple visual cortex maps. *J Neurosci*, 27(38), 10299-10310.
- Felleman, D. J., & Van Essen, D. C. (1991). Distributed hierarchical processing in the primate cerebral cortex. *Cereb Cortex*, 1(1), 1-47.
- Galambos, R. (1952). Microelectrode studies on medial geniculate body of cat. III. Response to pure tones. *J Neurophysiol*, 15(5), 381-400.
- Galambos, R., & Davis, H. (1943). The response of single auditory-nerve fibres to acoustic stimulation. *Journal of Neurophysiology*, 6(1), 39-57.
- Geisler, C. (1998). *From Sound to Synapse: Physiology of the Mammalian Ear*. New York: Oxford University Press.
- Godey, B., Atencio, C. A., Bonham, B. H., Schreiner, C. E., & Cheung, S. W. (2005). Functional organization of squirrel monkey primary auditory cortex: responses to frequency-modulation sweeps. *J Neurophysiol*, 94(2), 1299-1311.

- Harris, D. M., & Dallos, P. (1979). Forward masking of auditory nerve fiber responses. *J Neurophysiol*, 42(4), 1083-1107.
- Heil, P., Rajan, R., & Irvine, D. R. (1994). Topographic representation of tone intensity along the isofrequency axis of cat primary auditory cortex. *Hear Res*, 76(1-2), 188-202.
- Hromadka, T., Deweese, M. R., & Zador, A. M. (2008). Sparse representation of sounds in the unanesthetized auditory cortex. *PLoS Biol*, 6(1), e16.
- Imig, T. J., & Adrian, H. O. (1977). Binaural columns in the primary field (A1) of cat auditory cortex. *Brain Res*, 138(2), 241-257.
- Jesteadt, W., Bacon, S. P., & Lehman, J. R. (1982). Forward masking as a function of frequency, masker level, and signal delay. *J Acoust Soc Am*, 71(4), 950-962.
- Kelly, J. B., & Judge, P. W. (1994). Binaural organization of primary auditory cortex in the ferret (*Mustela putorius*). *J Neurophysiol*, 71(3), 904-913.
- Kiang, N. Y., Liberman, M. C., & Levine, R. A. (1976). Auditory-nerve activity in cats exposed to ototoxic drugs and high-intensity sounds. *Ann Otol Rhinol Laryngol*, 85(6 PT. 1), 752-768.
- Kiang, N. Y., Watanabe, T., Thomas, E. C., & Clark, L. F. (1965). *Discharge Patterns of Single Fibers in the Cat's Auditory Nerve*. Cambridge, MA: The MIT Press.
- Kilgard, M. P., & Merzenich, M. M. (1998). Cortical map reorganization enabled by nucleus basalis activity. *Science*, 279(5357), 1714-1718.
- Kilgard, M. P., Pandya, P. K., Vazquez, J., Gehi, A., Schreiner, C. E., & Merzenich, M. M. (2001). Sensory input directs spatial and temporal plasticity in primary auditory cortex. *J Neurophysiol*, 86(1), 326-338.
- Kohonen, T. (1990). The self-organizing map. *Proceedings of the IEEE*, 78(9), 1464-1480.
- Koulakov, A. A., & Chklovskii, D. B. (2001). Orientation preference patterns in mammalian visual cortex: a wire length minimization approach. *Neuron*, 29(2), 519-527.
- Kvale, M. N., & Schreiner, C. E. (2004). Short-term adaptation of auditory receptive fields to dynamic stimuli. *J Neurophysiol*, 91(2), 604-612.
- Langner, G., Sams, M., Heil, P., & Schulze, H. (1997). Frequency and periodicity are represented in orthogonal maps in the human auditory cortex: evidence from magnetoencephalography. *J Comp Physiol [A]*, 181(6), 665-676.
- Lee, C. C., & Winer, J. A. (2008a). Connections of cat auditory cortex: I. Thalamocortical system. *J Comp Neurol*, 507(6), 1879-1900.
- Lee, C. C., & Winer, J. A. (2008b). Connections of cat auditory cortex: III. Corticocortical system. *J Comp Neurol*, 507(6), 1920-1943.
- Liang, L., Lu, T., & Wang, X. (2002). Neural representations of sinusoidal amplitude and frequency modulations in the primary auditory cortex of awake primates. *J Neurophysiol*, 87(5), 2237-2261.
- Liberman, M. C. (1978). Auditory-nerve response from cats raised in a low-noise chamber. *J Acoust Soc Am*, 63(2), 442-455.
- Lüscher, E., & Zwislocki, J. (1949). Adaptation of the ear to sound stimuli. *J Acoust Soc Am*, 21(2), 135-139.

- Malone, B. J., & Semple, M. N. (2001). Effects of auditory stimulus context on the representation of frequency in the gerbil inferior colliculus. *J Neurophysiol*, *86*(3), 1113-1130.
- Matsubara, J., & Phillips, D. (1988). Intracortical connections and their physiological correlates in the primary auditory cortex (AI) of the cat. *The Journal of Comparative Neurology*, *268*(1), 38-48.
- Mendelson, J. R., Schreiner, C. E., & Sutter, M. L. (1997). Functional topography of cat primary auditory cortex: response latencies. *J Comp Physiol [A]*, *181*(6), 615-633.
- Mendelson, J. R., Schreiner, C. E., Sutter, M. L., & Grasse, K. L. (1993). Functional topography of cat primary auditory cortex: responses to frequency-modulated sweeps. *Exp Brain Res*, *94*(1), 65-87.
- Merzenich, M. M., Knight, P. L., & Roth, G. L. (1973). Cochleotopic organization of primary auditory cortex in the cat. *Brain Res*, *63*, 343-346.
- Merzenich, M. M., Knight, P. L., & Roth, G. L. (1975). Representation of cochlea within primary auditory cortex in the cat. *J Neurophysiol*, *38*(2), 231-249.
- Middlebrooks, J. C., Xu, L., Eddins, A. C., & Green, D. M. (1998). Codes for sound-source location in nontopographic auditory cortex. *J Neurophysiol*, *80*(2), 863-881.
- Mountcastle, V. B. (1997). The columnar organization of the neocortex. *Brain*, *120* (Pt 4), 701-722.
- Nagel, K. I., & Doupe, A. J. (2006). Temporal processing and adaptation in the songbird auditory forebrain. *Neuron*, *51*(6), 845-859.
- Nelson, P. C., Smith, Z. M., & Young, E. D. (2009). Wide-dynamic-range forward suppression in marmoset inferior colliculus neurons is generated centrally and accounts for perceptual masking. *J Neurosci*, *29*(8), 2553-2562.
- Obermayer, K., Blasdel, G. G., & Schulten, K. (1992). Statistical-mechanical analysis of self-organization and pattern formation during the development of visual maps. *Phys Rev A*, *45*(10), 7568-7589.
- Ojima, H., & Takayanagi, M. (2004). Cortical convergence from different frequency domains in the cat primary auditory cortex. *Neuroscience*, *126*(1), 203-212.
- Ojima, H., Takayanagi, M., Potapov, D., & Homma, R. (2005). Isofrequency band-like zones of activation revealed by optical imaging of intrinsic signals in the cat primary auditory cortex. *Cereb Cortex*, *15*(10), 1497-1509.
- Palmer, A. R., & Evans, E. F. (1980). Cochlear fibre rate-intensity functions: no evidence for basilar membrane nonlinearities. *Hear Res*, *2*(3-4), 319-326.
- Peirce, J. W. (2007). The potential importance of saturating and supersaturating contrast response functions in visual cortex. *J Vis*, *7*(6), 13.
- Pfingst, B. E., & O'Connor, T. A. (1981). Characteristics of neurons in auditory cortex of monkeys performing a simple auditory task. *J Neurophysiol*, *45*(1), 16-34.
- Philibert, B., Beitel, R. E., Nagarajan, S. S., Bonham, B. H., Schreiner, C. E., & Cheung, S. W. (2005). Functional organization and hemispheric comparison of primary auditory cortex in the common marmoset (*Callithrix jacchus*). *J Comp Neurol*, *487*(4), 391-406.
- Phillips, D. P. (1990). Neural representation of sound amplitude in the auditory cortex: effects of noise masking. *Behav Brain Res*, *37*(3), 197-214.

- Phillips, D. P., & Irvine, D. R. (1981). Responses of single neurons in physiologically defined primary auditory cortex (AI) of the cat: frequency tuning and responses to intensity. *J Neurophysiol*, *45*(1), 48-58.
- Phillips, D. P., Semple, M. N., & Kitzes, L. M. (1995). Factors shaping the tone level sensitivity of single neurons in posterior field of cat auditory cortex. *J Neurophysiol*, *73*(2), 674-686.
- Pickles, J. (1988). *An Introduction to the Physiology of Hearing* (2nd ed.). London: Academic Press.
- Polley, D. B., Heiser, M. A., Blake, D. T., Schreiner, C. E., & Merzenich, M. M. (2004). Associative learning shapes the neural code for stimulus magnitude in primary auditory cortex. *Proc Natl Acad Sci U S A*, *101*(46), 16351-16356.
- Polley, D. B., Steinberg, E. E., & Merzenich, M. M. (2006). Perceptual learning directs auditory cortical map reorganization through top-down influences. *J Neurosci*, *26*(18), 4970-4982.
- Rabinowitz, W. M., Lim, J. S., Braidia, L. D., & Durlach, N. I. (1976). Intensity perception. VI. Summary of recent data on deviations from Weber's law for 1000-Hz tone pulses. *J Acoust Soc Am*, *59*(6), 1506-1509.
- Ramachandran, R., Davis, K. A., & May, B. J. (1999). Single-unit responses in the inferior colliculus of decerebrate cats. I. Classification based on frequency response maps. *J Neurophysiol*, *82*(1), 152-163.
- Read, H. L., Winer, J. A., & Schreiner, C. E. (2001). Modular organization of intrinsic connections associated with spectral tuning in cat auditory cortex. *Proc Natl Acad Sci U S A*, *98*(14), 8042-8047.
- Read, H. L., Winer, J. A., & Schreiner, C. E. (2002). Functional architecture of auditory cortex. *Curr Opin Neurobiol*, *12*(4), 433-440.
- Reale, R. A., Brugge, J. F., & Feng, J. Z. (1983). Geometry and orientation of neuronal processes in cat primary auditory cortex (AI) related to characteristic-frequency maps. *Proc Natl Acad Sci U S A*, *80*(17), 5449-5453.
- Recanzone, G. H., Guard, D. C., & Phan, M. L. (2000). Frequency and intensity response properties of single neurons in the auditory cortex of the behaving macaque monkey. *J Neurophysiol*, *83*(4), 2315-2331.
- Recanzone, G. H., Schreiner, C. E., Sutter, M. L., Beitel, R. E., & Merzenich, M. M. (1999). Functional organization of spectral receptive fields in the primary auditory cortex of the owl monkey. *J Comp Neurol*, *415*(4), 460-481.
- Rees, A., & Palmer, A. R. (1988). Rate-intensity functions and their modification by broadband noise for neurons in the guinea pig inferior colliculus. *J Acoust Soc Am*, *83*(4), 1488-1498.
- Relkin, E. M., & Turner, C. W. (1988). A reexamination of forward masking in the auditory nerve. *J Acoust Soc Am*, *84*(2), 584-591.
- Rhode, W. S., & Smith, P. H. (1985). Characteristics of tone-pip response patterns in relationship to spontaneous rate in cat auditory nerve fibers. *Hear Res*, *18*(2), 159-168.

- Ritter, H., & Schulten, K. (1988). Convergence properties of Kohonen's topology conserving maps: fluctuations, stability, and dimension selection. *Biological Cybernetics*, 60(1), 59-71.
- Rose, J. E., Galambos, R., & Hughes, J. R. (1959). Microelectrode studies of the cochlear nuclei of the cat. *Bulletin of the Johns Hopkins Hospital*, 104, 211-251.
- Rose, J. E., Greenwood, D. D., Goldberg, J. M., & Hind, J. E. (1963). Some discharge characteristics of single neurons in the inferior colliculus of the cat. 1. Tonal organization, relation of spikes-counts to tone intensity, and firing patterns of single elements. *J. Neurophysiol.*, 26, 295-320.
- Rutkowski, R. G., Wallace, M. N., Shackleton, T. M., & Palmer, A. R. (2000). Organisation of binaural interactions in the primary and dorsocaudal fields of the guinea pig auditory cortex. *Hear Res*, 145(1-2), 177-189.
- Ryan, A., & Miller, J. (1978). Single unit responses in the inferior colliculus of the awake and performing rhesus monkey. *Exp Brain Res*, 32(3), 389-407.
- Sachs, M. B., & Abbas, P. J. (1974). Rate versus level functions for auditory-nerve fibers in cats: tone-burst stimuli. *J Acoust Soc Am*, 56(6), 1835-1847.
- Sadagopan, S., & Wang, X. (2008). Level invariant representation of sounds by populations of neurons in primary auditory cortex. *J Neurosci*, 28(13), 3415-3426.
- Sceniak, M. P., Ringach, D. L., Hawken, M. J., & Shapley, R. (1999). Contrast's effect on spatial summation by macaque V1 neurons. *Nat Neurosci*, 2(8), 733-739.
- Schalk, T. B., & Sachs, M. B. (1980). Nonlinearities in auditory-nerve fiber responses to bandlimited noise. *J Acoust Soc Am*, 67(3), 903-913.
- Schreiner, C. E. (1995). Order and disorder in auditory cortical maps. *Curr Opin Neurobiol*, 5(4), 489-496.
- Schreiner, C. E., & Mendelson, J. R. (1990). Functional topography of cat primary auditory cortex: distribution of integrated excitation. *J Neurophysiol*, 64(5), 1442-1459.
- Schreiner, C. E., Mendelson, J. R., & Sutter, M. L. (1992). Functional topography of cat primary auditory cortex: representation of tone intensity. *Exp Brain Res*, 92(1), 105-122.
- Schulze, H., & Langner, G. (1997a). Periodicity coding in the primary auditory cortex of the Mongolian gerbil (*Meriones unguiculatus*): two different coding strategies for pitch and rhythm? *J Comp Physiol [A]*, 181(6), 651-663.
- Schulze, H., & Langner, G. (1997b). Representation of periodicity pitch in the primary auditory cortex of the Mongolian gerbil. *Acta Otolaryngol Suppl*, 532, 89-95.
- Seiden, H. R. (1957). *Auditory Acuity of the Marmoset Monkey, Hapale jacchus*. Princeton University.
- Semple, M. N., & Kitzes, L. M. (1985). Single-unit responses in the inferior colliculus: different consequences of contralateral and ipsilateral auditory stimulation. *J Neurophysiol*, 53(6), 1467-1482.
- Shadlen, M. N., Britten, K. H., Newsome, W. T., & Movshon, J. A. (1996). A computational analysis of the relationship between neuronal and behavioral responses to visual motion. *J Neurosci*, 16(4), 1486-1510.

- Shamma, S. A. (2003). Auditory Cortex. In M. A. Arbib (Ed.), *The Handbook of Brain Theory and Neural Networks* (2nd ed., pp. 122-127). Cambridge, MA: The MIT Press.
- Shamma, S. A., Fleshman, J. W., Wiser, P. R., & Versnel, H. (1993). Organization of response areas in ferret primary auditory cortex. *J Neurophysiol*, *69*(2), 367-383.
- Shamma, S. A., & Symmes, D. (1985). Patterns of inhibition in auditory cortical cells in awake squirrel monkeys. *Hear Res*, *19*(1), 1-13.
- Sivaramakrishnan, S., Sterbing-D'Angelo, S. J., Filipovic, B., D'Angelo, W. R., Oliver, D. L., & Kuwada, S. (2004). GABA(A) synapses shape neuronal responses to sound intensity in the inferior colliculus. *J Neurosci*, *24*(21), 5031-5043.
- Smith, M. A., & Kohn, A. (2008). Spatial and temporal scales of neuronal correlation in primary visual cortex. *J Neurosci*, *28*(48), 12591-12603.
- Spirou, G. A., & Young, E. D. (1991). Organization of dorsal cochlear nucleus type IV unit response maps and their relationship to activation by bandlimited noise. *J Neurophysiol*, *66*(5), 1750-1768.
- Suga, N. (1977). Amplitude spectrum representation in the Doppler-shifted-CF processing area of the auditory cortex of the mustache bat. *Science*, *196*(4285), 64-67.
- Suga, N., & Manabe, T. (1982). Neural basis of amplitude-spectrum representation in auditory cortex of the mustached bat. *J Neurophysiol*, *47*(2), 225-255.
- Sutter, M. L., & Loftus, W. C. (2003). Excitatory and inhibitory intensity tuning in auditory cortex: evidence for multiple inhibitory mechanisms. *J Neurophysiol*, *90*(4), 2629-2647.
- Sutter, M. L., & Schreiner, C. E. (1995). Topography of intensity tuning in cat primary auditory cortex: single-neuron versus multiple-neuron recordings. *J Neurophysiol*, *73*(1), 190-204.
- Swindale, N. V. (1991). Coverage and the design of striate cortex. *Biol Cybern*, *65*(6), 415-424.
- Swindale, N. V. (2004). How different feature spaces may be represented in cortical maps. *Network*, *15*(4), 217-242.
- Swindale, N. V., Shoham, D., Grinvald, A., Bonhoeffer, T., & Hubener, M. (2000). Visual cortex maps are optimized for uniform coverage. *Nat Neurosci*, *3*(8), 822-826.
- Tan, A. Y., Atencio, C. A., Polley, D. B., Merzenich, M. M., & Schreiner, C. E. (2007). Unbalanced synaptic inhibition can create intensity-tuned auditory cortex neurons. *Neuroscience*, *146*(1), 449-462.
- Tootell, R. B., Hamilton, S. L., Silverman, M. S., & Switkes, E. (1988). Functional anatomy of macaque striate cortex. I. Ocular dominance, binocular interactions, and baseline conditions. *Journal of Neuroscience*, *8*(5), 1500-1530.
- Tootell, R. B., Silverman, M. S., Hamilton, S. L., De Valois, R. L., & Switkes, E. (1988). Functional anatomy of macaque striate cortex. III. Color. *Journal of Neuroscience*, *8*(5), 1569-1593.

- Tootell, R. B., Silverman, M. S., Hamilton, S. L., Switkes, E., & De Valois, R. L. (1988). Functional anatomy of macaque striate cortex. V. Spatial frequency. *Journal of Neuroscience*, *8*(5), 1610-1624.
- Tootell, R. B., Switkes, E., Silverman, M. S., & Hamilton, S. L. (1988). Functional anatomy of macaque striate cortex. II. Retinotopic organization. *Journal of Neuroscience*, *8*(5), 1531-1568.
- Ts'o, D., Gilbert, C., & Wiesel, T. (1986). Relationships between horizontal interactions and functional architecture in cat striate cortex as revealed by cross-correlation analysis. *Journal of Neuroscience*, *6*(4), 1160.
- Turner, C. W., Relkin, E. M., & Doucet, J. (1994). Psychophysical and physiological forward masking studies: probe duration and rise-time effects. *J Acoust Soc Am*, *96*(2 Pt 1), 795-800.
- Ulanovsky, N., Las, L., Farkas, D., & Nelken, I. (2004). Multiple time scales of adaptation in auditory cortex neurons. *J Neurosci*, *24*(46), 10440-10453.
- Ulanovsky, N., Las, L., & Nelken, I. (2003). Processing of low-probability sounds by cortical neurons. *Nat Neurosci*, *6*(4), 391-398.
- Van Essen, D. (1985). Functional organization of primate visual cortex. *Cerebral cortex*, *3*, 259-329.
- von Békésy, G. (1960). *Experiments in Hearing*. New York: McGraw-Hill.
- Wang, J., McFadden, S. L., Caspary, D., & Salvi, R. (2002). Gamma-aminobutyric acid circuits shape response properties of auditory cortex neurons. *Brain Res*, *944*(1-2), 219-231.
- Wang, X., Lu, T., Snider, R. K., & Liang, L. (2005). Sustained firing in auditory cortex evoked by preferred stimuli. *Nature*, *435*(7040), 341-346.
- Wark, B., Lundstrom, B. N., & Fairhall, A. (2007). Sensory adaptation. *Curr Opin Neurobiol*, *17*(4), 423-429.
- Wehr, M., & Zador, A. M. (2003). Balanced inhibition underlies tuning and sharpens spike timing in auditory cortex. *Nature*, *426*(6965), 442-446.
- Winer, J. A., Diamond, I. T., & Raczkowski, D. (1977). Subdivisions of the auditory cortex of the cat: the retrograde transport of horseradish peroxidase to the medial geniculate body and posterior thalamic nuclei. *J Comp Neurol*, *176*(3), 387-417.
- Wu, G. K., Li, P., Tao, H. W., & Zhang, L. I. (2006). Nonmonotonic synaptic excitation and imbalanced inhibition underlying cortical intensity tuning. *Neuron*, *52*(4), 705-715.
- Young, E. D., & Brownell, W. E. (1976). Responses to tones and noise of single cells in dorsal cochlear nucleus of unanesthetized cats. *J Neurophysiol*, *39*(2), 282-300.
- Yu, H., Farley, B. J., Jin, D. Z., & Sur, M. (2005). The coordinated mapping of visual space and response features in visual cortex. *Neuron*, *47*(2), 267-280.
- Zeng, F. G., Turner, C. W., & Relkin, E. M. (1991). Recovery from prior stimulation. II: Effects upon intensity discrimination. *Hear Res*, *55*(2), 223-230.
- Zhang, L. I., Bao, S., & Merzenich, M. M. (2001). Persistent and specific influences of early acoustic environments on primary auditory cortex. *Nat Neurosci*, *4*(11), 1123-1130.

- Zhang, L. I., Tan, A. Y., Schreiner, C. E., & Merzenich, M. M. (2003). Topography and synaptic shaping of direction selectivity in primary auditory cortex. *Nature*, *424*(6945), 201-205.
- Zhang, Y., Dyck, R. H., Hamilton, S. E., Nathanson, N. M., & Yan, J. (2005). Disrupted tonotopy of the auditory cortex in mice lacking M1 muscarinic acetylcholine receptor. *Hear Res*, *201*(1-2), 145-155.

Vita

Paul V. Watkins

Date of Birth	June 1, 1977
Place of Birth	Midland, Michigan
Degrees	B.S.E., Computer Engineering, University of Michigan, Ann Arbor, May 1999 Ph.D., Biomedical Engineering, Washington University, St. Louis, December 2009
Academic Honors	Graduated Summa Cum Laude, University of Michigan, 1999 James B. Angell Scholar, University of Michigan, 1997, 1999
Professional Societies	Association for Research in Otolaryngology IEEE Society for Neuroscience
Publications	Watkins, P. V., Chen, T. L., & Barbour, D. L. (2009). A computational framework for topographies of cortical areas. <i>Biol Cybern</i> , 100(3), 231-248. Watkins, P. V., & Barbour, D. L. (2008). Specialized neuronal adaptation for preserving input sensitivity. <i>Nat Neurosci</i> , 11(11), 1259-1261. Gu, Y., Watkins, P. V., Angelaki, D. E., & DeAngelis, G. C. (2006). Visual and nonvisual contributions to three-dimensional heading selectivity in the medial superior temporal area. <i>J Neurosci</i> , 26(1), 73-85.
Abstracts	Watkins, P. V., & Barbour, D. L. (2008). <i>Rate regulation of sound level encoding in auditory cortex</i> . Society for Neuroscience Abstracts, Washington, DC. Barbour, D. L., & Watkins, P. V. (2008). <i>Dynamic range preservation by auditory neurons</i> . Society for Neuroscience Abstracts, Washington, DC.

- Watkins, P. V., & Barbour, D. L. (2008). *Adaptation Rates of Specialized Sound Encoders in Auditory Cortex*. Biomedical Engineering Society Abstracts, St Louis, MO.
- Barbour, D. L., & Watkins, P. V. (2008). *Specialized Coding of Sound Intensity in Auditory Cortex*. Biomedical Engineering Society Abstracts, St Louis, MO.
- Chen, T. L., Watkins, P. V., & Barbour, D. L. (2008). *Virtual Functional Imaging in Primary Auditory Cortex*. Biomedical Engineering Society Abstracts, St Louis, MO.
- Watkins, P. V., & Barbour, D. L. (2008). *Natural Wideband Acoustic Stimuli Reveal Complex Spectral Integration in Auditory Cortex*. Association for Research in Otolaryngology Abstracts, Phoenix, AZ.
- Chen, T. L., Watkins, P. V., & Barbour, D. L. (2008). *Limitations on Functional Imaging Resolution in Auditory Cortex*. Association for Research in Otolaryngology Abstracts, Phoenix, AZ.
- Watkins, P. V., & Barbour, D. L. (2007). *Spectral Integration of Natural Wideband Acoustic Stimuli in Auditory Cortex*. Society for Neuroscience Abstracts, San Diego, CA.
- Barbour, D. L., Watkins, P. V., Killian, N. J., & Davidson, L. S. (2007). *Spectral Contrast Shaping of Noisy Speech for Cochlear Implant Users*. Society for Neuroscience Abstracts, San Diego, CA.
- Watkins, P. V., & Barbour, D. L. (2007). *Neuronal Adaptation to Sound Level in Auditory Cortex*. Association for Research in Otolaryngology Abstracts, Denver, CO.
- Watkins, P. V., Killian, N. J., & Barbour, D. L. (2007). *Improved Speech Intelligibility by Spectral Contrast Shaping*. Association for Research in Otolaryngology Abstracts, Denver, CO.
- Watkins, P. V., & Barbour, D. L. (2006). *Sound Level Response Adaptation in Auditory Cortex*. Society for Neuroscience Abstracts, Atlanta, GA.
- Killian, N. J., Watkins, P. V., & Barbour, D. L. (2006). *The Effect of Spectral Contrast Shaping on Speech Intelligibility*. Biomedical Engineering Society Abstracts, Chicago, IL.
- Watkins, P. V., & Barbour, D. L. (2006). *Orthogonal Stimulus Features in Computational Topographies of Auditory Cortex*. Association for Research in Otolaryngology Abstracts, Baltimore, MD.
- Watkins, P. V., & Barbour, D. L. (2005). *Computational topographies of auditory cortex*. Society for Neuroscience Abstracts, Washington, DC.

**Teaching
Experience**

Undergraduate Teaching Assistant, University of Michigan,
Ann Arbor, MI, Introduction to Electrical Engineering and
Computer Science Course, January 1998 – May 1998
Teaching Assistant, Washington University, St. Louis, MO,
Quantitative Physiology Course, August 2006 – December
2006

**Work
Experience**

Broadcom Corporation, San Jose, CA, Design Verification
Engineer, September 2000 – July 2003
ATI Research, Santa Clara, CA, Systems Software Engineer, Test
Automation Engineer, June 1999 – September 2000
Dow Chemical, Midland, MI, Information Systems Student
Intern, May 1998 – August 1998

December 2009